The Dissertation Committee for Babafemi Anthony Ogunyomi Certifies that this is the approved version of the following dissertation:

Simple Mechanistic Modeling of Recovery from Unconventional Oil Reservoirs

Committee:

Larry W. Lake, Supervisor

Kamy Sepehrnoori

Sanjay Srinivasan

Christopher J. Jablonowski

James E. Bickel

Simple Mechanistic Modeling of Recovery from Unconventional Oil Reservoirs

by

Babafemi Anthony Ogunyomi, B.S; M.S.E

Dissertation

Presented to the Faculty of the Graduate School of

The University of Texas at Austin

in Partial Fulfillment

of the Requirements

for the Degree of

Doctor of Philosophy

The University of Texas at Austin

May 2015

Dedication

I dedicate this work to;

my parents, Mr. Olatokunbo S. and Mrs. Olufunke A. Ogunyomi, my wife, Oyinkansola

and my daughter Oluwadarasimi and my siblings, Yemi, Tomi and Jide

Acknowledgements

I thank God for his faithfulness he has thoroughly overwhelmed me with many undeserved graces and favor. My sincere gratitude and appreciation goes to Dr. Lake for his unflinching support and encouragement during the course of this work. I want to thank him for giving me the opportunity to work with and learn from him. I also want to thank him for being patient and understanding and for funding my research. I would also like to thank Dr. Jablonowski, he was very influential in my decision to pursue a doctorate degree. Thank you very much for all your help and encouragement. I would also like to thank Dr. Sepehrnoori, Dr. Srinivasan and Dr. Bickel for serving on my committee. I greatly appreciate the support and help I received from Shah Kabir.

The work reported in this dissertation was funded by the Center for Petroleum Asset Risk Management (CPARM) whose sponsors include Chevron, Caesar Systems (PetroVR), Weatherford, Drilling Info, Hess, BP and Kuwait National Oil Corporation. I want to thank you all; without your support this work would have not have been possible. I especially want to thank Hess Corporation for providing field data to test the models developed in this work. And to the wonderful people I worked with at Caesar Systems, Victor Koosh, Ken Blott, Torben Riis and Jim Thom, thank you for your support.

It has been a great privilege and experience attending such a prestigious program and along the way I have meet a lot of wonderful people who have contributed to my success. I would like to thank Cheryl Kruzie, Frankie Hart, Heather Felauer, Esther Barrientes, Roger Terzain and John Cassibry for all their help. I would also like to thank all the good friends I made during the course of this work.

Finally, I would like to thank my dad for the words of wisdom he shared with me, my siblings Yemi, Tomi and Jide thank you for all your prayers. I would also like to thank my beautiful and lovely wife, Oyinkansola, thank you for everything you have been to me and for the gift of being a father. To my beautiful daughter, Oluwadarasimi, I love you and there is no pressure whatsoever. I also would like to thank my father and mother in law for their help and support.

Simple Mechanistic Modeling of Recovery from Unconventional Oil Reservoirs

Babafemi Anthony Ogunyomi, Ph.D.

The University of Texas at Austin, 2015

Supervisor: Larry W. Lake

Decline curve analysis is the most widely used method of performance forecasting in the petroleum industry. However, when these techniques are applied to production data from unconventional reservoirs they yield model parameters that result in infinite (nonphysical) values of reserves. Because these methods were empirically derived the model parameters are not functions of reservoir/well properties. Therefore detailed numerical flow simulation is usually required to obtain accurate rate and expected ultimate recovery (EUR) forecast. But this approach is time consuming and the inputs in to the simulator are highly uncertain. This renders it impractical for use in integrated asset models or field development optimization studies. The main objective of this study is to develop new and "simple" models to mitigate some of these limitations.

To achieve this object field production data from an unconventional oil reservoir was carefully analyzed to identify flow regimes and understand the overall decline behavior. Using the result from this analysis we use design of experiment (DoE), numerical reservoir simulation and multivariate regression analysis to develop a workflow to correlate empirical model parameters and reservoir/well properties. Another result from this analysis showed that there are at least two time scales in the production data (existing empirical and analytical model do not account for this fact). Double

porosity models that account for the multiple time scales only have complete solutions in Laplace space and this make them difficult to use in optimization studies. A new approximate analytical solution to the double porosity model was developed and validated with synthetic data. It was shown that the model parameters are functions of reservoir/well properties. In addition, a new analytical model was developed based on the parallel flow conceptual model.

A new method is also presented to predict the performance of fractured wells with complex fracture geometries that combines a fundamental solution to the diffusivity equation and line/surface/volume integral to develop solutions for complex fracture geometries. We also present new early and late time solutions to the double porosity model that provide explicit functions for skin and well/fracture storage, which can be used to improve the characterization of fractured horizontal wells from early-time production data.

Table of Contents

List of Tables

List of Figures

Chapter 1: Introduction

This chapter presents a thorough description of the problem this dissertation solves and a brief summary of the organization of this dissertation.

1.1 Problem Description

According to Exxonmobil's Energy outlook to 2040, global energy demand will be about 30 percent higher in 2040 compared to 2010 with an increasing share of the global energy supply coming from unconventional sources such as shale formations. The volume of unconventional hydrocarbons in the world far outweighs the volume of their conventional counterpart (National Petroleum Council NPC, 2007); thus, unconventional reservoirs represent a vast, long-term, global source of energy. The NPC defined an unconventional reservoir as a reservoir in which hydrocarbons cannot be produced at an economic rate or in economic volumes unless the wells in the reservoir are stimulated by a large hydraulic fracture treatment, a horizontal wellbore or by using multilateral wellbores or some other technique to expose more of the reservoir to the wellbore. Examples of unconventional reservoir include tight sands, coalbed methane, and shale gas.

The development of unconventional reservoirs in the United States began in the 1820s. Many studies have been, and are still being carried out to better understand and predict the performance of unconventional wells. In spite of this, the economic development of unconventional reservoirs is still very risky. More recently, the development of unconventional reservoirs has been driven by the increase in oil and gas prices and technological advancements in drilling, completions, production and geosciences. Unconventional reservoirs are typically developed with a multitude of horizontal wells that are stimulated using multistage, propped hydraulic fractures. The induced fractures have a complex geometry that maximizes the contact area between the reservoir and the wellbore. Thus, it is believed that the initial production rates from these wells depend on the quality of the hydraulic fracture treatment. Because unconventional reservoirs have a very small permeability (of the order of a nano-darcy) and the wells drilled in these reservoirs are typically fractured, the performances of these wells are difficult to understand and predict. For instance, it is not possible to differentiate between production from the induced hydraulic fractures and the reservoir matrix nor is it possible to have a complete knowledge of the fracture geometry and hence predict the flow through these fractures.

Also, hydrocarbons are stored in unconventional reservoirs by three main mechanisms

1. They can be trapped in the primary porosity of the reservoir (matrix pore spaces)
2. They can also be trapped in the secondary porosity (open fractures) and
3. In shale gas reservoir, the gas can also be adsorbed on the organic matter that is present in the shales.

The hydrocarbons trapped within the secondary porosity are produced when the wellbore transverses these fractures while the adsorbed gas is produced when the reservoir pressure is sufficiently small to cause gas desorption. Several authors (Cipolla et al., 2009 and Moridis et al., 2010) have shown that desorbed gas production is not significant at the early stage of production from an unconventional reservoir but it becomes more important late in the field life contributing between 5-10% of the ultimate gas recovery.

Reservoir properties cannot be reliably evaluated from traditional pressure transient analysis, interference test or material balance techniques because of the typically very long times required in unconventional reservoirs to achieve stable flow (because of the extremely low permeability).

According to Lee and Sidle (2010) decline curve analysis is the most widely used method of forecasting production from shale gas wells. The empirical decline curve equation presented by Arps (1945) has the following general form:

$$q(t) = \frac{q_i}{\left(1 + bD_i t\right)^{\frac{1}{b}}} \tag{1.1}$$

In typical applications, equation 1.1 is fitted to production rate-time data to determine parameters b and D_i. Once the parameters are obtained, the equation is used to forecast the well/reservoir performance and also to estimate the ultimate recovery (EUR). In unconventional wells/reservoirs, the parameter b is often greater than 1 (b>1; a consequence of the fact that flow is dominated by transient effects) which makes the cumulative production estimated from equation 1.2 at large time ($t \rightarrow \infty$) to be greater than is physically possible, that is, $\lim_{t \rightarrow \infty} N_p(t) \rightarrow \infty$.

$$N_p(t) = \int_{\tau=0}^{\tau=t} q d\tau = \frac{q_i}{D_i(b-1)}\left[(1+bD_i t)^{1-\frac{1}{b}} - 1\right] \quad (1.2)$$

Several authors (Harrell et al., 2004; Cheng et al., 2008) have suggested ways to overcome this problem but the different methods suggested by these authors lack physical basis (Lee and Sidle, 2010).

A general consensuses developing in the reservoir engineering community with regard to the modeling of unconventional well performance is centered on two main ideas

1. A stimulated reservoir volume (SRV) develops around the fractured wellbore and
2. External to the SRV is an un-stimulated low permeability reservoir volume (reservoir matix).

These two ideas are at the core of most conceptual models. In reality, it is difficult to estimate the size of the SRV even from micro-seismic data (if it is available) and the geometry of the fractures introduces non uniqueness issues in most of the analytical models; thus, uncertainty is inherent in predictions of production from unconventional reservoirs.

Because of these difficulties in characterizing and predicting the performance of unconventional wells, it is difficult to formulate an “optimal” field development plan for these types of reservoirs. McKinney et al. (2002) showed that non-optimal well spacing in unconventional gas reservoirs resulted in about fifty percent loss in value. This indicates that it is important to identify the optimal well spacing for these reservoirs as early as possible in the project life. A plausible method of arriving at the optimal well spacing is to conduct a detailed integrated reservoir study that involves a multi-disciplinary team. A problem with this approach it that the information needed to perform this type of study is not readily available and also very uncertain at the planning phase of a project. This approach is also time consuming and expensive. Using this method to account for uncertainty will increase the cost and time exponentially. An emerging modeling approach in field development planning is integrated asset modeling (IAM) where all components of the system are modeled independently and then coupled dynamically to provide a holistic view of the project. This approach accounts for the interactions between subsystems e.g. surface and subsurface variables, such as pressure interactions/interference, fluid mixing and flow assurance, facility constraints and identification of system bottlenecks and backpressures. Acosta et al. (2005), Saputeli et al. (2008) and Rotondi et al. (2008) have reported some of the numerous advantages to integrated asset modeling. Ogunyomi et al. (2011 and 2010) and Ettehad et al. (2009) have reported different applications of IAM for field development optimization studies. A major advantage of IAM is that it permits the evaluation of the impact of different options on the entire system thereby facilitating better decision making. However, at the heart of the IAM is the need to have simple models for each component of the project that runs very fast. The simple models that currently exist for the reservoir component have no physical basis and they do not account for the multiple time scales that are believed to exist in the production data from unconventional reservoirs.

Given that we are yet to fully understand how the various physical processes govern production from unconventional reservoirs, we must develop time and cost efficient methods that honor the basic physical processes while at the same time accounting for uncertainties in the reservoir, facilities and economic parameters. No study as yet been done to present such a method and the objective of this work is to address this issue. Thus, the overall objective of this study is to develop a simple rate – time model that honors the basic physical process that controls flow from these reservoirs and also accounts for the expected multiple time scales observable in the production data.

1.2 Research Objectives

The primary objectives of this research are summarized below:

1. Understand the decline behavior and producing characteristics of oil wells by carefully and thoroughly analyzing production data from unconventional reservoirs to identify the predominant flow regimes and producing characteristics from these reservoirs.
2. Investigate the existence of any relationship between empirical model parameters and reservoir and/or well completion properties. The two empirical models considered in this study are the parallel flow and the logistic growth models.
3. Develop “simple” analytical and physics based models that describe and predict the production rate performance of unconventional oil wells/reservoir.
4. Verify the ability of the models developed to accurately predict the performance of unconventional wells/reservoirs with synthetic data and show their utility by applying it to field data.
5. Present new analytical models that can be used to model the performance of fractured horizontal wells with complex geometries.

1.3 Organization of Dissertation

Chapter one gives a description of the problem this dissertation addresses and states the research objectives and presents the organization of this dissertation.

In chapter two a critical and thorough review of the literature is presented. Chapter three gives the details of the result of field data analysis using model and theoretical based analysis and the development of functional correlations between the model parameters and the reservoir/well properties.

Chapter four presents a new analytical expression for modeling and forecasting production (and EUR) from fractured horizontal wells that exhibit multiple time scales and long periods of transient flow. In addition this chapter presents a sensitivity analysis of the new model. In chapter five a new approximate solution to the double porosity model is presented. This solution was developed using first principles and was validated with synthetic data and shown to have model parameters that are function of the reservoir and/or well properties. Example application of the new solution to field data is also shown. New analytical expressions for the double porosity model are developed in chapter six but unlike the widely available solution, the solution presented is for a conceptual model that has radial/circular fracture geometry. A key result in this chapter is the development of new analytical expressions for wellbore storage and skin. A sensitivity analysis of the new solution is also presented. Chapter seven presents the fundamental solution to the (3D) diffusivity equation and how to combine this solution with line and/or surface integrals to develop analytical solutions for fractures with complex geometries. Chapter eight summarizes the results presented in this work and gives the important conclusion. It also gives some advice on possible future direction for continued research using the result presented.

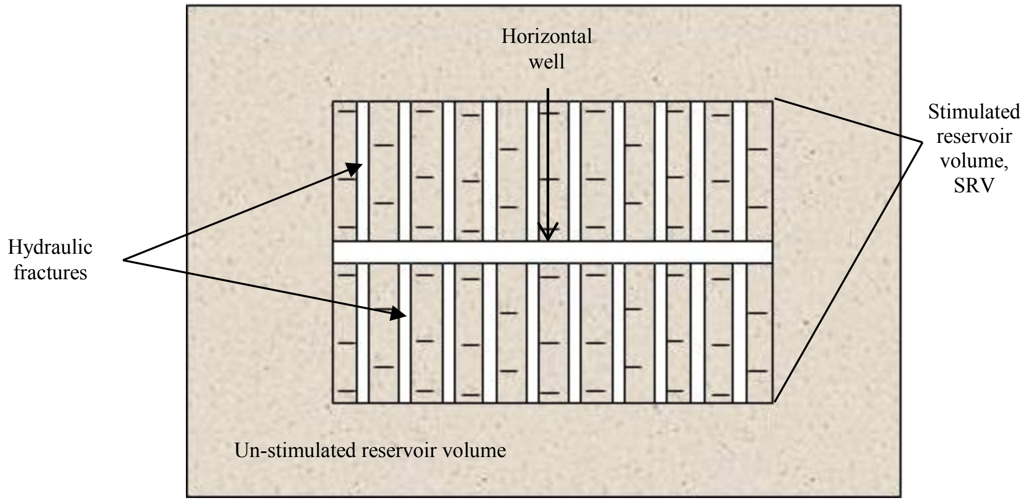

Figure 1-1: Conceptual model of a fractured horizontal well with a stimulated reservoir volume and the un-stimulated reservoir volume external to the SRV

Chapter 2: Review of Relevant Literature

This chapter provides a critical review of relevant literature to highlight the present gaps in knowledge that pertains to modeling and predicting production from unconventional oil reservoirs.

2.1 Traditional and Modern Decline Curve Analysis

After analyzing production data from conventional oil wells, Arps (1945) presented a family of equations that can be used to model the production decline behavior of these wells.

$$q(t) = \frac{q_i}{\left(1+bD_i t\right)^{\frac{1}{b}}}, \tag{2.1}$$

$$N_p(t) = \int_0^t q\,d\tau = \frac{q_i}{D_i(b-1)}\left[\left(1+bD_i t\right)^{1-\frac{1}{b}} - 1\right]. \tag{2.2}$$

Equation 2.1 is the general form of the decline equation and equation 2.2 is the cumulative form, where q_i D_i and b are the model parameters. When equation 2.1 is applied to production data from unconventional reservoirs the b parameter is often greater than one and when this occurs the ultimate recovery obtained from equation 2.2 is infinite (nonphysical), that is;

$$\lim_{t\to\infty} N_p(t) = \frac{q_i}{D_i(b-1)}\left[\left(1+bD_i t\right)^{1-\frac{1}{b}} - 1\right] = \infty. \tag{2.3}$$

Fetkovich (1980) presented a method of analyzing production decline using type curves, an idea analogous to that used in well testing. He presented different methods of constructing type curves for decline curve analysis and demonstrated that decline curve analysis has a strong fundamental basis by relating decline curve parameters to reservoir properties. An observation of his paper was that a decline exponent, $b > 1$ is required to match rate-time data for wells experiencing transient flow conditions. The data Arps analyzed were from wells drilled in conventional reservoirs as a result we can assume they were already in stabilized flow. Therefore the Arps' model(s) are not suitable for use in unconventional reservoirs. Palacio and Blasingame

(1993) presented a rigorous method for analyzing gas well performance with decline curve analysis via type curves. The curves are based on the use of modified time functions and a new algorithm to compute gas in place from production data for variable rate and/or variable pressures.

In a critical review of common methods used to estimate reserves in tight gas reservoirs, Cox et al (2002) concluded that the rate-time decline curve analysis should only be used when it is certain that flow is boundary dominated because the development of the rate-time decline curve method is based on the assumption that a drainage volume has been established by the well. Lee and Sidle (2010) also critiqued the volumetric, material balance, analog, decline curves, history matching and type curves methods of reserves determination and concluded that the understanding of the basic physics underlying the recovery processes is incomplete and that the commonly used decline curve models may be inappropriate for use in extremely low permeability reservoirs.

Kabir and Lake (2011) used a discretized form of the capacitance resistive model (CRM) to estimate the expected ultimate recovery from unconventional reservoirs. Their method was validated using synthetic and field data. In their study 3 blocks of the discretized CRM model was usually sufficient to match the historical production data. This probably corroborates the theory that hydraulically fractured shale gas wells have, in addition to the fractures created by the hydraulic fracturing process, a network of secondary fractures that are induced by the fracturing process. The stimulated reservoir volume (SRV) thus comprises the secondary network and the induced fractures (thus the first block could represent the network of secondary fractures; the second block could represent the main fractures while the third block could represent the undamaged volume adjacent to the SRV).

To overcome the nonphysical reserves estimate problem of the Arps model, Valko (2009) introduced the stretched exponential model (SEDM) for which the rate form is as shown in equation 2.4 and the cumulative form in equation 2.5:

$$q(t) = q_i e^{-(\frac{t}{\tau})^n}, \tag{2.4}$$

$$N_p(t) = \frac{q_i \tau}{n}\left[\Gamma\left[\frac{1}{n}\right] - \Gamma\left[\frac{1}{n}, \left[\frac{t}{\tau}\right]^n\right]\right], \tag{2.5}$$

qi, τ and n are the model parameters where $0 < n < 1$. In equation 2.5 Γ is the gamma function. According to Johnston (2008), the behavior described by equation 2.4 has been observed in a wide variety of physical systems and it can be interpreted as the global relaxation of system that contains many independent relaxing species or elements. Mathematically, $q(t) = q_i e^{-\left[\frac{t}{\tau}\right]^n} = \int_0^\infty P(s,n) e^{-\frac{s}{\tau^*}t} ds$; therefore, the SEDM is an empirical equation.

Ilk et al. (2010) presented the power law model which was also derived after analyzing production data from fractured horizontal wells in a shale gas reservoir. They found out that the decline rate plotted as a straight line on a log-log plot and with this observation they formulated and solved the problem given in equation 2.6 using appropriate boundary conditions

$$\frac{q(t)}{\left(\frac{dq}{dt}\right)} = -D_i t^{-(1-n)}. \tag{2.6}$$

The solution they obtained is given as shown below:

$$q(t) = q_i e^{(-D_i t^n)}. \tag{2.7}$$

But they found out that this solution is only valid during transient flow and decided to arbitrarily add another term to account for stabilized flow to obtain their final solution which is given by

$$q(t) = q_i e^{(-D_\infty t - D_i t^n)}. \tag{2.8}$$

The power law model given in equation 2.7 is identical to the SEDM, but for the arbitrary inclusion of a second term in the argument of the exponential term, the two models are essentially the same.

Duong (2011) also analyzed field production data from unconventional formations and observed that a graph of $\frac{q(t)}{G_p(t)}$ verses time plotted as a straight line on a log-log plot. Based on this observation he formulated the problem shown in equation 2.9:

$$\frac{1}{q(t)}\frac{dq(t)}{dt}=\frac{1}{\varepsilon(t)}\frac{d\varepsilon(t)}{dt}+\varepsilon(t), \tag{2.9}$$

where $\varepsilon(t)=at^{-m}$, *a* and *m* are constants. Upon solving the problem defined in equation 2.9 with appropriate initial condition, he obtained the rate and cumulative functions as:

$$q(t)=q_1 t^{-m} e^{\frac{a}{a-m}\left(t^{1-m}-1\right)}, \tag{2.10}$$

$$G_p(t)=\frac{q_1}{a}e^{\frac{a}{1-m}\left(t^{1-m}-1\right)}. \tag{2.11}$$

Clark et al. (2011) introduced the first application of the logistic growth model to forecast rate and EUR from unconventional formations. Logistic growth model have long been used in studies for predicting market penetration of new products, population growth, organ regeneration etc. A property of the logistic growth model that make them applicable to modeling flow from unconventional reservoirs is that in the limit to infinite time they have finite values. Tsoularis and Wallace (2002) presented the general form of the logistic growth model as:

$$\frac{dN(t)}{dt}=rN(t)^{\alpha}\left[1-\left(\frac{N(t)}{K}\right)^{\beta}\right]^{\gamma}, \tag{2.12}$$

where *K* is the carrying capacity, it is the maximum value the quantity *N* can ever get. r, α, β and γ are positive real parameters. In applying equation 2.12, Clark et al. (2011) after an empirical analysis of production data from gas wells made the following changes, $r=n\left(\frac{K}{a}\right)^{\frac{1}{n}}$, $\alpha=1-\frac{1}{n}$, $\beta=1$ and $\gamma=1+\frac{1}{n}$ (n is the hyperbolic exponent) to obtain the rate and cumulative equations:

$$q(t)=\frac{Knat^{n-1}}{\left(a+t^n\right)^2}, \tag{2.13}$$

$$N_p(t) = \frac{Kt^n}{a+t^n}\ . \tag{2.14}$$

All of these models were empirically derived as such they still suffer from the fact that the model parameters are not functions of the reservoir/well properties. They were all derived from analyzing production data from only gas wells. In addition none of these models accounts for the multiple time scales that these wells are expected to exhibit. If using the power law and Arps models, the user has to arbitrarily choose when transient flow ends which introduces a lot of uncertainty.

2.2 Reservoir/Fracture Characterization and Double Porosity Models

Barenblatt and Zheltov (1960) presented the first formulation of the double-porosity model and Warren and Root (1962) presented its first application to flow problems in the petroleum industry. The problem as formulated by Warren and Root (1962) is given by equations 2.15 and 2.16:

$$\frac{k_{2y}}{\mu}\frac{\partial^2 p_2}{\partial y^2} + \frac{k_{2x}}{\mu}\frac{\partial^2 p_2}{\partial x^2} - \phi_1 c_1 \frac{\partial p_1}{\partial t} = \phi_2 c_2 \frac{\partial p_2}{\partial t}\ , \tag{2.15}$$

$$\phi_1 c_1 \frac{\partial p_1}{\partial t} = \frac{\alpha k_1}{\mu}\left(p_2 - p_1\right). \tag{2.16}$$

The conceptual model for this problem is shown in **Figure 2-1**. They assumed that cross flow from the matrix into the fracture occurred under pseudo steady state condition (Equation 2.16). This assumption is likely not to be appropriate in unconventional reservoirs because of their typically very small permeability. They solved the problem for an infinite acting boundary condition and obtained the solution given below (s is the Laplace space variable):

$$p_2(s) = \frac{K_o\left(\sqrt{sf(s)}\right)}{s\sqrt{sf(s)}K_1\left(\sqrt{sf(s)}\right)}\ , \tag{2.17}$$

Where, $f(s) = \dfrac{\omega(1-\omega)s+\lambda}{(1-\omega)s+\lambda}$ is the inter-porosity transfer function, ω is the storativity ratio and λ is the inter-porosity flow parameter. A key result of their study was the presence of two time scales in the solution. The first time scale being attributed to the fracture while the second time scale is attributed to the matrix.

Since Warren and Root (1962) presented their solution, many authors (de Swaan, 1976; Mayerhofer, 2006; Carlson and Mercer, 1989; El-Banbi, 1998; Ozkan et al., 1987) have presented different applications of the model. All the analytical solutions presented have all been in Laplace space and have had to be numerically transformed to real time space using some form of inversion algorithm of which the Stehfest algorithm (Stehfest 1970) is the most popular.

Da Prat et al. (1982) presented a method of determining the permeability thickness product for a naturally fracture reservoir using the double porosity model. In another paper, Da Prat et al. (1981) presented type curves for decline curve analysis in double porosity systems. The curves were derived from the solution to the mathematical problem given by equations 2.15 and 2.16 for an infinite and closed outer boundary condition but in radial coordinates. Odeh (1965), Mavor and Cinco Ley (1979) also presented solutions for radial, infinite acting and closed outer boundary systems with and without skin and storage effects. All of these solutions assumed a pseudo steady state fluid transfer from the matrix to the fracture and were solved with Laplace transforms method.

El Banbi (1998) presented the solution for a double porosity reservoir with linear and used a transient matrix to fracture flow model. He presented a similar solution for the radial case but did not exploit the solution any further. More recently, Bello and Wattenbarger (2008) presented the solution to the double porosity model for linear flow in which they were able to obtain closed form analytical solutions for certain ranges of time. To do this they broke their Laplace space solution in to smaller intervals using special properties of the solution which they could invert to real-time space. This piece-wise solution would have to be applied sequentially.

Samandarli et al. (2011) presented the application of this solution to history matching and forecasting the performance of shale gas wells.

Song (2014) presented a finite-difference solution to this problem and its application to oil production from hydraulically fractured wells. Most of the solutions in the literature have assumed the fractures to have a quadrilateral/linear geometry and the few that have considered circular/radial fracture geometries did not analyze their solutions further.

Olanrewaju and Lee (1989) presented an analytical solution for double porosity reservoirs that permits modeling peudo steady and unsteady state matrix-fracture flow, for both finite and infinite acting reservoirs and it included the effect of gas desorption from the pore surfaces of shale matrix, wellbore storage and skin effect. Bumb and McKee (1988) presented an approximate analytical solution for single phase gas flow when gas is present both as free gas (in the pore volume) and adsorbed gas on the reservoir matrix. Gas desorption was modeled with the Langmuir isotherm, the approximate solution was verified with finite difference solution. They concluded that the effect of gas desorption cannot be detected from production test but can be easily determined from geologic information. Their solution also showed the effect of gas desorption as an increased compressibility term that is equivalent to a negative skin factor on the well production.

Ozkan et al. (2010) presented a study that investigated the effect advective and diffusive flow on the performance of fractured horizontal wells in unconventional reservoirs. Their result showed that while diffusive flow become important later in the life of the well it does not change the general characteristics of the flow rate profile and only increases the magnitude of the flow rate. These results suggest that a “useful model” can be developed if it is assumed that advective flow is the primary physical mechanism of flow while assuming the other mechanisms are negligible.

Miller et al., (2010) presented a work flow to characterize reservoir and hydraulic fracture properties for well performance evaluation and also developed a lump parameter model that can be used for stochastic forecasting of shale gas wells. The method is based on the assumption that a stimulated reservoir volume (SRV) develops around the fractured well and there is a region of un-damaged reservoir far from the well. They also assumed that four flow regimes can be observed in shale gas well performance; internal linear transient, internal depletion, external linear transient and drainage volume depletion. A weak point of the model they presented is that it has non-uniqueness issues and it is a lumped model.

2.3 Production Data Analysis

Doublet et al. (1994) presented a method of analyzing and interpreting production data in order to estimate reservoir volumes and flow characteristics using type curves matching techniques and material balance time function. The method involves plotting production rate functions (pressure drop normalized rate function, rate integral function and rate integral derivative function) against the material balance time and then matching the plots to the Fetkovich/McCray type curve, making sure that the boundary dominated portion of the production data falls on the Arps b = 1 region of the type curve. One of the match points is then used to compute the desired reservoir properties. The method can be used to obtain reliable estimates of the original and movable oil volumes as well as good estimates of permeability and skin factor.

Building on the work of Cox et al. (2002) and Bumb and Mckee (1988), Lewis and Hughes (2008) presented a method of analyzing production data from shale gas well accounting for adsorbed gas. They presented example applications of the method to a simulated data set as well as 2 field cases. But the sheer number of parameters in their model makes the analysis method difficult to interpret and corroborate the results obtained. The method did show the existence of the flow regimes used to constrain many of the model parameters. Anderson et al. (2010) also presented a method of analyzing production data from shale gas wells that considered the long term well performance that is typical ignored by other methods. Their method accounts for multiple transverse fractures in horizontal wells and also allows the stimulated reservoir volume to reside within an infinite acting reservoir. The paper presented a systematic way of using the log-log plot, specialized plot – square root-time plot and flowing material balance plot to identify flow regimes, derive reservoir and fracture parameter and also estimate reserves.

2.4 Analytical or Semi Analytical Solutions for Complex Fracture Geometries

Gringarten and Ramey (1973) presented the application of Green's functions and Source function for solving flow problems in petroleum engineering. They summarized the basic properties of the Green's function and the solution for problems with uniform flux sources and also showed how the solution reduces to the fundamental point source solution of heat conduction problems as presented by Lord Kelvin (1884). They also showed how to extend the solution to an infinite conductivity source. The solution used the Newman production method to obtain solutions to a wide variety of flow problems. Gringarten et al. (1974a) presented analytical solutions for a vertically fractured well by using Green's function and the Newman's product method. The solutions were for a uniform flux and infinite fracture conductivity case. They showed that the solution for the infinite conductivity fracture case can be obtained from the uniform flux solution when it is evaluated at the fracture plane with $x_D = 0.732$. A comparison of these solutions with the numerical solution of Russell and Truitt (1964) showed that there were errors in some cases of the Russell and Truitt solution.

Gringarten and Ramey (1974b) presented analytical solutions for a well (producing at a constant rate) with a single horizontal fracture of finite thickness at any position within a producing interval in an infinitely large reservoir. The solution is a general solution that can be used to model plane horizontal fractures, partial penetration of the producing formation and limited flow entry throughout a producing interval. The model presented showed that there are four possible different flow regimes that can be observed with horizontal fractures. The first flow regime due to fracture storage could be absent depending on the fracture size. A major conclusion of this study is that the behavior of horizontally fractured wells differs from that of vertical fractured wells for small values of h_D (dimensionless reservoir thickness) therefore it is possible to identify horizontal fractures from well-test data.

Cinco Ley et al. (1978) presented general solutions for the transient pressure behavior of a well intersected by a finite-conductivity vertical fracture. These solutions were obtained with Green and source functions and the Newman product method, due to the coupling of the fracture and matrix equations they obtained a Fredholm integral equation which was solved numerically and thus they obtained effectively a semi analytical solution.

Ramey and Gringarten (1975) presented the result of the application of the high-volume vertical fracture solution to steam well data from The Geysers. They presented the log-log type curve matching and semi-log graphing of transient pressure data. The solution used was derived using a finite difference simulator that was originally developed to study partially penetrating well with storage and skin effect.

Hagoort (2009) presented a solution to the diffusivity equation for pseudo steady state in a closed rectangular reservoir which was developed using Fourier finite transform. This solution was used to evaluate the productivity index of a vertical, infinite conductivity fracture in a closed rectangular reservoir for different fracture lengths, reservoir aspect ratios and fracture eccentricity. These PI were then compared to those reported using the equivalent pressure (EP) and the average pressure (AP) methods. The result of this comparison showed that the PI's obtained with the EP method were too optimistic while those obtained with the AP method were too pessimistic. Both methods gave the correct solution when the fracture was totally penetrating. They also presented a comparison of shape factors against the Earlougher shape factors. These results showed that the shape factors reported by Earlougher were considerably larger than those obtained using the exact solution they presented except when the fracture is completely penetrating.

Medeiros et al. (2010) presented a semi analytical method for computing pressure transients in heterogeneous formations with composite, layered and compartmentalized reservoirs. Amini and Valko (2010) introduced the distributed volume sources method of predicting production from fractured horizontal wells with non-Darcy flow conditions. Kuchuk and Biryukov (2013) investigated the pressure transient behavior of continuously and discretely fractured naturally fractured reservoirs using semi-analytical solutions. The basis function used in all of these methods is the Green's function solution. All the fracture geometry considered are the linear or quadrilateral types, no consideration was given to fractures with curved or more complex geometries. Wu (2014) has shown that hydraulic fractures tend to be curved or have complex geometries (see **Figure 2-2**) yet no analytical/semi-analytical solution has been presented for such geometries. Ozkan (1988) presented a point source solution to the diffusivity equation for an infinite acting reservoir in Laplace space and used the method of images to produce solutions for closed outer boundary reservoirs and he developed a library of solutions for regular shaped sources.

All the methods and tools that have been developed were based on the analysis of production data from gas fields. In addition all the analytical solutions available for the double porosity models are only available in Laplace space. Most solutions only considered hydraulic fractures with linear or quadrilateral geometries and those that considered radial flow in the fractures only obtained closed form analytical solutions in Laplace space and did not analyze the solutions any further. Beyond numerical solutions, no solutions for complex fracture geometries have been published in the literature. This dissertation develops solutions to fill the gaps highlighted above.

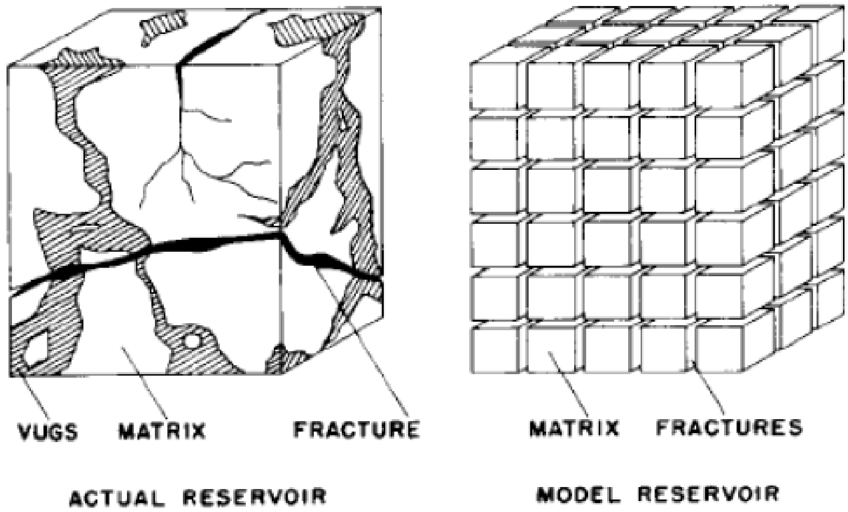

Figure 2-1: Schematic of an actual fractured reservoir and its corresponding idealization

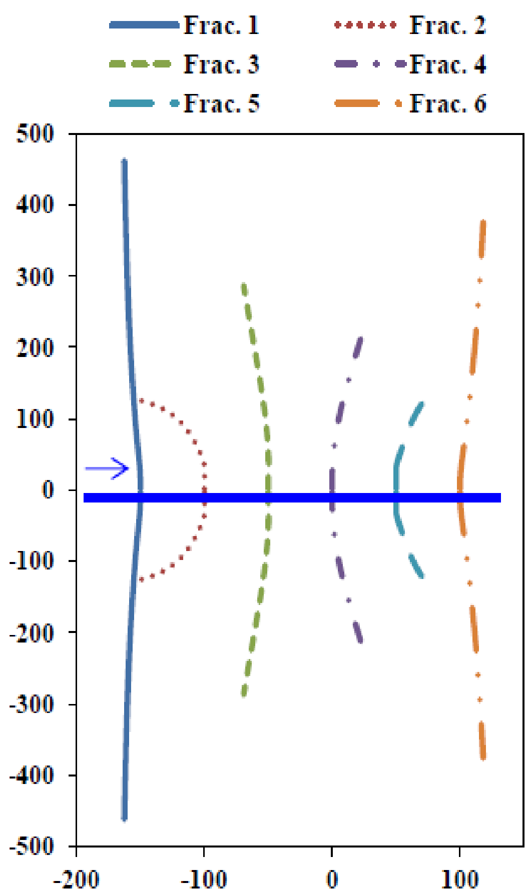

Figure 2-2: Predicted fracture geometry after hydraulic fracturing (Source: Kan Wu, 2014)

Chapter 3: Correlation Functions for Empirical Model Parameters and the Reservoir and Well properties

Most decline curve methods have two main limitations; the model parameters as a rule are not functions of reservoir parameters and in unconventional reservoirs may yield unrealistic (non-physical) values of expected ultimate recovery (EUR) because boundary-dominated flow may not develop in unconventional reservoirs. Over the past few years, several empirical models have emerged to address the second limitation, but they are challenged by the time to transition from infinite-acting flow period to the boundary-dominated flow. In the study presented in this chapter, we performed statistical and model-based analysis of production data from hydraulically fractured horizontal oil wells and present a method to mitigate some of the limitations highlighted above.

The production data were carefully analyzed to identify the flow regimes and understand the overall decline behavior. Following this step, we performed model-based analysis using the parallel-flow model (sum of exponential terms), and the logistic-growth model (Clark et al., 2011). After the model-based analysis, the model parameters were analyzed statistically and cross plotted against available reservoir and well completion parameters. Based on the conclusion from the cross-plots and statistical analysis, we used design of experiments (DoE) and numerical-reservoir simulations to develop functions that relate the model parameters and reservoir/well completion properties.

3.1 Method

The data used for this study comes from a liquid-rich shale play in North America. This dataset contains data from 80 wells, with varying well lengths and completion properties. These wells have also been on production for varying amounts of time, ranging from 50 – 1500 days. Water production from these wells was relatively low with average water cut between 0.1 and 0.3. This data are reported on a daily basis and therefore constitute high-frequency information.

The work flow used for this study is summarized as follow:

1. Analyze oil rate and well head pressure data to identify the predominant flow regime and signatures from this data set.
2. Perform model-based data analysis by fitting oil rate to empirical models to estimate the model parameters.
3. Analyze and crossplot the model parameters obtained in step 2 against available reservoir and well completion properties. This step enabled investigation of the existence of any relationship between the empirical model parameters and the reservoir and well completion properties.
4. Because the previous steps did not reveal any significant relationship; a workflow was developed that uses design of experiment (DoE) and numerical reservoir flow simulations to develop relationships between the model parameters and the reservoir and well completion properties.

3.1.1 Theoretical Basis for Flow Regime Identification

Wattenbarger et al. (1998) presented an application of the solution to the one dimensional diffusivity (linear coordinates) equation for a closed rectangular boundary to facilitate the analysis of production data in tight gas wells. The solution shows that for the constant pressure inner boundary condition, a log-log plot of rate versus time plots as a straight line with a slope of one half at early times and as an exponential decline at late times. This solution is given by the following expression:

$$q_D\left(t_D\right) = -2\sum_{n=1}^{\infty}\left(-1\right)^n e^{-\left[\left[\frac{(2n-1)\pi}{2}\right]^2 t_D\right]} sin\frac{(2n-1)\pi}{2}, \tag{3.18}$$

where, q_D is the dimensionless production rate and t_D is the dimensionless time.

For the constant rate inner boundary condition, a log-log plot of wellbore pressure versus time also plots as a straight line with a slope of one half and transitions to another straight line with unit slope. The solution for this case is given as

$$p_{wD}\left(t_D\right) = \frac{t_D}{2} + \frac{1}{\pi^2}\sum_{n=1}^{\infty}\frac{\left(-1\right)^n}{n^2}\left(1-e^{-n^2\pi^2 t_D}\right)\cos\left[n\pi\right], \tag{3.19}$$

where p_{wD} is the dimensionless pressure at the wellbore.

Plots of these solutions (equations 3.1 and 3.2) are in Figure 3-1. The characteristics of these solutions have been observed in production data from many hydraulically fractured horizontal wells in unconventional formations. Patzek et al. (2013) analyzed production data from 8,294 stimulated horizontal wells in North America and observed that the flow rate from these wells obeyed a simple scaling theory where the flow rate is proportional to the inverse of the square root of time. A behavior that can be modeled with equation 3.1.

Cinco-Ley and Samaniego (1981), Kuchuk and Biryukov (2013) and Bello et al. (2008) have shown that a quarter slope on a log-log plot of rate versus time (constant pressure inner boundary condition) can be interpreted as the simultaneous linear flow of fluid in the fracture and reservoir matrix. Equation 3.1 does not capture the quarter slope because it is for the case where there is flow from the reservoir matrix in the fracture face. On this basis we analyzed the data set.

The data set had both production rates and tubinghead pressures. We use the tubinghead pressures as a proxy for the bottomhole well flowing pressure by assuming that there is a constant pressure difference between the tubinghead pressure and the bottomhole pressure because of the pressure head of fluids in the wellbore. Figure 3-2 shows a typical dashboard from the flow regime identification exercise.

From the log-log plots of rate versus time and tubinghead pressure versus time for all the wells in the data set we make the following observations:

1. The rate-time plots showed slopes of one-half, one, one-and-a-half and exponential decline in no particular order. But in general the wells exhibit a power law behavior with the one-half slope being the predominant slope observed.
2. The plot of the tubinghead pressures versus time show the existence of at least two time scales in most of the wells. We make this conclusion because we observe a one half slope followed by an exponential curve and this is followed by a constant tubinghead pressure. The exponential curve defines the fracture boundary and the constant tubinghead pressure indicates flow from the reservoir matrix.

3.1.2 Model Based Analysis

This section presents the results of the model based analysis. We considered two empirical models in this analysis, the logistic-growth model and the parallel-flow model (sum of exponential terms). These models were fitted to rate and cumulative production data to obtain the model parameters, which were statistically analyzed. We then investigated the existence of any relationship between the model parameters and the reservoir and well completion properties by cross-plotting them against available well completion and reservoir properties.

Parallel Flow Model:

The parallel-flow model or sum of exponential model is based on the conception that when a horizontal well is hydraulically fractured, the reservoir rock is broken into or subdivided into discrete blocks, each of which makes independent flow contribution to surrounding the fractures. Flow from each piece of block is assumed to decline exponentially, which is consistent with boundary-dominated flow. A model that accounts for both transient flow and boundary dominated flow is present in Chapter 4. The mathematical expression for rate is then given by

$$q_T(t) = \sum_{k=1}^{N_e} q_{i_k} e^{-\frac{t}{\tau_k}} , \quad (3.20)$$

where,

$q_T(t)$ = production rate from the fractured horizontal well

q_{ik} = initial production rate from the reservoir matrix element k

τ_k = time constant for reservoir matrix k, defined mathematically as $\frac{v_p c_t}{J}$,

v_p is the matrix pore volume, c_t is the total matrix compressibility and J is the productivity index of the matrix, with units b/d/psi. This definition of the time constant is identical to that used in the capacitance resistance model (CRM) (Sayapour et al. (2008); Nguyen et al., 2010; Cao et al. 2014).

For the parallel flow model the model parameter estimation was done by minimizing the problem defined below

$$\min e = \sum_{m=1}^{M} \left[f_m - \left[\sum_{k=1}^{N_e} f_k e^{-\frac{t}{\tau_k}} \right]_m \right]^2 , \quad (3.21)$$

subject to:

$$\sum_{k=1}^{N_e} f_k = 1$$

where,

$f_k = \frac{q_{i_k}}{q_{i_T}}$; q_{iT} is the maximum value of production rate in the data and $f_m = \frac{q_m^{data}}{q_{i_T}}$.

In formulating the model fitting problem, equation 3.4, we have normalized the model and data with the maximum value of production rate and then included the constraint that the coefficient of the exponential terms must be fractions that sum to 1. The objective of this formulation is so that we need not specify the number of exponential terms in the model beforehand, that is, N_e can be set to large number and the optimization process would return a value for N_e that will give the best fit to the data. The number of terms required is obtained as the number of fractional coefficients (f_k) of the exponential terms that are not equal to zero. The model was fitted to data by finding values of f_k and τ_k that minimize equation 3.4. Song (2014) while using an 11 cell finite difference model to analyze field production data revealed that a minimum of two to three cells were adequate in modeling production data.

<u>Logistic Growth Model</u>:

Logistic growth models are often used to model growth (population, market penetration of new products and technologies), see Tsoularis and Wallace (2001). Clark et al. (2011) presented the first application of the logistic growth model for predicting performance of unconventional reservoirs. The logistic growth model presented by Clark et al. (2011) is given as

$$N_p(t) = \frac{Nt^n}{a+t^n}, \tag{3.22}$$

where,

N = carrying capacity, bbls

a = constant, time^n

n = hyperbolic exponent, unitless

$t =$ time.

An expression for the production rate, q, is obtained by differentiating equation 3.5 with respect to time,

$$q(t) = \frac{Nant^{n-1}}{\left(a + t^n\right)^2}. \tag{3.23}$$

Clark et al. (2011) described the carrying capacity in equations 3.5 and 3.6 as the estimated ultimate recovery for a well without an economic constraint and it acts as an upper limit on the cumulative production. The logistic growth model would not account for multiple scales observed in the production data. Note that in equation 3.5 $N_p(t) \to N$ as $t \to \infty$. For the logistic growth model we applied equations 3.5 and 3.6 to the data set by finding the values of the model parameters (N , n and a) that minimized the squared difference between the model predictions and field production rate data, that is

$$\min e = \sum_{m=1}^{M} \left[q_m^{data} - q_m^{\text{model}} \right]^2 + \sum_{m=1}^{M} \left[N_{p,m}^{data} - N_{p,m}^{\text{model}} \right]^2. \tag{3.24}$$

3.1.3 Results of Model-Based Analyses

3.1.3.1 Example Application of Parallel-Flow Model

In estimating the model parameters with the parallel flow model, N_e (the number of exponential terms) was initially set equal to four. An example application of the model to a well (UT-ID4) in the data set is in Figure 3-3. As shown in Figure 3-3 the parallel flow model gives a good fit to the production data (rate and cumulative), Figure 3-3b shows that the coefficient of determination is large at a value of 0.94. Figure 3-3d is a plot of the error versus time; error is defined as the squared difference between the model predictions and data. The error is larger at early time because there is more scatter in the data compared to late time. A summary of the model parameters obtained for this case is in Table 3-1.

This well only needs two exponential terms in the parallel flow model to obtain a good fit between the model and data. The fact that f_2 and f_3 turned out to be zero is most likely because of the initial condition. The estimated EUR for this well is 1.77×10^5 STB.

3.1.3.2 Example Application of Logistic Growth Model

Figure 3-4 presents an example application of the logistic growth model to the same well (UT-ID4) in the data set. From this figure the coefficient of determination is also large with a value of 0.83 (not as large as the 0.94 obtained with the parallel flow model). Again, there is more error at early time because there is more scatter in the data at early time. The model parameters obtained for this example are summarized in Table 3-2. The carrying capacity obtained for this well is $1.1\text{x}10^5$ STB; therefore, the EUR from this well based on the logistic growth model is $1.1\text{x}10^5$ STB.

3.1.4 Results of Statistical Analysis of Model Parameters

3.1.4.1 Analysis of Parallel-Flow Model Parameters

After applying the parallel flow model to all the 87 wells in the data set it was observed that 58 wells required only three exponential terms, 28 wells required only 2 exponential terms and only 1 well required four exponential terms. The resulting distribution of the fitting parameters is in Figure 3-5. Figure 3-5a, 3-5c, and 3-5e all present the distribution of initial production rates for each term in the parallel flow model that was not equal to zero. From these figures we conclude that all of the distributions are log-normally distributed, therefore initial production rates with values close to the mean value are more frequent than initial production rates with large value. The lognormal distribution also suggests that some extremely high values of initial production rates are also possible although infrequent. Figure 3-5b, Figure 3-5d and Figure 3-5f are the corresponding distributions of time constants. The distributions of the time constants also appear to follow a log normal distribution. The values of the time constants in Figure 3-5d and Figure 3-5f appear to have the same order of magnitude with mean values of $4.7x10^4$ and $4.1x10^4$ days, respectively. The values of time constants in Figure 3-5d and 8-5f appear to be a factor of 10 greater than the values in Figure 3-5b, the mean value of the time constants in Figure 3-5b is 381. This observation suggests that the time constants in Figure 3-5d and 8-5f are from the same distribution and the time constants in Figure 3-5b are from another distribution.

Physically, the time constants can be interpreted as a measure of how fast the fluids in a reservoir would drain; small values indicate that the fluids would drain very fast and large values imply that it would take longer for the fluids to drain from the reservoir (Ogunyomi et al., 2014). Based on this definition of the time constant we can state that there are at least two time scales in the data set, one time scale accounts for the high transmissibility, low storativity fractures (τ_1) and the second time scale accounts for the low transmissibility, high storativity reservoir matrix (τ_2 and τ_3). Table 3-3 presents the statistical summary of the model parameters for the parallel flow model. The range of each of the parameters in this table is quite large; this indicates that there is a great degree of variability in the well performance in the data set.

3.1.4.2 Analysis of Logistic Growth Model Parameters

Figure 3-6: presents the distributions (PDF and CDF) of the model parameters obtained for the logistic growth model. A general observation from this figure is that they also all appear to be log normally distributed.

Table 3-4 presents the statistical summary of the logistic growth model parameters for wells in the dataset. The mean value of the carrying capacity is 1.3×10^5 stb with a standard deviation of 6.9×10^4 stb. It has a range of 4.1×10^5 stb. The hyperbolic constant and the constant a have mean values of 0.62 and 5897, respectively. The range of n and a are 2.13 and 4.8×10^5 respectively. This outcome can also be interpreted as the result of high degree of variability in well performance.

3.2 Correlation between Model Parameters and the Reservoir and Well Completion Properties

We investigate the existence of relationships between the model derived parameters and the reservoir and well completion properties with the two methods. For the first method, we investigated the existence of a linear relationship between variables by computing the correlation coefficient. Navidi (2008) defined the correlation coefficient (ρ) as a measure of the degree of linear relationship between two variables, and it varies between +1 and -1. A value of +1 implies a strong positive linear relationship, a value of -1 means a strong negative linear relationship and a value of zero implies that there is no linear relationship between the two variables.

With the second method, nonlinear relationships were investigated by making cross-plots of the model parameters (including its transforms) and the reservoir and well completion properties. These cross-plots are then evaluated for any recognizable functional relationship. The reservoir and well completion properties that were considered are:

1. Initial number of fracture stages
2. Lateral length of horizontal well
3. Porosity

4. Thickness
5. Initial reservoir pressure
6. Fluid injected and
7. Weight of proppant of injected

3.2.1 Parallel Flow Model

The computed correlation coefficients for the parallel flow model and the reservoir and well completion properties are summarized in Table 3-5 in which we have highlighted values of $|\rho| \geq 0.2$. From this table we notice that the initial production rates show some level of correlation with most of the reservoir and well completion properties. The time constants on the other hand do not show the same level of correlation. The result of the statistical analysis of model parameters revealed that there are at least two time scales in the producing characteristic of the wells; therefore, in this section we use two terms of the PFM which yields the rate time function shown below;

$$q_T(t) = q_{i_1} e^{-\frac{t}{\tau_1}} + q_{i_2} e^{-\frac{t}{\tau_2}}, \tag{3.25}$$

where q_{i_1} and q_{i_2} are the initial production rate one and initial production rate two respectively. τ_1 and τ_2 are the time constant one and time constant two respectively.

<u>*Initial Number of Fracture Stages*</u>: The cross plots in Figure 3-7 show the cross plot of PFM parameters and the initial number of fracture stages. Figure 3-7a is the cross plot of initial production rate one and the initial number of fracture stages. Figure 3-7b is the cross plot of time constant one and initial number of fracture stages. Figure 3-7c is plot for the initial production rate two and the initial number of fracture stages and Figure 3-7d shows the time constant two plotted against the initial number of fracture stages. Although there is some scatter in all the plots shown in Figure 3-7 we can make the

following general comments; the initial production rates (one and two) increase as the initial number of fracture stages increases. The increase in the initial production rates was steep initially until the initial number of fracture stage is about 10 – 15 after which it became less steep. The time constants do not show any significant trend on the plots. Physically, this observation suggests that increasing the number of initial fracture stages beyond 15 will not significantly increase the performance of the well.

Lateral Length (l_w): The cross plots shown in Figure 3-8 are identical to those in Figure 3-7 except that the x-axis is now the lateral well length. From this figure no discernable relationship can be inferred between the model parameters and the lateral well length.

Porosity: The cross plots shown in Figure 3-9 are identical to those in Figure 3-7 except that the x-axis has been replaced by the reservoir porosity. No discernable relationship in observed in the plots presented in Figure 3-9.

Thickness: The cross plots shown in Figure 3-10 are identical to those in Figure 3-7 except that the x-axis has been replaced by the reservoir thickness. No discernable relationship in observed in the plots presented in Figure 3-10.

Initial reservoir pressure: The cross plots shown in Figure 3-11 are identical to those in Figure 3-7 except that the x-axis has been replaced by the initial reservoir pressure. No discernable relationship in observed in the plots presented in Figure 3-11.

Fracture Fluid Injected: The cross plots shown in Figure 3-12 are identical to those in Figure 3-7 except that the x-axis has been replaced by the volume of fracture fluid injected. The initial production rates (one and two) increases as the volume of fracture fluid injected increases. The increase in the initial production rates was very steep initially until the injected fluid volume is about $2.5 x 10^{4}$[1] after which it became less steep. This observation suggests that increasing the volume of injected fluid beyond $2.5 x 10^{4}$ will not significantly increase the performance of the well. The time constants show a negative exponential relationship with the volume of fluid injected.

Weight of Proppant Injected: The cross plots shown in Figure 3-13 are identical to those in Figure 3-7 except that the x-axis has been replaced by the weight of proppant injected. The initial production rates (one and two) increases as the volume of fracture fluid injected increases. The increase in the initial production rates was very steep until the weight of proppant injected is about 10^{6} after which it became less steep. This observation suggests that increasing the weight of proppant injected beyond 10^{6} will not significantly increase the performance of the well. The time constants show a negative exponential relationship with the volume of fluid injected.

3.2.2 Logistic Growth Model (LGM)

Table 3-6 presents the computed correlation coefficients between the model parameters and the reservoir and well completion properties. In this table we have highligted $|\rho| \geq 0.2$. Based on these criteria, the carrying capacity possibly has a linear relationship with well spacing, porosity, the average injection pressure, total fluid injected and the weight of proppant injected. The fact that the carrying capacity correlates with well spacing and porosity suggests that there is a relationship between the carrying capacity and the drainage volume of the well. The hyperbolic constant, n, and the constant, a, do not have any linear relationship with the reservoir and well completion properties.

[1] The unit for the volume of fluid injected was not included in the data set.

Nonlinear relationships were investigated by making cross plots of model parameters and the reservoir and well completion properties. The results are summarized below:

Initial Number of Fracture Stage: The cross plots in Figure 3-14 show the cross plot of logistic growth model parameters and the initial number of fracture stages. From this figure the carrying capacity and hyperbolic exponent have no nonlinear relationship with the initial number of fracture stages. Constant a on the other hand has a power law relationship with the initial number of fracture stages.

Lateral Length (l_w): The cross plots in Figure 3-15 show the cross plot of LGM parameters and the lateral well length. It can be concluded from this figure that the carrying capacity and hyperbolic exponent do not have any systematic nonlinear relationship with the lateral well length. Constant a has a logarithmic relationship with the lateral well length.

Porosity: Refereeing to Figure 3-16. The carrying capacity appears to have a linear relationship with the reservoir porosity. While the hyperbolic exponent and constant *a* do not show any relationship with the reservoir porosity.

Thickness: From Figure 3-17 it is observed that there is no relationship between the LGM parameters and the reservoir thickness.

Initial reservoir pressure: There are no relationships between the LGM parameters and initial reservoir pressure; refer to Figure 3-18.

Fracture Fluid Injected: From Figure 3-19a and Figure 3-19b we infer that the carrying capacity and hyperbolic exponent do not have any discernable relationship with the volume of fracture fluid injected. Figure 3-19c suggests that constant a has a power law relationship with the volume of fluid injected.

Weight of Proppant Injected: Figure 3-20 suggests that there is no relationship between the LGM parameters and the weight of proppants injected.

3.3 Development of Mathematical Relationships between Empirical Model Parameters and Reservoir and Well Completion Properties

The results of the statistical analysis of the model parameters in the previous sections show that the model parameters correlate to some degree with the reservoir and well completion properties. In this section we use design of experiment (DoE), numerical reservoir simulation and response surface modeling (RSM) to develop functional relationships between the model parameters and the reservoir and well completion properties. More details on the theory of DoE and RSM can be found in Box et al. (2005) and Myers and Montgomery (2002).

We developed the functional relationship by:

1. Generating data from numerical reservoir simulation, where we built the numerical simulation models based on the result of a fractional factorial design experiment. We used a 2_{VI}^{9-2} fractional factorial design, which resulted in 256 numerical reservoir simulation runs. The reservoir and well properties used for this experiment are in Table 3-7. The size of the reservoir used is 10100 ft by 5575 ft and it was divided into a 101 × 25 grid blocks. The fracture were refined into an 11 × 5 × 1 grids and geomechanics effect was ignored. Figure 3-21 is a schematic representation of the process described above and Figure 3-22 is one of the numerical simulation models used for data generation.
2. After generating the synthetic data, we estimated the parameters for the empirical models (logistic growth and parallel flow model) by fitting them to data using the

method described earlier. Rate and cumulative production data was used in the fitting exercise.

3. Identify the reservoir and well completion properties that have the strongest effects on each parameter in the empirical models. We identified the strongest effects by performing regression analysis on each parameter in the empirical model and all the variables in Table 3-7. Using the t-statistic from the regression analysis, we eliminate those variables whose coefficient is most likely equal to zero based on their P-values from testing the null hypothesis. More details on hypothesis testing can be found in Jensen et al. (200) and Navidi (2008). The P value is the probability that the coefficient of a variable is equal to zero. The larger the P values the more likely the coefficient is equal to zero and the smaller it is, the less likely the coefficient is equal to zero. A P-value of 10^{-4} was chosen as cut off (the cut off P-value was arbitrarily chosen and has no physical or mathematical basis), if the P-value is greater than 10^{-4}, the coefficient of that variable is not significantly different from zero and we can eliminate such variables from further analysis. Table 3-8 provides a summary of the result of this step; the solid dots indicate that the reservoir/well property that has a strong effect on the value of the corresponding model parameter. For example fracture half-length has a strong effect on the value of the carrying capacity for the logistic growth model while it does not have a strong effect on the remaining parameters.

4. From step 3, we have a list of variables that have the strongest effect on each model parameter. We then perform a full factorial design of experiment with the variables in this list for each model parameter after which we build the numerical reservoir model to generate data with the result (unimportant properties were kept unperturbed at their expected values). The design table for the carrying capacity, N, is presented

in Table 3-9 this design is for a 2^3 full factorial experiment with 8 numerical simulation models. Because the constant a has all its main effect variables in common with the hyperbolic constant, we use the same design table for their experiment. Table 3-10 is the design table for n and a, the experiment design was for a 2^4 full factorial design with 16 numerical simulation models. We also combined the design table for the parallel flow model parameters because they have many of the main effects variables in common. The design for the parallel flow model parameters was a 2^7 full factorial design with 128 numerical simulation models; the design table is presented in Table 3-11.

5. Repeat step 2 to obtain the model parameters that would be used to develop the response surface function.
6. Using regression analysis we develop a functional relationship between each of the model parameters and the reservoir and well completion properties. The developed relationship is then validated with synthetic examples.

The results obtained for step 6 are presented in the next subsection:

3.3.1 Correlations for Logistic Growth Model Parameters

3.3.1.1 Carrying Capacity, N

$$N\left(h, L_w, x_f\right)^{0.17} = 5.74 + 2.63\times10^{-2}h + 2.1\times10^{-4}L_w + 1.1\times10^{-3}x_f \, . \tag{3.26}$$

Equation 3.9 is the response surface function for carrying capacity that shows the relationship between the carrying capacity and the reservoir thickness (h), well length (L_w) and the fracture half length (x_f). Different transformations of the carrying capacity were evaluated; we chose the transformation that gave the largest coefficient of variation when the model predictions are cross plotted against actual values. This transformation has a coefficient of variation of 0.95. Figure 3-23a shows a cross plot of the predicted values of carrying capacity using equation 3.9 and the actual values. Figure 3-23b are the residuals plotted on a normal probability graph, because it plots as a straight line on this graph, the residuals are normally distributed. Figure 3-24a and 8-10b are response surfaces constructed with equation 3.9 and they show how the carrying capacity varies for varying values of the independent variables. Figure 3-24a is the plot when fracture half-length is at its smallest value and Figure 3-24b is when fracture half-length is at its largest value.

3.3.1.2 Hyperbolic Exponent, n

$$n\left(k_f, k_m, L_w\right) = 6.6\times10^{-1} - 8.2\times10^{-4} k_f + 2.03\times10^{-5} k_m + 8.8\times10^{-6} L_w, \quad (3.27)$$

Equation 3.10 is the developed relationship between the hyperbolic exponent and the reservoir and well properties. A linear relationship has the highest coefficient of variation of 0.95 when compared to the other transformations evaluated. We evaluated a linear, quadratic, power and logarithmic transforms. Figure 3-25 shows a comparison of the values of the hyperbolic exponent predicted by equation 3.10 and the actual values.

3.3.1.3 Constant, a

$$a\left(k_f, k_m\right)^{-0.26} = 1.5\times10^{-1} + 2.9\times10^{-4} k_f - 5.5\times10^{-6} k_m. \quad (3.28)$$

Equation 3.11 is the relationship developed for the constant a. This relationship had the highest coefficient of variation of 0.81 from the transforms evaluated. A comparison of the values of, constant *a*, computed from equation 3.11 and actual values of constant *a* is shown in Figure 3-26.

3.3.2 Correlations for Parallel Flow Model Parameters

3.3.2.1 Initial Production Rate One, q_{i1}

$$\begin{aligned}\ln(q_{i1}) &= 6.4\times10^{-2}+6.7\times10^{-3}k_f+4.0k_m+1.8\times10^{-4}p_i-5.4\times10^{-4}p_{wf}\\ &-2.1\times10^{-3}h-3.9\phi-1.1\times10^{-4}L_w+7.4\times10^{-5}k_f h+3.6\times10^{-7}k_f L_w\\ &+2.3\times10^{-2}k_m L_w+4.7\times10^{-8}p_i p_{wf}+5.4\times10^{-6}hL_w-2.1\times10^{-8}k_f hL_w\end{aligned}\quad. \tag{3.29}$$

Equation 3.12 is the response surface function for initial production rate one, q_{i1}. It shows a relationship between the initial production rate one and the reservoir thickness (h), fracture permeability (k_f), matrix permeability (k_m), porosity (ϕ), well length (WL), initial reservoir pressure (p_i) and the bottomhole flowing pressure (p_{wf}). Different transformations of the initial production rate one were evaluated and the transformation that gave the highest value of coefficient of variation is the natural log transform. This transformation has a coefficient of variation of 0.98. A comparison of the actual and the values on time constant computed with equation 3.12 is shown in Figure 3-27.

3.3.2.2 Time Constant One, τ_1 (Largest Time Constant)

$$\begin{aligned}\tau_1^{1.12} &= 6.9\times10^{2}-3.8k_f+4.2\times10^{5}k_m-16.1h+1.3\times10^{4}\phi-1.5\times10^{-2}L_w\\ &-5.9\times10^{6}k_m\phi-4.5hL_w\end{aligned}\quad. \tag{3.30}$$

Equation 3.13 is the response surface function for time constant one, τ_1. A power transformation gave the highest value of coefficient of variation when the model predictions are cross plotted against actual values. This transformation has a coefficient of variation of 0.73. The actual values and predicted values from equation 3.13 are cross plotted as shown in Figure 3-28.

3.3.2.3 Initial Production Rate Two, q_{i2}

$$\begin{aligned}\ln(q_{i2}) &= -1.7+2.0\times10^{-3}k_f+1.7\times10k_m+2.4\times10^{-4}p_i-2.1\times10^{-4}p_{wf}\\ &+1.6\times10^{-2}h+6.4\phi+6.1\times10^{-5}L_w+5.9\times10^{-1}k_f k_m\end{aligned}\quad. \tag{3.31}$$

Equation 3.14 is the response surface function for initial production rate two, q_{i2}. It shows a relationship between the initial production rate two and the reservoir thickness (h), fracture permeability (k_f), matrix permeability (k_m), porosity (ϕ), well length (WL), initial reservoir pressure (p_i) and the bottomhole flowing pressure (p_{wf}). The log transformation gave the highest coefficient of variation of 0.99. Figure 3-29 presents a cross plot of the predictions made with equation 3.14 and the actual values.

3.3.2.4 Time Constant Two, τ_2

$$\begin{aligned} \tau_2^{0.67} &= 7.6\times10^2 - 9.7\times10^{-1}k_f - 7.4\times10^3 k_m + 2.3h \\ &+4.3\times10^{-3}L_w - 2.3\times10^2 k_f k_m + 18.4 k_m L_w - 6.5\times10^{-4} hL_w \end{aligned} \quad (3.32)$$

Equation 3.15 is the response surface function for time constant two, τ_2. A power transformation gave the highest value of coefficient of variation when the model predictions are cross plotted against actual values. This transformation has a coefficient of variation of 0.82. The actual values and predicted values from equation 3.15 are cross plotted as shown in Figure 3-30.

3.4 Summary and Conclusions

Both models used in this study can predict the EUR; for the logistic growth model the carrying capacity is a parameter in the fitting, and for the parallel flow model the function converges to a finite value when extrapolated to infinity. Because both methods require numerical fitting of model parameters, neither offers a clear advantage over the other. The logistic model does not have physically meaningful parameters (except for the carrying capacity) and does not fit the data quite as well as does the parallel model, although both result in good fits. The parallel model has more parameters, four for the two compartment model- as opposed to three for the logistic model. Therefore, the latter approach is less likely to result in non-unique solutions. The logistic model does not have the multiple scales that are such a prevalent feature of the data.

The model-based analysis with the parallel flow model clearly indicates the existence of multiple time scales in the production profiles of these wells. The parallel flow model is based on the concept that the reservoir contains multiple independently declining reservoir elements (compartments) that have different and unique time constants (declining characteristics). Therefore, when two or more reservoir compartments are present, this will be reflected in the number of terms in the parallel flow model. The observed time scales also highlight the importance of high-frequency data and integrating all available information in analyzing production data. Most analysis techniques ignore the early-time production data (which we included in the analysis) because of wellbore effects (wellbore storage or skin and frac fluid flow-back) and noise, thereby missing the first time scale and only analyzing data that is dominated by production from the second time scale. While it is possible that these phenomena affect early-time production only, it does not eliminate the possibility of analyzing early time data to estimate the dimensions of the reservoir element/compartment (this could be the fracture or fracture network) that accounts for early time flow. Ogunyomi et al. (2014) presented a rate-time relation capable of modeling flow from a double porosity model that typically exhibits two time scales. The model they presented is also valid for early and late time flow (transient and boundary dominated flow).

Analysis of the model parameters for the logistic growth and parallel flow models showed that they have some correlation with the reservoir and well completion properties. For example, the carrying capacity in the logistic growth model correlated with the well spacing, total fluid injected and the mass of sand injected. In an ideal situation these properties can be used to define the drainage volume of a well. It therefore seems reasonable, as suggested by Clark et al. (2011), to use the carrying capacity as a constraint on the recoverable reserves from a well.

We have presented the results of a detailed statistical and model-based analysis of production data from an unconventional oil reservoir. We also analyzed this production data to identify different flow regimes and the flow signatures using linear-flow theory. Based on the results of these analyses the following conclusions are pertinent:

1. Primary production performance from wells in unconventional reservoirs should be expected to be highly variable. The production signatures show varying slopes on a diagnostic log-log plot that ranges from one-half to one-and-a-half. By far the most frequent slope observed on the diagnostic plot was the one-half slope. This observation corroborates the notion that 1D linear flow is adequate in modeling recovery from these reservoirs.
2. The analysis showed that at least two terms of the parallel flow model are needed to adequately model production from these reservoirs. A statistical analysis of the time constants confirms that there are two distributions of time constants. Therefore, we can conclude that there are at least two time scales in the production history from these wells. An important corollary of this observation is that any forecasting effort that does not account for the multiple time scales will result in conservative EUR.
3. Based on the general observation that the parameters from the empirical models correlated with the reservoir and well completion properties in the data set, we developed functions that relate the model parameters to reservoir and well properties by using design of experiment and numerical reservoir simulations. If the reservoir and well properties are known, these relations can be used to compute the model parameters, which can then be used in the models to forecast production. These

functions are only valid within the range that was used to develop them and any application should put this fact in consideration before use.

Table 3-1: Summary of model fitting parameters obtained for the parallel flow model applied to a well in the dataset

q_{oiT} (STB/D)	f_1	f_2	f_3	f_4	$\sum f_i$	q_{i1} (STB/D)	q_{i2} (STB/D)	q_{i3} (STB/D)	q_{i4} (STB/D)	τ_1 (days)	τ_2 (days)	τ_3 (days)	τ_4 (days)
557	0.3	0	0	0.7	1	151	0	0	407	1020	-	-	59

Table 3-2: Summary of logistic growth model parameters obtained for a well in the dataset

N (STB)	n	a(days^n)
112631	0.54	52

Table 3-3: Statistical summary of model fitting parameters for the parallel flow model (86 wells)

	q_{i1} (STB/D)	q_{i2} (STB/D)	q_{i3} (STB/D)	τ_1 (Days)	τ_2 (Days)	τ_3(Days)
Mean	398	182	62	381	2.7×10^4	2.1×10^4
Median	289	119	20	57	448	222
Standard Deviation	391	201	116	2570	1.6×10^5	1.1×10^5
Kurtosis	5	5	21	86	45	39
Skewness	2	2	4	9	7	6
Range	2×10^3	1×10^3	7×10^2	2×10^4	1×10^6	7×10^5
Minimum	14	0	0	0	0	0
Maximum	2×10^3	1×10^3	7×10^2	2×10^4	1×10^6	7×10^5

Table 3-4: Statistical summary of model fitting parameters for the logistic growth model (86 wells)

	N (STB)	**n**	**a**
Mean	133135.35	0.62	5897.30
Median	111940.75	0.58	75.96
Standard Deviation	69011.60	0.23	52876.12
Kurtosis	3.12	63.29	84.00
Skewness	1.32	7.47	9.16
Range	408248.15	2.13	484738.60
Minimum	20000.00	0.46	4.52
Maximum	428248.15	2.59	484743.12

Table 3-5: Summary of the computed correlation coefficient between the model parameters and the reservoir and model completion properties for the parallel flow model. The shaded cells indicate $|\rho| \geq 0.2$.

	q_{i1} (STB/D)	q_{i2} (STB/D)	q_{i3} (STB/D)	τ_1 (Days)	τ_2 (Days)	τ_3 (Days)
Number of stages	0.47	0.43	0.31	-0.07	-0.10	-0.06
Lateral length (ft)	-0.19	-0.21	-0.30	-0.13	0.15	0.03
Spacing (acres)	0.32	0.35	0.22	-0.34	0.10	0.09
Initial water saturation (fraction)	-0.35	-0.54	-0.30	0.18	-0.18	-0.02
Porosity (fraction)	0.28	0.21	0.27	-0.09	-0.12	0.22
True vertical thickness, TVT (ft)	-0.40	-0.59	-0.40	0.29	-0.03	-0.11
Net to gross (fraction)	0.15	0.21	0.29	-0.14	-0.18	0.32
Overpressure (psi)	0.18	0.33	0.19	-0.02	0.07	-0.12
Pressure (psi)	0.18	0.33	0.19	-0.02	0.07	-0.12
Depth (ft)	0.15	0.30	0.17	-0.05	0.14	-0.14
Average injection pressure (psig)	0.35	0.36	0.16	-0.21	0.09	0.02
Total fluid injected	0.46	0.44	0.30	-0.37	0.08	0.12
Sand (lbs)	0.48	0.40	0.36	0.02	-0.12	-0.06

Table 3-6: Summary of the computed correlation coefficient between the model parameters and the reservoir and model completion properties for the logistic growth model.

	N (STB)	n	a
Number of stages	0.14	0.02	-0.02
Lateral length (ft)	0.00	-0.13	-0.09
Spacing (acres)	0.25	0.02	0.04
Initial water Saturation (fraction)	-0.11	-0.09	-0.01
Porosity (fraction)	0.46	-0.12	-0.05
True vertical thickness, TVT (ft)	-0.05	-0.09	0.02
Net to gross (fraction)	0.19	0.02	0.01
Overpressure (psi)	-0.04	0.10	0.00
Pressure (psi)	-0.04	0.10	0.00
Depth (ft)	-0.03	0.10	0.02
Average injection pressure (psig)	0.23	-0.02	0.09
Total fluid injected	0.39	-0.02	-0.02
Sand injected (lbs)	0.26	0.02	0.01

Table 3-7: Reservoir and well completion properties used in the fractional factorial design of experiments used to build the numerical simulation model.

Property	Max (+)	Min (-)
Fracture half length, x_f (ft)	1000	150
Fracture permeability, k_f (md)	150	15
Initial oil saturation, S_{oi} (fraction)	0.70	0.48
Initial reservoir pressure, P_i (psi)	7700	5500
Wellbore pressure, P_{wf} (psi)	2000	50
Matrix permeability, k_m (md)	$5x10^{3}$	$5x10^{-4}$
Number of fracture cluster per stage	5	1
Number of fracture stages	5	3
Porosity, φ (fraction)	0.08	0.04
Reservoir thickness, h (ft)	100	30
Well length, L (ft)	3600	900
Fracture width, w (ft)	0.2	0.05
Fracture spacing, (ft)	100	400
Viscosity, μ (cp)	2	1
Compressibility, c_t (psi^{-1})	$1x10^{-5}$	$1x10^{-6}$

Table 3-8: Summary of reservoir and well properties that have the strongest effect on the model parameters

Property	*Parallel flow model*				*Logistic growth model*		
	q_{i1} (STB/D)	q_{i2} (STB/D)	τ_1 (Day)	τ_2 (Day)	N (STB)	n	a
Fracture half length, x_f (ft)					●		
Fracture permeability, k_f (md)	●	●		●		●	
Initial oil saturation, S_{oi} (fraction)							
Initial reservoir pressure, P_i (psi)	●	●		●			
Flow well pressure, P_{wf} (psi)		●				●	
Matrix permeability, k_m (md)	●	●				●	●
Number of fracture cluster per stage							
Number of fracture stages							
Porosity, φ (fraction)		●					
Thickness, h (ft)	●	●			●		
Well length, L (ft)	●	●	●	●	●	●	●
Width, w (ft)							
Fracture spacing, (ft)							
Viscosity, μ (cp)							
Compressibility, c_t (psi^{-1})							

Table 3-9: Design table for variables with the main effect on the carrying capacity, N.

Run number	Thickness	Well length	Fracture half length	N (STB)
1	+	-	+	497338
2	+	-	-	453284
3	-	+	+	319600
4	-	-	+	177726
5	-	-	-	82599.3
6	+	+	+	956178
7	+	+	-	434510
8	-	+	-	117092

Table 3-10: Design table for variables with the main effect on the hyperbolic constant, n, and the constant a.

Run number	Fracture permeability	Matrix permeability	Well pressure	Well length	n	a
1	-	-	-	+	0.67	1104.20
2	+	+	-	-	0.63	569.14
3	+	+	+	+	0.69	1052.55
4	+	-	+	-	0.57	741.38
5	-	-	-	-	0.63	838.84
6	-	+	-	-	0.77	2995.93
7	-	+	+	+	0.79	3236.21
8	-	-	+	+	0.67	1371.62
9	+	-	-	+	0.57	516.44
10	-	-	+	-	0.70	1729.04
11	+	+	-	+	0.69	1558.57
12	+	+	+	-	0.62	815.20
13	+	-	-	-	0.56	562.49
14	-	+	+	-	0.77	2192.00
15	-	+	-	+	0.79	3830.52
16	+	-	+	+	0.57	502.11

Table 3-11: Design table for variables with the main effect on the parallel flow model parameters

Run number	Fracture permeability	Matrix permeability	Initial res. pressure	Wellbore pressure	Thickness	Porosity	Well length	q_{i1} (stb/d)	D_{i1} (Days)	q_{i2} (stb/d)	D_{i2} (Days)
1	-	-	-	-	-	-	-	3.18	1.31E-03	1.70	4.70E-05
2	-	+	-	-	-	-	-	3.77	8.84E-04	3.81	4.96E-05
3	+	-	-	-	-	-	-	9.99	2.24E-03	2.23	6.04E-05
4	+	+	-	-	-	-	-	12.49	9.61E-04	5.93	7.16E-05
5	-	-	-	-	+	-	-	5.52	9.25E-04	4.80	3.83E-05
6	-	+	-	-	+	-	-	5.33	6.70E-04	9.63	3.66E-05
7	+	-	-	-	+	-	-	25.07	1.82E-03	7.04	5.55E-05
8	+	+	-	-	+	-	-	27.17	7.10E-04	17.60	6.17E-05
9	-	-	-	+	-	-	-	1.89	1.21E-03	1.05	4.59E-05
10	-	+	-	+	-	-	-	2.30	8.60E-04	2.37	4.92E-05
11	+	-	-	+	-	-	-	5.92	2.07E-03	1.35	5.89E-05
12	+	+	-	+	-	-	-	7.50	9.06E-04	3.67	7.26E-05
13	-	-	-	+	+	-	-	3.32	8.72E-04	2.98	3.74E-05
14	-	+	-	+	+	-	-	3.20	6.34E-04	5.96	3.56E-05
15	+	-	-	+	+	-	-	14.63	1.64E-03	4.30	5.50E-05
16	+	+	-	+	+	-	-	16.51	7.04E-04	11.19	6.34E-05
17	-	-	-	-	-	+	-	12.00	1.66E-02	3.00	8.81E-05
18	-	+	-	-	-	+	-	4.78	1.40E-03	4.90	4.72E-05
19	+	-	-	-	-	+	-	11.19	1.61E-03	2.82	5.62E-05
20	+	+	-	-	-	+	-	15.36	1.57E-03	9.82	8.24E-05
21	-	-	-	-	+	+	-	5.41	7.09E-04	5.67	3.35E-05
22	-	+	-	-	+	+	-	5.40	9.35E-04	11.45	3.20E-05
23	+	-	-	-	+	+	-	25.89	1.21E-03	8.74	5.09E-05
24	+	+	-	-	+	+	-	27.14	1.10E-03	28.18	6.96E-05
25	-	-	-	+	-	+	-	1.96	9.22E-04	1.28	4.15E-05
26	-	+	-	+	-	+	-	2.80	1.30E-03	3.03	4.62E-05
27	+	-	-	+	-	+	-	6.52	1.45E-03	1.70	5.47E-05
28	+	+	-	+	-	+	-	8.78	1.40E-03	6.08	8.19E-05
29	-	-	-	+	+	+	-	3.27	6.74E-04	3.51	3.27E-05
30	-	+	-	+	+	+	-	3.26	9.26E-04	7.10	3.15E-05
31	+	-	-	+	+	+	-	15.58	1.11E-03	5.30	4.91E-05
32	+	+	-	+	+	+	-	15.97	1.00E-03	17.43	6.78E-05
33	-	-	+	-	-	-	-	4.96	1.38E-03	2.58	4.75E-05
34	-	+	+	-	-	-	-	6.05	1.02E-03	5.87	5.20E-05
35	+	-	+	-	-	-	-	15.59	2.34E-03	3.35	6.09E-05
36	+	+	+	-	-	-	-	19.48	1.05E-03	9.26	7.66E-05
37	-	-	+	-	+	-	-	8.57	9.64E-04	7.26	3.86E-05

Table 3-11 (continued)

38	-	+	+	-	+	-	-	*8.13*	*6.77E-04*	*14.52*	*3.68E-05*
39	+	-	+	-	+	-	-	38.31	1.86E-03	10.66	5.72E-05
40	+	+	+	-	+	-	-	41.45	7.94E-04	28.05	6.75E-05
41	-	-	+	+	-	-	-	3.60	1.30E-03	1.92	4.66E-05
42	-	+	+	+	-	-	-	4.28	9.20E-04	4.35	5.03E-05
43	+	-	+	+	-	-	-	11.38	2.22E-03	2.48	6.00E-05
44	+	+	+	+	-	-	-	14.26	1.02E-03	7.01	7.74E-05
45	-	-	+	+	+	-	-	6.18	9.03E-04	5.41	3.76E-05
46	-	+	+	+	+	-	-	5.92	6.87E-04	10.94	3.67E-05
47	+	-	+	+	+	-	-	28.27	1.77E-03	7.91	5.60E-05
48	+	+	+	+	+	-	-	30.03	7.34E-04	20.76	6.54E-05
49	-	-	+	-	-	+	-	5.20	1.08E-03	3.17	4.40E-05
50	-	+	+	-	-	+	-	7.91	1.61E-03	7.45	4.81E-05
51	+	-	+	-	-	+	-	17.20	1.65E-03	4.25	5.73E-05
52	+	+	+	-	-	+	-	24.52	1.75E-03	15.06	8.47E-05
53	-	-	+	-	+	+	-	8.30	7.41E-04	8.60	3.42E-05
54	-	+	+	-	+	+	-	8.52	9.99E-04	17.31	3.24E-05
55	+	-	+	-	+	+	-	40.73	1.26E-03	13.19	5.16E-05
56	+	+	+	-	+	+	-	42.65	1.21E-03	42.96	7.05E-05
57	-	-	+	+	-	+	-	3.78	1.03E-03	2.37	4.34E-05
58	-	+	+	+	-	+	-	5.55	1.47E-03	5.55	4.69E-05
59	+	-	+	+	-	+	-	12.55	1.56E-03	3.15	5.66E-05
60	+	+	+	+	-	+	-	17.72	1.67E-03	11.31	8.40E-05
61	-	-	+	+	+	+	-	6.05	7.14E-04	6.45	3.39E-05
62	-	+	+	+	+	+	-	6.19	9.87E-04	12.93	3.18E-05
63	+	-	+	+	+	+	-	29.93	1.22E-03	9.91	5.19E-05
64	+	+	+	+	+	+	-	30.58	1.13E-03	32.09	6.89E-05
65	-	-	-	-	-	-	+	4.13	1.52E-03	1.76	4.68E-05
66	-	+	-	-	-	-	+	5.46	1.36E-03	4.42	3.09E-05
67	+	-	-	-	-	-	+	11.43	2.48E-03	2.23	5.79E-05
68	+	+	-	-	-	-	+	15.49	1.54E-03	7.31	4.54E-05
69	-	-	-	-	+	-	+	13.79	1.52E-03	5.90	4.68E-05
70	-	+	-	-	+	-	+	18.25	1.36E-03	14.77	3.09E-05
71	+	-	-	-	+	-	+	38.18	2.48E-03	7.47	5.80E-05
72	+	+	-	-	+	-	+	51.66	1.54E-03	24.43	4.53E-05
73	-	-	-	+	-	-	+	2.43	1.41E-03	1.09	4.61E-05
74	-	+	-	+	-	-	+	3.16	1.24E-03	2.72	2.99E-05
75	+	-	-	+	-	-	+	6.67	2.26E-03	1.34	5.59E-05

Table 3-11 (continued)

76	+	+	-	+	-	-	+	*8.68*	*1.32E-03*	*4.45*	*4.30E-05*
77	-	-	-	+	+	-	+	8.11	1.40E-03	3.64	4.60E-05
78	-	+	-	+	+	-	+	10.90	1.30E-03	9.16	3.03E-05
79	+	-	-	+	+	-	+	22.26	2.25E-03	4.49	5.59E-05
80	+	+	-	+	+	-	+	28.99	1.31E-03	14.90	4.29E-05
81	-	-	-	-	-	+	+	4.56	1.27E-03	2.23	4.71E-05
82	-	+	-	-	-	+	+	7.61	1.72E-03	5.28	3.29E-05
83	+	-	-	-	-	+	+	12.94	1.84E-03	2.92	5.94E-05
84	+	+	-	-	-	+	+	19.71	1.70E-03	9.50	4.94E-05
85	-	-	-	-	+	+	+	15.24	1.26E-03	7.46	4.71E-05
86	-	+	-	-	+	+	+	25.40	1.72E-03	17.65	3.29E-05
87	+	-	-	-	+	+	+	43.22	1.84E-03	9.77	5.95E-05
88	+	+	-	-	+	+	+	65.52	1.68E-03	31.71	4.92E-05
89	-	-	-	+	-	+	+	2.69	1.18E-03	1.38	4.62E-05
90	-	+	-	+	-	+	+	4.32	1.54E-03	3.25	3.18E-05
91	+	-	-	+	-	+	+	7.36	1.59E-03	1.72	5.55E-05
92	+	+	-	+	-	+	+	10.99	1.45E-03	5.81	4.74E-05
93	-	-	-	+	+	+	+	9.00	1.17E-03	4.60	4.62E-05
94	-	+	-	+	+	+	+	14.38	1.53E-03	10.88	3.17E-05
95	+	-	-	+	+	+	+	25.32	1.65E-03	5.82	5.67E-05
96	+	+	-	+	+	+	+	36.69	1.44E-03	19.44	4.74E-05
97	-	-	+	-	-	-	+	6.76	2.00E-03	2.95	6.34E-05
98	-	+	+	-	-	-	+	10.39	2.19E-03	7.11	4.09E-05
99	+	-	+	-	-	-	+	18.94	3.13E-03	3.77	7.95E-05
100	+	+	+	-	-	-	+	26.63	2.22E-03	12.27	6.30E-05
101	-	-	+	-	+	-	+	22.56	2.00E-03	9.84	6.33E-05
102	-	+	+	-	+	-	+	34.56	2.18E-03	23.75	4.09E-05
103	+	-	+	-	+	-	+	64.12	3.22E-03	12.74	8.16E-05
104	+	+	+	-	+	-	+	91.48	2.35E-03	41.49	6.50E-05
105	-	-	+	+	-	-	+	4.71	1.54E-03	2.00	4.74E-05
106	-	+	+	+	-	-	+	6.17	1.37E-03	4.98	3.10E-05
107	+	-	+	+	-	-	+	12.80	2.41E-03	2.48	5.74E-05
108	+	+	+	+	-	-	+	17.53	1.54E-03	8.26	4.55E-05
109	-	-	+	+	+	-	+	15.73	1.54E-03	6.70	4.74E-05
110	-	+	+	+	+	-	+	20.56	1.36E-03	16.65	3.09E-05
111	+	-	+	+	+	-	+	43.60	2.48E-03	8.36	5.85E-05
112	+	+	+	+	+	-	+	58.39	1.53E-03	27.59	4.54E-05
113	-	-	+	-	-	+	+	7.33	1.52E-03	3.57	5.54E-05

Table 3-11 (continued)

114	-	+	+	-	-	+	+	*13.03*	*2.10E-03*	*8.08*	*3.53E-05*
115	+	-	+	-	-	+	+	21.70	2.46E-03	5.17	8.81E-05
116	+	+	+	-	-	+	+	35.23	2.57E-03	15.93	6.71E-05
117	-	-	+	-	+	+	+	24.44	1.52E-03	11.92	5.52E-05
118	-	+	+	-	+	+	+	43.37	2.08E-03	26.99	3.52E-05
119	+	-	+	-	+	+	+	72.40	2.46E-03	17.26	8.81E-05
120	+	+	+	-	+	+	+	117.50	2.56E-03	53.15	6.70E-05
121	-	-	+	+	-	+	+	5.11	1.26E-03	2.53	4.75E-05
122	-	+	+	+	-	+	+	8.64	1.74E-03	5.95	3.28E-05
123	+	-	+	+	-	+	+	14.60	1.79E-03	3.24	5.90E-05
124	+	+	+	+	-	+	+	22.27	1.69E-03	10.75	4.95E-05
125	-	-	+	+	+	+	+	17.08	1.26E-03	8.47	4.76E-05
126	-	+	+	+	+	+	+	28.73	1.72E-03	19.87	3.27E-05
127	+	-	+	+	+	+	+	48.70	1.79E-03	10.82	5.88E-05
128	+	+	+	+	+	+	+	71.97	1.59E-03	35.56	4.83E-05

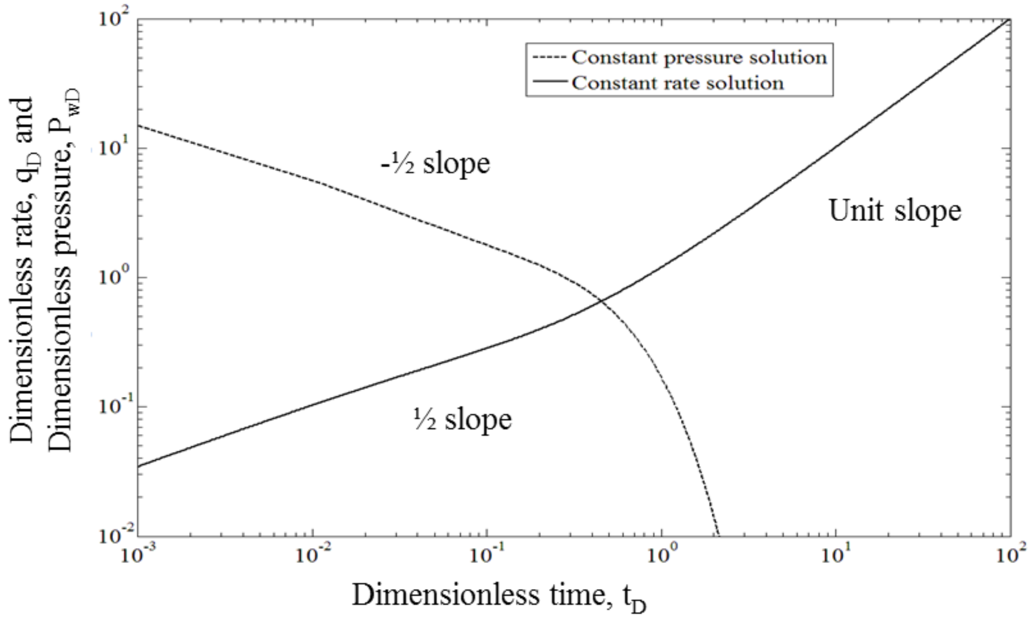

Figure 3-1: A log-log plot of the solutions to the diffusivity equation in one-dimension for a no-flow outer boundary condition. The dashed line represents the constant rate inner boundary condition and the solid line represents the constant pressure inner boundary condition

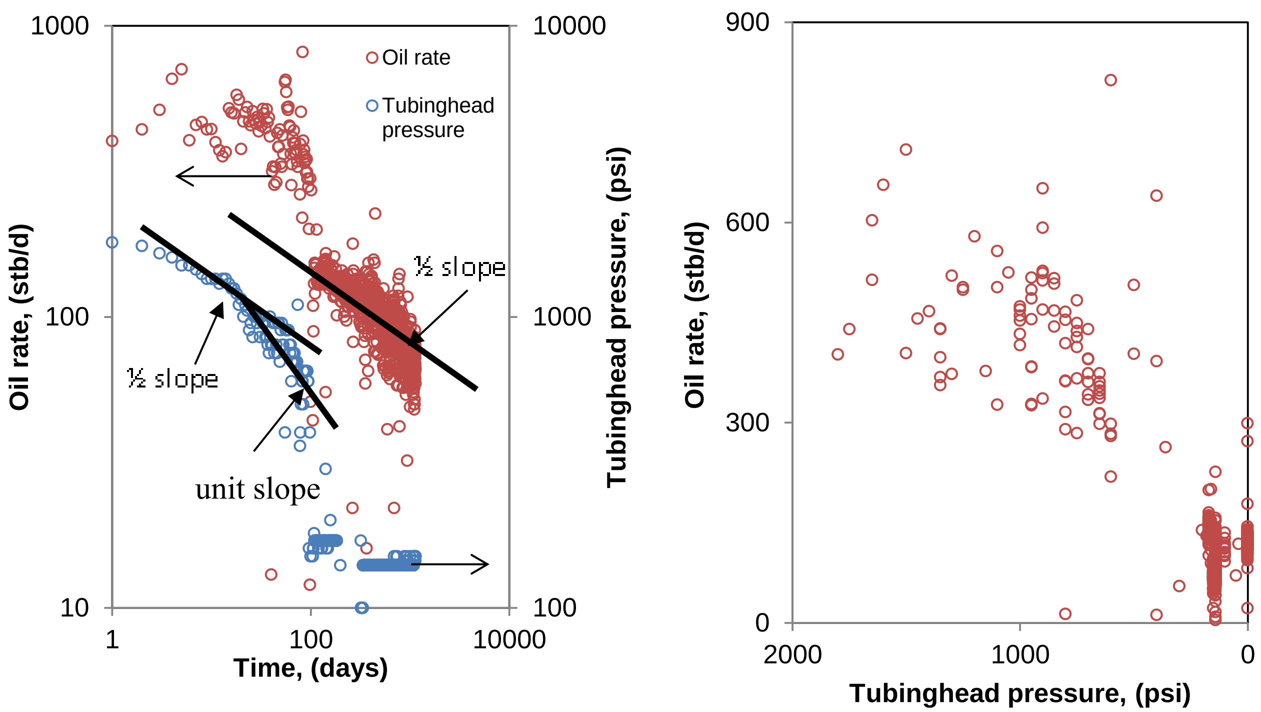

(a) (b)

Figure 3-2: Diagnostic figures for a well in the data set. Figure 3-2a. presents the log-log plot of oil rate versus time and the log-log plot of the tubinghead pressure versus time. Figure 3-2b. shows a cross plot of the oil rate versus tubinghead pressure

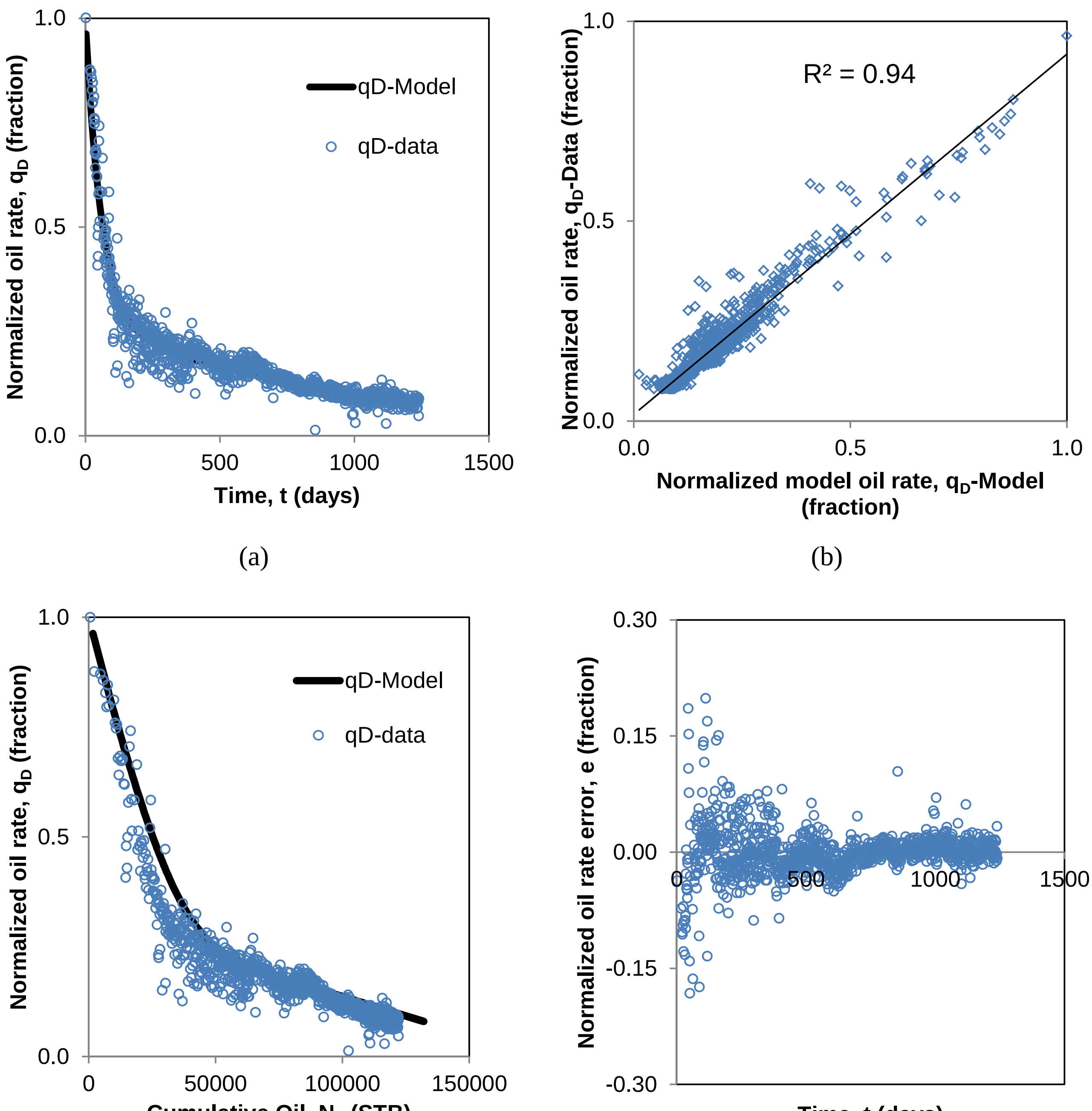

Figure 3-3: Example application of the parallel flow model. Figure 3-3a. is the normalized rate - time plot for the data and model history match and Figure 3-3:c. is the normalized rate - cumulative plot for the data and model history match. Figure 3-3b shows the cross plot of the normalized rate data and the normalized model rate prediction. Figure 3-3d. shows a plot of the error in normalized rate prediction (q_D-Data – q_D-Model) versus time

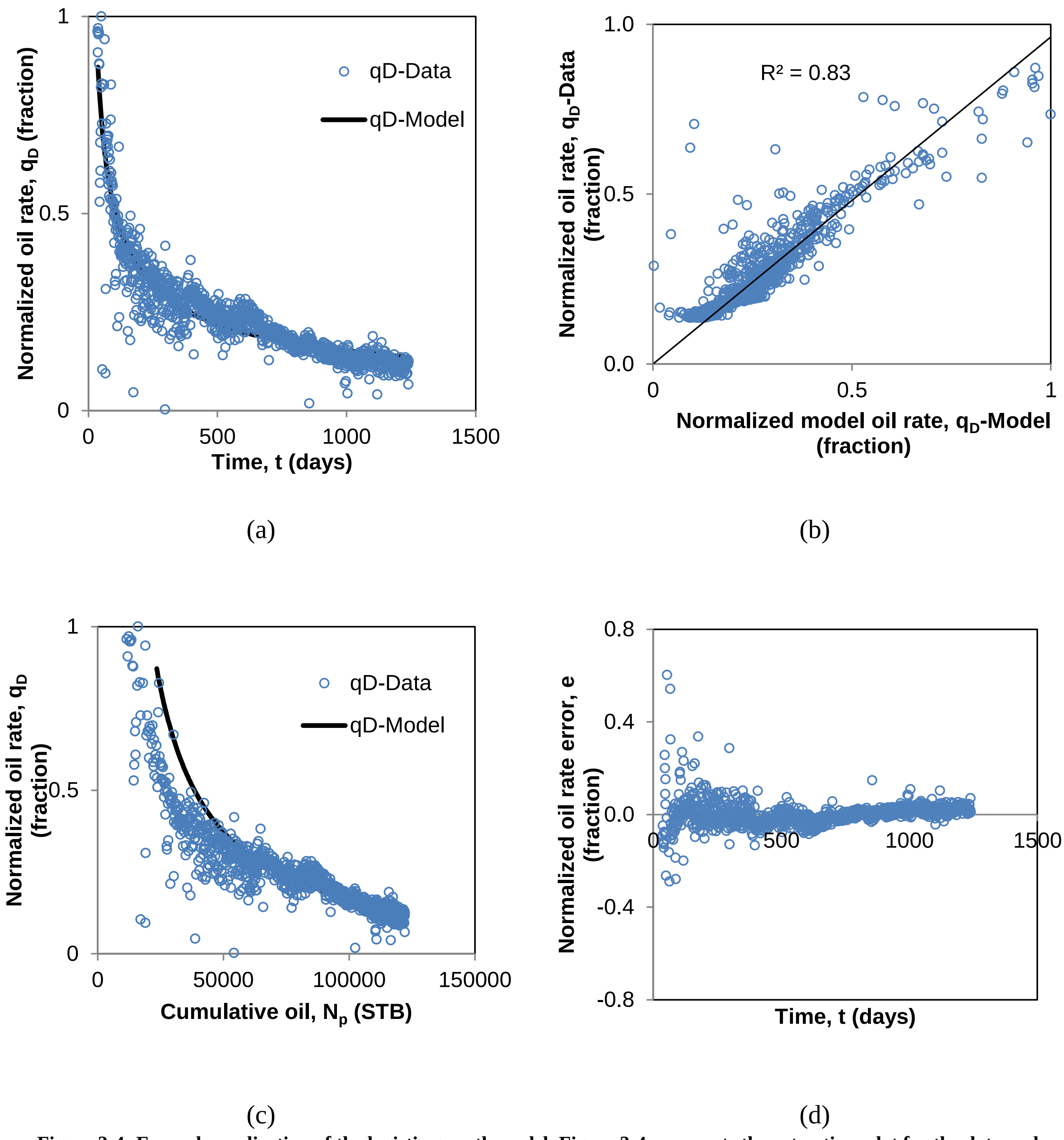

Figure 3-4: Example application of the logistic growth model. Figure 3-4a. presents the rate - time plot for the data and model history match and Figure 3-4c. presents the rate - cumulative plot for the data and model history match. Figure 3-4b shows the cross plot of the normalized rate data and the normalized model rate prediction. Figure 3-4d. shows a plot of the error in rate prediction ($q_{Data} - q_{Model}$) versus time.

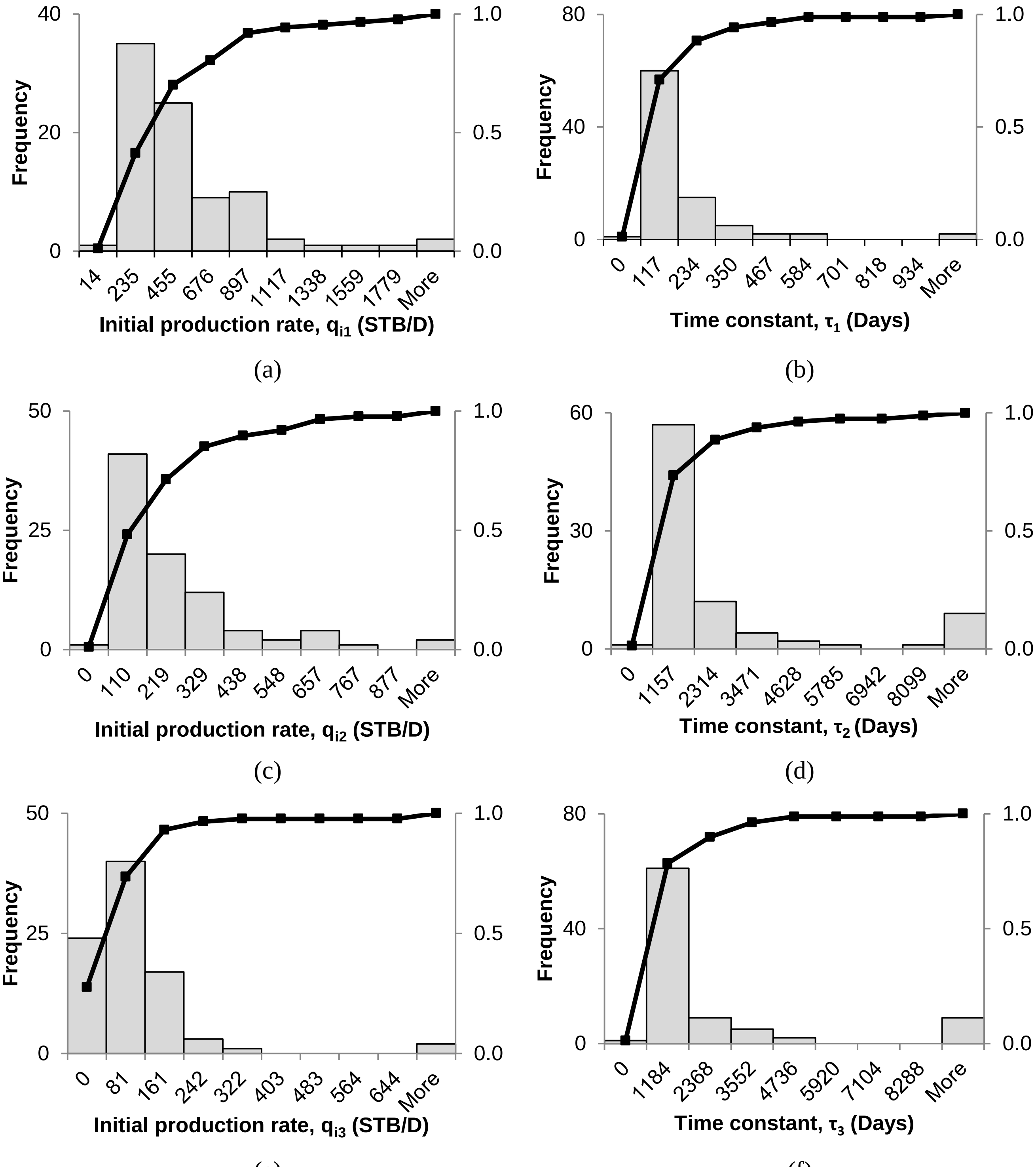

Figure 3-5: Probability density function (PDF) and cumulative distribution function (CDF) obtained for the parallel flow model applied to the data set

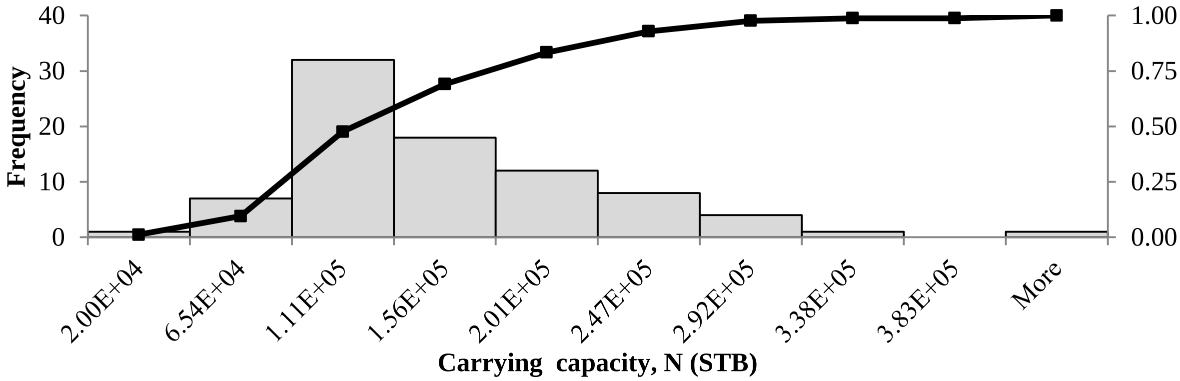

(a)

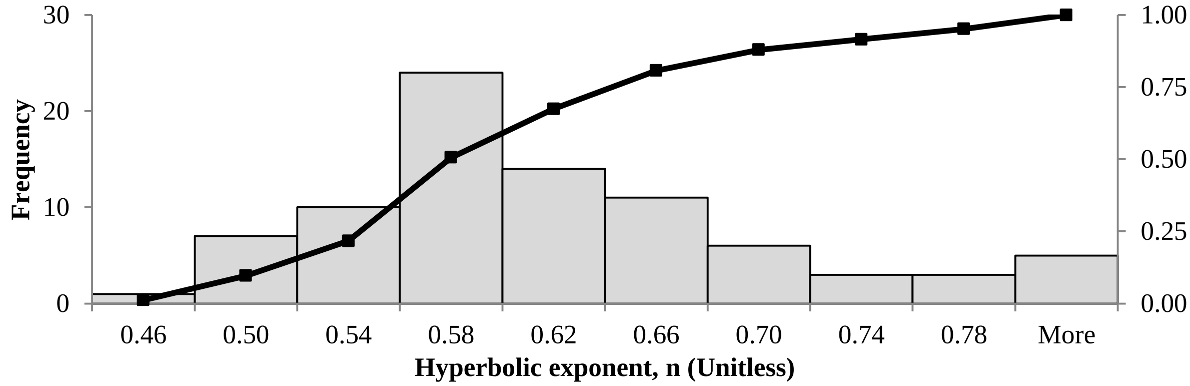

(b)

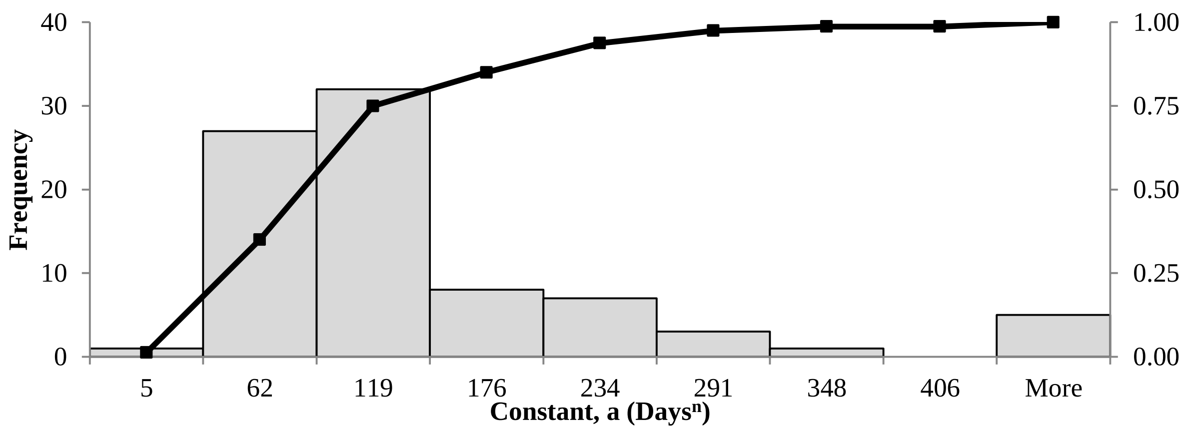

(c)

Figure 3-6: Probability density function (PDF) and cumulative distribution function (CDF) obtained for the logistic growth model applied to the data set. Fig. 6a show PDF and CDF for the carrying capacity, Fig. 6b shows the PDF and CDF for the hyperbolic exponent and Fig. 6c show the PDF and CDF for the constant a.

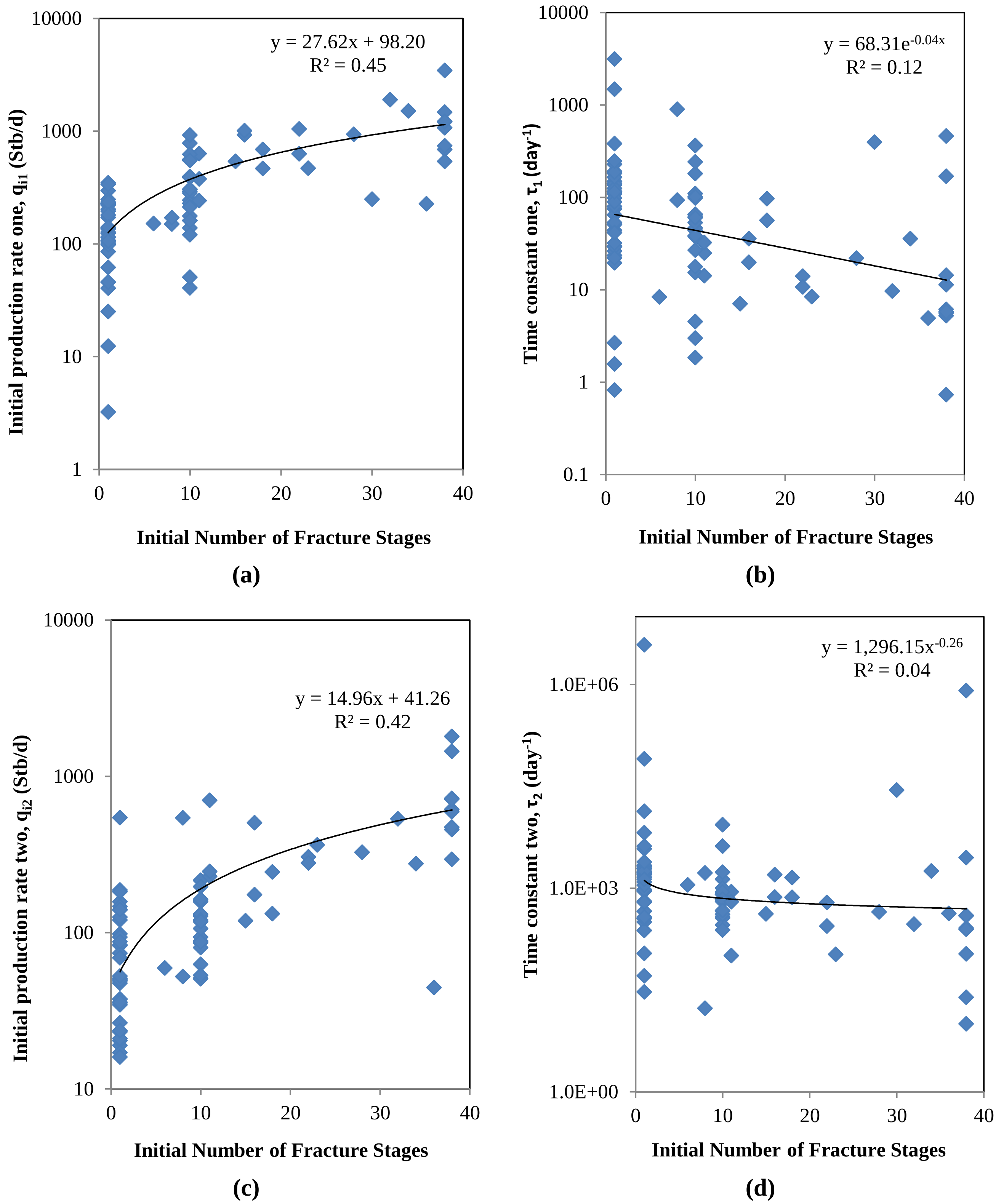

Figure 3-7: Cross plot of Parallel Flow Model parameters and the initial number of fracture stages

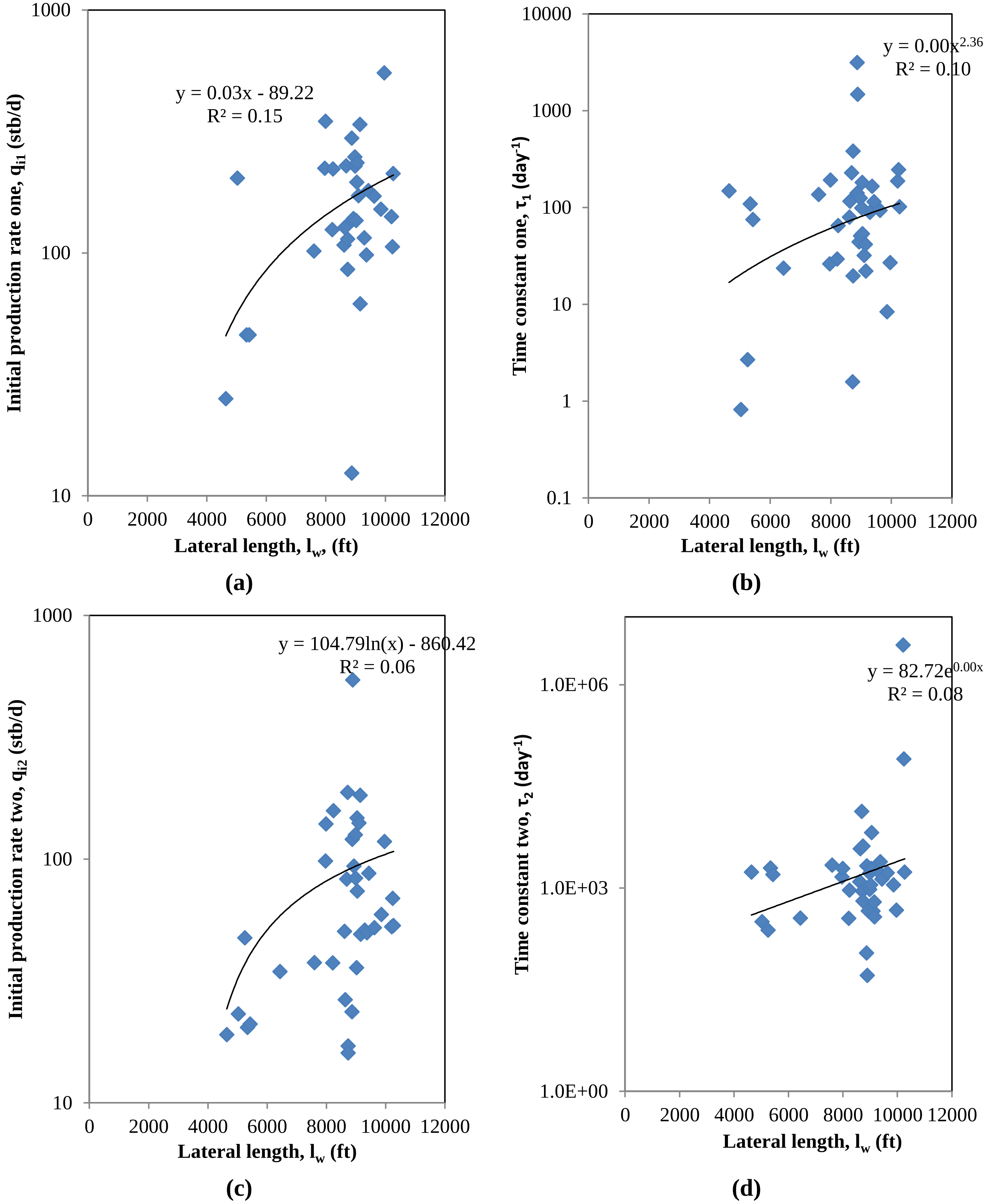

Figure 3-8: Cross plot of Parallel Flow Model parameters and the lateral length of the horizontal well

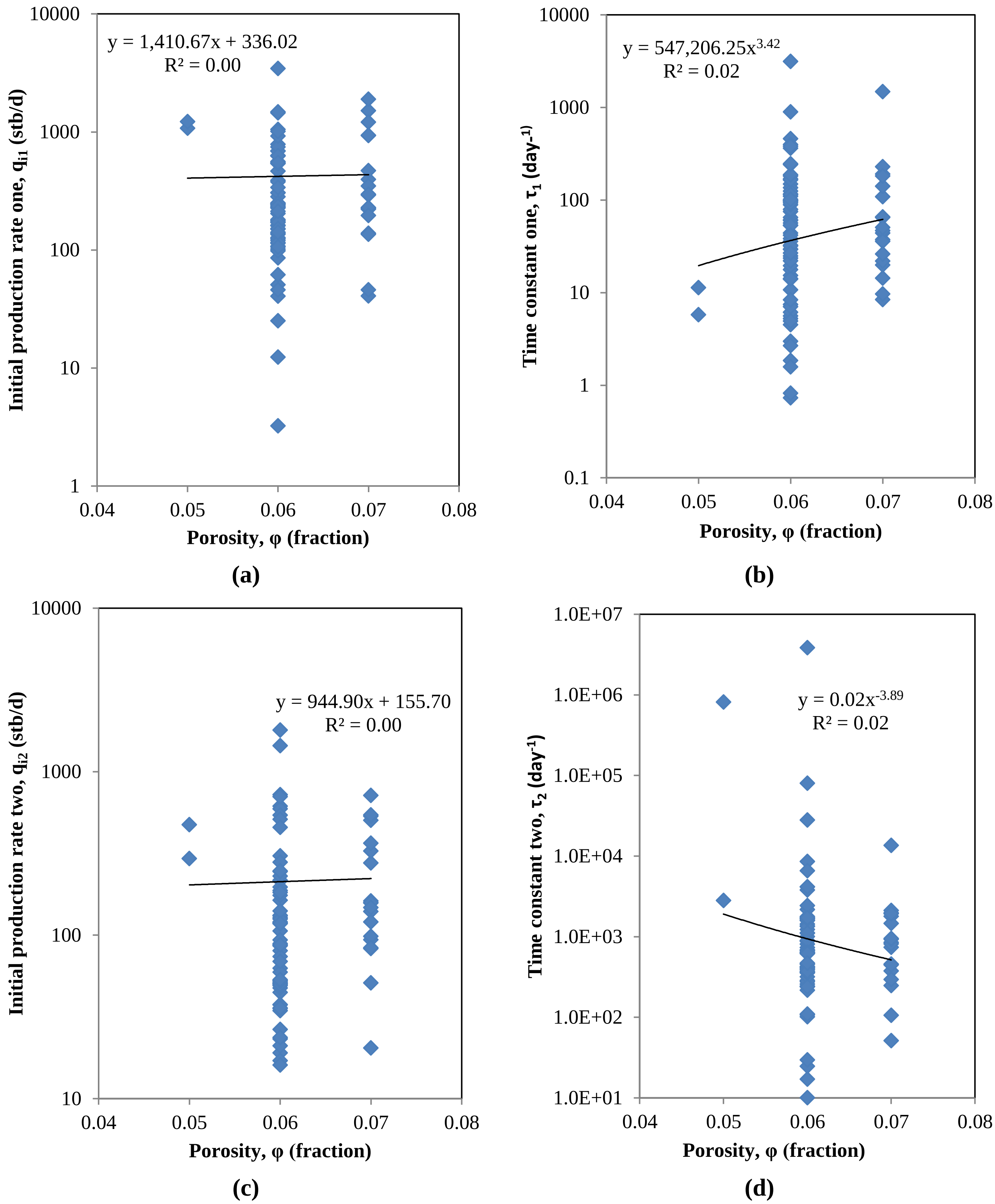

Figure 3-9: Cross plot of Parallel Flow Model parameters and reservoir porosity

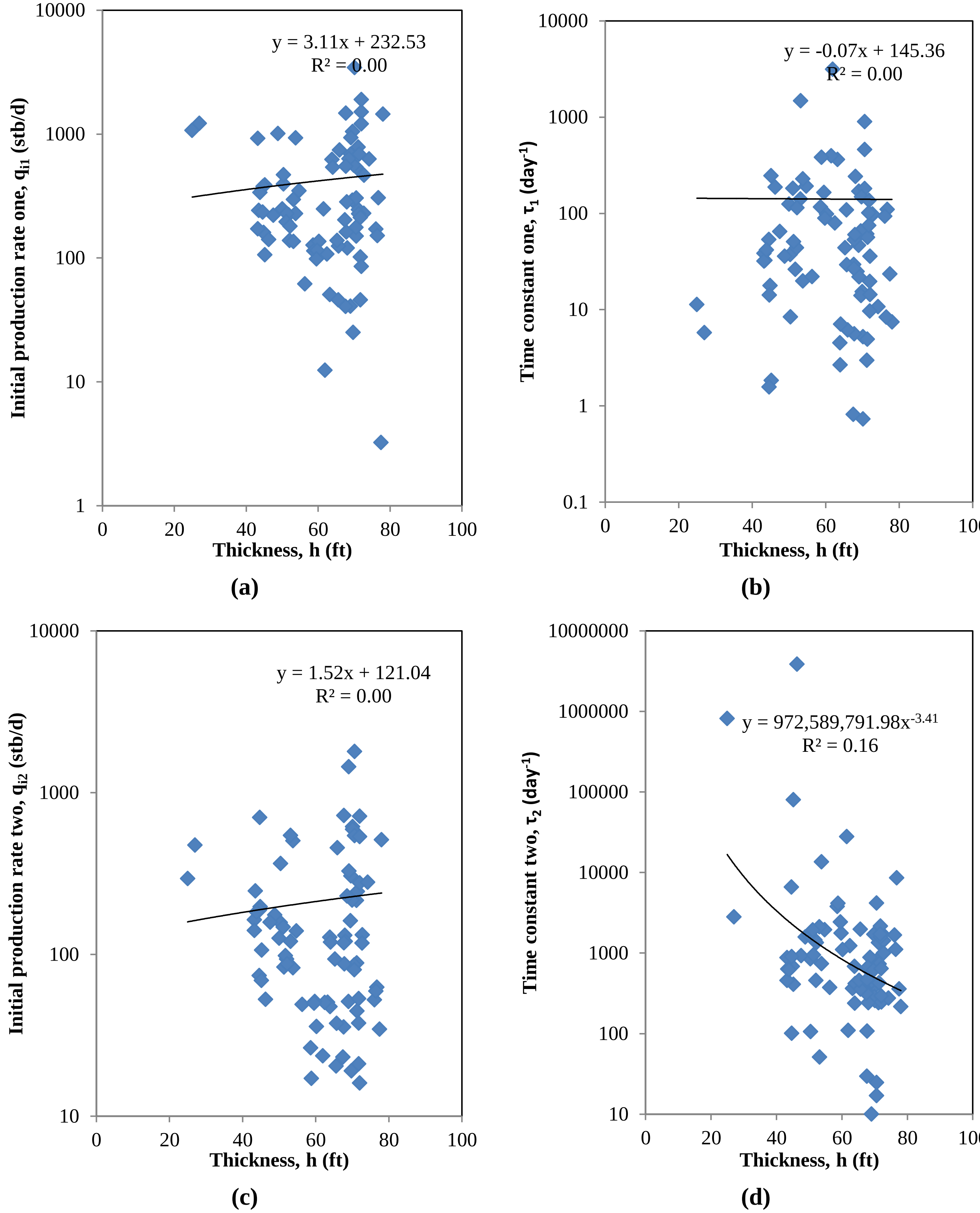

Figure 3-10: Cross plot of Parallel Flow Model parameters and reservoir thickness

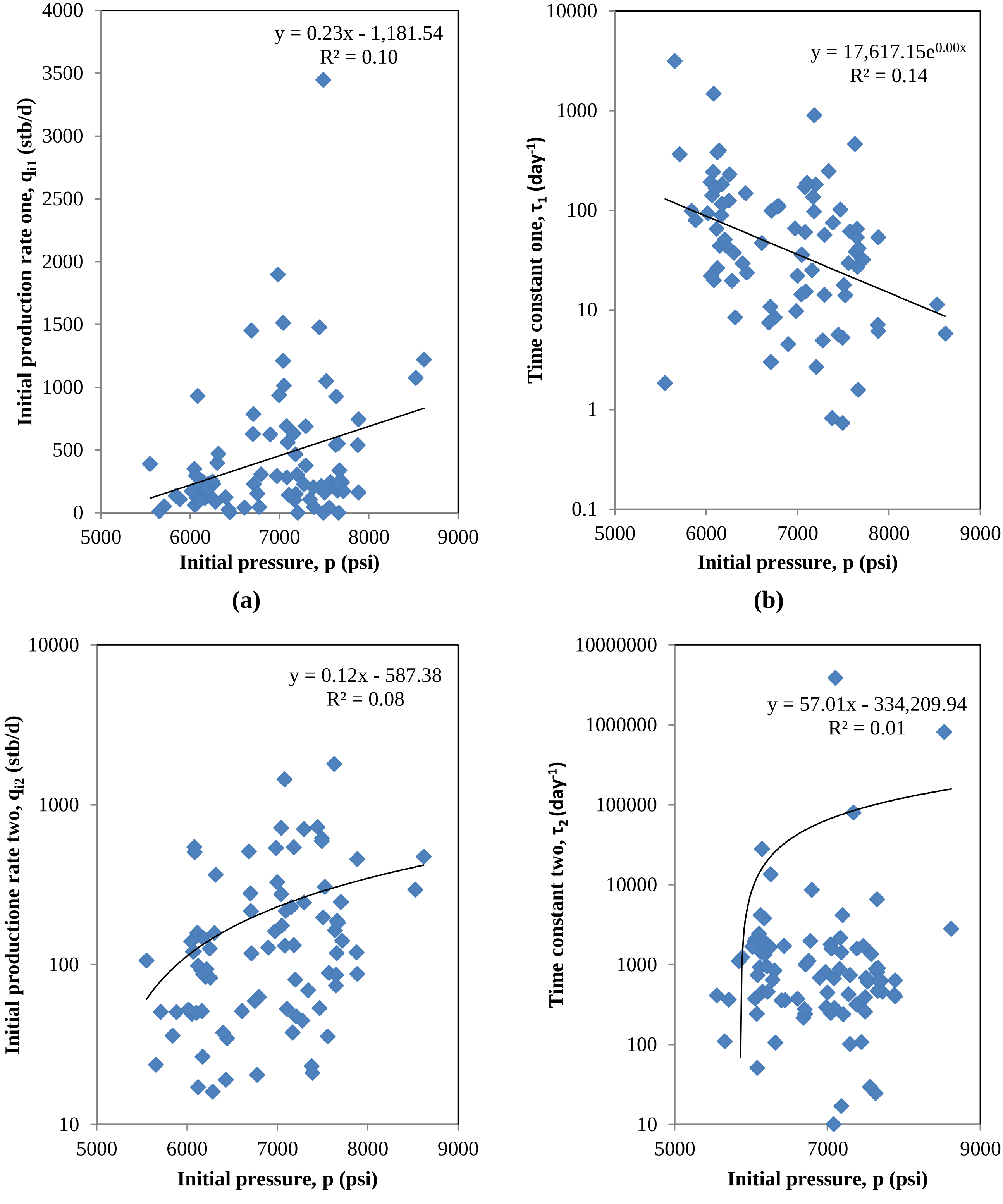

Figure 3-11: Cross plot of Parallel Flow Model parameters and the initial reservoir pressure

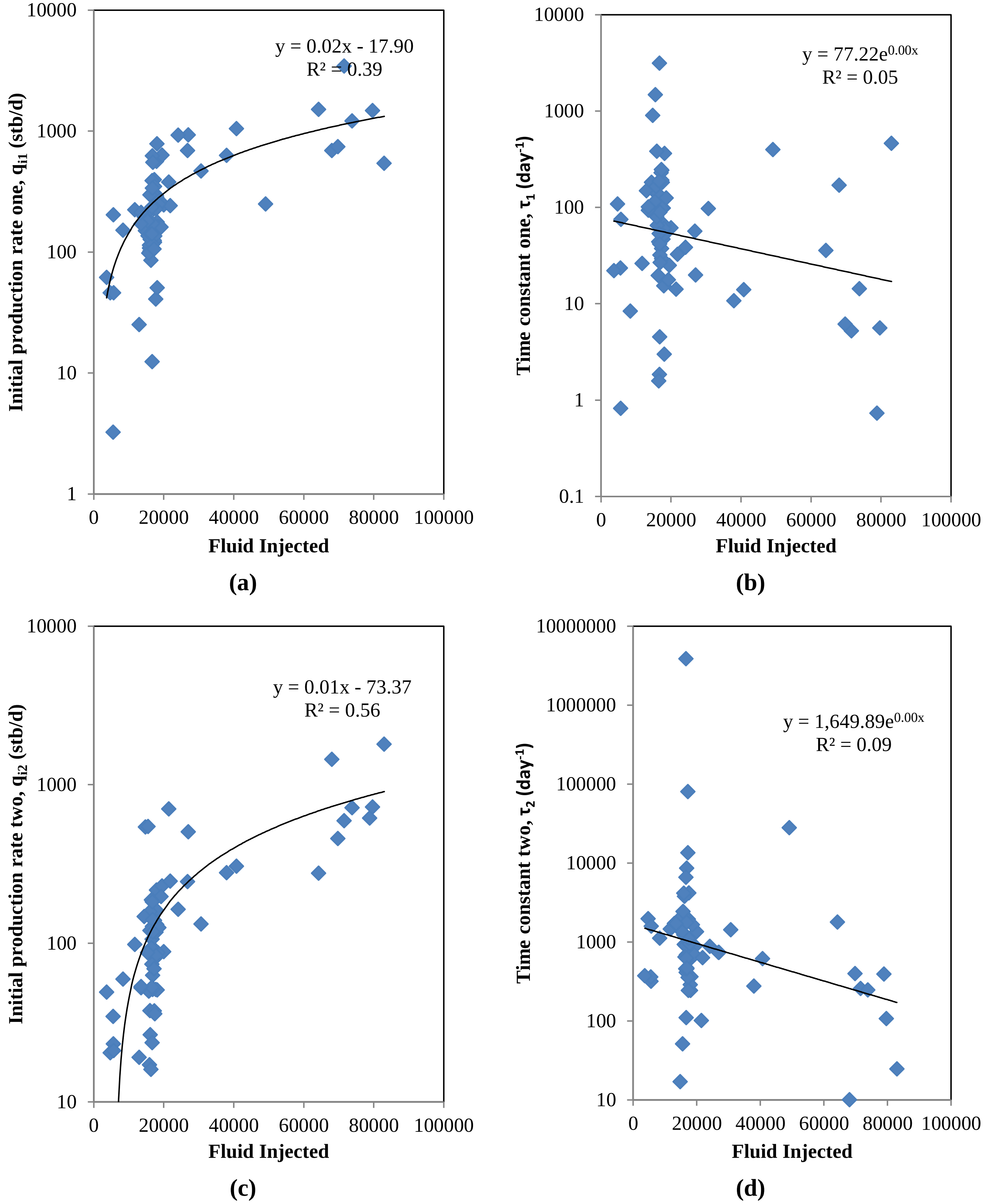

Figure 3-12: Cross plot of Parallel Flow Model parameters and the volume of fracturing fluid injected

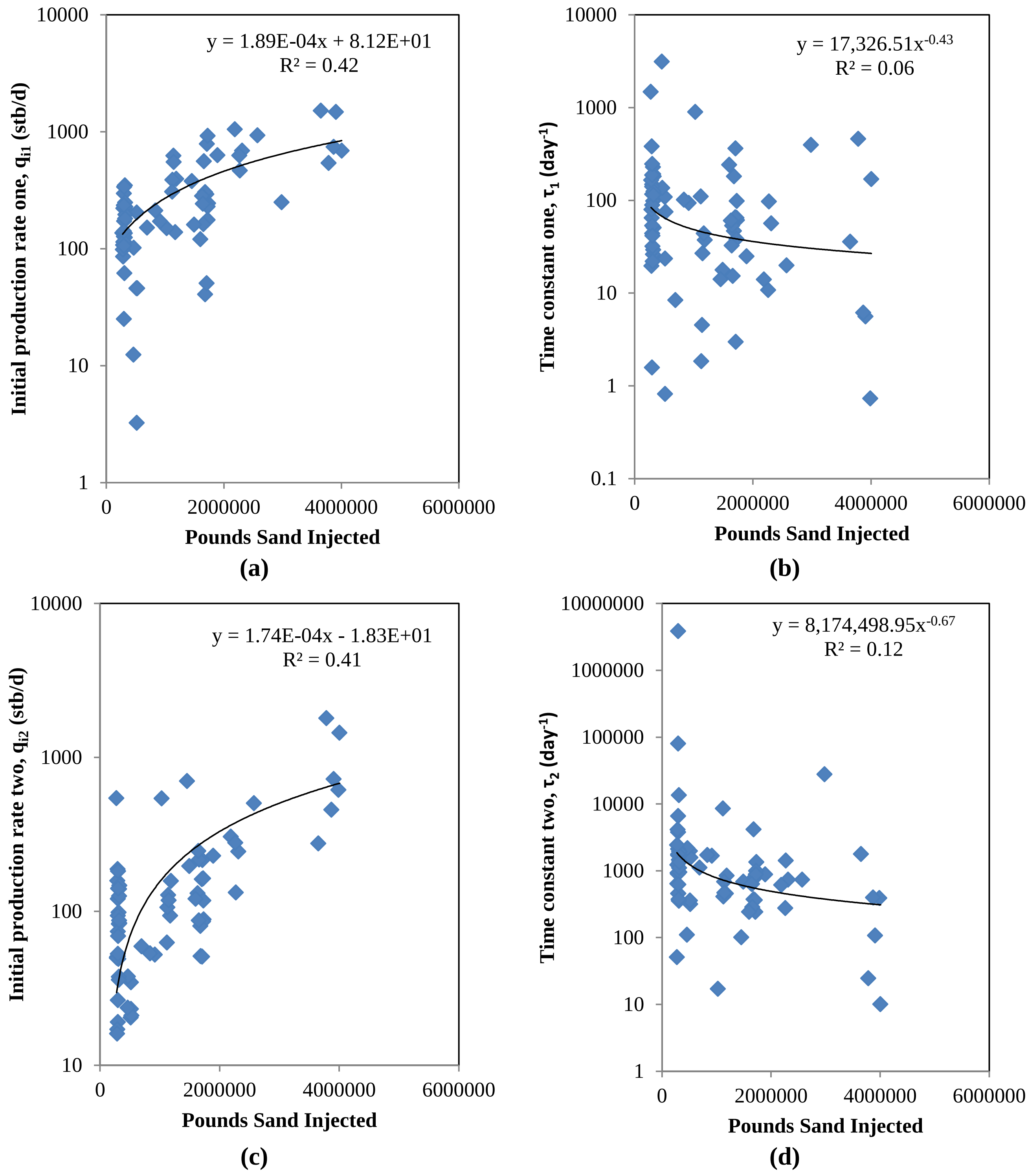

Figure 3-13: Cross plot of Parallel Flow Model parameters and the weight of proppant injected

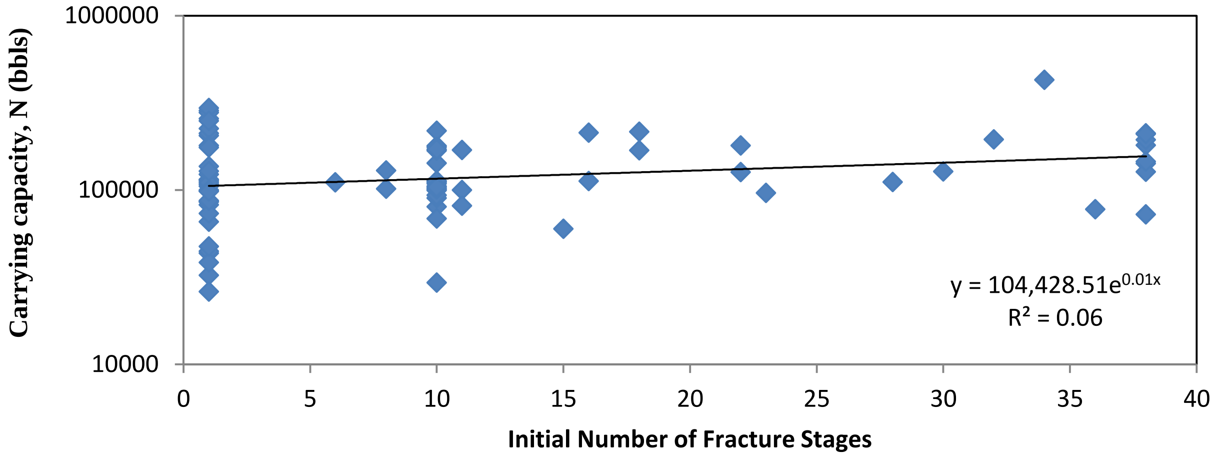

(a)

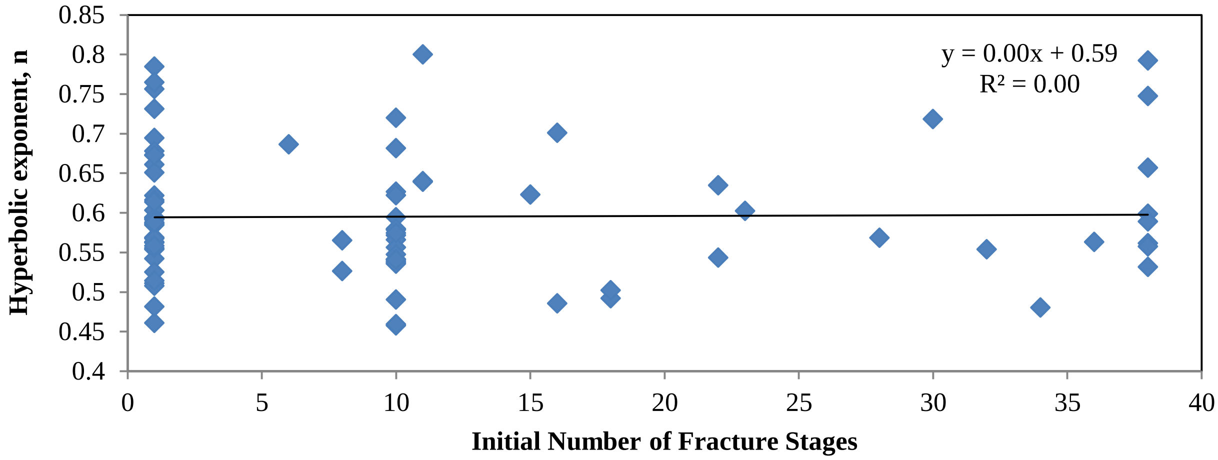

(b)

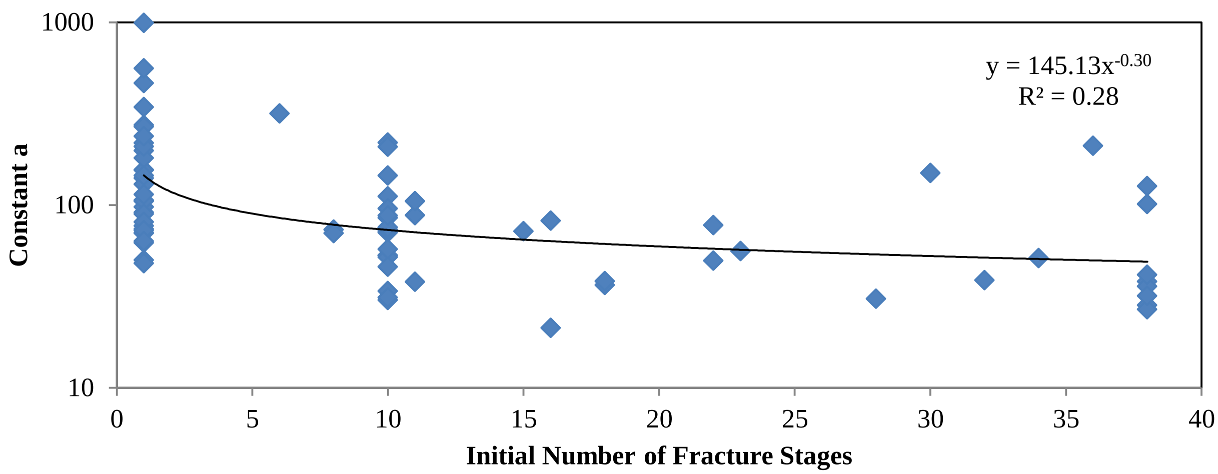

(c)

Figure 3-14: Cross plot of Logistic Growth Model parameters and the initial number of fracture stages

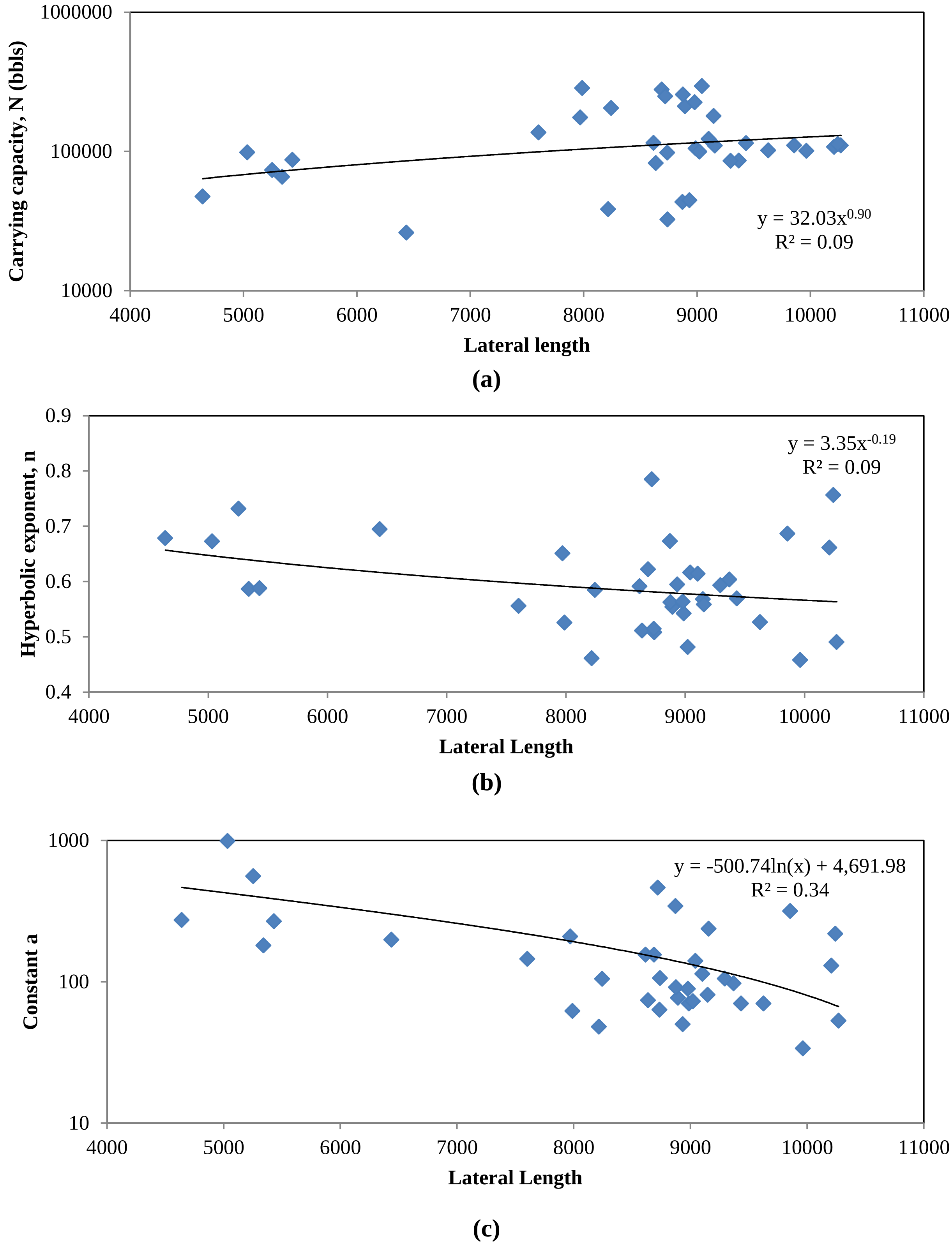

Figure 3-15: Cross plot of Logistic Growth Model parameters and lateral length of the horizontal well

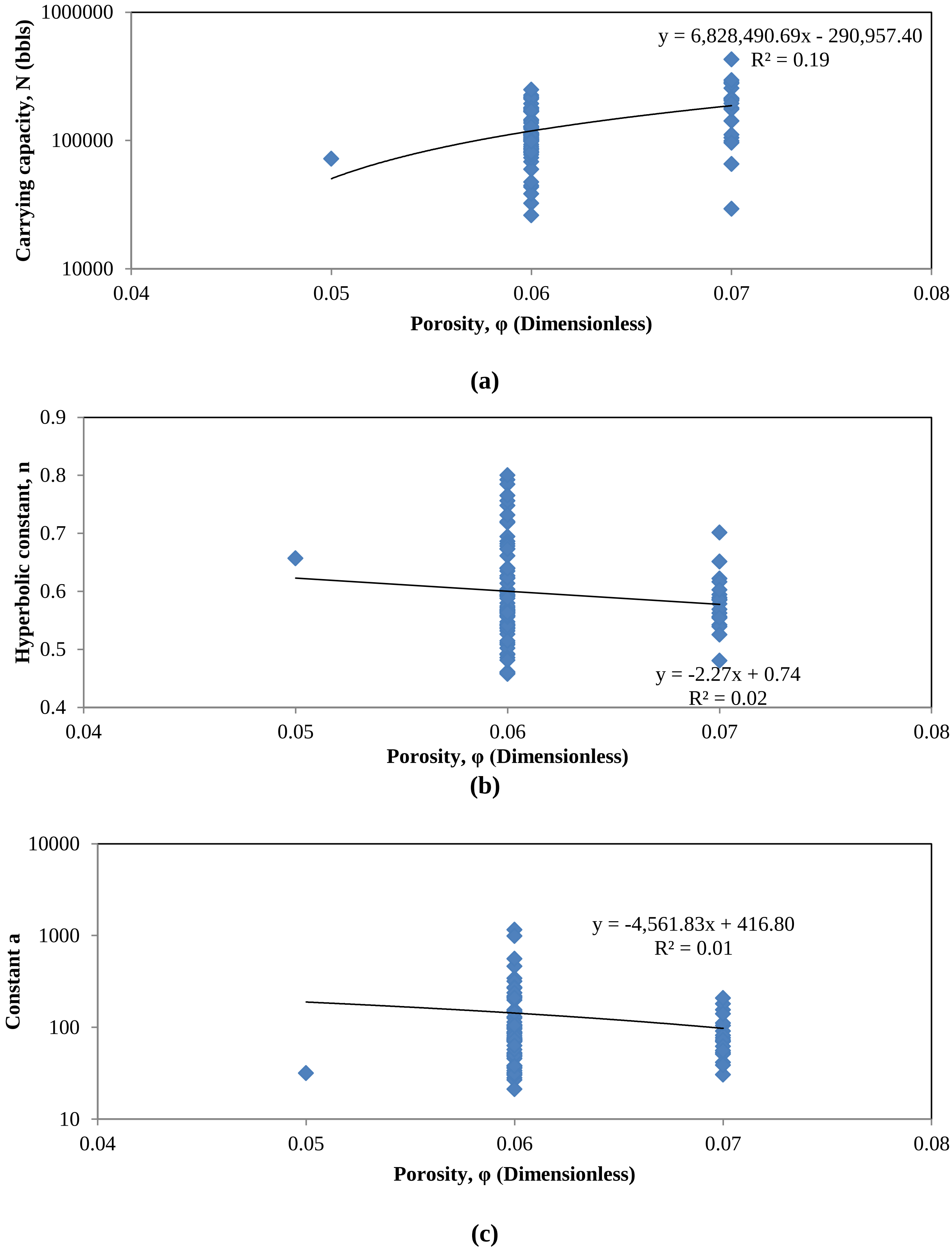

Figure 3-16: Cross plot of Logistic Growth Model parameters and the reservoir porosity

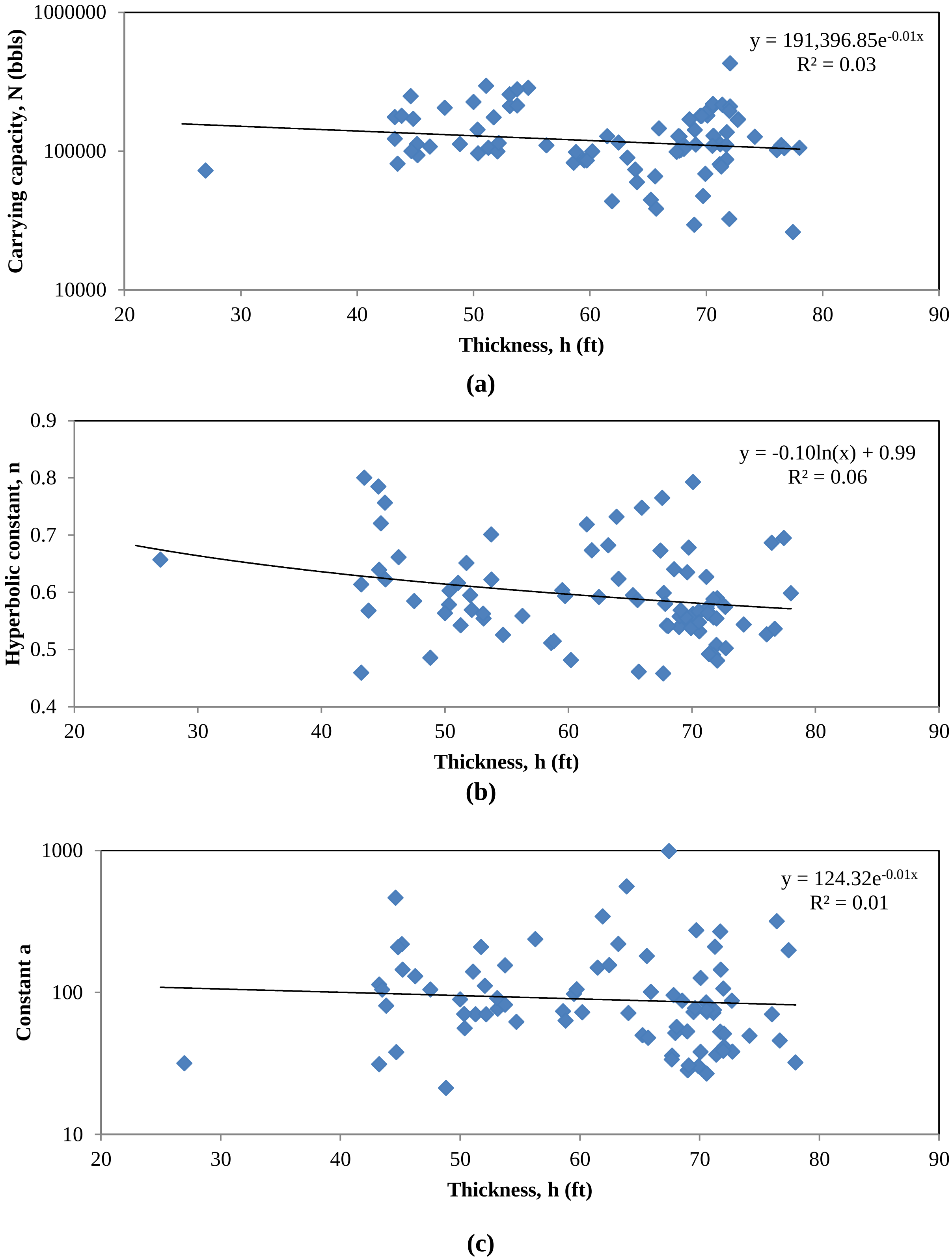

Figure 3-17: Cross plot of Logistic Growth Model parameters and reservoir thickness

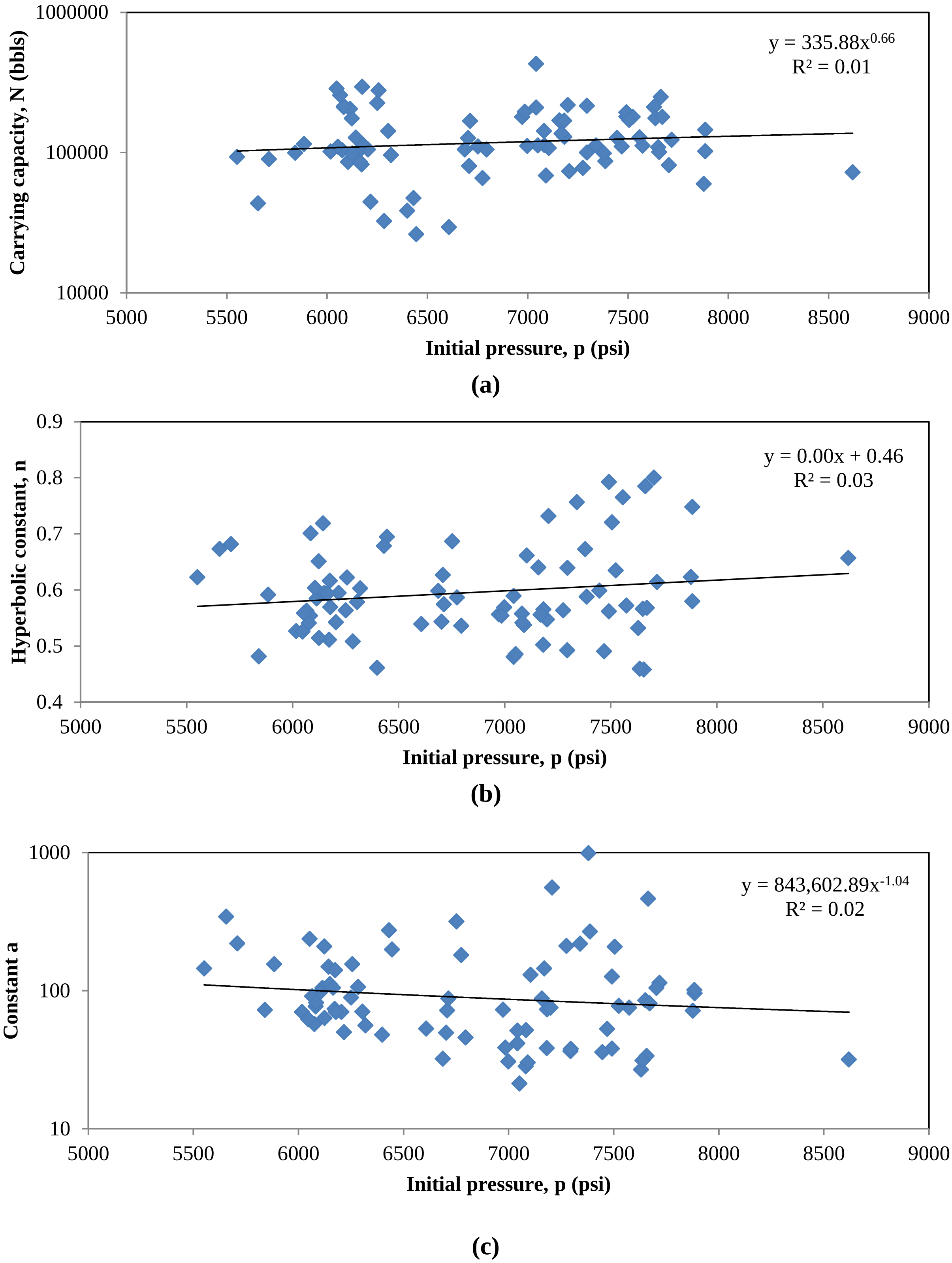

Figure 3-18: Cross plot of Logistic Growth Model parameters and initial reservoir pressure

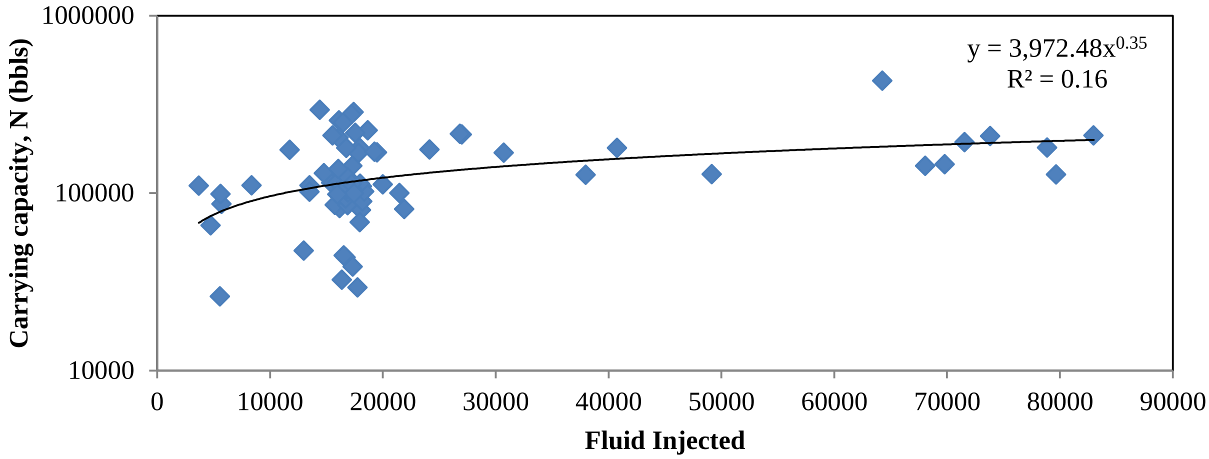

(a)

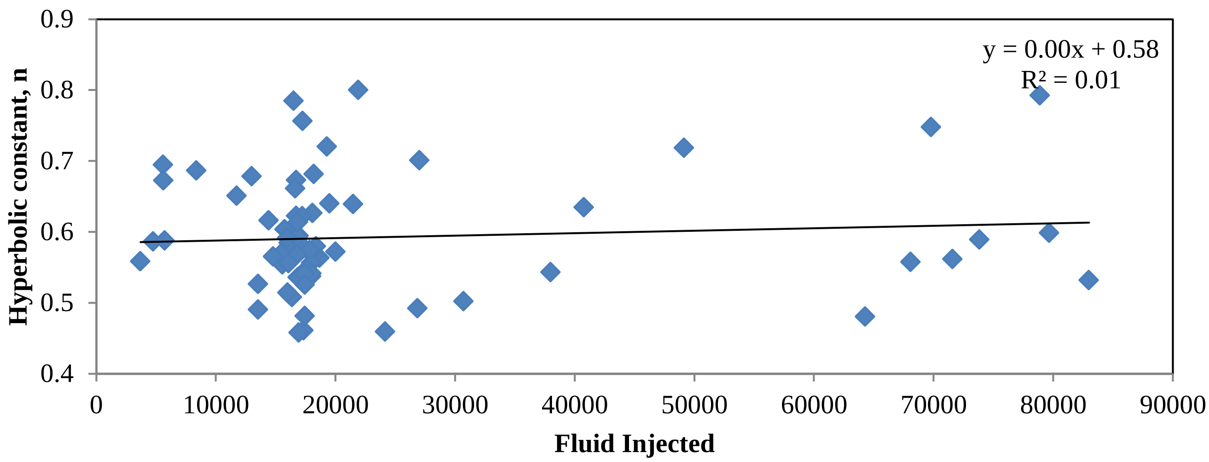

(b)

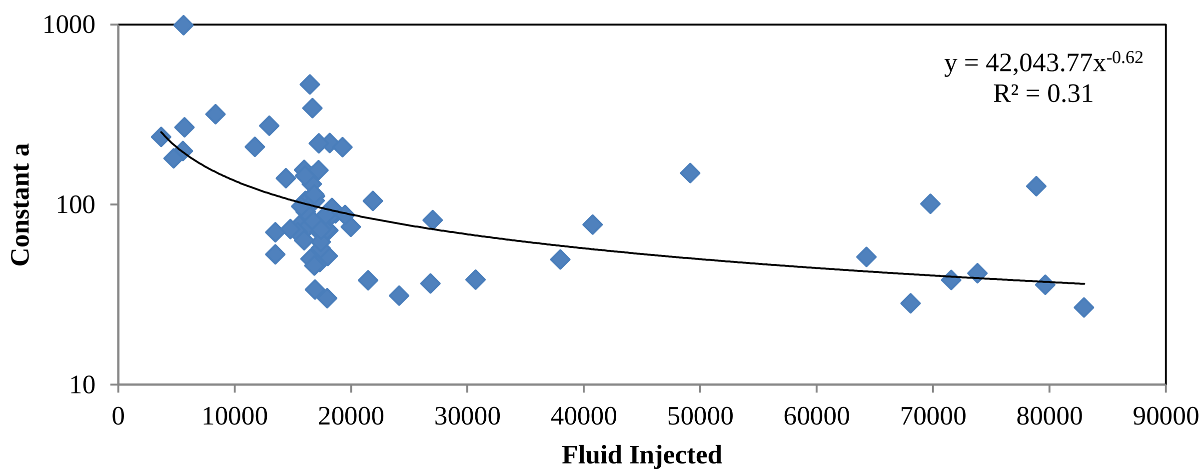

(c)

Figure 3-19: Cross plot of Logistic Growth Model parameters and the volume of injected fracture fluid

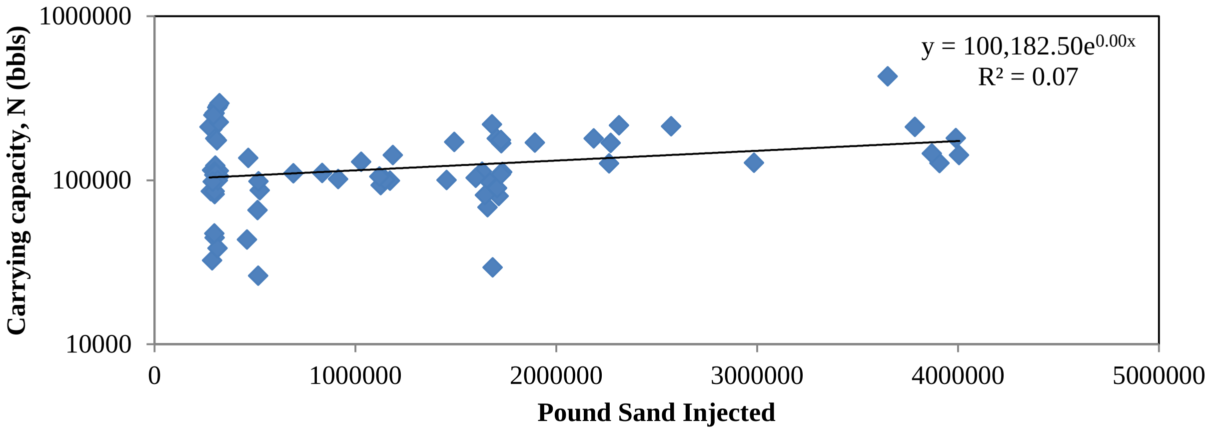

(a)

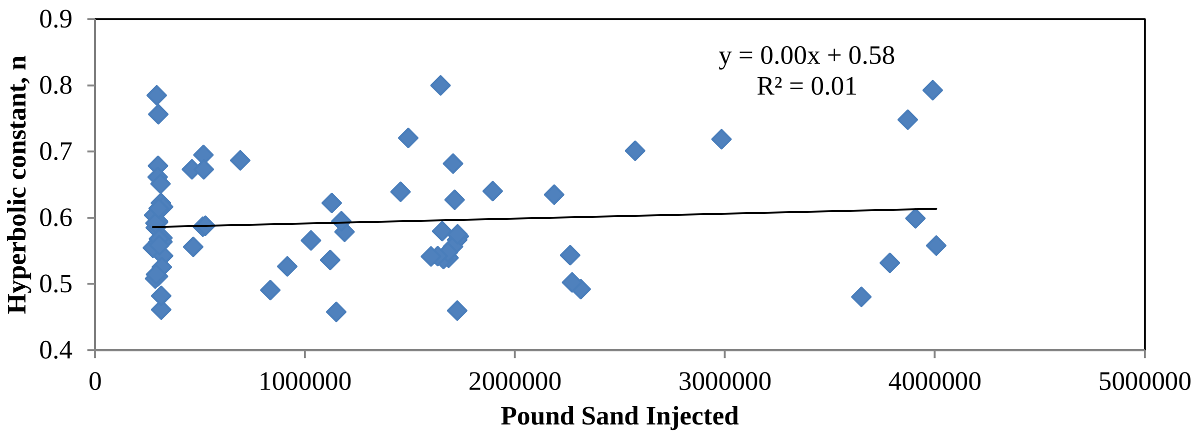

(b)

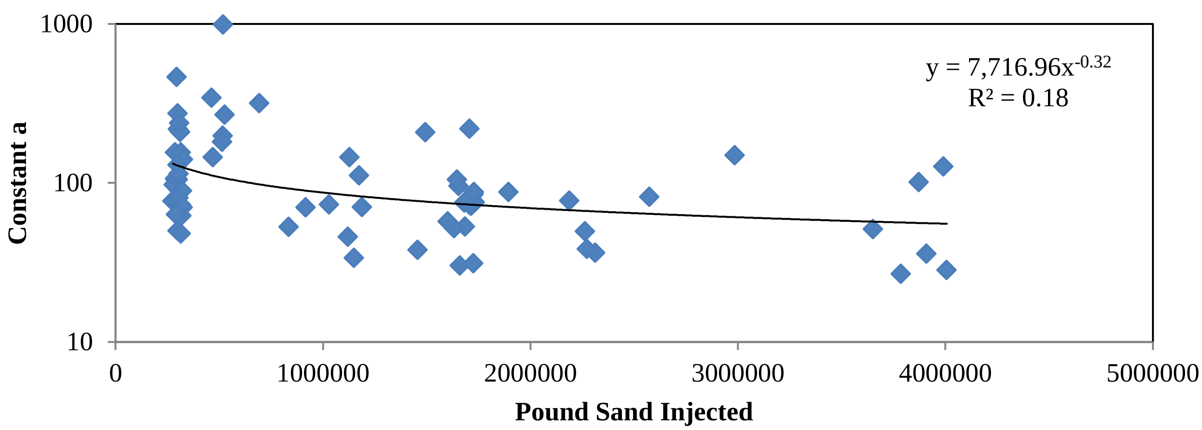

(c)

Figure 3-20: Cross plot of Logistic Growth Model parameters and weight of proppant injected

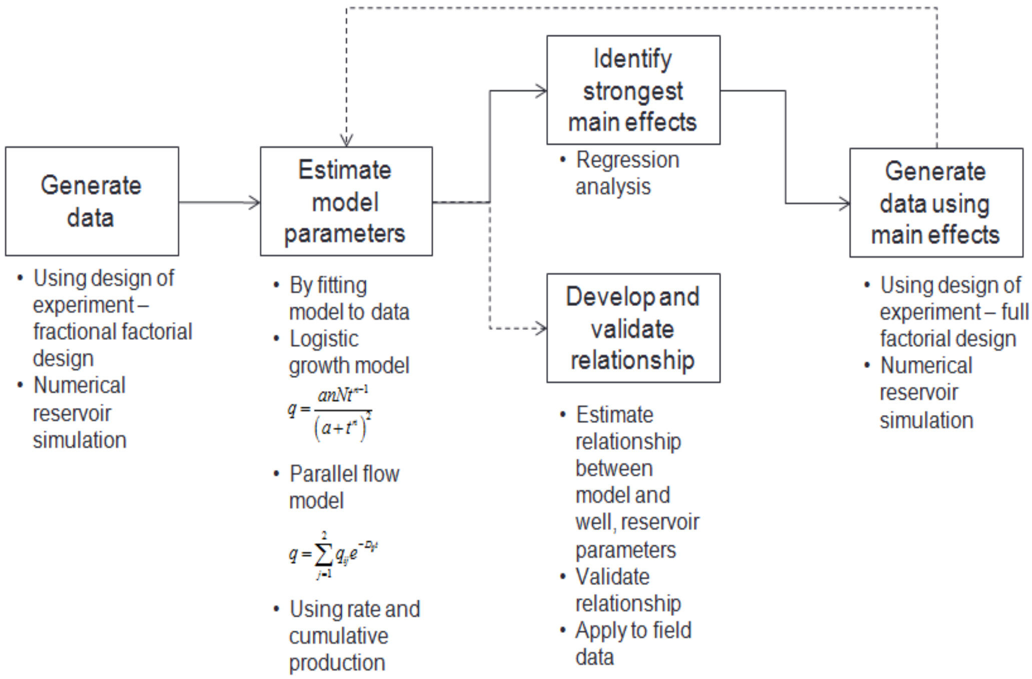

Figure 3-21: Schematic diagram of the process used in developing the mathematical relationship between the model parameter and the reservoir and well completion properties

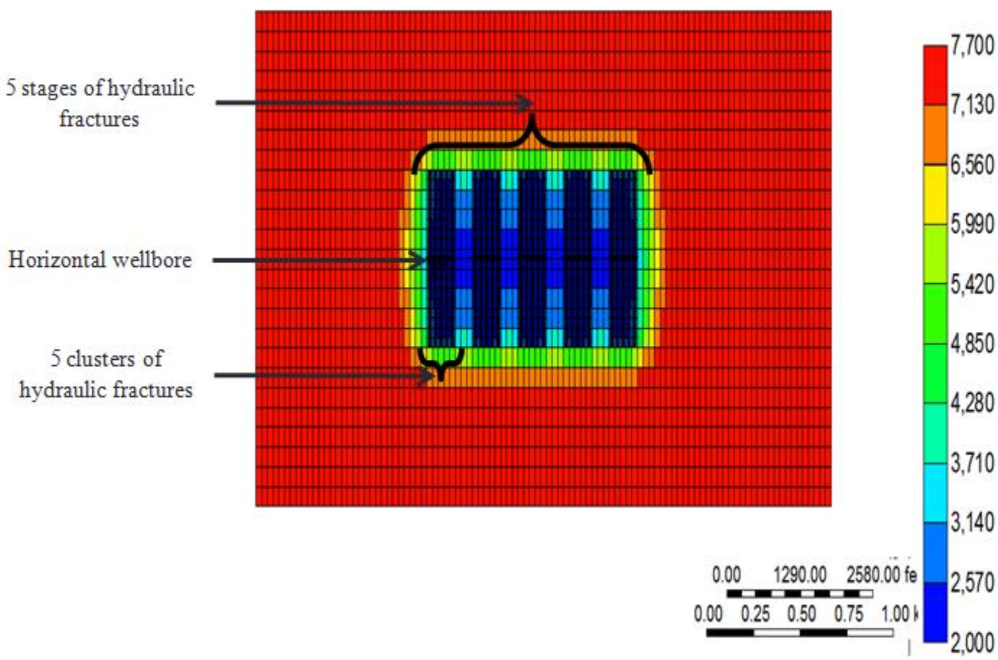

Figure 3-22: Pressure distribution in one of the numerical simulation models. Showing the number of fracture stages and the number of hydraulic fracture clusters

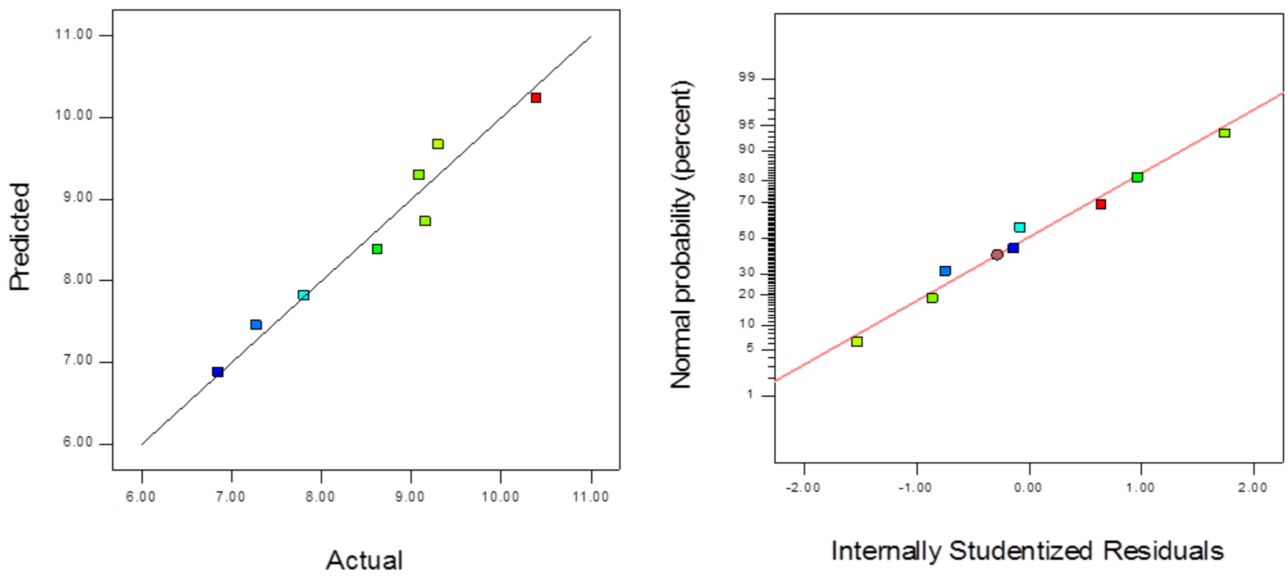

(a) (b)

Figure 3-23: Validation of developed relationship for carrying capacity. Fig. 9a shows a cross plot of the predicted values carrying capacity versus the actual values of the carrying capacity. Fig. 9b is a diagnostic plot that shows the residuals of the regression are normally distributed

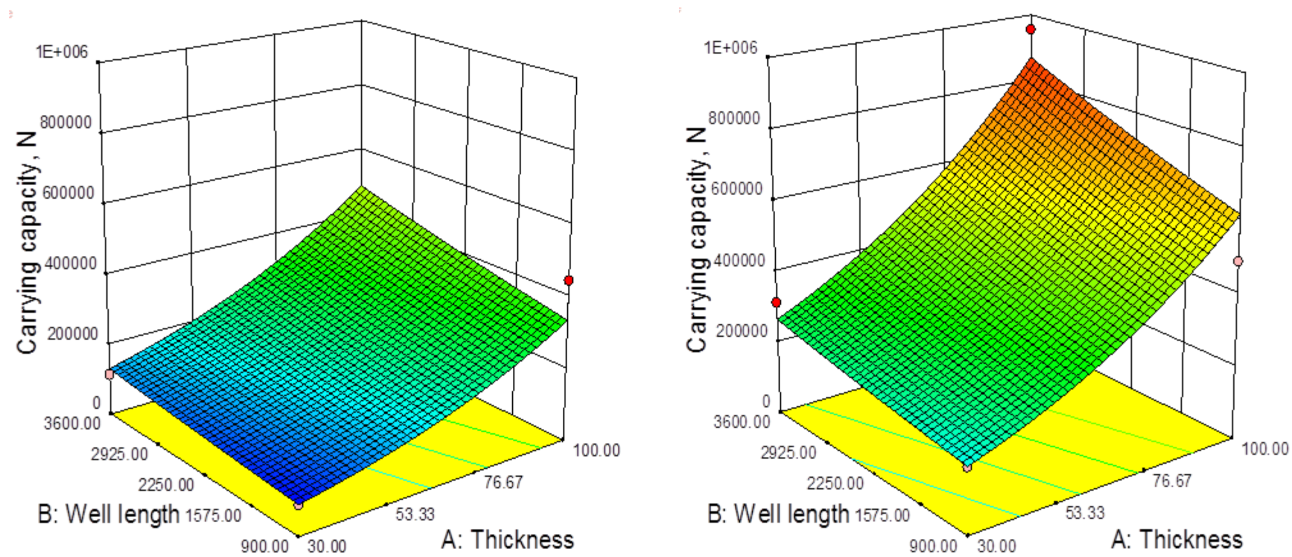

(a) (b)

Figure 3-24: Response surfaces for carrying capacity, N

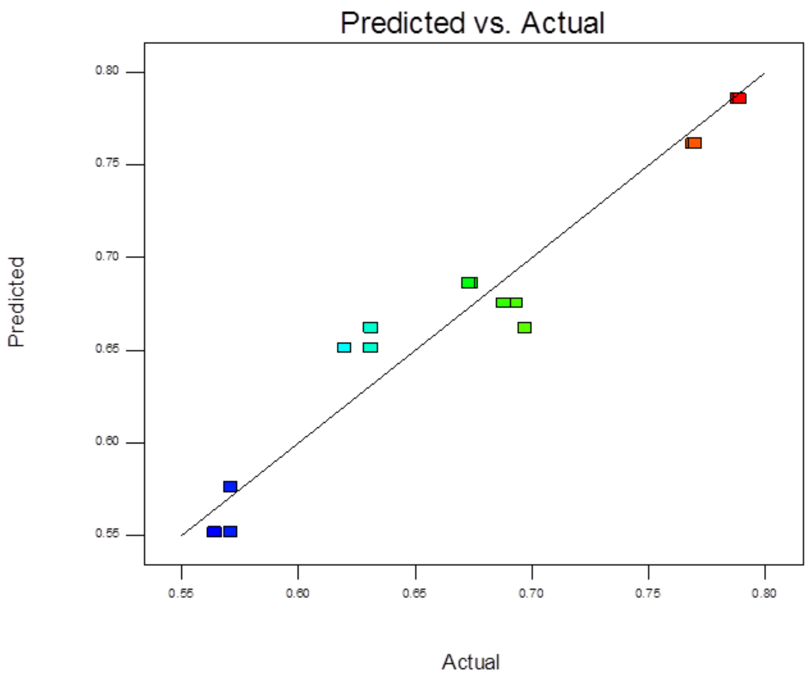

Figure 3-25: Comparison of the predicted versus actual values of the hyperbolic exponent, n

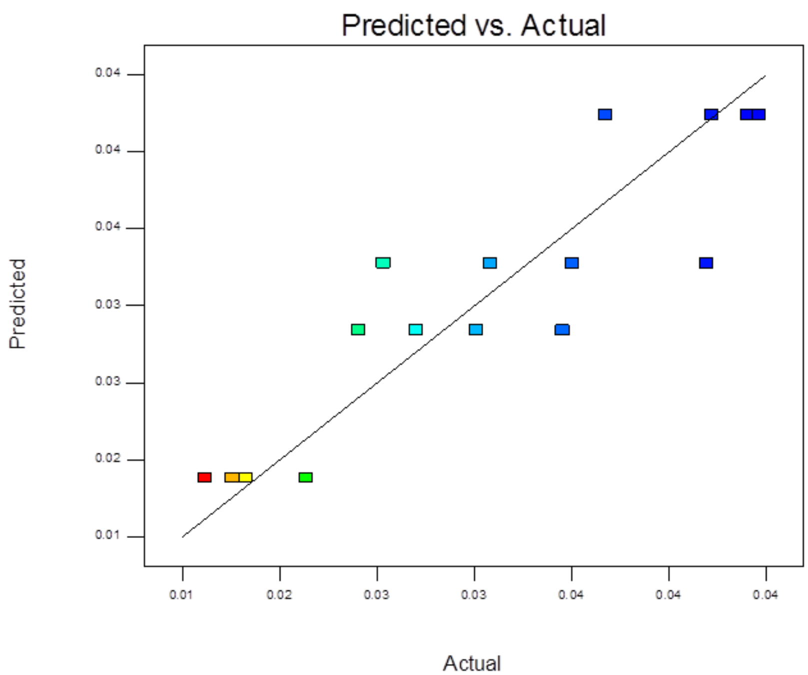

Figure 3-26: Comparison of the predicted versus actual values of the constant, a

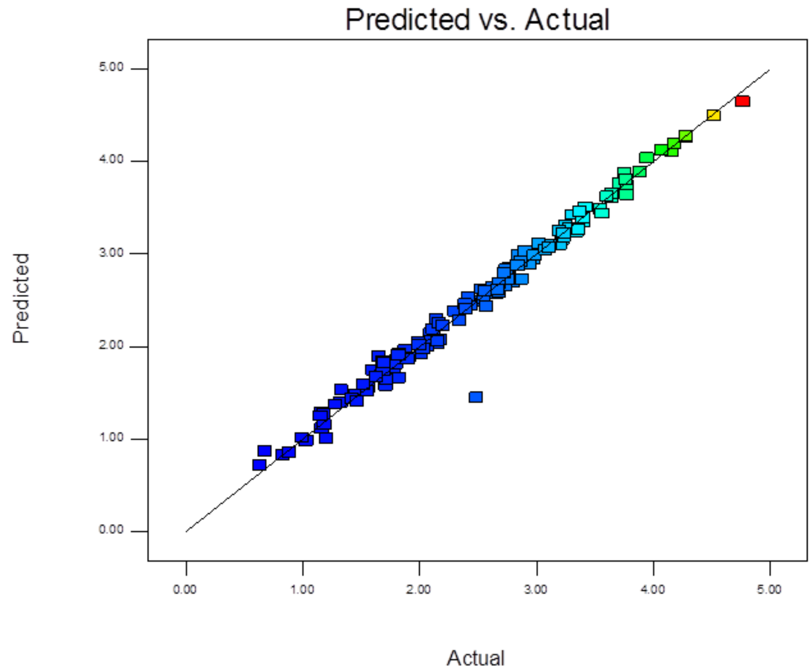

Figure 3-27: Comparison of the predicted versus actual values for initial production rate one, q_{i1}

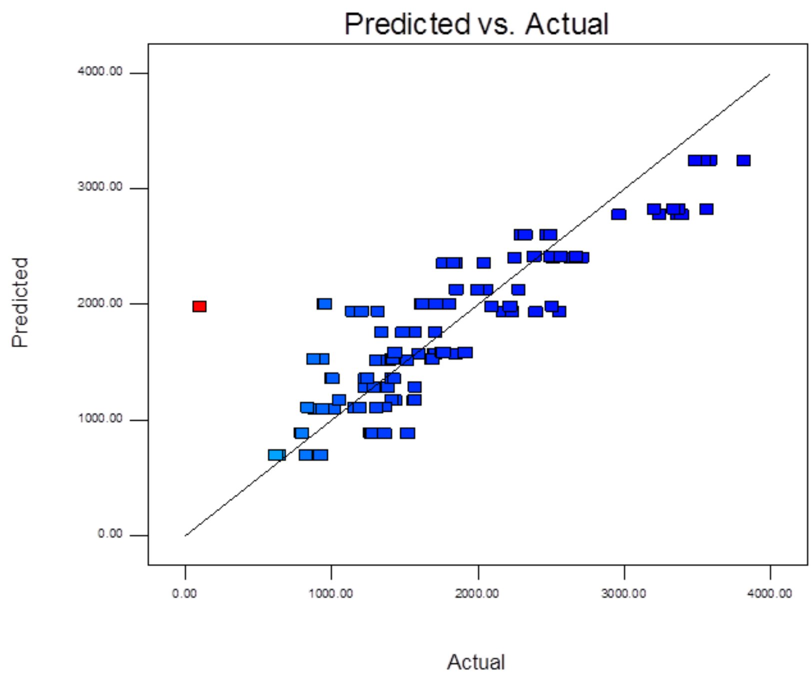

Figure 3-28: Comparison of the predicted versus actual values for time constant one, τ_1

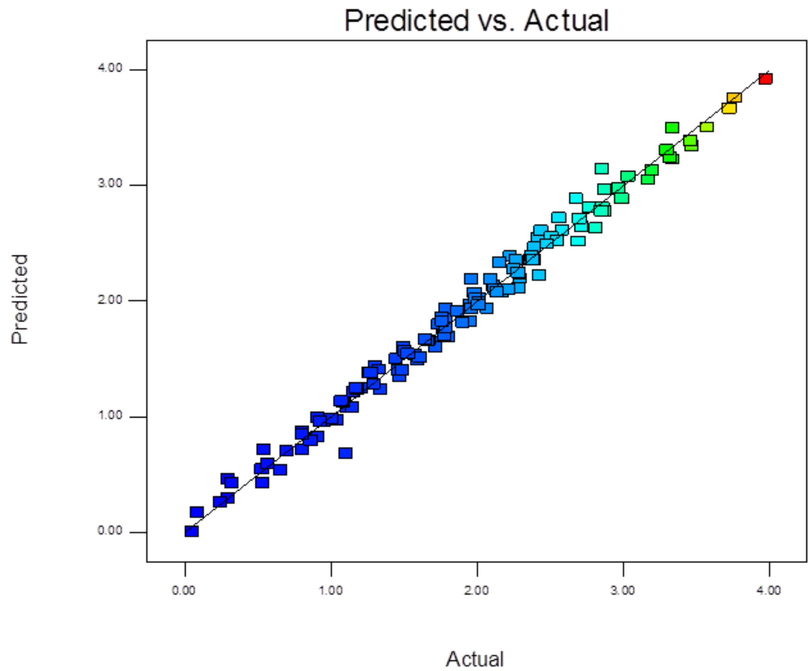

Figure 3-29: Comparison of the predicted versus actual values for initial production rate two, q_{i2}

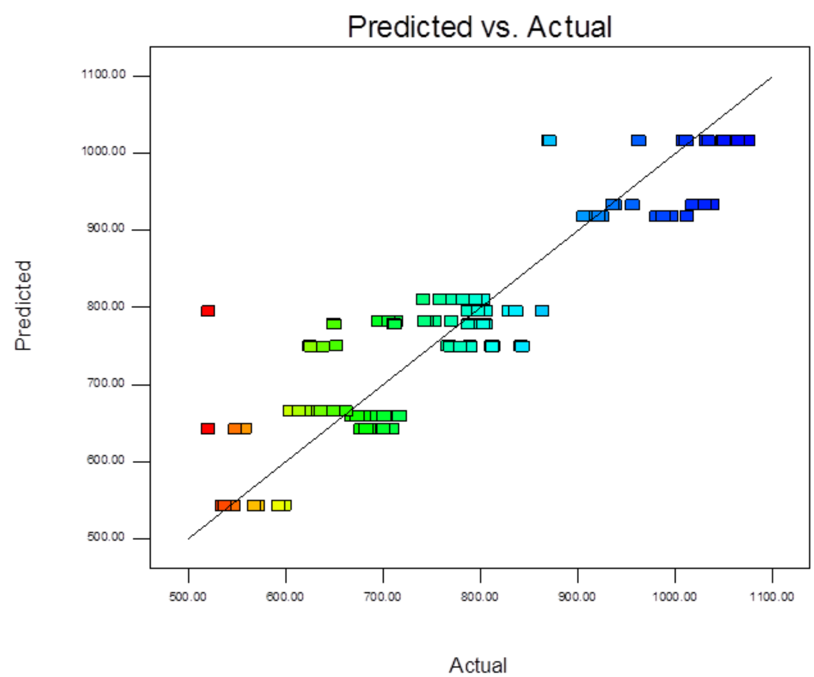

Figure 3-30: Comparison of the predicted versus actual values for time constant two, τ_2

Chapter 4: A Conceptual Model for Parallel Flow in Unconventional Reservoirs

In the previous chapter, it was observed that production data from unconventional reservoirs exhibit multiple time scales where the early time scales are characterized by a much larger rate as compared to subsequent time scales. It was also observed that pure statistical analysis of the data may not reveal insights into the interaction of reservoir and well properties with the production characteristics. Existing analytical models do not all for the modeling of the multiple time scales and often times only focus on the transient flow regime during the first or second time scale. It is therefore necessary to explore and formulate a new conceptual model for the mathematical modeling of flow from unconventional reservoirs. We validated the analytical solution obtained from the conceptual model with synthetic data and also performed a sensitivity study to understand how the model parameters affect production forecasts from the model. In addition we demonstrate its utility in forecasting production in unconventional reservoirs.

4.1 Conceptual Model Development

When a horizontal well is hydraulically fractured it is believed that a main transverse fracture (perpendicular to the wellbore) is produced. In addition to this main fracture, micro-seismic surveys have shown that a network of secondary fractures is also produced as a result of the hydraulic fracturing. Figure 4-1 shows two hydraulically fractured horizontal wells and the micro-seismic events recorded during the fracturing process. If a cross-section is drawn across any of these horizontal wellbore, it can be assumed that the schematic diagram shown in Figure 4-2 would be obtained.

From this cross-section it is conceivable that we have flow from both the small permeability reservoir matrix and the secondary network of fractures. This is in contrast to the general assumption that the reservoir matrix does not directly communicate with the wellbore (Miller et al., 2010 and Chapter 5 of this dissertation). In developing the new conceptual model we make the following simplifying assumptions:

a) The permeability in the main transverse fracture is significantly greater than the permeability of the network of secondary fractures. Therefore, the main hydraulic fracture can be treated as a pseudo wellbore because its pressure would almost instantaneously be equal to that of the wellbore.
b) There is direct flow of fluids from the reservoir matrix into the pseudo wellbore and flow from the matrix to the fracture network is negligible.
c) There is direct flow of fluids from the secondary fracture network into the pseudo wellbore

From these assumptions it is possible to idealize this production system as a reservoir with 2 layers where one layer represents the fracture network and the second layer represents the matrix. Figure 4-3 presents a schematic diagram of this idealized conceptual model. In the subsequent section we present the mathematical model for this conceptual model and its solution.

4.1.1 Analytical Parallel Flow Model without Cross Flow

When there is no cross flow between the layers, the partial differential equation (PDE) governing flow from each layer can be solved independently and the production rate added together to obtain the total production rate from the system. Wattenberger et al. (1998) and Patzek et al. (2012) have shown that flow from low permeability reservoirs can be modeled by using the one dimensional (Cartesian coordinates) form of the diffusivity equation. Therefore, the following development uses the 1-D linear diffusivity equation.

Constant pressure inner boundary condition: The 1-D partial differential equation (PDE) that governs flow from the matrix into the pseudo-wellbore (constant pressure at the fracture face) for each layer is given below:

$$\frac{\partial^2 p_j}{\partial {x_j}^2} = \left(\frac{\phi \mu c_t}{k}\right)_j \frac{\partial p_j}{\partial t}, \tag{4.1}$$

$$p_j(x,0) = p_{i_j}, \tag{4.2}$$

$$\left.\frac{\partial p_j}{\partial x_j}\right|_{x=x_e} = 0, \tag{4.3}$$

$$p_j(x_f,t) = p_{wf}, \tag{4.4}$$

where, p_j and $\left(\frac{\phi \mu c_t}{k}\right)_j$ are the pressure and diffusivity coefficient in layer j, respectively. The subscript j represents the layer number and equation 4.3 represents the no-flow boundary at the external boundary and equation 4.4 is the constant pressure inner boundary condition at the fracture face. If we define the following dimensionless variables $p_{Dj} = \frac{p_j - p_{i_j}}{p_f - p_{i_j}}$, $t_{Dj} = \left(\frac{k}{\phi \mu c_t}\right)_j \frac{t}{L^2}$ and $x_{Dj} = \frac{x_j - x_e}{x_{wf} - x_e}$ we obtain the dimensionless form of equations 4.1 through to 4.4 as:

$$\frac{\partial^2 p_{jD}}{\partial {x_{jD}}^2} = \frac{\partial p_{jD}}{\partial t_{jD}}, \tag{4.5}$$

$$p_{jD}(x_{jD},0) = 0, \tag{4.6}$$

$$\left.\frac{\partial p_{jD}}{\partial x_{jD}}\right|_{x_{jD}} = 0, \tag{4.7}$$

$$p_{jD}(1,t_{jD})=1. \tag{4.8}$$

By using Laplace transform method (Kreyszig E., 2006), the solution to this set of equations was obtained as:

$$p_{Dj}\left(t_D,x_D\right)=1+\frac{4}{\pi}\sum_{n=1}^{\infty}\frac{(-1)^n}{2n-1}e^{-\left[\frac{(2n-1)^2\pi^2}{4}t_{Dj}\right]}\cos\left[\frac{(2n-1)\pi}{2}x_{Dj}\right]. \tag{4.9}$$

A detailed derivation of equation 4.9 is available in appendix A. We derive the production rate in layer j from equation 4.9 by taking its derivative with respect to x_{Dj} and evaluating its value at $x_{Dj}=1$;

$$q_{Dj}\left(t_D\right)=\left.\frac{dp_{Dj}}{dx_{Dj}}\right|_{x_{Dj}=1}=-2\sum_{n=1}^{\infty}(-1)^n e^{-\left[\frac{(2n-1)^2\pi^2}{4}t_{Dj}\right]}\sin\left[\frac{(2n-1)\pi}{2}\right]. \tag{4.10}$$

It is shown in appendix A that equation 4.10 can be simplified by using the Riemann integral (Taylor, 1946) to eliminate the semi-infinite sum. After this simplification we obtain the production rate from layer j as show below:

$$q_{Dj}\left(t_D\right)=2e^{-\frac{\pi^2}{4}t_{Dj}}+\frac{erfc\left[\frac{3}{2}\pi\sqrt{t_{Dj}}\right]}{\sqrt{\pi t_{Dj}}}. \tag{4.11}$$

Equation 4.11 represents the complete solution; it is valid during both the early and late time flow periods. The first term in equation 4.11 is the late time (pseudo steady state) solution and the second term is the early time (transient) solution. If we define $q_D=\dfrac{443.6q\mu B_oL}{x_fkh\left(p_i-p_{wf}\right)}$, we can write equation 4.11 in dimensional form (field units) as shown below:

$$q(t)=\frac{x_f kh(p_i-p_{wf})}{221.8\mu B_o L}e^{-\frac{\pi^2}{4}\frac{6.33E-3kt}{(\phi\mu c_t)L^2}}+\frac{x_f\sqrt{k}h(p_i-p_{wf})\sqrt{(\phi c_t)}erfc\left[\frac{3}{2}\pi\sqrt{\frac{6.33E-3kt}{(\phi\mu c_t)L^2}}\right]}{62.6B_o\sqrt{\mu t}}. \tag{4.12}$$

Because we have assumed that there is no interaction between the matrix and fracture network the total production rate at the fracture face (pseudo wellbore) is determined by summing the individual layer production rate over the total number of layers. The total production rate at the fracture face is therefore,

$$q_{DT}\left(t_{Dj}\right)=\sum_{j=1}^{N_L}f_j\left[2e^{-\frac{\pi^2}{4}t_{Dj}}+\frac{erfc\left[\frac{3}{2}\pi\sqrt{t_{Dj}}\right]}{\sqrt{\pi t_{Dj}}}\right]. \tag{4.13}$$

In equation 4.13, N_L is the total number of layers in the idealized conceptual model, f_i is the contribution of layer i to the total flow, ω_i is the fractional storativity of layer i to the total storativity of the entire system (fractional storativity ratio), λ_i is the ratio of the permeability of layer i to layer 1. The mathematical definitions of these variables are given below:

$$f_j=\frac{q_{ij}}{\sum_{j=1}^{N_L}q_{ij}},$$

$$q_{DT}=\frac{q_T}{\sum_{j=1}^{N_L}q_{ij}},$$

$$t_{Dj}=\frac{\lambda_j}{\omega_j}t_d$$

where $\lambda_j = \dfrac{k_j}{k_1}$, $\omega_i = \dfrac{\left(\phi c_t L^2\right)_i}{\sum_{j=1}^{N_L}\left(\phi c_t L^2\right)_j}$ and $t_d = \dfrac{k_1 t}{\mu \sum_{j=1}^{N_L}\left(\phi c_t L^2\right)_j}$.

For a two layer system, $N_L = 2$, equation 4.13 can be written as shown below:

$$q_D\left(t_{D1},t_{D2}\right) = 2e^{-\frac{\pi^2}{4}t_{D1}} + \frac{erfc\left[\frac{3}{2}\pi\sqrt{t_{D1}}\right]}{\sqrt{\pi t_{D1}}} + 2e^{-\frac{\pi^2}{4}t_{D2}} + \frac{erfc\left[\frac{3}{2}\pi\sqrt{t_{D2}}\right]}{\sqrt{\pi t_{D2}}}. \tag{4.14}$$

In dimensional form equation 4.14 becomes;

$$\begin{aligned} q_T\left(t\right) = {} & \frac{x_{f1}k_1h_1(p_{i1}-p_{wf})}{221.8\mu B_o L} e^{-\frac{\pi^2}{4}\frac{6.33E-3k_1 t}{(\phi\mu c_t)_1 L^2}} + \frac{x_{f1}\sqrt{k_1}h_1(p_{i1}-p_{wf})\sqrt{(\phi c_t)_1}\, erfc\left[\frac{3}{2}\pi\sqrt{\frac{6.33E-3k_1 t}{(\phi\mu c_t)_1 L^2}}\right]}{62.6B_o\sqrt{\mu t}} \\ & + \frac{x_{f2}k_2h_2(p_{i2}-p_{wf})}{221.8\mu B_o L} e^{-\frac{\pi^2}{4}\frac{6.33E-3k_2 t}{(\phi\mu c_t)_2 L^2}} + \frac{x_{f2}\sqrt{k_2}h_2(p_{i2}-p_{wf})\sqrt{(\phi c_t)_2}\, erfc\left[\frac{3}{2}\pi\sqrt{\frac{6.33E-3k_2 t}{(\phi\mu c_t)_2 L^2}}\right]}{62.6B_o\sqrt{\mu t}}. \end{aligned} \tag{4.15}$$

For convenience let $q_{ij} = \dfrac{x_{fj}k_jh_j(p_{ij}-p_{wf})}{221.8\mu B_o L}$, $\bar{q}_{ij} = \dfrac{x_{fj}\sqrt{k_1}h_1(p_{ij}-p_{wf})\sqrt{\left(\phi c_t\right)_j}}{62.6B_o\sqrt{\mu}}$ and

$\tau_{tj} = \dfrac{4\left(\phi\mu c_t\right)_j L^2}{\pi^2 6.33E-3k_j}$ then equation 4.15 can be re-written as shown below:

$$q_T\left(t\right) = q_{i1}e^{-\frac{t}{\tau_1}} + \bar{q}_{i1}\frac{erfc\left[\frac{3}{2}\pi\sqrt{\frac{t}{\tau_1}}\right]}{\sqrt{t}} + q_{i2}e^{-\frac{t}{\tau_2}} + \bar{q}_{i2}\frac{erfc\left[\frac{3}{2}\pi\sqrt{\frac{t}{\tau_2}}\right]}{\sqrt{t}}. \tag{4.16}$$

We can re-write equation 4.13 as:

$$q_T\left(t\right) = \sum_{j=1}^{N_L}\left[q_{ij}e^{-\frac{t}{\tau_j}} + \bar{q}_{ij}\frac{erfc\left[\frac{3}{2}\pi\sqrt{\frac{t}{\tau_j}}\right]}{\sqrt{t}}\right]. \tag{4.17}$$

Equation 4.17 is the complete solution for the idealized parallel flow model with no cross flow. The cumulative production is obtained by integrating equation 4.17 with respect to time $N_{pT} = \sum_{j=1}^{N_L} \left[\int_{t_0}^{t} q_j(\varsigma) d\varsigma \right]$, therefore:

$$N_{pT}(t) = \sum_{j=1}^{N_L} \left[q_{ij}\tau_j \left(1 - e^{-\frac{t}{\tau_j}} \right) + \frac{\bar{q}_{ij} 4\sqrt{\tau_j}}{3\pi^{\frac{3}{2}}} \left(1 - e^{-\frac{t}{\tau_j}} \right) + 2\sqrt{t}\,\bar{q}_{ij} erfc\left[\frac{3}{2}\pi\sqrt{\frac{t}{\tau_j}} \right] \right]. \tag{4.18}$$

In the limit as t tends to infinity (that is $\lim_{t\to\infty}$) equation 4.18 simplifies to

$$\lim_{t\to\infty} N_{pT} = \sum_{j=1}^{N_L} \left[q_{ij}\tau_j + \frac{\bar{q}_{ij} 4\sqrt{\tau_j}}{3\pi^{\frac{3}{2}}} \right]. \tag{4.19}$$

Equation 4.19 provides a means of estimating reserves.

4.1.2 Validation of Parallel Flow Model without Cross Flow

The parallel flow model developed in the previous section was validated using a simple numerical model developed with CMG-GEM. The simulation model has a 21x1x1 grid with dimension 10x150x50. The grid in the z-direction was locally refined into 13 grids or layers. The first grid block in the x-direction is used to model the hydraulic fracture and was assigned a very large permeability of 100 md. Similarly the first 3 layers (grid blocks) in the z-direction is used to model the idealized fracture network layer, the permeability in this layer was set equal to 5 md. The fourth layer in the z-direction was designated a no flow boundary to prevent cross flow between the fracture network layer and the matrix layer. The permeability in this layer was set equal to zero md (0 md). The remaining layers (layers 5 to 13) were used to model the idealized matrix layer and were assigned a permeability of 0.05 md. Other important properties in the simulation model are summarized in Table 4-1.

To validate the analytical model, the numerical simulation model was used to generate a production history of over 20 years. After the production history from the simulation model was obtained, the analytical model parameters were computed using the simulator input data. Refer to Table 4-2 for a summary of these parameters. A production history is then obtained from the analytical model that is then compared with simulator production history. In Table 4-2, index 1 represents the fracture network layer while index 2 represents the matrix layer. A comparison of the production history from the analytical parallel flow and numerical simulation model is in Figure 4-5. From Figure 4-5 the production histories from the analytical parallel flow model and numerical simulation model are identical; therefore the analytical parallel flow model is validated.

4.2 Effect of Model Parameters on Production Forecast Using the Parallel Flow Model without Cross Flow

In this section we perform a sensitivity analysis on the parallel flow model to understand how the model parameters affect production forecasts made with the model. The sensitivity analysis would be performed using equation 4.20 with $N_L = 2$

$$q_{_T D}\left(t_d\right) = \sum_{j=1}^{N_L} f_j \left[2e^{-\frac{\pi^2}{4}\frac{\lambda_j}{\omega_j}t_d} + \frac{erfc\left[\frac{3}{2}\pi\sqrt{\frac{\lambda_j}{\omega_j}t_d}\right]}{\sqrt{\pi\frac{\lambda_j}{\omega_j}t_d}} \right] \tag{4.20}$$

4.2.1 Effect of Transient Terms

The effect of the transient terms on the production forecast is determined by comparing the forecast without the transient terms with the forecast with the transient terms. The input used for this analysis is summarized in Table 4-3 below.

We specified 2 cases for this analysis,

1. Case one: with transient (early time solution) terms and pseudo (late time solution) steady state terms,
2. Case two: This is identical to case one but without the transient terms.

Each of these cases use the inputs summarized in Table 4-3. The result of this analysis is presented in Figure 4-6 as a log-log plot of rate versus time. The solid line in Figure 4-6 is case two while the dashed line represents case one. The dashed line starts with a slope of half which is followed by a pseudo steady state flow (exponential decline) after which another half slope is observed and a final exponential decline is observed. The solid line on the other hand exhibits two sequential exponential declines. There are two time scales on this plot and they are about two orders of magnitude different at the start of each time scale. Therefore, omitting the transient terms in the model will result in a significant error in the production forecast.

4.2.2 Effect of Pseudo Steady Terms

Using the same procedure as in section 4.2 we investigate the effect of the pseudo steady state terms on the production forecast. The input used for this analysis is identical to those summarized in Table 4-3.

The two cases specified for this analysis are:

1. Case one: with transient (early time solution) terms and pseudo (late time solution) steady state terms

2. Case two: This is identical to case one but without the pseudo steady state terms. Both case one and case two use the inputs summarized in Table 4-3.

   The result of this analysis is presented in Figure 4-7 as a log-log plot of rate versus time. The solid line in Figure 4-7 is case one while the dashed line represents case two. At early time both cases have the same production forecast that scales with a half slope and at a dimensionless time of about 10^{-3} the production rate from case two begins to deviate from the production forecast made by case one. Therefore omitting the exponential terms would introduce some error in the late time forecast.

4.2.3 Effect of Storativity Ratio, ω

To investigate the effect of storativity ratio on model forecast we defined three cases that have identical inputs. We only change the storativity ratio in each case and then generate the production forecast and compare them on a log-log plot of rate versus time.

The three cases specified for this analysis and their respective inputs are in Table 4-4. The result of this analysis is presented in Figure 4-8. As defined the storativity ratios ($\omega_i = \dfrac{\left(\phi c_t L^2\right)_i}{\sum_{j=1}^{N_L}\left(\phi c_t L^2\right)_j}$) for all the layers must add up to 1 and it is a measure of the storage capacity of each layer. From Figure 4-8 we observe that as the storativity ratio of layer 1 increases, the longer the duration of production from layer 1 (observed increasing hump at early time). For really small values of the storativity ratio the function behaves as a single porosity system and as the storativity ratio increases it becomes obvious that the system is a double porosity system. At late time all the curves collapse on the same curve. Therefore we can conclude that the storativity ratio will have a significant impact on early time production forecast.

4.2.4 Effect of Permeability Ratio, λ

We investigate the effect of the permeability ratio by defining three cases as shown in Table 4-5. In the three cases considered all the other parameters are fixed at the values shown in Table 4-5 while the permeability ratio is different for all the three cases. In case one, λ is set equal to 2.5×10^{-3}, in case two λ is set equal to 2.5×10^{-2} and λ is set equal to 2.5×10^{-1} in case three.

A comparison of the rate forecast from the three cases in presented in Figure 4-9. At early time there is no significant difference between the three curves but at late time the difference between the three curves is more pronounced. Recall the definition of permeability ratio is given as $\lambda_j = \frac{k_j}{k_1}$, therefore $\lambda_1 = \frac{k_1}{k_1} = 1$ for all the three cases as a result the curves are identical at early time. At late time the permeability ratio is different therefore there is significant difference in the model performance. The smaller the value of λ_2, the longer the production duration this is because the small values of λ correspond to small values of diffusivity constant. Physically this means that the production rate would exhibit transient flow characteristics for a longer period as observed in Figure 4-9. Therefore the permeability ratio has the greatest impact on the late time performance.

4.3 Application to Field Data

An application of the parallel flow model to field data is presented in this section. The production data used for this example is showed in Figure 4-10. Figure 4-10a shows the log-log plot of production rate versus time and the tubinghead pressure versus time. In order to apply the model to the data, we find the values of ω_i, λ_i and f_i that minimize the sum of the squared error difference between the model predictions and data for the rate and cumulative production, that is,

$$\min\ e=\sum_{j=1}^{n}\left(q_j^{data}-q_j^{\mathrm{model}}\right)^2+\left(N_{p,j}^{data}-N_{p,j}^{\mathrm{model}}\right)^2. \tag{4.21}$$

The result of the application is presented in Figure 4-10b and c. Figure 4-10b contains three curves, the original rate data (red markers), the history matched data (black markers) and the model forecast (blue markers). It can be observed from this figure that the model predictions provide a good match to the data. The model parameters that gave this fit shown in Figure 4-10 summarized in Table 4-6. The forecast was done until a production rate of 0.16 stb/d and this is equivalent to a cumulative production of 0.23 MMSTB. The cumulative – time plot for this example is shown in Figure 4-10c.

4.4 Summary and Conclusions

This chapter presented a new simple analytical model for predicting production from fractured horizontal wells in unconventional reservoirs that exhibit linear flow. The model presented is based on an idealized conceptual model that assumes after hydraulic fracturing a well a main fracture and a network of fractures are created. Therefore the reservoir contains 3 different continuum based on permeability. With the main fracture having a permeability, much greater than the fracture network which in turn has a permeability that is much greater than that of the reservoir matrix. Because of this assumption we regard the main fracture as a pseudo wellbore, and in addition, we treat the fracture network and reservoir matrix as reservoir layers that independent contribute to flow from the well.

With the conceptual model we proceed to develop the mathematical model from which the analytical model was derived. We also presented the result of a sensitivity study on the model. The sensitivity study showed that when the transient terms in the solution are neglected a significant amount of error is introduced in the model forecast.

When the pseudo steady state terms are ignored some error is also introduced into any forecast made with the model however the error introduced is not as large as that introduced when the transient terms are ignored. The sensitivity study also showed that the storativity ratio would only have a significant effect on the production forecast at early time. The permeability ratio was found to only affect late time flow, at its resultant effect is to prolong transient flow from the reservoir matrix compartment as its value decreases. We also showed that the model can reliably trend the observed producing characteristics of hydraulically fractured horizontal wells (within engineering limit) and presented an example application to field data.

Table 4-1: Summary of data input to numerical simulation model used to validate parallel flow model

Simulator Input		
	Fracture network layer	**Reservoir matrix layer**
Permeability, k (md)	5	0.05
Fracture half length, $x_{f\,(ft)}$	75	75
Porosity, φ	0.3	0.3
Viscosity, μ (cp)	2	2
Total compressibility, $c_{t\,(psi^{-1})}$	2.86×10^{-5}	2.86×10^{-5}
Reservoir length, L (ft)	210	210
Bottom hole pressure, P_{wf} (psi)	50	50
Initial reservoir pressure, P_i (psi)	5300	5300
Thickness, h (ft)	11.54	34.62
Formation volume factor, B_o (rb/stb)	1.25	1.25

Table 4-2: Summary of computed model parameters for the validation of the parallel flow model without cross flow

Computed model parameters	Values
q_{i1} (stb/d)	244
$\overline{q}_{i1}$(stb/d$^{0.5}$)	336
τ_1 (Days)	10
q_{i2} (stb/d)	7
$\overline{q}_{i2}$(stb/d$^{0.5}$)	101
τ_2 (Days)	970

Table 4-3: Summary of model input parameters for sensitivity analysis of transient terms on production forecast

Model parameters	Values
f_1 (Fraction)	0.99
λ_1 (Fraction)	1.00
ω_1 (Fraction)	0.20
f_2 (Fraction)	0.01
λ_2 (Fraction)	2.50E-03
ω_2 (Fraction)	0.80

Table 4-4: Summarized model input parameters used to investigate the effect of storativity ratio on model forecast

Model parameters	Case 1	Case 2	Case 3
f_1 (Fraction)	0.99	0.99	0.99
λ_1 (Fraction)	1.00	1	1.00
ω_1 (Fraction)	1.0×10^{-5}	1.0×10^{-3}	1.0×10^{-1}
f_2 (Fraction)	0.01	0.01	0.01
λ_2 (Fraction)	2.5×10^{-2}	2.5×10^{-2}	2.5×10^{-2}
ω_2 (Fraction)	1.00	0.999	0.90

Table 4-5: Summarized model input parameters used to investigate the effect of permeability ratio on model forecast

Model parameters	Case 1	Case 2	Case 3
f_1 (Fraction)	0.99	0.99	0.99
λ_1 (Fraction)	1.00	1.00	1.00
ω_1 (Fraction)	0.20	0.20	0.20
f_2 (Fraction)	0.01	0.01	0.01
λ_2 (Fraction)	2.5×10^{-3}	2.5×10^{-2}	2.5×10^{-1}
ω_2 (Fraction)	0.80	0.80	0.8

Table 4-6: Summary of model parameters for example 1

Fit parameters	Values
q_{i1} (stb/d)	135
$\overline{q}_{i1}$(stb/d$^{0.5}$)	2302
τ_1 (Days)	1,480.16
q_{i2} (stb/d)	504
$\overline{q}_{i2}$(stb/d$^{0.5}$)	1632
τ_2 (Days)	53.37

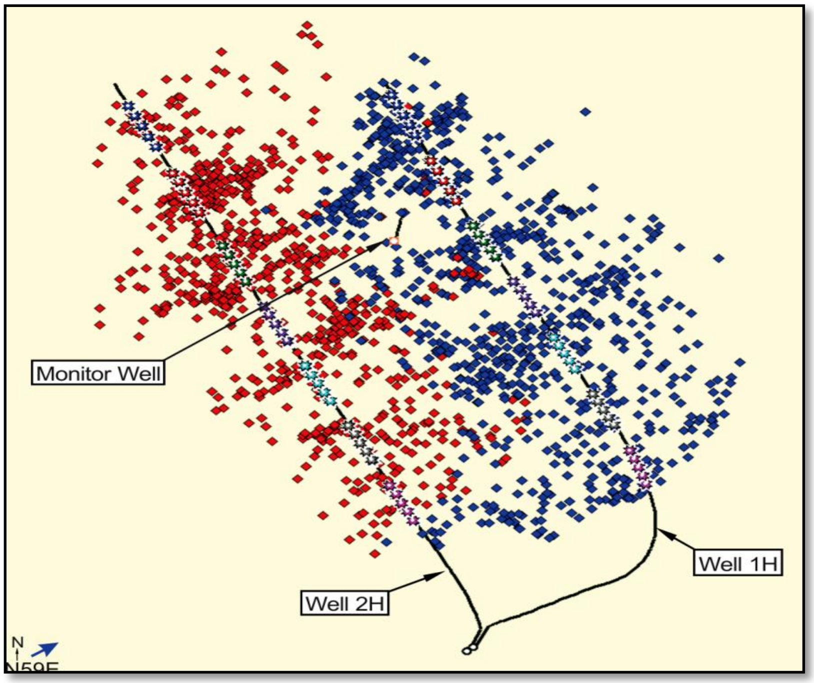

Figure 4-1: Micro-seismic survey data showing two horizontal wells and the recorded micro-seismic events from hydraulically fracturing the wells. Source: Bello (2009)

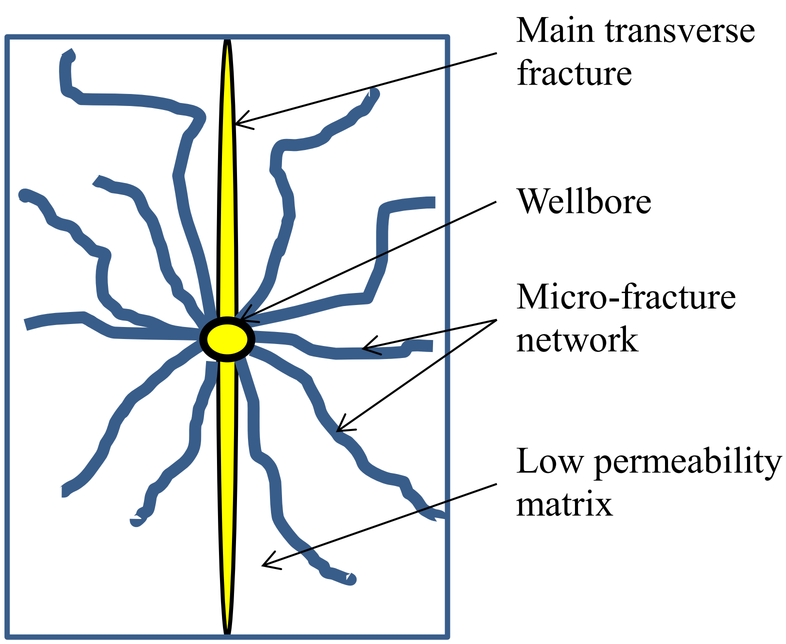

Figure 4-2: Schematic of a cross-section drawn across a horizontal wellbore showing the main hyraulic fracture and the network of fractures

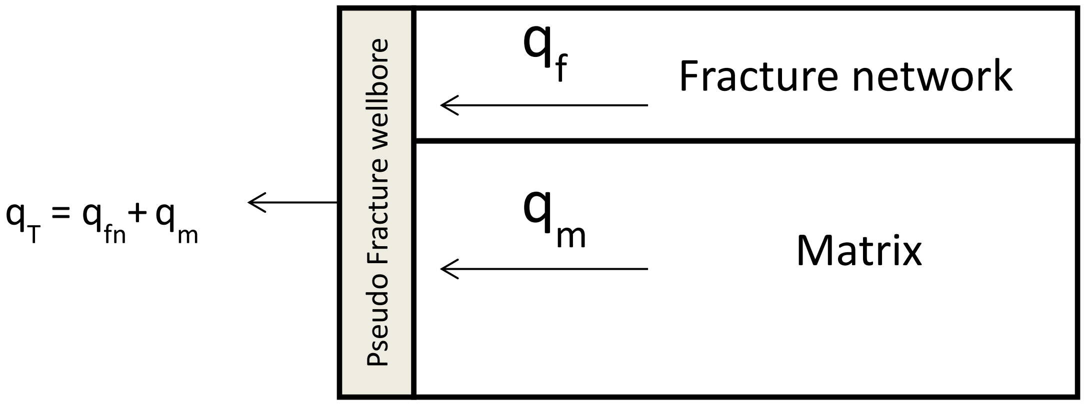

Figure 4-3: Idealized conceptual model of a fractured horizontal well in an unconventional reservoir with no crossflow between the matrix and fracture network layer

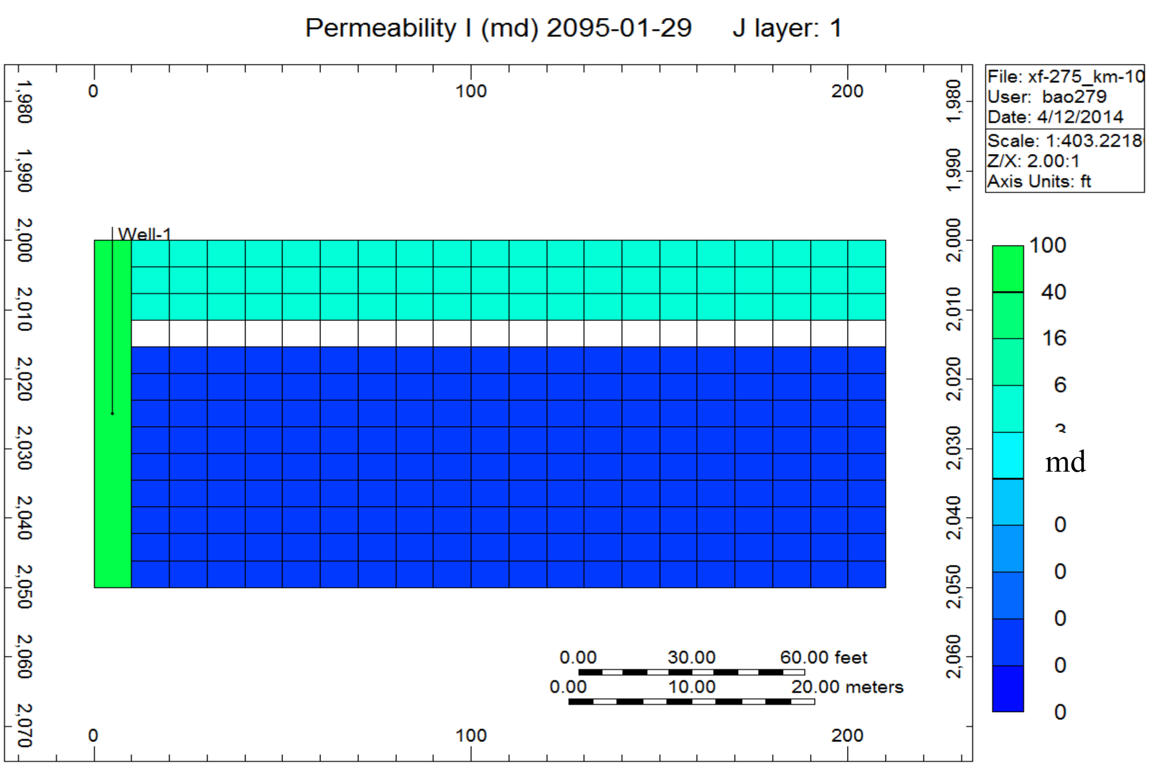

Figure 4-4: CMG-GEM numerical simulation model used to validate the parallel flow model without cross flow

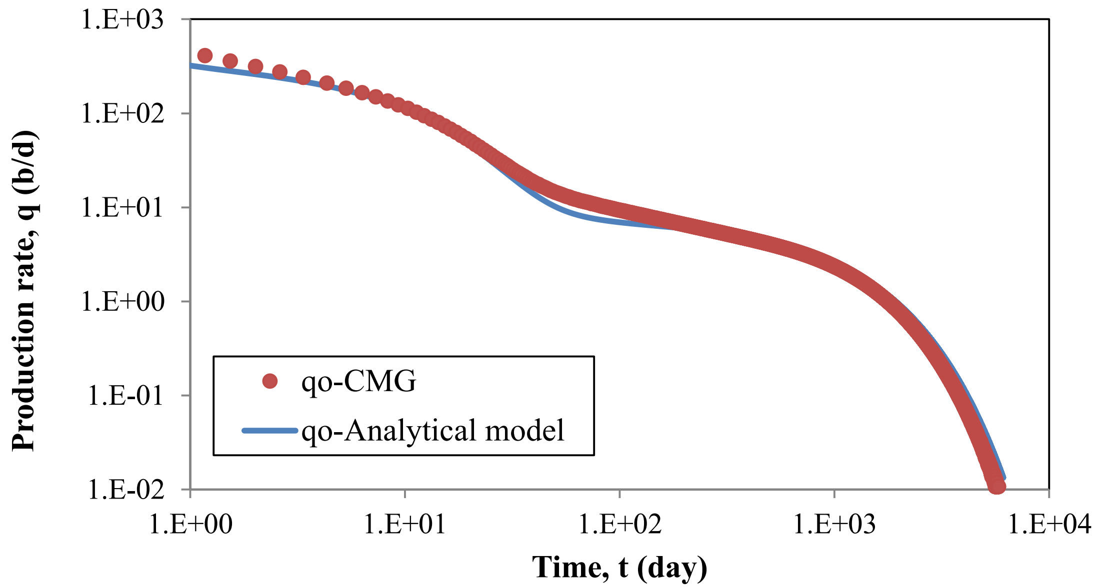

Figure 4-5: Comparison of the production history from the analytical parallel flow model without cross flow and the numerical simulation model

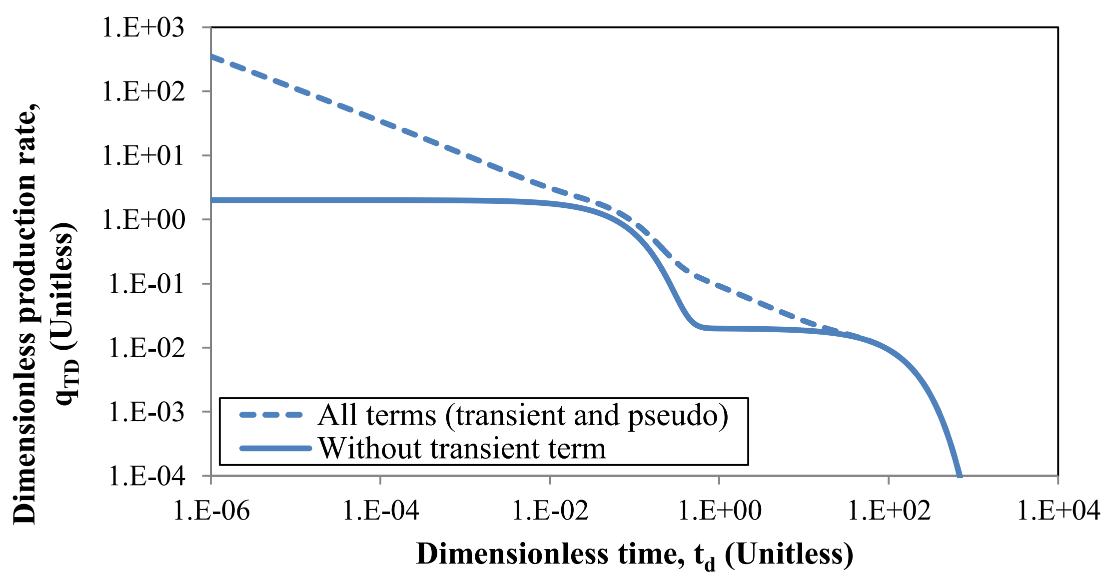

Figure 4-6: Effect of omitting transient terms on the production forecast

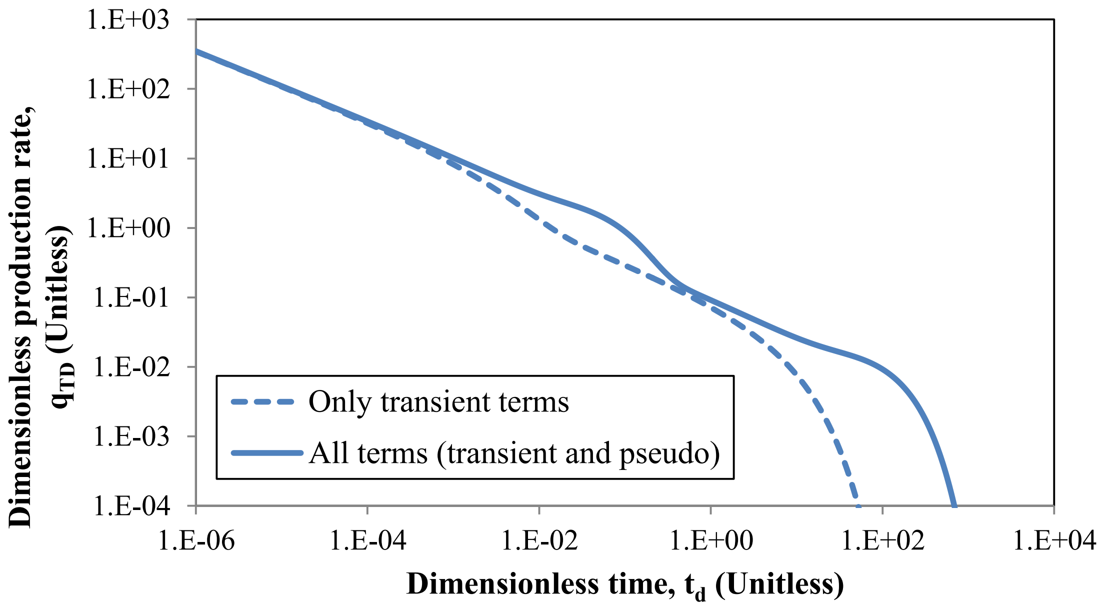

Figure 4-7: Effect of omitting pseudo steady state terms on the production forecast

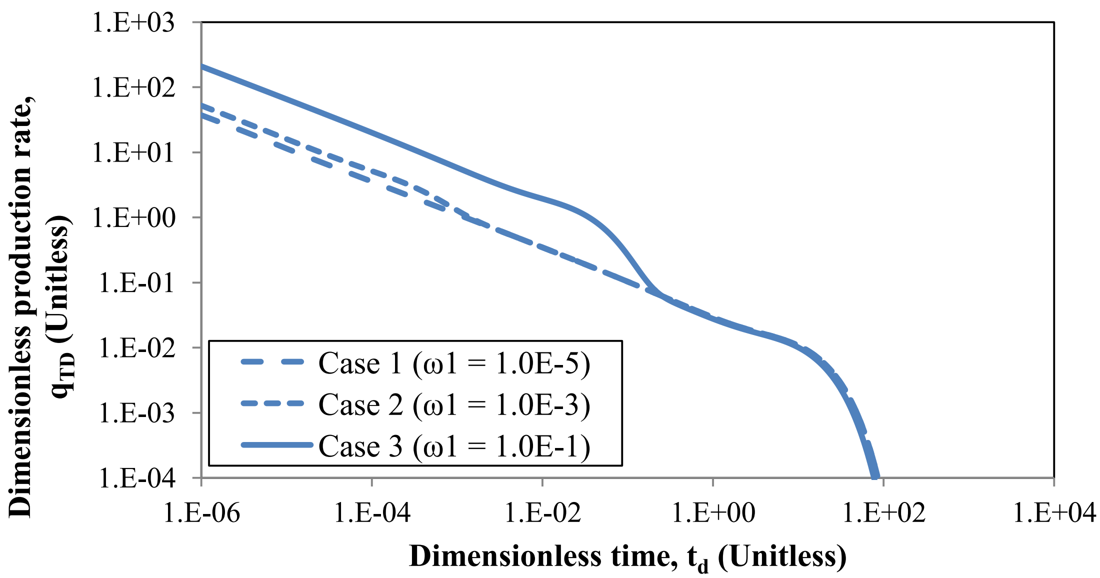

Figure 4-8: Effect of storativity ratio on the production forecast

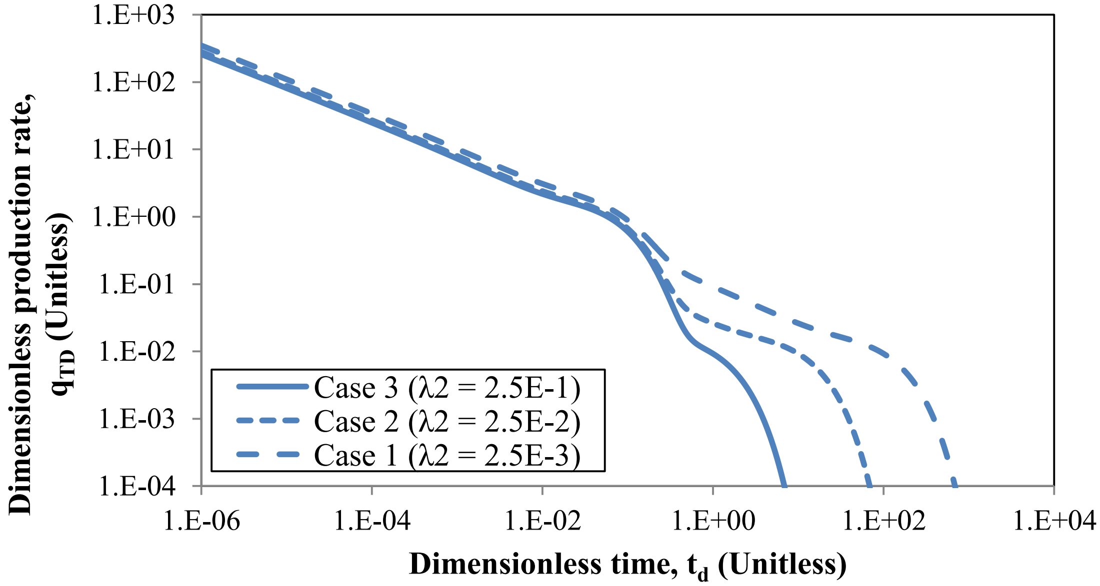

Figure 4-9: Effect of permeability ratio on the production forecast

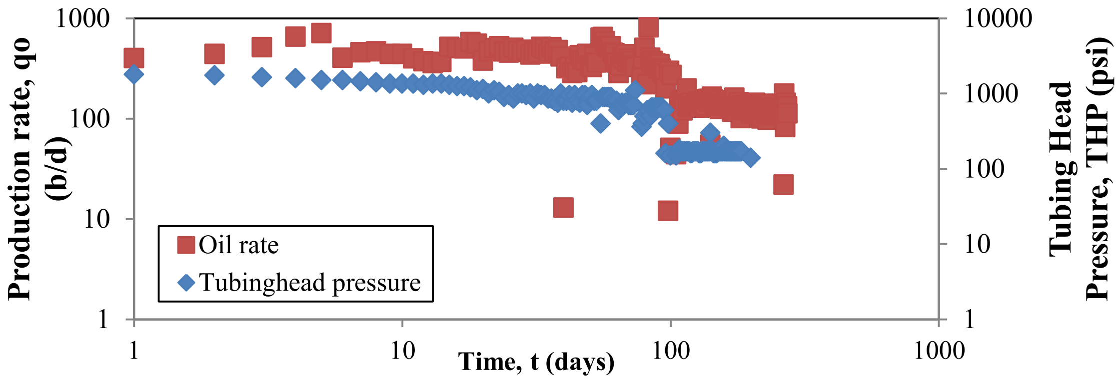

(a)

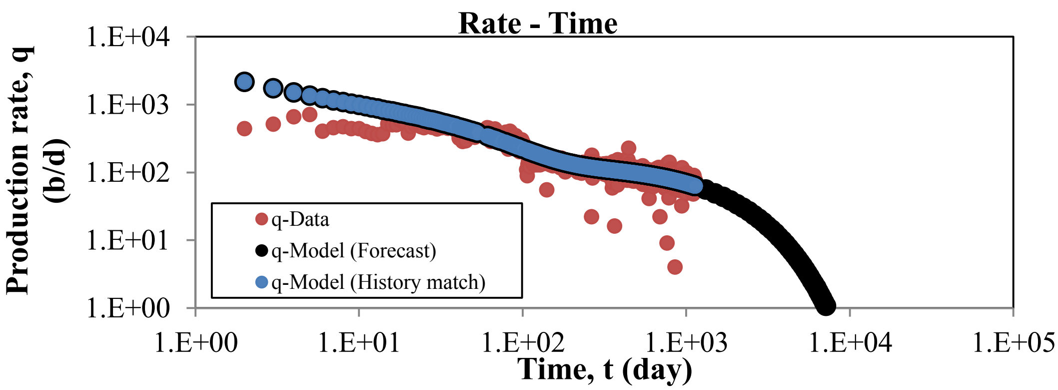

(b)

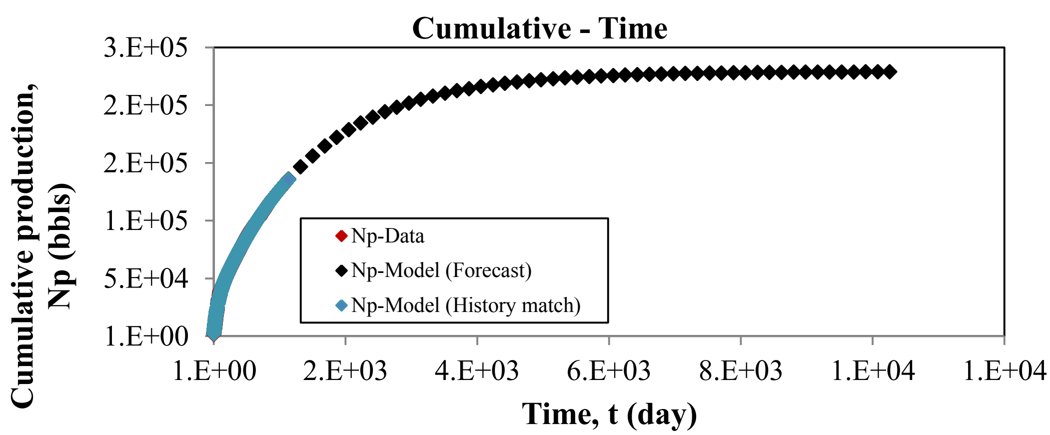

(c)

Figure 4-10: Application of parallel flow model to field data, (a). is the production rate plotted on a log-log scale. (b). represents the history match result and the forecast of production rate. (c). represents the history match of the cumulative production and reserves forecast

Chapter 5: Approximate Analytical Solution to the Double Porosity Model

Production data from most fractured-horizontal wells in gas and liquid-rich unconventional reservoirs plot as straight lines with a one half slope on a log-log plot of rate versus time. This production signature (half slope) is identical to that expected from a one-dimensional linear flow from reservoir matrix to the fracture face when production occurs at constant bottom-hole pressure. In addition, micro-seismic data obtained around these fractured wells suggest that an area of enhanced permeability is developed around the horizontal well, outside this region is an undisturbed part of the reservoir with low permeability. Based on these observations geoscientists have, in general, adopted the conceptual double-porosity model in modeling production from fractured horizontal wells in unconventional reservoirs. The analytical solution to this mathematical model exists in Laplace space but it cannot be inverted back to real-time space without using numerical inversion. In this chapter a new approximate analytical solution to the double-porosity model in real-time space is presented. In addition, example applications of this model are presented using synthetic and field data.

5.1 Model Development

Figure 5-1 is a schematic diagram of a hydraulically fractured horizontal well where the single fracture is perpendicular to the wellbore. Between successive fractures are low permeability reservoir matrixes. The dashed blue lines represent the no-flow boundaries created by the interference of flow from the matrix into the fracture face. The development presented assumes that the fracture face is at a constant pressure equal to the bottom hole well pressure. In addition we make the following assumptions:

1. Flow is single phase and slightly compressible,
2. Flow occurs in the reservoir isothermally,
3. The reservoir is isotropic and homogeneous in each compartment,
4. There is no direct communication between the matrix and wellbore,
5. There is a large contrast in permeability between the fracture and matrix compartments,
6. Secondary effects such as stress dependent permeability (porosity) and desorption are neglected.

The system of equations that describes this conceptual model is presented as follows; for the low permeability reservoir matrix the governing partial differential equation, initial condition and boundary conditions are summarized below:

$$\frac{\partial^2 p_m}{\partial z^2}+\frac{\partial^2 p_m}{\partial y^2}+\frac{\partial^2 p_m}{\partial x^2}=\frac{(\phi\mu c_t)_m}{k_m}\frac{\partial p_m}{\partial t}, \tag{5.1}$$

$$p_m(x,y,z,0)=p_i, \tag{5.2}$$

$$\left.\frac{\partial p_m}{\partial x}\right|_{x=x_e}=0, \tag{5.3}$$

$$\left.\frac{k_f}{\mu}\frac{\partial p_f}{\partial x}\right|_{x_{wf}}=\left.\frac{k_m}{\mu}\frac{\partial p_m}{\partial x}\right|_{x_{wf}}, \tag{5.4}$$

$$\left.\frac{\partial p_m}{\partial y}\right|_{y=y_e}=0, \tag{5.5}$$

$$\left.\frac{\partial p_m}{\partial y}\right|_{y=y_{wf}}=0, \tag{5.6}$$

$$\left.\frac{\partial p_m}{\partial z}\right|_{z=z_0}=0, \tag{5.7}$$

$$\left.\frac{\partial p_m}{\partial z}\right|_{z=z_e}=0. \tag{5.8}$$

Equation 5.1 is the 3D diffusivity equation for the reservoir matrix and equation 5.2 is the initial condition. Equation 5.3 means that there is a no-flow boundary at the external boundary of the reservoir matrix. Equation 5.4 states that flow from the matrix into the fracture face ($x = x_{wf}$) is equal to the out flow from the fracture face. Equation 5.5 states that there is a no-flow boundary at the external boundary of the reservoir matrix in the y direction and equation 5.6 states that there is no interaction between the matrix and the wellbore, that is, there is no cross flow from the matrix into the wellbore. Equations 5.7 and 5.8 are no flow boundary conditions and they model the fact that the reservoir is sealed at the top and bottom boundaries.

For the fracture, the governing partial differential equation is presented below:

$$\frac{\partial^2 p_f}{\partial z^2} + \frac{\partial^2 p_f}{\partial y^2} + \frac{\partial^2 p_f}{\partial x^2} = \frac{(\phi \mu c_t)_f}{k_f} \frac{\partial p_f}{\partial t}, \tag{5.9}$$

$$p_f(x, y, 0) = p_i, \tag{5.10}$$

$$\left.\frac{\partial p_f}{\partial y}\right|_{y=y_e} = 0, \tag{5.11}$$

$$p_f(x, y_{wf}, z, t) = p_{wf}, \tag{5.12}$$

$$\left.\frac{\partial p_f}{\partial x}\right|_{x=0} = 0, \tag{5.13}$$

$$\left.\frac{k_f}{\mu} \frac{\partial p_f}{\partial x}\right|_{x_{wf}} = \left.\frac{k_m}{\mu} \frac{\partial p_m}{\partial x}\right|_{x_{wf}}, \tag{5.14}$$

$$\left.\frac{\partial p_f}{\partial z}\right|_{z=z_0} = 0, \tag{5.15}$$

$$\left.\frac{\partial p_f}{\partial z}\right|_{z=z_e} = 0. \tag{5.16}$$

Equation 5.9 is the 3D diffusivity equation for the fracture. Equation 5.10 is the initial condition and equation 5.11 is the no-flow boundary at the fracture tip. Equation 5.12 states that at the wellbore, the fracture pressure is equal to the wellbore pressure.

Equation 5.13 states that there is a no flow boundary at the center line of the fracture and equation 5.14 is identical to equation 5.4 and they have the same physical meaning. Equations 5.15 and 5.16 are no flow boundary conditions at the top and bottom of the reservoir, they represent the fact that the reservoir is sealed at the top and bottom boundaries. Equations 5.1 and 5.9 form a coupled system of partial differential equations (PDEs) because of the continuity condition defined by the boundary condition specified by equation 5.4 and 5.14.

We are interested in developing a rate–time function for forecasting production rate from a system described by these set of equations. To achieve this goal we eliminate the spatial dependences in these sets of equations by integrating equations 5.1 and 5.9 over the spatial x, y and z domains, respectively. Integrating equation 5.1 with respect to x, y and z with x varying from x_{wf} to x_e, y from y_{wf} to y_e and z from z_0 to z_e, we obtain

$$\int_{z_0}^{z_e}\int_{y_{wf}}^{y_e}\int_{x_{wf}}^{x_e}\left[\frac{\partial^2 p_m}{\partial z^2}+\frac{\partial^2 p_m}{\partial y^2}+\frac{\partial^2 p_m}{\partial x^2}\right]dxdydz=\frac{(\phi\mu c_t)_m}{k_m}\int_{z_0}^{z_e}\int_{y_{wf}}^{y_e}\int_{x_{wf}}^{x_e}\frac{\partial p_m}{\partial t}dxdydz\,. \tag{5.17}$$

Equation 5.17 can be re-written as

$$\int_{z_0}^{z_e}\int_{y_{wf}}^{y_e}\int_{x_{wf}}^{x_e}\frac{\partial}{\partial z}\left[\frac{\partial p_m}{\partial z}\right]dxdydz+\int_{z_0}^{z_e}\int_{y_{wf}}^{y_e}\int_{x_{wf}}^{x_e}\frac{\partial}{\partial y}\left[\frac{\partial p_m}{\partial y}\right]dxdydz+\int_{z_0}^{z_e}\int_{y_{wf}}^{y_e}\int_{x_{wf}}^{x_e}\frac{\partial}{\partial x}\left[\frac{\partial p_m}{\partial x}\right]dxdydz=\frac{(\phi\mu c_t)_m}{k_m}\frac{\partial}{\partial t}\left[\int_{z_0}^{z_e}\int_{y_{wf}}^{y_e}\int_{x_{wf}}^{x_e}p_m dxdydz\right]. \tag{5.18}$$

In equation 5.18 we have used the fact that time, t, is independent of the spatial coordinates to move the time derivative outside of the spatial integral. Defining the average pressure in the reservoir matrix as the volume weighted average, the right side of equation 5.18 becomes

$$\int_{x_{wf}}^{x_e}\int_{y_{wf}}^{y_e}\left[\frac{\partial p_m}{\partial z}\bigg|_{z_e} - \frac{\partial p_m}{\partial z}\bigg|_{z_0}\right]dydx + \int_{z_0}^{z_e}\int_{x_{wf}}^{x_e}\left[\frac{\partial p_m}{\partial y}\bigg|_{y_e} - \frac{\partial p_m}{\partial y}\bigg|_{y_{wf}}\right]dxdz + \int_{z_0}^{z_e}\int_{y_{wf}}^{y_e}\left[\frac{\partial p_m}{\partial x}\bigg|_{x_e} - \frac{\partial p_m}{\partial x}\bigg|_{x_{wf}}\right]dydz = \frac{(\phi\mu c_t)_m v_{b_m}}{k_m}\frac{d\overline{p}_m}{dt},$$

(5.19)

where, the average pressure is given as

$$\overline{p}_m(t) = \frac{\int_{z_0}^{z_e}\int_{y_{wf}}^{y_e}\int_{x_{wf}}^{x_e} p_m dxdydz}{\int_{z_0}^{z_e}\int_{y_{wf}}^{y_e}\int_{x_{wf}}^{x_e} dxdydz} \Rightarrow \int_{z_0}^{z_e}\int_{y_{wf}}^{y_e}\int_{x_{wf}}^{x_e} p_m dxdydz = \left[\int_{z_0}^{z_e}\int_{y_{wf}}^{y_e}\int_{x_{wf}}^{x_e} dxdydz\right]\overline{p}_m(t) = v_{b_m}\overline{p}_m(t).$$

(5.20)

Using the boundary conditions defined by equations 5.3 – 5.8 in equation 5.19 and multiplying both sides by $\frac{k_m}{\mu}$, equation 5.19 simplifies to

$$-\int_{z_0}^{z_e}\int_{y_{wf}}^{y_e}\frac{k_m}{\mu}\frac{\partial p_m}{\partial x}\bigg|_{x_{wf}} dydz = (\phi c_t)_m v_{b_m}\frac{d\overline{p}_m(t)}{dt}. \quad (5.21)$$

Defining the effective matrix pore volume as $v_{p_m} = \phi_m v_{b_m}$ and noting that from Darcy's law, $q_m(t) = \int_{z_0}^{z_e}\int_{y_{wf}}^{y_e}\left[\frac{k_m}{\mu}\frac{\partial p_m}{\partial x}\bigg|_{x_{wf}}\right]dydz$. Therefore, we can rewrite equation 5.21 as shown below:

$$\left(v_{p_m}c_t\right)_m\frac{d\overline{p}_m(t)}{dt} = -q_m(t). \quad (5.22)$$

In equation 5.22, $\overline{p}_m$ is the average pressure in the reservoir matrix and q_m is the net flow rate from the reservoir matrix. This equation is a macroscopic equation and the parameters are therefore representative average values that describe the properties of matrix compartment. Equation 5.22 is identical to the equation used in the development of the capacitance resistance model (Sayarpour, 2008; Nguyen, 2012 and Cao, 2014).

The next step in the model development is to also integrate the fracture equation over the spatial x, y and z domains. Therefore,

$$\int_{z_0}^{z_e}\int_{y_{wf}}^{y_e}\int_{0}^{x_{wf}}\left[\frac{\partial^2 p_f}{\partial z^2}+\frac{\partial^2 p_f}{\partial y^2}+\frac{\partial^2 p_f}{\partial x^2}\right]dxdydz=\frac{(\phi\mu c_t)_f}{k_f}\int_{z_0}^{z_e}\int_{y_{wf}}^{y_e}\int_{0}^{x_{wf}}\frac{\partial p_f}{\partial t}dxdydz\,, \tag{5.23}$$

$$\int_{y_{wf}}^{y_e}\int_{0}^{x_{wf}}\left[\left.\frac{\partial p_f}{\partial z}\right|_{z_e}-\left.\frac{\partial p_f}{\partial z}\right|_{z_0}\right]dxdy+\int_{z_0}^{z_e}\int_{0}^{x_{wf}}\left[\left.\frac{\partial p_f}{\partial y}\right|_{y_e}-\left.\frac{\partial p_f}{\partial y}\right|_{y_{wf}}\right]dxdz+\int_{z_0}^{z_e}\int_{y_{wf}}^{y_e}\left[\left.\frac{\partial p_f}{\partial x}\right|_{x_{wf}}-\left.\frac{\partial p_f}{\partial x}\right|_{0}\right]dydz=\frac{(\phi\mu c_t)_f v_{b_f}}{k_f}\frac{d\overline{p}_f(t)}{dt}. \tag{5.24}$$

We have made use of the average pressure in the fracture in equation 5.24. The average pressure used is the volume weighted pressure defined for the fracture as shown below:

$$\overline{p}_f(t)=\frac{\int_{z_0}^{z_e}\int_{y_{wf}}^{y_e}\int_{x_{wf}}^{x_e}p_f dxdydz}{\int_{z_0}^{z_e}\int_{y_{wf}}^{y_e}\int_{x_{wf}}^{x_e}dxdydz}\Rightarrow\left[\int_{z_0}^{z_e}\int_{y_{wf}}^{y_e}\int_{x_{wf}}^{x_e}dxdydz\right]\overline{p}_f(t)=v_{b_f}\,\overline{p}_f(t). \tag{5.25}$$

Multiplying equation 5.24 by $\frac{k_f}{\mu}$ and applying the boundary conditions from equations 5.11, 5.13, 5.15 and 5.16; equation 5.24 simplifies to

$$-\int_{z_0}^{z_e}\int_{0}^{x_{wf}}\left[\left.\frac{k_f}{\mu}\frac{\partial p_f}{\partial y}\right|_{y_{wf}}\right]dxdz+\int_{z_0}^{z_e}\int_{y_{wf}}^{y_e}\left[\left.\frac{k_f}{\mu}\frac{\partial p_f}{\partial x}\right|_{x_{wf}}\right]dydz=(\phi c_t)_f\,v_{b_f}\frac{d\overline{p}_f(t)}{dt}. \tag{5.26}$$

Noting that $q_f(t)=\int_{z_0}^{z_e}\int_{0}^{x_{wf}}\left[\left.\frac{k_f}{\mu}\frac{\partial p_f}{\partial y}\right|_{y_{wf}}\right]dxdz$ and $v_{p_f}=\phi_f v_{b_f}$, equation 5.26 can be written as shown below:

$$-q_f(t)+\int_{z_0}^{z_e}\int_{y_{wf}}^{y_e}\left[\left.\frac{k_f}{\mu}\frac{\partial p_f}{\partial x}\right|_{x_{wf}}\right]dydz=\left(v_{p_f}c_t\right)_f\frac{d\overline{p}_f(t)}{dt}. \tag{5.27}$$

From the boundary condition given by equation 5.14, $\left.\frac{k_f}{\mu}\frac{\partial p_f}{\partial x}\right|_{x_{wf}} = \left.\frac{k_m}{\mu}\frac{\partial p_m}{\partial x}\right|_{x_{wf}}$, substituting this into equation 5.27, it becomes

$$-q_f(t) + \int_{z_0}^{z_e}\int_{y_{wf}}^{y_e}\left[\left.\frac{k_m}{\mu}\frac{\partial p_m}{\partial x}\right|_{x_{wf}}\right]dydz = \left(v_{p_f} c_t\right)_f \frac{\partial \overline{p}_f(t)}{\partial t}. \tag{5.28}$$

Noting that $q_m(t) = \int_{z_0}^{z_e}\int_{y_{wf}}^{y_e}\left[\left.\frac{k_m}{\mu}\frac{\partial p_m}{\partial x}\right|_{x_{wf}}\right]dydz$, then equation 5.28 is rewritten as:

$$\left(v_{p_f} c_t\right)_f \frac{d\overline{p}_f(t)}{dt} = -q_f(t) + q_m(t) \tag{5.29}$$

In equations 5.29, $\overline{p}_f(t)$ is the average fracture pressure, $q_f(t)$ is the net flow rate out of the fracture compartment and $q_m(t)$ is the net matrix flow in to the fracture compartment from the matrix. We have thus transformed the system of PDEs in to a system of ordinary differential equations (ODEs). One advantage of transforming the system of PDEs into a system of ODEs is that the problem is now easier to solve because it is now a system of ordinary differential equations which can be solve by eigenvalue decomposition. Another advantage is that it eliminates the need to know the specific location and geometry/dimensions of the fracture(s). Nobakht et al. (2013) and Ambrose et al. (2011) presented a method of forecasting production from a multi-fractured horizontal well that considered planar hydraulic fractures of different lengths. The new model is in terms of the average pressure in a fracture of any arbitrary shape or geometry (planar or otherwise). Figure 5-2 is a simplified representation of the new problem, which is a schematic representation of the reservoir as a two-compartment system in series flow.

The first compartment can be thought of as the aggregated volume of all the fractures in the reservoir. It is the only compartment that is directly connected to the wellbore. The average pressure in compartment one is $\bar{p}_f(t)$ and the flow rate from this compartment into the wellbore is $q_f(t)$. The second compartment is the aggregated volume of the reservoir matrix. The average pressure in the second compartment is $\bar{p}_m(t)$. The matrix compartment does not communicate directly with the wellbore; it only has a cross flow term, $q_m(t)$, into the fracture compartment.

The next step in the solution is to eliminate the average pressures in equations 5.22 and 5.29 by using a relationship between the average reservoir pressure and flow rate. This step is achieved by using an analytical solution to the one dimensional linear flow problem (Wattenbarger et al., 1998, Bello et al., 2009 and Patzek et al. 2014) with constant pressure at the fracture face; from which the average reservoir pressure, as shown in appendix A, is given by:

$$\bar{p}(t) = p_{wf} + \frac{8}{\pi^2}\left(p_i - p_{wf}\right)\sum_{n=1}^{\infty}\frac{e^{-\frac{(2n-1)^2 k}{4\phi\mu c_t L^2}\pi^2 t}}{\left(2n-1\right)^2}. \tag{5.30}$$

It is also shown in appendix A that the dimensionless flow rate from such a system is given by:

$$q_D(t) = 2\sum_{n=1}^{\infty} e^{-\frac{(2n-1)^2\pi^2 t}{4\phi\mu c_t L^2}}. \tag{5.31}$$

From equation 5.31 we note that $q_{Dn}(t) = 2e^{-\frac{(2n-1)^2\pi^2 t}{4\phi\mu c_t L^2}}$, n is an index used to represent an independent solution and it is usually called the normal mode, therefore, $q_{Dn}(t)$ is the dimensionless flow rate associated with an independent solution. If we define the productivity index as $J = \frac{\pi^2 q_i}{4\left(p_i - p_{wf}\right)}$. Then after substituting the expression for $q_{Dn}(t)$ and J into equation 5.30 we obtain:

$$\bar{p}(t) = p_{wf} + \frac{q_i}{J}\sum_{n=1}^{\infty}\frac{q_{Dn}(t)}{(2n-1)^2}. \tag{5.32}$$

We can therefore write equation 5.32 for the fracture and matrix compartments as:

$$\bar{p}_f(t) = p_{wf} + \frac{q_{fi}}{J_f}\sum_{n=1}^{\infty}\frac{q_{Df_n}(t)}{(2n-1)^2}, \tag{5.33}$$

$$\bar{p}_m(t) = \bar{p}_f(t) + \frac{q_{mi}}{T_x}\sum_{n=1}^{\infty}\frac{q_{Dm_n}(t)}{(2n-1)^2}. \tag{5.34}$$

where,

$q_{Df_n}(t) = 2e^{-\frac{(2n-1)^2 k_f}{4(\phi\mu)_f c_t x_f^2}\pi^2 t}$: is the dimensionless production rate for the nth normal mode for the fracture compartment

$q_{Dm_n}(t) = 2e^{-\frac{(2n-1)^2 k_f}{4(\phi\mu)_f c_t x_f^2}\pi^2 t}$: is the dimensionless production rate for the nth normal mode for the matrix compartment

$q_{f_i} = \frac{k_f A_f}{\mu x_f}(p_i - p_{wf})$: is the initial production rate from the fracture's nth normal mode

$q_{m_i} = \frac{k_m A_m}{\mu L}(p_i - p_{wf})$: is the initial production rate from the matrix's nth normal mode

$J_f = \frac{\pi^2}{4}\frac{q_{fi}}{(p_i - p_{wf})}$: is the fracture productivity index

$T_x = \frac{\pi^2}{4}\frac{q_m}{(\bar{p}_m - \bar{p}_f)}$: is the transmissibility between the fracture and matrix

In writing equation 5.34 for the matrix compartment, we have assumed that a constant p_{wf} solution is valid even when it is changing. This assumption is a good approximation when there is a large contrast in permeability between the two adjacent compartments because the high permeability of the fracture compartment ensures a quick pressure equilibration with the wellbore pressure in the fracture compartment and, hence, the pressure at the interface between the two compartments is approximately constant.

Differentiating equation 5.33 with respect to time we obtain:

$$\frac{d\overline{p}_f(t)}{dt} = \frac{q_{fi}}{J_f}\sum_{n=1}^{\infty}\frac{1}{(2n-1)^2}\frac{dq_{f_n}(t)}{dt}. \tag{5.35}$$

If in equation 5.31 we define $q_D(t_D)$ as $q_D(t) = \dfrac{q(t)}{q_i}$, then, we can write the flow rate as:

$$q_D(t) = 2\sum_{n=1}^{\infty} e^{-\frac{(2n-1)^2\pi^2 t}{4\phi\mu c_t L^2}} \Rightarrow q(t) = q_i\sum_{n=1}^{\infty} 2e^{-\frac{(2n-1)^2\pi^2 t}{4\phi\mu c_t L^2}} = q_i\sum_{n=1}^{\infty} q_{Dn}(t). \tag{5.36}$$

Substituting equations 5.35 and 5.36 into equation 5.29 and simplifying results in

$$q_{fi}\sum_{n=1}^{\infty}\frac{1}{(2n-1)^2}\frac{dq_{f_n}(t)}{dt} = -\frac{J_f}{\left(v_p c_t\right)_f} q_{fi}\sum_{n=1}^{\infty} q_{f_n}(t) + \frac{J_f}{\left(v_p c_t\right)_f} q_{mi}\sum_{n=1}^{\infty} q_{m_n}(t). \tag{5.37}$$

For the matrix compartment, we differentiate equation 5.34 with respect to time, t, to obtain:

$$\frac{d\overline{p}_m(t)}{dt} = \frac{d\overline{p}_f(t)}{dt} + \frac{q_{mi}}{T_x}\sum_{n=1}^{\infty}\frac{1}{(2n-1)^2}\frac{dq_{m_n}(t)}{dt}. \tag{5.38}$$

Substituting equations 5.38 and 5.36 into equation 5.22 results in

$$\left(v_p c_t\right)_m\left[\frac{d\overline{p}_f(t)}{dt} + \frac{q_{mi}}{T_x}\sum_{n=1}^{\infty}\frac{1}{(2n-1)^2}\frac{dq_{m_n}(t)}{dt}\right] = -q_{mi}\sum_{n=1}^{\infty} q_{m_n}(t). \tag{5.39}$$

Using equation 5.35, we substitute for $\dfrac{d\overline{p}_f(t)}{dt}$ in equation 5.39 to obtain:

$$\left(v_p c_t\right)_m\left[\frac{q_{fi}}{J_f}\sum_{n=1}^{\infty}\frac{1}{(2n-1)^2}\frac{dq_{f_n}(t)}{dt} + \frac{q_{mi}}{T_x}\sum_{n=1}^{\infty}\frac{1}{(2n-1)^2}\frac{dq_{m_n}(t)}{dt}\right] = -q_{mi}\sum_{n=1}^{\infty} q_{m_n}(t). \tag{5.40}$$

Substituting equation 5.37 in equation 5.40 and simplifying we obtain:

$$q_{mi}\sum_{n=1}^{\infty}\frac{1}{(2n-1)^2}\frac{dq_{m_n}(t)}{dt}=\frac{J_f}{(v_p c_t)_f}\frac{T_x}{J_f}q_{fi}\sum_{n=1}^{\infty}q_{f_n}(t)-\left[\frac{T_x}{(v_p c_t)_m}+\frac{J_f}{(v_p c_t)_f}\frac{T_x}{J_f}\right]q_{mi}\sum_{n=1}^{\infty}q_{m_n}(t). \tag{5.41}$$

If we define:

$\tau_f=\dfrac{(v_p c_t)_f}{J_f}$: as the fracture time constant

$\tau_m=\dfrac{(v_p c_t)_m}{T_x}$: as the matrix time constant

Then we can re-write equations 5.37 and 5.41 as:

$$\sum_{n=1}^{\infty}\frac{1}{(2n-1)^2}\frac{d\left(q_{fi}q_{f_n}(t)\right)}{dt}=-\frac{1}{\tau_f}\sum_{n=1}^{\infty}\left(q_{fi}q_{f_n}(t)\right)+\frac{1}{\tau_f}\sum_{n=1}^{\infty}\left(q_{mi}q_{m_n}(t)\right), \tag{5.42}$$

$$\sum_{n=1}^{\infty}\frac{1}{(2n-1)^2}\frac{d\left(q_{mi}q_{m_n}(t)\right)}{dt}=\frac{T_x}{\tau_f J_f}\sum_{n=1}^{\infty}\left(q_{fi}q_{f_n}(t)\right)-\left[\frac{1}{\tau_m}+\frac{T_x}{\tau_f J_f}\right]\sum_{n=1}^{\infty}\left(q_{mi}q_{m_n}(t)\right). \tag{5.43}$$

Equations 5.42 and 5.43 can be thought of as the decomposition of equations 5.22 and 5.29 where flow is predominantly linear. Multiplying both sides of equations 5.42 and 5.43 by $(2n-1)^2$ we obtain:

$$\sum_{n=1}^{\infty}\frac{d\left(q_{fi}q_{f_n}(t)\right)}{dt}=-\frac{1}{\tau_f}\sum_{n=1}^{\infty}(2n-1)^2\left(q_{fi}q_{f_n}(t)\right)+\frac{1}{\tau_f}\sum_{n=1}^{\infty}(2n-1)^2\left(q_{mi}q_{m_n}(t)\right), \tag{5.44}$$

$$\sum_{n=1}^{\infty}\frac{d\left(q_{mi}q_{m_n}(t)\right)}{dt}=\frac{T_x}{\tau_f J_f}\sum_{n=1}^{\infty}(2n-1)^2\left(q_{fi}q_{f_n}(t)\right)-\left[\frac{1}{\tau_m}+\frac{T_x}{\tau_f J_f}\right]\sum_{n=1}^{\infty}(2n-1)^2\left(q_{mi}q_{m_n}(t)\right). \tag{5.45}$$

The index n in equations 5.44 and 5.45 is the normal mode index, as a result, we can solve the system of ODEs represented by equations 5.44 and 5.45 for each mode and then sum these solutions to obtain the complete solution. We re-write this system of ODEs in matrix form as shown below for the nth mode and then solve it with eigenvalue-decomposition, Kreyszig (2006).

$$\begin{pmatrix} \dfrac{dq_{f_n}(t)}{dt} \\ \dfrac{dq_{m_n}(t)}{dt} \end{pmatrix} = (2n-1)^2 \begin{pmatrix} -\dfrac{1}{\tau_f} & \dfrac{1}{\tau_f} \\ \dfrac{T_x}{\tau_f J_f} & -\dfrac{1}{\tau_m} - \dfrac{T_x}{\tau_f J_f} \end{pmatrix} \begin{pmatrix} q_{f_n}(t) \\ q_{m_n}(t) \end{pmatrix}, \tag{5.46}$$

where the initial conditions to solve the system represented by equation 5.46 are:

$$q_f(t=0) = q_{fi}, \tag{5.47}$$

$$q_m(t=0) = 0. \tag{5.48}$$

Equation 5.47 simply states that at time, t = 0, the production rate from the fracture volume is equal to a finite value q_{fi}. While equation 5.48 states that at time, t = 0, the production rate from the matrix volume is equal to zero, $q_m = 0$. This is because at time zero, the pressure everywhere in the formation is equal to the initial reservoir pressure as a result there is no pressure gradient for flow from the matrix in to the fracture because the pressure at the interface between the fracture and matrix is still at the initial reservoir pressure.

Next we solve the system defined by equation 5.46 by the eigenvalue-decomposition method. The system in matrix – vector notation is

$$\dot{\mathbf{q}}_n = \mathbf{A}_n \mathbf{q}_n. \tag{5.49}$$

where

$$\dot{\mathbf{q}}_n = \begin{pmatrix} \dfrac{dq_{f_n}(t)}{dt} \\ \dfrac{dq_{m_n}(t)}{dt} \end{pmatrix},$$

$$\mathbf{A}_n = \begin{pmatrix} -\frac{(2n-1)^2}{\tau_f} & \frac{(2n-1)^2}{\tau_f} \\ \frac{(2n-1)^2 T_x}{\tau_f J_f} & -\frac{(2n-1)^2}{\tau_m} - \frac{(2n-1)^2 T_x}{\tau_f J_f} \end{pmatrix},$$

and

$$\mathbf{q}_n = \begin{pmatrix} q_{f_n}(t) \\ q_{m_n}(t) \end{pmatrix}.$$

Re-writing $\mathbf{A}_n$ as

$$\mathbf{A}_n = (2n-1)^2 \begin{pmatrix} -\frac{1}{\tau_f} & \frac{1}{\tau_f} \\ \frac{T_x}{\tau_f J_f} & -\frac{1}{\tau_m} - \frac{T_x}{\tau_f J_f} \end{pmatrix} = (2n-1)^2 \begin{pmatrix} a & b \\ c & d \end{pmatrix},$$

where $a = -\frac{1}{\tau_f}$, $b = \frac{1}{\tau_f}$, $c = \frac{T_x}{\tau_f J_f}$ and $d = -\frac{1}{\tau_m} - \frac{T_x}{\tau_f J_f}$. We find the eigenvalues of $\mathbf{A}_n$ to be given by:

$$\bar{\lambda}_{1_n} = (2n-1)^2 \lambda_1 = (2n-1)^2 \left[\frac{a+d+\sqrt{(a+d)^2 - 4(ad-cb)}}{2} \right],$$

$$\bar{\lambda}_{2_n} = (2n-1)^2 \lambda_2 = (2n-1)^2 \left[\frac{a+d-\sqrt{(a+d)^2 - 4(ad-cb)}}{2} \right].$$

The eigenvectors corresponding to $\bar{\lambda}_{1_n}$ and $\bar{\lambda}_{2_n}$ are found to be given respectively as:

$$p_1 = \begin{pmatrix} \frac{1}{2c}\left[a-d+\sqrt{(a+d)^2 - 4(ad-cb)} \right] \\ 1 \end{pmatrix},$$

$$p_2 = \begin{pmatrix} \frac{1}{2c}\left[a - d - \sqrt{(a+d)^2 - 4(ad-cb)}\right] \\ 1 \end{pmatrix}.$$

Therefore,

$$p = \begin{pmatrix} \frac{1}{2c}\left[a - d + \sqrt{(a+d)^2 - 4(ad-cb)}\right] & \frac{1}{2c}\left[a - d - \sqrt{(a+d)^2 - 4(ad-cb)}\right] \\ 1 & 1 \end{pmatrix} = \begin{pmatrix} \rho & \gamma \\ 1 & 1 \end{pmatrix}$$

(5.50)

where

$$\rho = \frac{1}{2c}\left[a - d + \sqrt{(a+d)^2 - 4(ad-cb)}\right],$$

$$\gamma = \frac{1}{2c}\left[a - d - \sqrt{(a+d)^2 - 4(ad-cb)}\right].$$

The solution to equation 5.46 is therefore;

$$q_n(t) = \begin{pmatrix} \rho & \gamma \\ 1 & 1 \end{pmatrix} \begin{pmatrix} c_{1_n} e^{\bar{\lambda}_{1_n} t} \\ c_{2_n} e^{\bar{\lambda}_{2_n} t} \end{pmatrix}, \tag{5.51}$$

$$q_{f_n}(t) = \rho c_{1_n} e^{\bar{\lambda}_{1_n} t} + \gamma c_{2_n} e^{\bar{\lambda}_{2_n} t}, \tag{5.52}$$

$$q_{m_n}(t) = c_{1_n} e^{\bar{\lambda}_{1_n} t} + c_{2_n} e^{\bar{\lambda}_{2_n} t}. \tag{5.53}$$

Using the initial condition we derive the constants c_{1_n} and c_{2_n} as:

$$c_{2_n} = \frac{q_{fi_n} - \rho q_{mi_n}}{\gamma - \rho},$$

$$c_{1_n} = \frac{\gamma q_{mi_n} - q_{fi_n}}{\gamma - \rho}.$$

Substituting these constants into equations 5.52 and 5.53 we obtain the following expressions for q_{f_n} and q_{m_n}.

$$q_{f_n}(t) = \frac{q_{fi}}{\gamma-\rho}\left[\gamma e^{\bar{\lambda}_{2_n} t} - \rho e^{\bar{\lambda}_{1_n} t}\right] + \frac{q_{mi}}{\gamma-\rho}\left[\gamma\rho e^{\bar{\lambda}_{1_n} t} - \gamma\rho e^{\bar{\lambda}_{2_n} t}\right], \tag{5.54}$$

$$q_{m_n}(t) = \frac{q_{fi}}{\gamma-\rho}\left[e^{\bar{\lambda}_{2_n} t} - e^{\bar{\lambda}_{1_n} t}\right] + \frac{q_{mi}}{\gamma-\rho}\left[\gamma e^{\bar{\lambda}_{1_n} t} - \rho e^{\bar{\lambda}_{2_n} t}\right]. \tag{5.55}$$

If we set $q_{mi} = 0$ as defined by the initial condition of the problem, equations 5.54 and 5.55 simplify to

$$q_{f_n}(t) = \frac{q_{fi}}{\gamma-\rho}\left[\gamma e^{\bar{\lambda}_{2_n} t} - \rho e^{\bar{\lambda}_{1_n} t}\right], \tag{5.56}$$

$$q_{m_n}(t) = \frac{q_{fi}}{\gamma-\rho}\left[e^{\bar{\lambda}_{2_n} t} - e^{\bar{\lambda}_{1_n} t}\right]. \tag{5.57}$$

As a result the complete solution to the problem is given as:

$$q_f(t) = \sum_{n=1}^{\infty} q_{f_n} = \sum_{n=1}^{\infty} q_{fi}\frac{\gamma}{\gamma-\rho}e^{\bar{\lambda}_{2_n} t} - \sum_{n=1}^{\infty} q_{fi}\frac{\rho}{\gamma-\rho}e^{\bar{\lambda}_{1_n} t}, \tag{5.58}$$

$$q_m(t) = \sum_{n=1}^{\infty} q_{m_n} = \sum_{n=1}^{\infty} q_{fi}\frac{e^{\bar{\lambda}_{2_n} t}}{\gamma-\rho} - \sum_{n=1}^{\infty} q_{fi}\frac{e^{\bar{\lambda}_{1_n} t}}{\gamma-\rho}. \tag{5.59}$$

We now eliminate the infinite sum in equation 5.58 by converting the summation to an indefinite integral.

$$q_f(t) = q_{fi}\frac{\gamma}{\gamma-\rho}e^{(2n-1)^2\lambda_2 t} - q_{fi}\frac{\rho}{\gamma-\rho}e^{(2n-1)^2\lambda_1 t} + \sum_{n=2}^{\infty}\left[q_{fi}\frac{\gamma}{\gamma-\rho}e^{(2n-1)^2\lambda_2 t} - q_{fi}\frac{\rho}{\gamma-\rho}e^{(2n-1)^2\lambda_1 t}\right]\Delta n \tag{5.60}$$

Equation 5.60 is equation 5.58 written with index n = 1 expanded out of the summation and recalling that $\bar{\lambda}_{1_n} = (2n-1)^2\lambda_1$ and $\bar{\lambda}_{2_n} = (2n-1)^2\lambda_2$. Now let $z = (2n-1)\sqrt{\lambda_2 t}$ then $dn = \frac{dz}{2\sqrt{\lambda_2 t}}$. Upon substituting these expressions into equation 5.60 we obtain:

$$q_f\left(t\right)=q_{fi}\frac{\gamma}{\gamma-\rho}e^{(2n-1)^2\lambda_2 t}-q_{fi}\frac{\rho}{\gamma-\rho}e^{(2n-1)^2\lambda_1 t}+\lim_{z\to\infty}\int_{3\sqrt{\lambda_2 t}}^{z}\left[q_{fi}\frac{\gamma}{\gamma-\rho}e^{z^2}-q_{fi}\frac{\rho}{\gamma-\rho}e^{\frac{\lambda_1}{\lambda_2}z^2}\right]\frac{dz}{2\sqrt{\lambda_2 t}}$$

(5.61)

Simplifying equation 5.61 we obtain:

$$q_f\left(t\right)=q_{fi}\frac{\gamma}{\gamma-\rho}e^{(2n-1)^2\lambda_2 t}-q_{fi}\frac{\rho}{\gamma-\rho}e^{(2n-1)^2\lambda_1 t}+\left(\frac{q_{fi}}{2\sqrt{\lambda_2 t}}\right)\lim_{z\to\infty}\int_{3\sqrt{\lambda_2 t}}^{z}\left[\frac{\gamma}{\gamma-\rho}e^{z^2}-\frac{\rho}{\gamma-\rho}e^{\frac{\lambda_1}{\lambda_2}z^2}\right]dz$$

(5.62)

Evaluating the integral yields

$$\begin{aligned}q_f\left(t\right)&=q_{fi}\frac{\gamma}{\gamma-\rho}e^{(2n-1)^2\lambda_2 t}-q_{fi}\frac{\rho}{\gamma-\rho}e^{(2n-1)^2\lambda_1 t}\\&+\left(\frac{q_{fi}}{2\sqrt{\lambda_2 t}}\right)\lim_{z\to\infty}\left[\frac{\gamma}{\gamma-\rho}\frac{\sqrt{\pi}}{2}erf\,(\xi)-\frac{\rho}{\gamma-\rho}\frac{\sqrt{\pi}}{2\sqrt{\frac{\lambda_1}{\lambda_2}}}erf\,(\sqrt{\frac{\lambda_1}{\lambda_2}}\xi)\right]\Bigg|_{3\sqrt{\lambda_2 t}}^{z},\end{aligned} \quad (5.63)$$

$$\begin{aligned}q_f\left(t\right)&=q_{fi}\frac{\gamma}{\gamma-\rho}e^{(2n-1)^2\lambda_2 t}-q_{fi}\frac{\rho}{\gamma-\rho}e^{(2n-1)^2\lambda_1 t}\\&+\lim_{z\to\infty}\frac{q_{fi}}{4}\frac{\gamma}{\gamma-\rho}\frac{\sqrt{\pi}}{\sqrt{\lambda_2 t}}\left(erf\,(z)-erf\,(3\sqrt{\lambda_2 t})\right)-\lim_{z\to\infty}\frac{q_{fi}}{4}\frac{\rho}{\gamma-\rho}\frac{\sqrt{\pi}}{\sqrt{\lambda_1 t}}\left(erf\,(z)-erf\,(3\sqrt{\lambda_1 t})\right).\end{aligned}$$

(5.64)

Taking the limit as $z\to\infty$, $\lim_{z\to\infty}erf\,(z)=1$, equation 5.64 therefore simplifies to

$$\begin{aligned}q_f\left(t\right)&=q_{fi}\frac{\gamma}{\gamma-\rho}e^{(2n-1)^2\lambda_2 t}-q_{fi}\frac{\rho}{\gamma-\rho}e^{(2n-1)^2\lambda_1 t}\\&+\frac{q_{fi}}{4}\frac{\gamma}{\gamma-\rho}\frac{\sqrt{\pi}}{\sqrt{-\lambda_2 t}}erfc(3\sqrt{-\lambda_2 t})-\frac{q_{fi}}{4}\frac{\rho}{\gamma-\rho}\frac{\sqrt{\pi}}{\sqrt{-\lambda_1 t}}erfc(3\sqrt{-\lambda_1 t})\end{aligned}. \quad (5.65)$$

In arriving at equation 5.65 we have evaluated the limit $z\to\infty$ in equation 5.64 and used the identity $erfc(x)=1-erf\,(x)$. Equation 5.65 is the approximate analytical solution to the double porosity model. The negative sign under the square root in equation 5.65 is necessary because the values of λ_1 and λ_2 are always negative. The model parameters are defined as:

$$\lambda_1 = \frac{1}{2}\left[-\frac{1}{\tau_f}-\frac{1}{\tau_m}-\frac{T_x}{J_f\tau_f}+\sqrt{\left[\frac{1}{\tau_f}-\frac{1}{\tau_m}\right]^2+\frac{2T_x}{J_f\tau_f^2}+\frac{2T_x}{J_f\tau_m\tau_f}+\left(\frac{T_x}{\tau_f J_f}\right)^2}\right], \tag{5.66}$$

$$\lambda_2 = \frac{1}{2}\left[-\frac{1}{\tau_f}-\frac{1}{\tau_m}-\frac{T_x}{J_f\tau_f}-\sqrt{\left[\frac{1}{\tau_f}-\frac{1}{\tau_m}\right]^2+\frac{2T_x}{J_f\tau_f^2}+\frac{2T_x}{J_f\tau_m\tau_f}+\left(\frac{T_x}{\tau_f J_f}\right)^2}\right], \tag{5.67}$$

$$\rho = \frac{\tau_f J_f}{2T_x}\left[-\frac{1}{\tau_f}+\frac{1}{\tau_m}+\frac{T_x}{\tau_f J_f}+\sqrt{\left[\frac{1}{\tau_f}-\frac{1}{\tau_m}\right]^2+\frac{2T_x}{\tau_f^2 J_f}+\frac{2T_x}{\tau_m\tau_f J_f}+\left(\frac{T_x}{\tau_f J_f}\right)^2}\right], \tag{5.68}$$

$$\gamma = \frac{\tau_f J_f}{2T_x}\left[-\frac{1}{\tau_f}+\frac{1}{\tau_m}+\frac{T_x}{\tau_f J_f}-\sqrt{\left[\frac{1}{\tau_f}-\frac{1}{\tau_m}\right]^2+\frac{2T_x}{\tau_f^2 J_f}+\frac{2T_x}{\tau_m\tau_f J_f}+\left(\frac{T_x}{\tau_f J_f}\right)^2}\right]. \tag{5.69}$$

We verify that λ_1 and λ_2 are always negative by constructing their response surfaces, where we use τ_f and τ_m as independent variables and $\frac{T_x}{J_f}$ as a single parameter. Figure 5-3 and Figure 5-5 are the response surfaces of equation 5.66 with the parameter $\frac{T_x}{J_f}$ equal to 10^2 and 10^{-2}, respectively. And Figure 5-4 and Figure 5-6 are the response surfaces of equation 5.67 with the parameter $\frac{T_x}{J_f}$ equal to 10^2 and 10^{-2}, respectively. It can be verified from these figures that the equivalent time constants are always negative for realistic values of the fracture and matrix time constants and the lumped parameter, $\frac{T_x}{J_f}$. These equations show the mathematical relationship between the eigenvalues and the fracture, matrix time constants, the transmissibility coefficient between the fracture and the matrix compartment and the ratio of their permeability.

Physically, λ_1 and λ_2 are the time constants of an equivalent parallel flow model that will yield the same results as the original problem when appropriately weighted with the eigenvectors. One can regard equations 5.66 through to 5.69 as expressions for scaling parameters that can be used to transform a two compartment series flow model into a two compartment parallel-flow model without cross flow, Ogunyomi (2014). An extension of the model development to 3 compartments (triple porosity system) is available in appendix E.

5.2 Model Validation

5.2.1. Validation with Numerical Reservoir Simulation

The approximate analytical solution to the double porosity model, represented by equation 5.65, is validated with a synthetic case. The synthetic case was developed with CMG – GEM. The model used in the synthetic case was designed to have two adjoining reservoir compartments in which the compartment containing the producing well has a higher permeability when compared with the second compartment. The compartment with the high permeability can be thought of as the aggregated collection of the fracture volume while the second compartment is used to represent the reservoir matrix and hence it has a lower permeability. The volume of the fracture compartment is equal to 25 percent of the volume of the matrix compartment. All other properties are identical for the two compartments. The other inputs for the synthetic model are summarized in Table 5-1. Figure 5-7 is the numerical simulation model used in the validation case and it shows the permeability field.

To validate the approximate analytical model, the production rate obtained from running the synthetic case is shown to be identical to the production rate obtained from the approximate analytical solution. Figure 5-8 presents a comparison of the production rate obtained from the synthetic case and the approximate analytical solution. The graph in red represents the production rate from the analytical solution while the graph in blue is the production rate from the synthetic case.

The production history in Figure 5-8 exhibits two time scales, the first time scale initially starts as a straight line with a slope of half which is indicative of transient linear flow in one dimension and this is followed by an exponential decline that is indicative of boundary dominated flow from the first compartment. After the boundary dominated flow from the first compartment has dissipated the transient flow from the second compartment starts and it has the expected straight line with half slope signature. This transient flow regime is then followed by a boundary dominated flow regime from the second compartment. From this figure, both graphs, from the simulator and the analytical solution, overlay each other; therefore, validating the analytical solution. A summary of the fitting parameters for the analytical solution are presented in Table 5-2 below.

5.2.2. Validation with Laplace Space Analytical Solution

In this section we present a comparison of the analytical solution derived in the previous section with the actual solution to the double porosity model (in Laplace space). The equivalent solution to a double porosity model using Laplace transforms, Bello et al. (2008) is given as

$$p_{fD}(y_D, s) = \frac{\cosh\left[\sqrt{sf(s)}\,y_D\right]}{s\cosh\left[\sqrt{sf(s)}\right]}, \tag{5.70}$$

where;

$f(s) = \omega + \sqrt{\dfrac{\lambda(1-\omega)}{3s}}\tanh\left[\sqrt{\dfrac{3(1-\omega)s}{\lambda}}\right]$: Inter-porosity transfer function

$p_D = \dfrac{p - p_i}{p_{wf} - p_i}$: Dimensionless pressure

$t_D = \dfrac{k_f t}{\mu((\phi c_t)_f + (\phi c_t)_m) x_f^2}$: Dimensionless time

$x_D = \dfrac{x - x_e}{x_{wf} - x_e}$: Dimensionless distance in the x - direction

$y_D = \dfrac{y - y_e}{y_f - y_e}$: Dimensionless distance in the y - direction

$\lambda = 12 \dfrac{k_m}{k_f} \left[\dfrac{x_f}{L} \right]^2$: Inter-porosity transfer parameter

$\omega = \dfrac{(\phi c_t)_f}{(\phi c_t)_f + (\phi c_t)_m}$: Storativity ratio

The solution given by equation 5.70 is the constant pressure solution, that is, it assumes an instantaneous constant pressure at the fracture face. The details of its derivation can be found in Bello et al. (2008) and also in appendix A for convenience. A problem with using this solution is that it cannot be inverted back in to the real time space to obtain a closed form analytical solution hence a numerical inversion algorithm is employed to compute pressures and rate from this solution. From this solution we obtain the production rate at the fracture face by taking its derivative and evaluating its value at the fracture face ($y_D = 1$), that is, $\left.\dfrac{dp_{fD}}{dy_D}\right|_{y_D=1}$

$$q_D(y_D = 1, s) = \sqrt{\frac{f(s)}{s}} \tanh\left[\sqrt{sf(s)} \right]. \tag{5.71}$$

Bello et al. (2008) also provided a detailed sensitivity analysis on equation 5.71 to understand how the model parameters affect its production characteristics. We summarize the result of this sensitivity analysis below: Figure 5-9 presents a plot of the dimensionless rate versus the dimensionless time where the inter-porosity transfer and the storativity ratio have been varied. The red colored lines on the plot correspond to a storativity ratio of 10^{-1} and the inter-porosity transfer parameter varying from 10^{-3} to 10^{-9}, the blue colored lines correspond to a storativity ratio of 10^{-3} and the inter-porosity transfer parameter varying from 10^{-3} to 10^{-9} while the green colored lines correspond to a storativity ratio of 10^{-6} and the inter-porosity transfer parameter varying from 10^{-3} to 10^{-9}. The physical meaning of the general characteristic observed on this plot can be explained as follows; at the start of production, flow is predominantly linear with a slope of half and represents transient flow from the fracture, this is followed by an exponential decline period when the effects of the fracture boundary is felt and becomes dominant. After the effect of the fracture boundary, another linear flow period starts (also characterized by a half slope) and this is believed to be the transient flow from the reservoir matrix. After this transient flow period another exponential decline period is observed and this is believed to correspond to the matrix boundary effect.

We now compare the production rate from the approximate analytical solution (equation 5.65) to the production rate from the actual analytical solution (equation 5.71). For our approximate analytical solution to be useful, it should reasonably reproduce the observed characteristics in Figure 5-9. The result of the comparison is presented in Figure 5-10. In Figure 5-10 we present three cases of history matching of production rate from the actual solution and the approximate solution. Case one shows the match for $\omega = 10^{-3}$ and $\lambda = 10^{-5}$, case two shows the match for $\omega = 10^{-1}$ and $\lambda = 10^{-5}$ and case three shows the match for $\omega = 10^{-1}$ and $\lambda = 10^{-9}$. From Figure 5-10 it obvious that the production rate predicted by the approximate analytical solution provides a good match to the production rate predicted by the actual solution, hence the approximate analytical solution can be used to reliably forecast production from fractured horizontal wells.

5.3 Analysis of Model Parameters

5.3.1. Physical Meaning of the Model Parameters:

The time constants in the approximate analytical solution are identical in definition $\tau = \frac{v_p c_t}{J}$ to that defined in the capacitance resistance model (CRM), as a result we conclude that τ has a similar physical meaning in our solution as it does in the CRM. It is important to note that τ is a function of the storage capacity and the transmissibility (permeability) of the compartment, In the CRM, Cao (2014), Nguyen et al. (2012) following the work of Seborg et al. (2003) have defined the time constant to mean the time it takes for 63.2 percent of an input pulse to be observed as the output. The input pulse for our model would be the pressure difference that is responsible for flow while in the CRM it is the injection rate.

5.3.2. Inferring Fracture and Matrix Volume from Model Parameters

In this section, we investigate the possibility of estimating the size (volume) of the fractures induced by the hydraulic fracture and the reservoir matrix from the model parameters with the approximate analytical solution. To accomplish this task, we took the following steps (the numerical model was built with CMG's IMEX black oil simulator):

1. Build a numerical model with two compartments where one compartment has a high permeability and the second compartment has a low permeability with a commercial reservoir simulator.
2. Perform a history match of the production rate from the numerical model to the approximate analytical solution to obtain the model parameters.
3. Change the relative volume of each compartment in the numerical simulation model while keeping the total pore volume constant and repeat step 2.

4. After obtaining the model parameters for a few cases we make a cross plot of each model parameter with the volume of each compartment as defined in the numerical simulation model.

The model parameters considered for this analysis are the fracture compartment time constant (τ_f), the matrix compartment time constant (τ_m) and the initial fracture production rate (q_{fi}). The numerical model used for this analysis is identical to that presented in Figure 5-7 and the model used is equation 5.65. The result of this numerical experiment is summarized in Table 5-3, which presents a summary of the cases considered and the model parameters obtained from the history matching exercise.

a) **Fracture time constant**:

Figure 5-11a presents the crossplot of the fracture time constant and the pore volume of the high permeability compartment. Figure 5-11b presents the same for the low-permeability compartment. From Figure 5-11a as the pore volume of the high permeability compartment increases the fracture time constant increases, indicating a positive correlation between them. The coefficient of determination is large, R^2 = 0.98. Recall that the fracture time constant is defined as $\tau_f = \frac{\left(v_{p_f} c_t\right)_f}{J_f}$, where v_{p_f} is the fracture pore volume. This definition of the fracture time constant suggests that we can infer the size of the fracture volume from the value of the fracture time constant. In contrast, Figure 5-11b suggests that the fracture time constant decreases with increasing pore volume of the low-permeability compartment. This figure also has a large coefficient of determination, R^2 = 0.98. This observation is because the fracture volume shares a boundary with the matrix volume and this shared boundary was held constant during this experiment while the other boundaries changed.

b) **Matrix time constant**:

Figure 5-12a is the cross plot of the matrix time constant and the pore volume of the high permeability compartment, whereas Figure 5-12b represents the same for the low permeability compartment. Figure 5-12a suggests that, as the pore volume of the high permeability compartment increases, the matrix time constant decreases. This relationship indicates a negative correlation between them. The coefficient of determination is high, $R^2 = 1.0$, suggesting that there is a relationship between the size of the fracture volume and the matrix time constant. This transmissibility factor is a function of the fracture dimension. From Figure 5-12b, we observe that as the pore volume of the low-permeability compartment increases, the matrix time constant increases. This observation is expected because in the definition of the matrix time constant, as shown above, the matrix time constant is directly related to the matrix pore volume, v_{p_m}. This cross-plot also has a high coefficient of determination.

c) **Initial production rate**:

Figure 5-13a presents a cross plot of the initial production rate and the pore volume of the high permeability compartment. Figure 5-13b is the cross plot of the initial production rate and the pore volume of the low permeability compartment. From Figure 5-13a as the pore volume of the high permeability compartment increases the initial production rate from the fracture decreases, indicating a negative correlation between them. The coefficient of determination is high, $R^2 = 0.84$, suggesting that we can infer the size of the fracture volume from the initial production rate from the fracture. The definition of the initial production rate is given as $q_{f_i} = \frac{(p_i - p_{wf})k_f A_f}{\mu L_f}$. In the numerical simulation model $A_f = hw_f$ and $v_{p_f} = \phi A_f L_f$. In the experiments conducted, when we increased the fracture pore volume we increased L_f and as this variable is in the denominator of the definition of q_{f_i}. From this definition there is an inverse relationship between the initial production rate and the fracture volume, which explains the observation in Figure 5-13a.

From Figure 5-13b we see that as the pore volume of the low permeability (matrix) compartment increases the initial production rate from the fracture increases. This observation is consistent with the total pore volume of the reservoir being kept constant, which implies that by increasing the fracture pore volume we decrease the matrix pore volume, $v_{p_m} = \phi A_f (L - L_f) = v_{p_T} - v_{p_f}$. Therefore the initial production rate should increase as the matrix pore volume is increased. Given the good correlation, we can estimate the matrix pore volume from the initial production rate.

5.4 Application to Field Data

This section presents example applications of the approximate solution to field data and demonstrate how to use it to estimate reserves from hydraulically fractured horizontal wells in liquid rich unconventional formations. The model was fitted to production rate data from 88 hydraulically fractured horizontal wells. Song (2014) presented the application of a finite difference solution to this data set. All the fits obtained were within the limits of engineering accuracy. To apply the model to field data from a well, we fit the model to available historical production rate data from the well to obtain the model parameters by minimizing the squared difference between the model estimates and the field production data, that is, $\min\left[q_{\text{Data}} - q_{\text{model}}\right]^2$ by changing τ_f, τ_m and $\frac{T_x}{J_f}$. After obtaining the model parameters, we proceed to forecast future production rates and cumulative production until 100,000 days. We present an example application of the model to a well in the data set; some more examples are presented in appendix D.

Example 1:

For this example, the well details are summarized in Table 5-4. This well has been on production for 1,136 days. Figure 5-14a presents both the rate and tubinghead pressure on a log-log plot. The figure suggests that the production rate is relatively constant until about 90 days after which the production rate from the well declined exponential until it started declining with a slope of one-half. The tubinghead pressure for this well declined with a slope of one half until about 90 days (transient flow) after which it declined with a slope of one indicating boundary dominated flow (BDF) until about 100 days when it becomes constant. If we assume that production during the first 100 days is from the fracture volume and the production after 100 days is from the matrix then we can match the model to this data, making sure we match the exponential decline and the half-slope portions of the data. Figure 5-14b presents the results of the rate history match and future performance. This figure contains three plots, the original production data (red markers), the history match (green colored markers) and the forecast (black markers). We summarized the model parameters obtained from the history match exercise in Table 5-5. The mismatch at the start of the production history is because the well was produced at a variable bottomhole pressure during this period while the analytical model presented is based on the wellbore pressure being constant. After obtaining the model parameters from the history match exercise we use the model to forecast future production rate and reserves until 10,000 days. Figure 5-14c presents the performance forecasting results.

Example 2:

The well details for this example are in Table 5-6. This well has been on production for 531 days. The production rate from this well is shown in Figure 5-15a on a log-log plot. This figure suggests that the production rate is relatively constant until about 10 days after which the well rate declined exponentially until it started declining with a slope of one-half. The tubinghead pressure for this well started declining with a slope of one-half (indicating transient flow) until about 10 days after which it started declining with a slope of one (indicating boundary dominated flow). After about 100 days the tubinghead pressure was relatively constant. Again if we assume that production during the first 100 days is from the fracture volume and the production after 100 days is from the matrix then we can match the model to this data making sure we match the exponential decline and the half-slope portions of the data. The result of the production rate history match is shown in Figure 5-15b and that of future performance in Figure 5-15c. This figure contains three plots, the original production data (red markers), the history match (green colored markers) and the forecast (black markers). From this figure we have matched the exponential decline portion of the rate data and we also matched the linear decline portion of the rate data. We have summarized the model parameters obtained from the history match exercise in Table 5-7. After obtaining the model parameters from the history match exercise, the model was used to forecast future production rate and cumulative production until 8,000 days. The result of the forecasting process is shown in Figure 5-15c.

The model parameters obtained from these two examples and others not shown here are all functions of the well and reservoir properties. Consequently, the forecasted results have high degree of confidence particularly when the fracture boundary is observed in the production rate data, which provided an opportunity for defining the geometry of the adjoining compartment.

5.5 Summary and Conclusions

A generally accepted conceptual model for fractured horizontal wells is that a stimulated reservoir volume (SRV) develops around the well and there is a region of undamaged reservoir beyond the SRV (Miller et al. 2010). The SRV is expected to be comprised of a complex network of fractures of different geometries ranging from planar, curved, slanted etc and of different lengths. However, for ease of solution, existing "physics" based models assume that the hydraulic fractures are planar and perpendicular to the wellbore. The new solution presented in this work overcomes this limitation of existing models because the assumption of planar fractures is not necessary.

Most empirical models do not account for the second time scale and the end of transient linear flow must be determined arbitrarily before switching to a boundary dominated flow model. The new solution presented here also eliminates this limitation of empirical models. For cases where there is no production data from the second time scale the single porosity solution should be used. This solution is shown below:

$$q_D\left(t_D\right) = 2e^{-\frac{\pi^2 t_D}{4}} + \frac{erfc\left[\frac{3}{2}\pi\sqrt{t_D}\right]}{\sqrt{\pi t_D}}. \tag{5.72}$$

In equation 5.72, the first term accounts for boundary dominated flow and the second term is the transient solution. The dimensionless time t_D is defined as t/τ where τ is the time constant of compartment 1 and *t* is time. We have shown that the model parameters derived from the use of the new solution are functions of the reservoir and well completion properties. Particularly, the model parameters can be used to estimate the drainage volume of a well; this characteristic of the model could have potential application in in-fill drilling and well spacing optimization studies. Because the model has a closed analytical form, it is especially suited for optimization studies that account for uncertainties in reservoir properties and the outcome of well stimulations (hydraulic fracturing).

Table 5-1: Summary of input parameters for the synthetic case as used in CMG - GEM

Parameter	value
Δx x Δy x Δz (ft)	100 x 50 x 50
Grid	51 x 11 x 1
Depth, D (ft)	2000
Thickness, h (ft)	50
Compartment 1	
Permeability, k_f (md)	70
Porosity	0.3
Volume, (ft^3)	$8.25 x 10^6$
Compartment 2	
Permeability, k_m (md)	10
Porosity	0.3
Volume, (ft^3)	$3.3 x 10^7$

Table 5-2: Summary of model parameters used in the validation case. These parameters provided the best fit between the synthetic case and the analytical model

Parameter	Value
q_{fi} (stb/d)	4695.61
τ_f (day)	56.00
τ_m (day)	6087.00
T_x/J_f	0.03670
λ_1 (day^{-1})	-0.00016
λ_2 (day^{-1})	-0.01852
ϒ (day^{-1})	-27.0051
ρ (day^{-1})	1.0090
ϒ /(ϒ -ρ)	0.9640
ρ/(ϒ -ρ)	-0.0360

Table 5-3: Summary of model parameters obtained from the numerical experiments performed to investigate the possibility of inferring fracture and matrix volumes by using the approximate analytical solution

Case	CMG V_{pf} (ft^3)	CMG V_{pm} (ft^3)	τ_f (days)	τ_m (days)	$-1/\lambda_1$ (days)	$-1/\lambda_2$ (days)	q_{fi} (stb/d)
1	8.25E+06	3.30E+07	56	6087	6312.4	54	4695.61
2	1.65E+07	2.48E+07	176	3998	4247.01	165.68	2695.61
3	2.48E+07	1.65E+07	267	1900	2462.16	206.04	2080.02
4	4.13E+06	3.71E+07	15	7455	7639.51	14.64	8195.61
5	0.00E+00	4.13E+07	-	8634	8855.91	-	7095.61

Table 5-4: Well properties for example one

Well ID:	**UT-ID67**
Well length, (ft^3)	8894
Spacing (acres)	1280
Initial pressure, P_i (psi)	6082.87
Porosity, (fraction)	0.07
Thickness, h (ft)	53.14
Initial number of stages	1

Table 5-5: Summary of model parameters for example one

Parameter	**Value**
q_{fi} (stb/d)	$8.68\text{x}10^{2}$
τ_f (day)	34.00
τ_m (day)	955.00
T_x/J_f (ratio)	$1.98\text{x}10^{-1}$
λ_1 (day^{-1})	$-8.7\text{x}10^{-4}$
λ_2 (day^{-1})	$-3.54\text{x}10^{-2}$
Υ (Unitless)	-4.9
ρ (Unitless)	1.03
$\Upsilon/(\Upsilon-\rho)$ (ratio)	$8.26\text{x}10^{-1}$
$\rho/(\Upsilon-\rho)$ (ratio)	$-1.74\text{x}10^{-1}$

Table 5-6: Well properties for example two

Well ID:	**UT-ID265**
Well length, (ft^3)	9965
Spacing, (acres)	1280
Initial pressure, P_i (psi)	7656.69
Porosity, (fraction)	0.07
thickness, h (ft)	67.69
Initial number of stages	10

Table 5-7: Summary of model parameters for example two

Parameter	**Value**
q_{fi} (stb/d)	4.37×10^{2}
τ_f (day)	5.19×10^{1}
τ_m (day)	3.93×10^{2}
T_x/J_f (ratio)	2.67×10^{-1}
λ_1 (day^{-1})	-1.96×10^{-3}
λ_2 (day^{-1})	-2.50×10^{-2}
Υ (Unitless)	-3.37
ρ (Unitless)	1.11
$\Upsilon/(\Upsilon-\rho)$ (ratio)	7.51×10^{-1}
$\rho/(\Upsilon-\rho)$ (ratio)	-2.49×10^{-1}

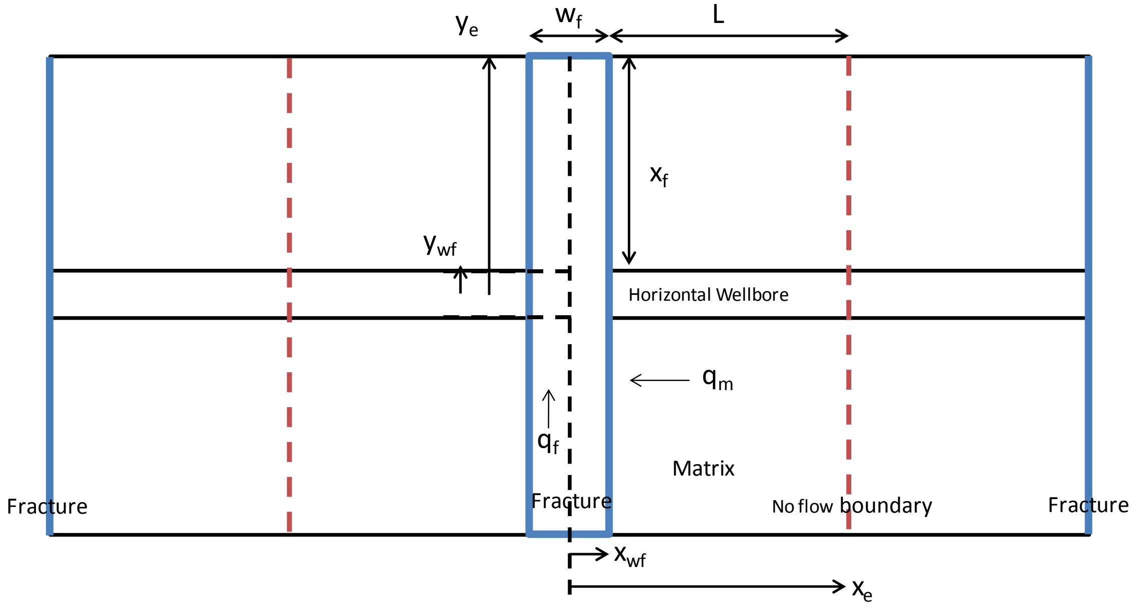

Figure 5-1: Schematic diagram of a single fractured horizontal well with a planar fracture

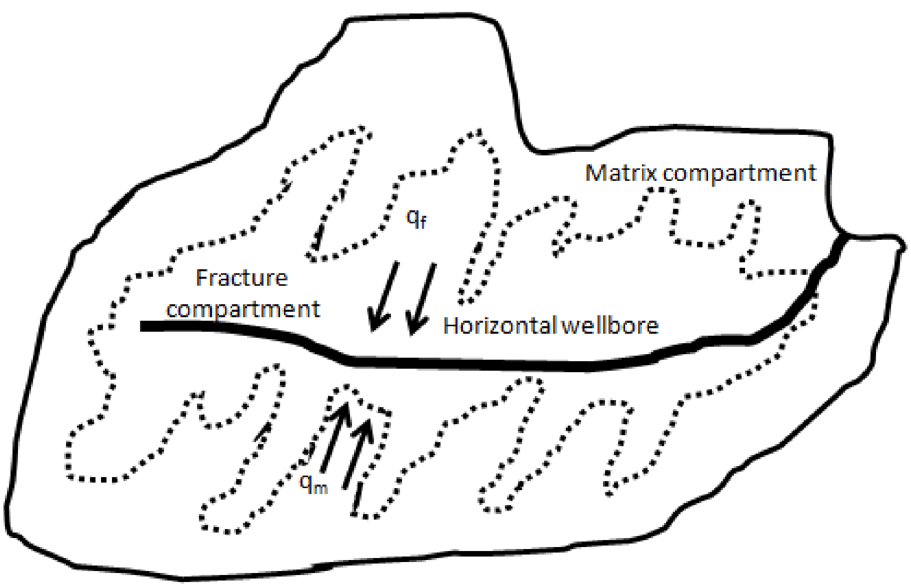

Figure 5-2: A simplified representation of the double porosity model as a series model with two compartments (tanks) where the first compartment represents the volume of the fracture and the second compartment represents the pore volume of the reservoir matrix

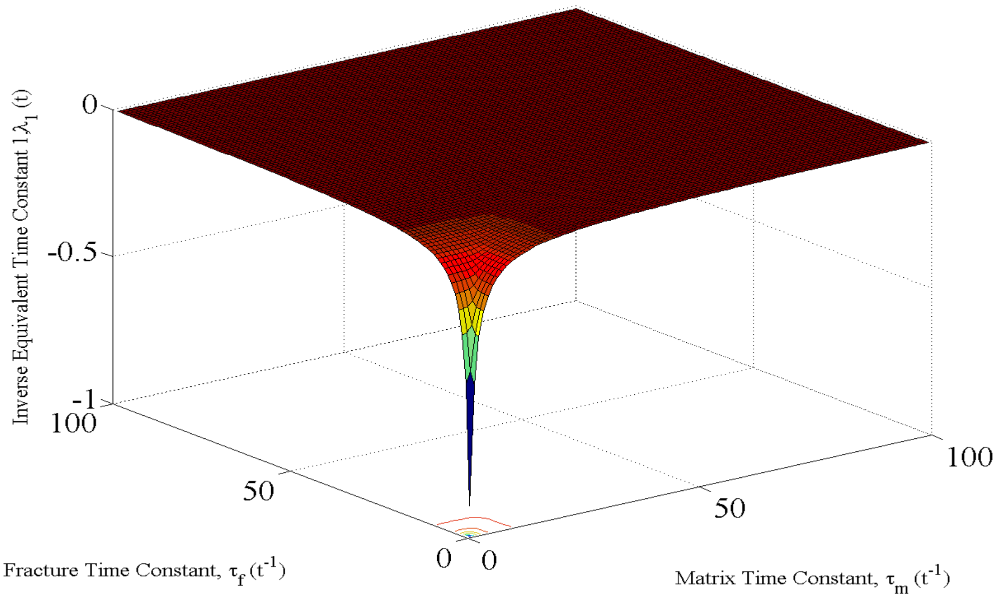

Figure 5-3: Response surface for equivalent time constant 1, λ_1, when the parameter $\dfrac{T_x}{J_f}$ is equal to 10^{-2}

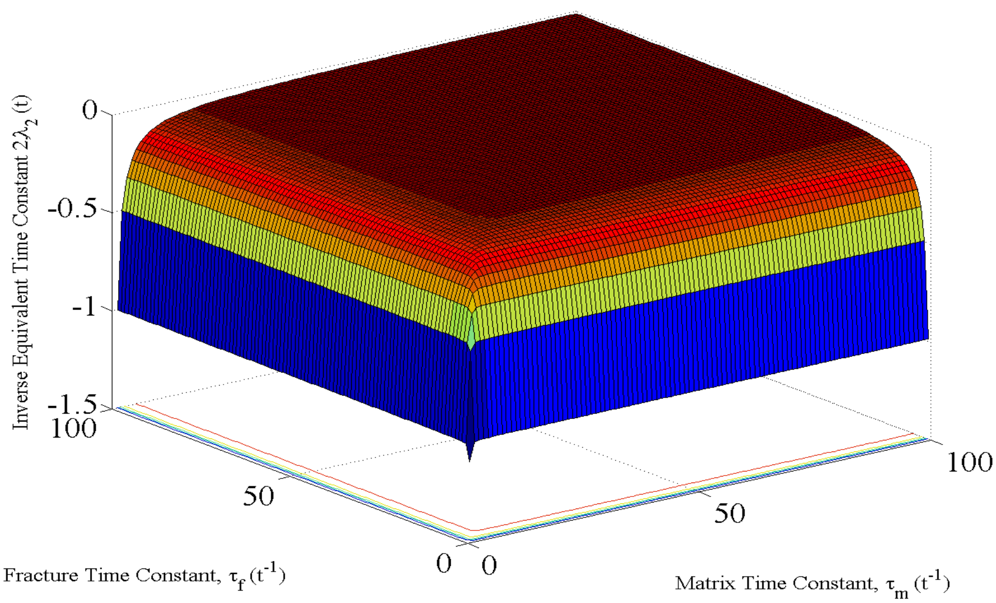

Figure 5-4: Response surface for equivalent time constant 2, λ_2, when the parameter $\dfrac{T_x}{J_f}$ is equal to 10^{-2}

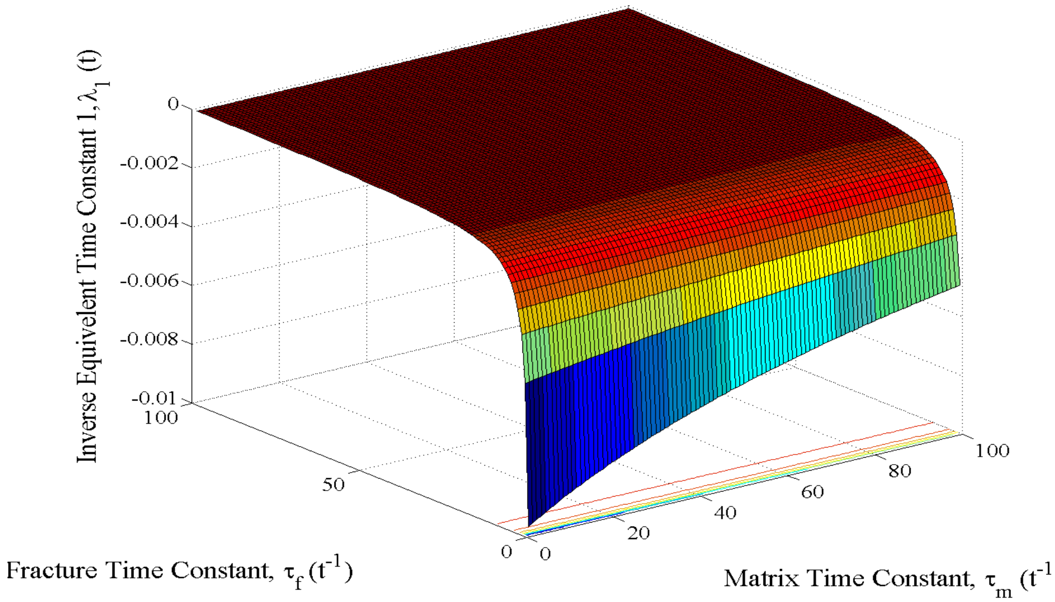

Figure 5-5: Response surface for equivalent time constant 1, λ_1, when the parameter $\dfrac{T_x}{J_f}$ is equal to 10^2

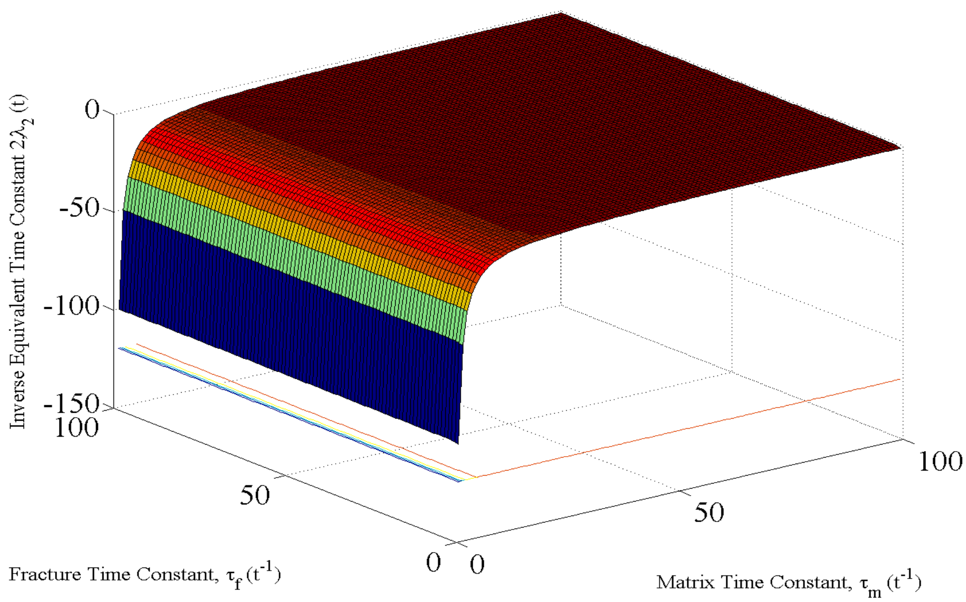

Figure 5-6: Response surface for equivalent time constant 2, λ_2, when the parameter $\dfrac{T_x}{J_f}$ is equal to 10^2

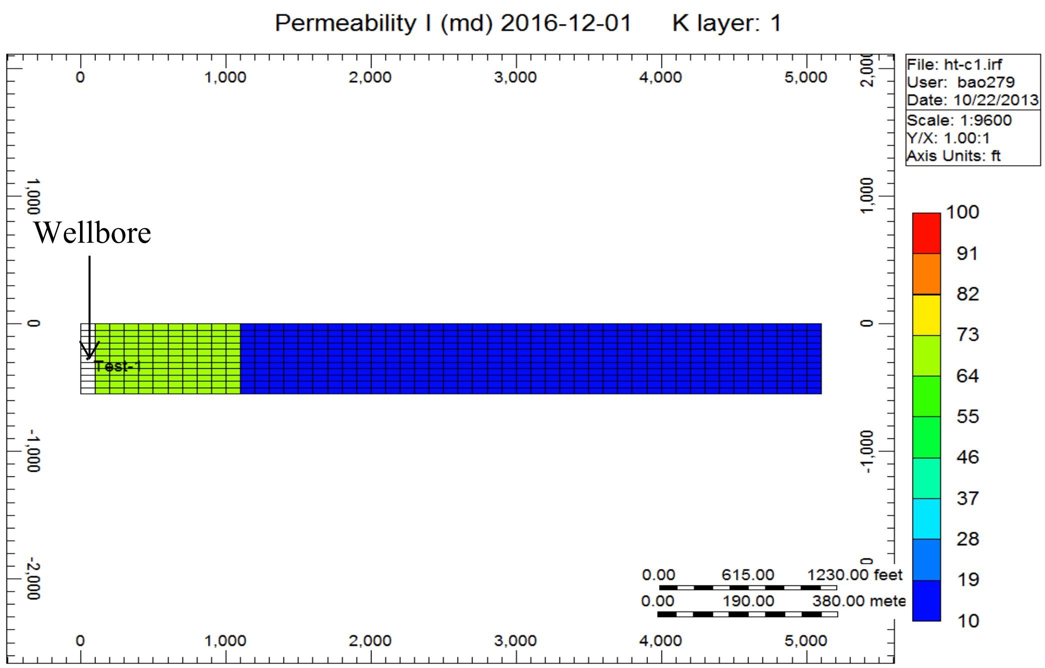

Figure 5-7: Reservoir grid for the synthetic case showing the permeability field. The grid blocks in green are the high permeability compartment and the blue grids are the lower permeability compartment

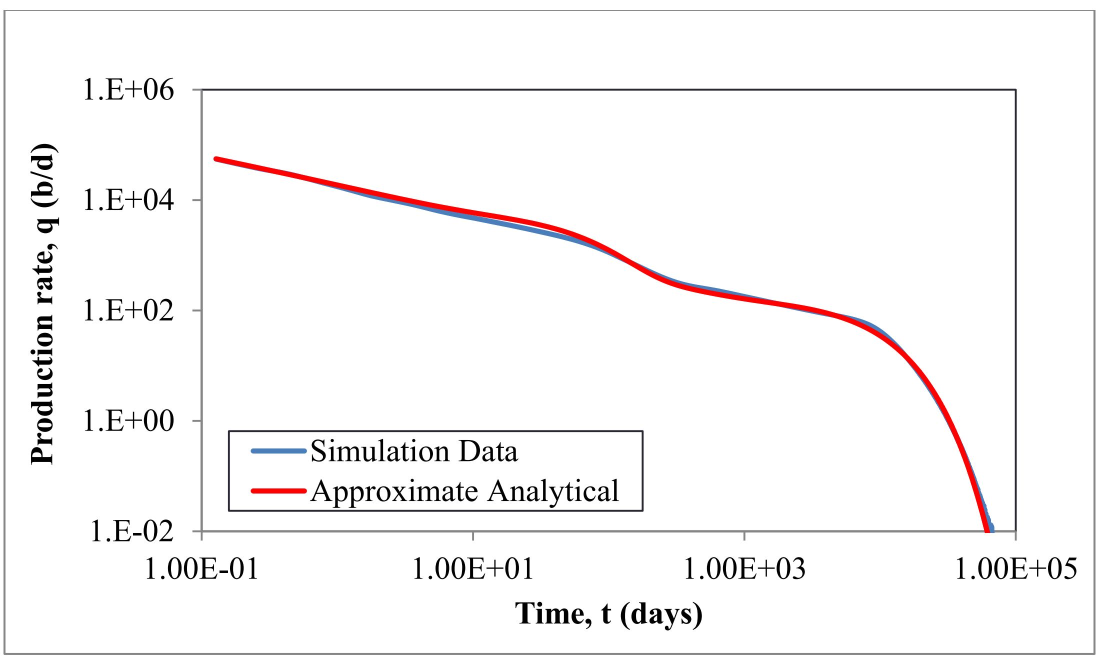

Figure 5-8: Comparison of the production rate from the synthetic case and the approximate analytical model

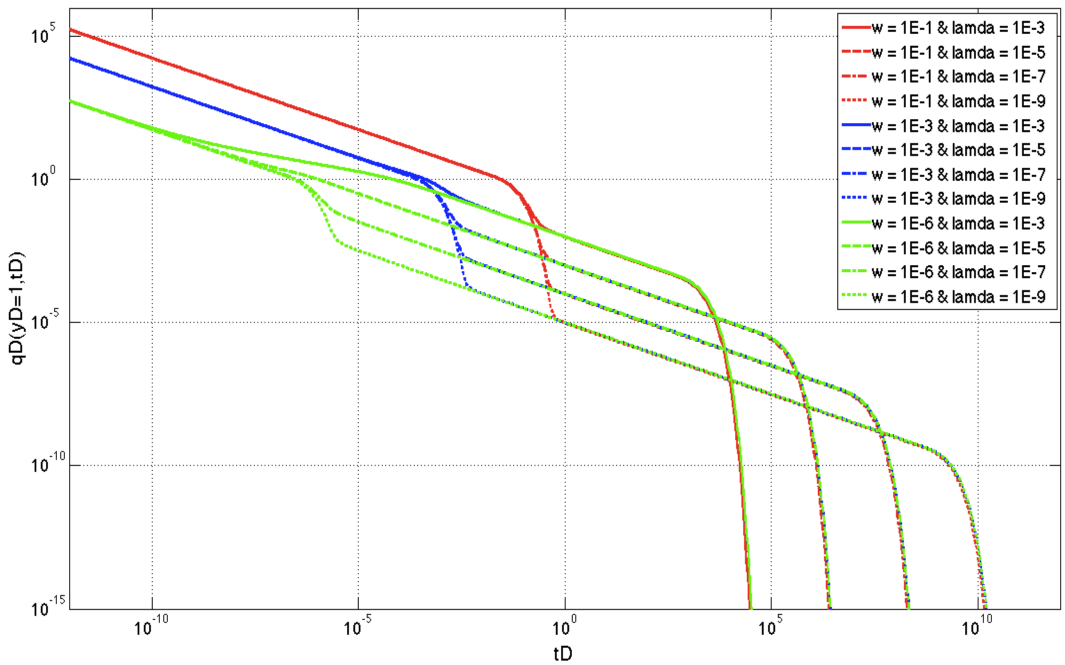

Figure 5-9: Effect of storativity ratio and inter-porosity transfer parameter on the production rate from the double porosity model

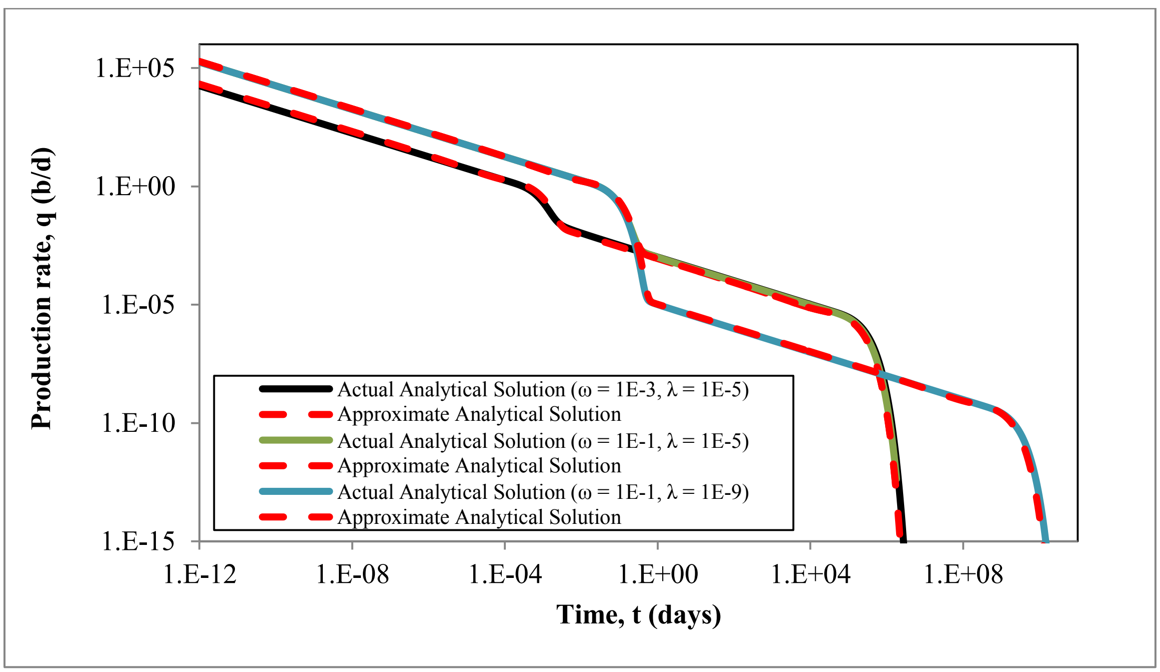

Figure 5-10: Comparison of production rate from the approximate analytical solution to the actual analytical solution

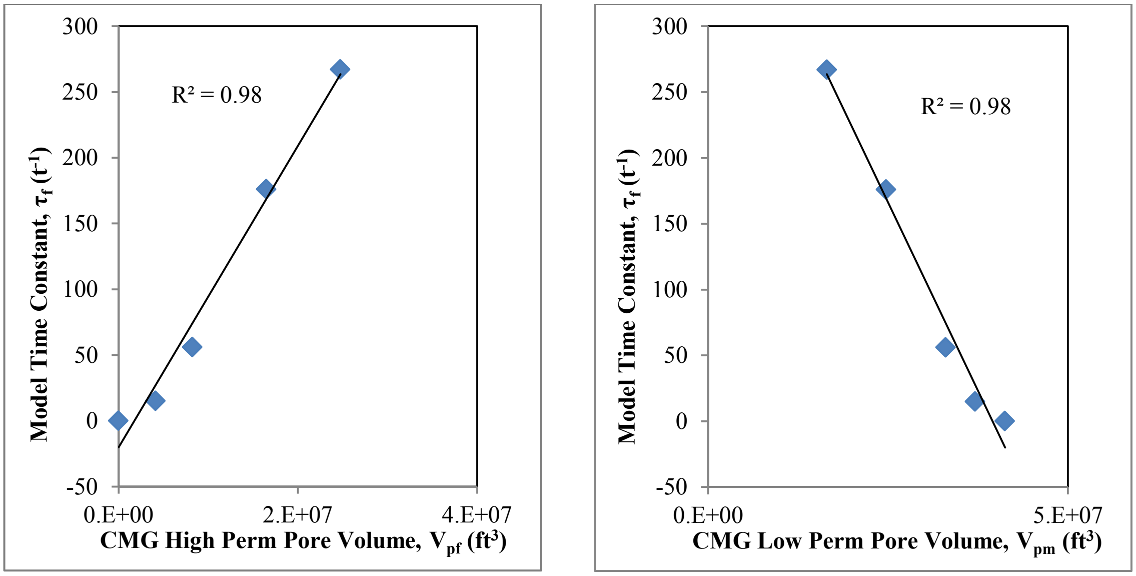

(a). (b).

Figure 5-11: a. Cross plot of fracture time constant and the pore volume of the high permeability compartment in the numerical model b. cross plot of fracture time constant and the pore volume of the low permeability compartment in the numerical model

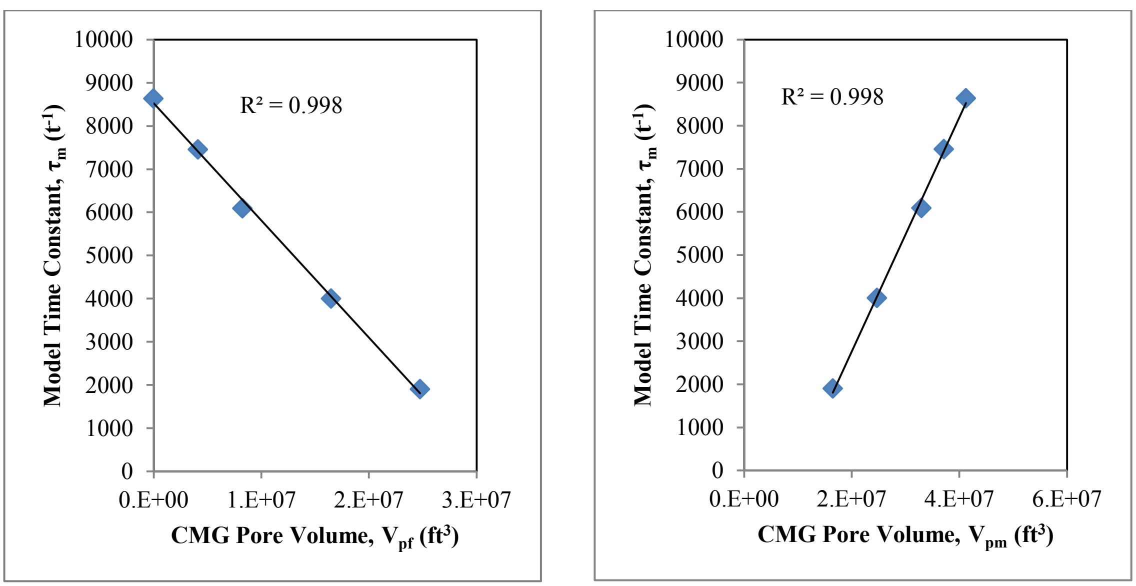

(a). (b).

Figure 5-12: a. Cross plot of matrix time constant and the pore volume of the high permeability compartment in the numerical model b. cross plot of matrix time constant and the pore volume of the low permeability compartment in the numerical model

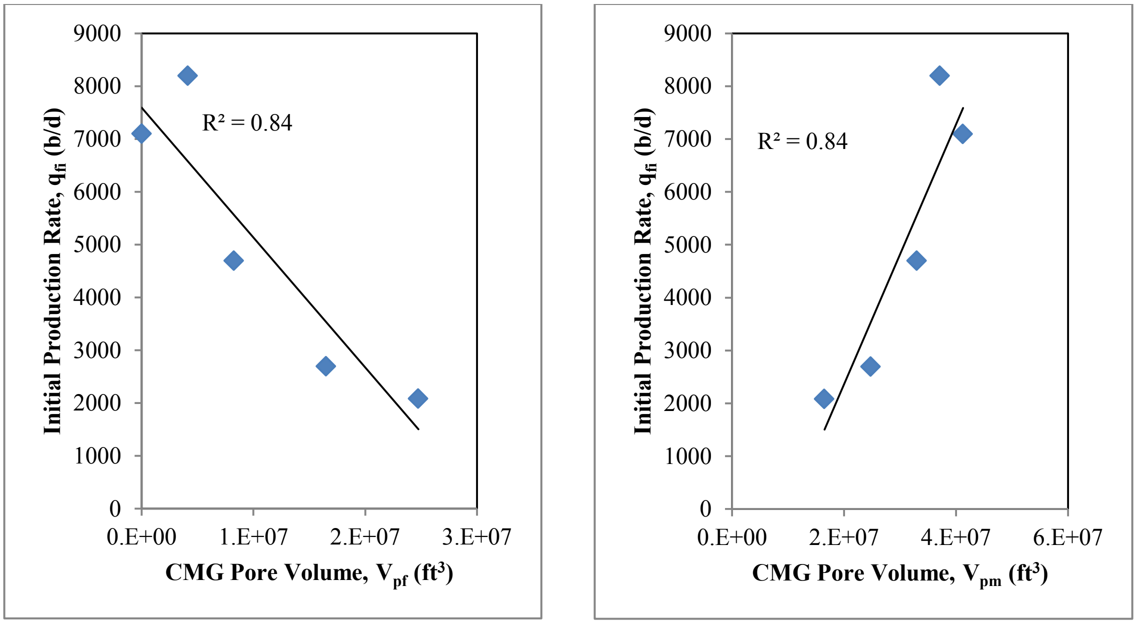

Figure 5-13: a. Cross plot initial production rate and the pore volume of the high permeability compartment in the numerical model b. cross plot of initial production rate and the pore volume of the low permeability compartment in the numerical model

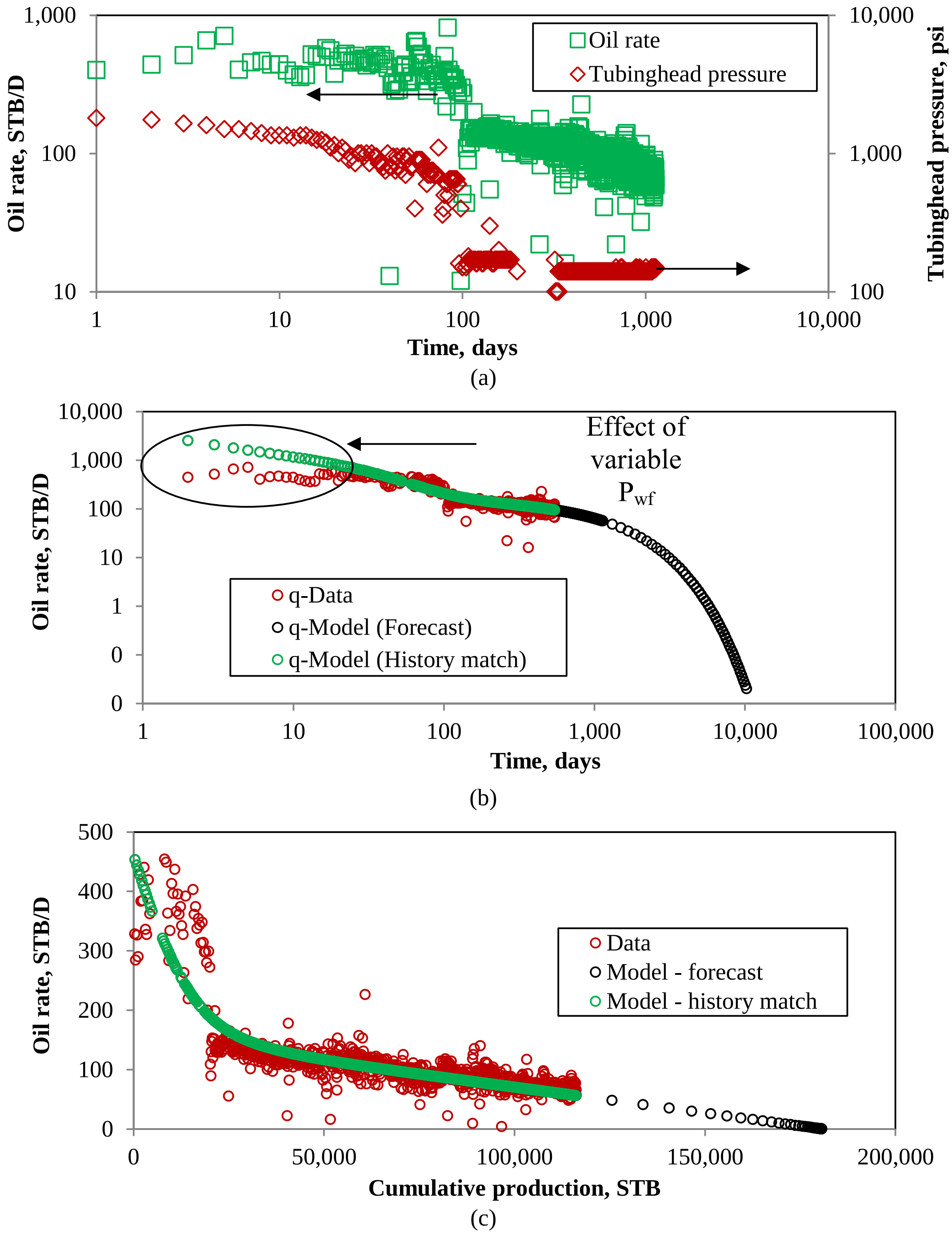

Figure 5-14: Summary of production profile for example 1, (a). is the production rate plotted on a log-log scale. (b). represents the history match result and the forecast of production rate. (c). represents the history match of the cumulative production and reserves forecast

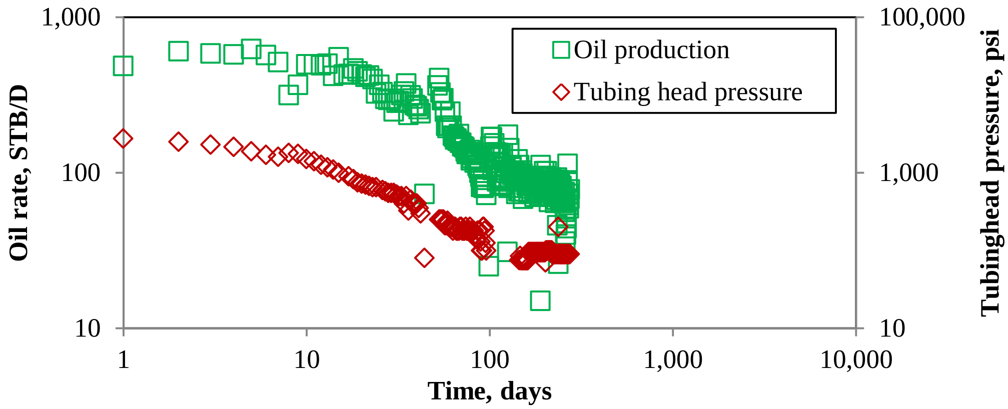

(a)

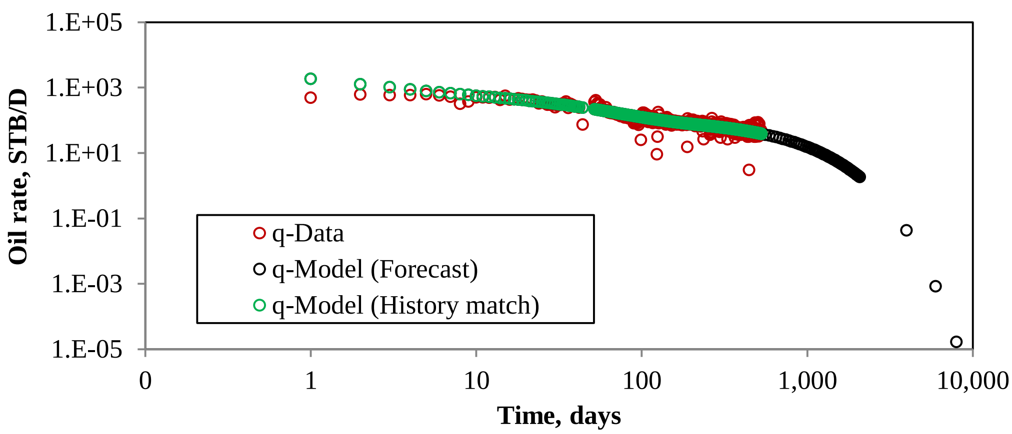

(b)

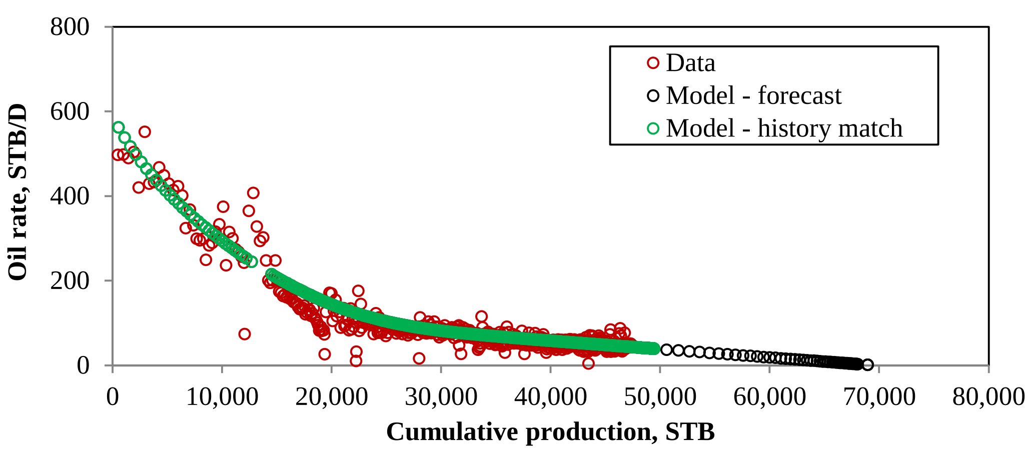

(c)

Figure 5-15: Summary of production profile for example 1, (a). is the production rate plotted on a log-log scale. (b). represents the history match result and the forecast of production rate. (c). represents the history match of the cumulative production and reserves forecast

Chapter 6: New Analytical Expressions for a Skin and Storage Effect – An Insight to Decouple Fracture Half-Length and Square-Root of Permeability

Most of the models used in well testing and production data analysis of fractured horizontal wells (and fractured reservoirs) are based on the assumption that the induced fractures have a quadrilateral geometry. From a practical perspective this assumption might not be true, in the simplest case if the stress distribution in the reservoir is homogenous and isotropic, then fractures induced after hydraulic fracturing should have a circular geometry. The objective of this chapter is to present new analytical models for the case where the fracture geometry is circular. The solutions presented are for two inner boundary conditions, the constant pressure and the constant rate cases with sealed/no-flow outer boundaries.

6.1 Analytical Model Development

In reality, if it is assumed that the stress distribution in the formation is isotropic it should be expected that the fracture geometry will be circular. If the stress distribution is anisotropic, the fracture geometry should be expected to be elliptical in shape. Figure 6-1 presents the conceptual model of a fracture in the isotropic case.

We make the following assumptions in the model development:

1. Flow is single-phase and slightly compressible,
2. Flow occurs in the reservoir isothermally,
3. The reservoir is isotropic and homogeneous in each compartment,
4. Hydraulic fractures are equidistant from each other,
5. There is no direct communication between the matrix and wellbore because of the casing and cement used to isolate the well,
6. Only linear flow exist in the reservoir matrix and only radial flow exists in the fracture,
7. Secondary effects are negligible such as stress dependent permeability (porosity) and desorption,

6.1.1 Solution with Constant Pressure Inner Boundary Condition

For flow in the reservoir matrix, the diffusivity equation, the initial condition and the associated boundary conditions, in dimensionless form, are given as shown below:

$$\frac{1}{r_D}\frac{\partial}{\partial r_D}\left[r_D\frac{\partial p_{mD}}{\partial r_D}\right]+\frac{\lambda}{12}\frac{\partial^2 p_{mD}}{\partial z_D^2}=(1-\omega)\frac{\partial p_{mD}}{dt_D}, \tag{6.1}$$

$$\left.\frac{\partial p_{mD}}{\partial r_D}\right|_{r_D=r_{De}}=0, \tag{6.2}$$

$$\left.\frac{\partial p_{mD}}{\partial r_D}\right|_{r_D=r_{Dw}=1}=0, \tag{6.3}$$

$$\left.\frac{\partial p_{mD}}{\partial z_D}\right|_{z_D=z_{De}=1}=0, \tag{6.4}$$

$$p_{mD}(r_D,z_{Dw},t_D)=p_{fD}(r_D,z_{Dw},t_D), \tag{6.5}$$

$$p_{mD}(r_D,z_{Dw},0)=0. \tag{6.6}$$

For flow in the fracture the diffusivity equation, the initial condition and the associated boundary conditions, in dimensionless form, are given as:

$$\frac{1}{r_D}\frac{\partial}{\partial r_D}\left[r_D\frac{\partial p_{fD}}{\partial r_D}\right]+\frac{\lambda}{12}\frac{\partial^2 p_{fD}}{\partial z_D^2}=\omega\frac{\partial p_{fD}}{dt_D}, \tag{6.7}$$

$$\left.\frac{\partial p_{fD}}{\partial r_D}\right|_{r_D=r_{De}}=0, \tag{6.8}$$

$$p_{fD}(r_{Dw}=1,z_D,t_D)=1, \tag{6.9}$$

$$\left.\frac{\partial p_{fD}}{\partial z_D}\right|_{z_D=0}=0, \tag{6.10}$$

$$p_{fD}(r_D,z_{Dw},t_D)=p_{mD}(r_D,z_{Dw},t_D), \tag{6.11}$$

$$p_{fD}\left(r_D, z_{Dw}, 0\right) = 0, \tag{6.12}$$

The dimensionless variables in equations 6.1 through to 6.12 are as defined below:

$p_D = \dfrac{p - p_i}{p_{wf} - p_i}$: Dimensionless pressure

$r_D = \dfrac{r}{r_w}$: Dimensionless radius

$z_D = \dfrac{z}{z_e}$: Dimensionless distance in the z-direction

$t_D = \dfrac{k_f t}{\mu\left[\left(\phi c_t\right)_f + \left(\phi c_t\right)_m\right] r_w^2}$: Dimensionless time

$\omega = \dfrac{\left(\phi c_t\right)_f}{\left(\phi c_t\right)_f + \left(\phi c_t\right)_m}$: Storativity ratio

$\lambda = 12\dfrac{k_m r_w^2}{k_f z_e^2}$: Transmissibility ratio

Equation 6.1 is the diffusivity equation in cylindrical coordinates where the z-coordinate is along the axis of the horizontal well and the r-coordinate represents the perpendicular distance to the well axis. Equation 6.2 is the no flow boundary at the fracture tip and equation 6.3 is the no flow boundary at the wellbore due to the casing and cementing of the well. Equation 6.4 is the no flow boundary created because of flow from the reservoir matrix into adjacent planar fracture face. Equation 6.5 is the continuity condition that specifies that the pressure at the interface between the fracture and matrix are equal and equation 6.6 is the initial condition that states that the matrix pressure is initially equal to the initial reservoir pressure. p_m is the pressure in the reservoir matrix, r_w is the wellbore radius, r_e is the external radius of the fracture equivalently the fracture half-length, z_w is the distance measured from the place of the origin in the z direction that specifies the position of the interface between the fracture and the matrix, physically it can be interpreted as the fracture width. z_e is half the distance between adjacent fractures. k_f is the fracture permeability. k_m is the matrix permeability, and p_i is the initial reservoir pressure. Equation 6.7 is the diffusivity equation for the fracture. Equations 6.8 and 6.10 are no flow boundaries at the fracture tip and the centerline of the fracture, respectively. Equation 6.9 states that the fracture pressure is equal to the wellbore pressure at the wellbore and equation 6.11 is the continuity condition that states that the fracture pressure is equal to the matrix pressure at the interface between the fracture and the matrix. Equation 6.12 is the initial condition that states that initially the fracture pressure is everywhere equal to the initial reservoir pressure.

Because only linear flow occurs in the reservoir matrix and radial flow occurs in the fracture, we proceed to integrate equation 6.1 over the radial domain and equation 6.7 over z-domain to obtain the final set of equations that describe the conceptual model as presented in Figure 6-1. The coupled set of partial differential equations is presented below. For the reservoir matrix:

$$\frac{\partial^2 \overline{p}_{mD}}{\partial z_D^2} = \frac{12(1-\omega)}{\lambda} \frac{\partial \overline{p}_{mD}}{dt_D}, \tag{6.13}$$

$$\left.\frac{\partial \overline{p}_{mD}}{\partial z_D}\right|_{z_D=1} = 0, \tag{6.14}$$

$$\overline{p}_{mD}(z_{Dw}, t_D) = p_{fD}(r_D, z_{Dw}, t_D) z_{Dw}, \tag{6.15}$$

$$\overline{p}_{mD}(z_D, 0) = 0. \tag{6.16}$$

For the fracture:

$$\frac{1}{r_D}\frac{\partial}{\partial r_D}\left[r_D \frac{\partial \overline{p}_{fD}}{\partial r_D}\right] + \frac{\lambda}{12 z_{Dw}} \left.\frac{\partial \overline{p}_{mD}}{\partial z_D}\right|_{z_D=z_{Dw}} = \omega \frac{\partial \overline{p}_{fD}}{dt},$$

(6.17)

$$\left.\frac{\partial \overline{p}_{fD}}{\partial r_D}\right|_{r_D=r_{De}} = 0\,, \tag{6.18}$$

$$\overline{p}_{fD}(r_{Dw}=1, z_D, t_D) = 1\,, \tag{6.19}$$

$$\overline{p}_{fD}\left(r_D, z_{Dw}, 0\right) = 0\,. \tag{6.20}$$

The second term in equation 6.17 is a source term that accounts for the cross flow of fluids from the reservoir matrix into the fracture. $\overline{p}_{mD}$ in equations 6.13 through to 6.16 is the area-weighted matrix pressure defined as:

$$\overline{p}_{mD}\left(z_D,t_D\right) = \frac{\int\limits_{r_D=1}^{r_D=r_{De}} p_{mD}\,dA}{\int\limits_{r_D=1}^{r_D=r_{De}} dA} = \frac{\int\limits_{r_D=1}^{r_D=r_{De}} 2\pi p_{mD} r_D dr_D}{\int\limits_{r_D=1}^{r_D=r_{De}} 2\pi r_D dr_D} \Rightarrow \int\limits_{r_D=1}^{r_D=r_{De}} 2\pi p_{mD} r_D dr_D = \overline{p}_{mD}\left(z_D,t_D\right)\int\limits_{r_D=1}^{r_D=r_{De}} 2\pi r_D dr_D\,. \tag{6.21}$$

And $\overline{p}_{fD}$ in equations 6.17 through to 6.20, is the length weighted average fracture pressure defined as:

$$\overline{p}_{fD}\left(r_D,t_D\right) = \frac{\int\limits_{z_D=0}^{z_D=z_{Dw}} p_{fD}\,dz_D}{\int\limits_{z_D=0}^{z_D=z_{Dw}} dz_D} = \frac{\int\limits_{z_D=0}^{z_D=z_{Dw}} p_{fD}\,dz_D}{\int\limits_{z_D=0}^{z_D=z_{Dw}} dz_D} \Rightarrow \int\limits_{z_D=0}^{z_D=z_{Dw}} p_{fD}\,dz_D = \overline{p}_{fD}\left(r_D,t_D\right)\int\limits_{z_D=0}^{z_D=z_{Dw}} dz_D\,. \tag{6.22}$$

The solution to the mathematical model defined by equations 6.13 through to 6.20 is obtained by using Laplace transforms method (Kreyzsig, 2006; Carslaw and Jaeger, 1959; Churchill, 1958) and it is shown below:

$$\overline{\overline{p}}_{fD}\left(r_D,\mathrm{s}\right) = \frac{k_1(r_{De}\sqrt{sf(s)})I_o(r_D\sqrt{sf(s)}) + k_o(r_D\sqrt{sf(s)})I_1(r_{De}\sqrt{sf(s)})}{s\left[k_1(r_{De}\sqrt{sf(s)})I_o(\sqrt{sf(s)}) + k_o(\sqrt{sf(s)})I_1(r_{De}\sqrt{sf(s)})\right]}, \tag{6.23}$$

where,

$$f(s) = \omega + \sqrt{\frac{\lambda(1-\omega)}{12s}} \tanh\left[\sqrt{\frac{12(1-\omega)s}{\lambda}}(1-z_{Dw})\right]. \tag{6.24}$$

$\bar{\bar{p}}_{fD}$ is the dimensionless fracture pressure in Laplace space and $f(s)$ is the inter-porosity transfer function. In equation 6.23, I_1 is the modified Bessel function of the first kind of order one, k_1 is the modified Bessel function of the second kind of order one, I_o is the modified Bessel function of the first kind of order zero and k_o is the modified Bessel function of the second kind of order zero (Karman and Biot, 1940; Abramowitz and Stegun, 1964). We derive the dimensionless rate equation in Laplace space from equation 6.23 by differentiating it with respect to r_D and evaluating the value of the derivative at the wellbore, that is, $\bar{\bar{q}}_D(s) = \left.\frac{d\bar{\bar{p}}_{fD}}{dr_D}\right|_{r_D=1}$. The dimensionless rate equation (in Laplace space) is obtained to be:

$$\bar{\bar{q}}_D(s) = \sqrt{\frac{f(s)}{s}} \frac{\left[k_1(r_{De}\sqrt{sf(s)})I_1(\sqrt{sf(s)}) - k_1(\sqrt{sf(s)})I_1(r_{De}\sqrt{sf(s)})\right]}{\left[k_1(r_{De}\sqrt{sf(s)})I_o(\sqrt{sf(s)}) + k_o(\sqrt{sf(s)})I_1(r_{De}\sqrt{sf(s)})\right]}. \tag{6.25}$$

The solution in equation 6.25 is identical to the solution presented by Da Prat (1981) when skin and wellbore storage is set equal to zero. The solution presented by Da Prat (1981) assumed a pseudo steady state fluid transfer between the matrix and fracture. In this study we used an unsteady state fluid transfer function between the fracture and the reservoir matrix. This difference in assumption results in a significantly different late time approximate analytical solution. El-Banbi (1998) and Bello (2008) also presented the same solution but did not exploit it further. The work presented in this work is new because we analyze the solution in equation 6.25 in a manner that has not been done before now. There is no known analytical form of inversion for equation 6.25 into real time space; however we can invert it numerically using any one of the standard numerical inversion algorithms such as the Stehfest algorithm (Stehfest, 1970).

An approach to obtaining analytical forms of solution in real time space for equation 6.25 is to obtain approximate forms of the solution for limiting conditions. Then these simple approximate forms are inverted to obtain closed form analytical solutions in real time space. The limiting solutions are presented next.

6.1.1.1 Early Time Approximation

For large values of the argument, the following approximations can be made for the Bessel functions (Abramowitz and Stegun, 1964) in equation 6.25

$$k_o(s) \cong k_1(s) \cong \sqrt{\frac{\pi}{2s}} e^{-s}, \tag{6.26}$$

$$I_o(s) \cong I_1(s) \cong \frac{e^s}{\sqrt{2\pi s}}, \tag{6.27}$$

In Laplace space, early-time corresponds to large values of the Laplace space parameter s Bourgeois (1992). Therefore, $\lim\limits_{s \to \infty} f(s) = \omega$, ideally this is the value of $f(s)$ to use in the approximate solution but we will assume that $f(s)$ can be used as defined in equation 6.24. Substituting equations 6.26 and 6.27 in to equation 6.25 we have;

$$\overline{\overline{q}}_D(s) = \sqrt{\frac{f(s)}{s}} \frac{\left[\sqrt{\frac{\pi}{2x}} e^{-x} \frac{e^y}{\sqrt{2\pi y}} - \sqrt{\frac{\pi}{2y}} e^{-y} \frac{e^x}{\sqrt{2\pi x}} \right]}{\left[\sqrt{\frac{\pi}{2x}} e^{-x} \frac{e^y}{\sqrt{2\pi y}} + \sqrt{\frac{\pi}{2y}} e^{-y} \frac{e^x}{\sqrt{2\pi x}} \right]}, \tag{6.28}$$

where, for simplicity we have defined $x = r_{De}\sqrt{sf(s)}$ and $y = \sqrt{sf(s)}$ in equation 6.28. After simplifying equation 6.28 we obtain;

$$q_D(s) = \sqrt{\frac{f(s)}{s}} \frac{\left[e^{(y-x)} - e^{-(y-x)} \right]}{\left[e^{(y-x)} + e^{-(y-x)} \right]}. \tag{6.29}$$

According to Becker and Van Orstrand (1909) $\tanh(x) = \dfrac{e^x - e^{-x}}{e^x + e^{-x}}$, we can therefore rewrite equation 6.29 as shown below:

$$\bar{\bar{q}}_D(s) = \sqrt{\frac{f(s)}{s}} \tanh\left[\sqrt{sf(s)}(r_{De}-1)\right]. \tag{6.30}$$

Equation 6.30 is the approximate early-time solution to the problem. It has four parameters; the storativity ratio, ω; transmissibility ratio between the matrix and fracture, λ; the fracture radius, r_{De} and the fracture thickness, z_{Dw}.

6.1.1.2 Late-Time Approximation

For small values of the argument, the following approximation can be made for the Bessel functions (Abramowitz and Stegun, 1964) in equation 6.25:

$$k_o(s) \cong -\ln(s), \tag{6.31}$$

$$k_1(s) \cong \frac{1}{s}, \tag{6.32}$$

$$I_o(s) \cong 1, \tag{6.33}$$

$$I_1(s) \cong \frac{s}{2}. \tag{6.34}$$

In Laplace space, late-time corresponds to small values of the Laplace space parameter s Bourgeois (1992). Therefore, $\lim_{s\to 0} f(s) \approx 1 + (\omega - 1)z_{Dw}$, again, this is the value of $f(s)$ to use in the approximate late-time solution but we will assume that $f(s)$ can be used as defined in equation 6.24. Substituting the functions defined by equations 6.31 through to 6.34 into equation 6.25 we obtain;

$$\bar{\bar{q}}_D(s) = \sqrt{\frac{f(s)}{s}} \frac{\left[\frac{1}{x}\frac{y}{2} - \frac{x}{2}\frac{1}{y}\right]}{\left[\frac{1}{x} + \ln(y)\frac{x}{2}\right]}. \tag{6.35}$$

The definition of x and y are the same as presented in the section 6.1.1.1. Introducing the definition of x and y in to equation 6.35 and simplifying we obtain;

$$\bar{\bar{q}}_D(s) = \frac{f(s)(r_{De}^2 - 1)}{2\left[1 - \frac{r_{De}^2 sf(s)}{4}\ln(sf(s))\right]}. \tag{6.36}$$

Equation 6.36 is the late-time approximate solution.

6.1.1.3 Validation of Approximate Solutions

The approximate solutions were validated by comparing them to the widely published and validated solutions for the quadrilateral shaped fractures. The solution for a quadrilateral shaped fracture is presented below; complete details can be found in Bello (2008).

$$\bar{\bar{q}}_{D_{lin}}(s) = \sqrt{\frac{f(s)_{lin}}{s}}\tanh\left[\sqrt{sf(s)_{lin}}\right], \tag{6.37}$$

where, $f(s)_{lin} = \omega + \sqrt{\frac{\lambda(1-\omega)}{3s}}\tanh\left[\sqrt{\frac{3(1-\omega)s}{\lambda}}\right]$, $\lambda = 12\frac{k_m}{k_f}\left[\frac{x_f}{L}\right]^2$ and ω is as defined previously. The dimensionless time is defined as $t_D = \frac{k_f t}{\mu\left[(\phi c_t)_f + (\phi c_t)_m\right]x_f^2}$. Equation 6.37 is the complete (transient and pseudo-steady state) solution for the case where the fracture shape is a quadrilateral. A validation of this solution with numerical simulation can be found in Bello (2008).

6.1.1.3.1 Validation of Approximate Early-Time Solution

By comparing the solution in equation 6.37 with the early-time approximate solution (equation 6.30) for the radial fracture, these solutions are identical except for the argument of the hyperbolic tangent which has the variable y_{De} in the quadrilateral case and $(r_{De} - 1)$ in the radial case. Their inter porosity transfer function, $f(s)$, is also identical except that the argument under the square root sign in the quadratic case has a factor of 3 while the radial case has a factor of 12.

At early time (large values of Laplace space parameter, s) the inter porosity transfer function for both cases is equal to ω ($\lim_{s\to\infty} f(s) = \omega$) and the hyperbolic tangent is equal to one ($\lim_{x\to\infty} \tanh(x) = 1$). If we substitute these limiting expressions in to equations 6.37 and 6.30 we obtain:

$$\bar{\bar{q}}_{D_{lin}}(s) = \sqrt{\frac{\omega}{s}}\,, \tag{6.38}$$

$$\bar{\bar{q}}_{D}(s) = \sqrt{\frac{\omega}{s}}\,. \tag{6.39}$$

Equations 6.38 and 6.39 are the approximate early-time solutions for quadrilateral and radial cases respectively. These two equations are identical therefore we can conclude that the approximate early-time solution is validated.

6.1.1.3.2 Validation of Approximate Late-Time Solution

We validate the late-time solution the same way as the early-time solution was validated. The approximate late-time solution for the quadrilateral case is obtained from equation 6.37 by using the following approximation of the hyperbolic tangent at small values of the argument, $\tanh(x) \approx x$. Therefore the late-time approximate solution for the quadrilateral case is given as shown below:

$$\bar{\bar{q}}_{D_{lin}}(s) = f(s)_{lin} = \left[\omega + \sqrt{\frac{\lambda(1-\omega)}{3s}}\tanh\left[\sqrt{\frac{3(1-\omega)s}{\lambda}}\right]\right]. \tag{6.40}$$

We can write the argument under the square root sign in equation 6.40 as shown in equation 6.41. Equation 6.41 was obtained by substituting for the definition of the dimensionless parameters;

$$\frac{\lambda(1-\omega)}{3s} = 12\frac{k_m}{k_f}\left[\frac{x_f}{L}\right]^2 \frac{(\phi c_t)_m}{(\phi c_t)_m + (\phi c_t)_f\, 3s}\,. \tag{6.41}$$

s in equation 6.41 is the dimensionless Laplace space parameter. Bourgeois (1992) gave the relationship between the dimensionless Laplace space parameter and its dimensional form as;

$$s = \frac{s_f t}{t_D} = \alpha_t s_f \,, \tag{6.42}$$

where s_f is the dimensional Laplace variable and $\alpha_t = \frac{t}{t_D} = \frac{\mu\left[(\phi c_t)_m + (\phi c_t)_f\right] x_f^2}{k_f}$. After substituting for the dimensionless Laplace space variable in equation 6.41 it can be written as $\frac{\lambda(1-\omega)}{3s} = \frac{(\phi c_t)_m k_m}{\mu\left[(\phi c_t)_m + (\phi c_t)_f\right]^2 L^2 s_f}$. If we assume that the matrix storativity is greater than the fracture storativity, that is, $(\phi c_t)_m >> (\phi c_t)_f$ and that the fracture storativity is very small, $(\phi c_t)_f \approx 0$ then, we can approximate this expression as $\frac{k_m}{\mu(\phi c_t)_m L^2 s_f}$. We can now re-write equation 6.40 as shown below:

$$\bar{\bar{q}}_{D_{lin}}(s_f) = \frac{1}{\sqrt{\frac{\mu(\phi c_t)_m L^2 s_f}{k_m}}} \tanh\left[\sqrt{\frac{\mu(\phi c_t)_m L^2 s_f}{k_m}}\right] = \frac{1}{\sqrt{s_m}} \tanh\left[\sqrt{s_m}\right]. \tag{6.43}$$

In arriving at equation 6.43 we have used the fact that $\frac{\mu(\phi c_t)_m L^2 s_f}{k_m} = s_m$ is only a function of the matrix properties and therefore it is the dimensional form the Laplace space variable is we solved the original problem for the case where flow is from the reservoir matrix into the fracture face that is at constant pressure. Therefore s_m is the dimensionless Laplace space variable for 1D matrix flow. If we include the effect of skin, equation 6.43 would become;

$$\bar{\bar{q}}_{D_{lin}}(s_m) = \frac{\tanh\left[\sqrt{s_m}\right]}{\sqrt{s_m}\left[1 + s_{skin}\sqrt{s_m}\tanh[\sqrt{s_m}]\right]}. \tag{6.44}$$

Using the same reasoning as explained above the inter porosity transfer parameter in the radial fracture case becomes;

$$f(s_m) = \frac{\tanh\left[\sqrt{s_m}\right]}{\sqrt{s_m}}. \tag{6.45}$$

In equation 6.45, $s_m = \frac{\mu(\phi c_t)_m z_e^2 s_f}{k_m}$, where $z_e^2 \equiv L^2$. Therefore the dimensionless Laplace space parameter in the radial case is the same as that of the quadrilateral case. After substituting equation 6.45 into equation 6.36 the late-time approximate solution simplifies to;

$$\overset{=}{q}_D(s_m) = \frac{(r_{De}^2 - 1)}{2} \frac{\tanh\left[\sqrt{s_m}\right]}{\sqrt{s_m}\left[1 + g_{skin}\sqrt{s_m}\tanh\left[\sqrt{s_m}\right]\right]}, \tag{6.46}$$

where $g_{skin} = \left[-\frac{r_{De}^2}{4}\ln\left[\sqrt{s_m}\tanh\left[\sqrt{s_m}\right]\right]\right]$. By comparing equation 6.44 and 6.46 we note that $g_{skin} = s_{skin}$. g_{skin} can be interpreted as a function that accounts for the skin effect created by radial fracture. The definition of $\overset{=}{q}_D$ (dimensionless production rate) in equation 6.46 is given by $\overset{=}{q}_D = \frac{141.2 q\mu B_o z_e}{k_m r_w^2 (p_i - p_{wf})}$. If we rescale equation 6.46 by $\frac{r_{De}^2 - 1}{2}$, $\overset{=}{q}_D$ becomes $\overset{=}{q}_D = \frac{282.4 q\mu B_o z_e}{k_m\left(r_e^2 - r_w^2\right)(p_i - p_{wf})}$ then equation 6.46 simplifies to;

$$\overset{=}{q}_D(s_m) = \frac{\tanh\left[\sqrt{s_m}\right]}{\sqrt{s_m}\left[1 + g_{skin}\sqrt{s_m}\tanh\left[\sqrt{s_m}\right]\right]}. \tag{6.47}$$

If the skin effect is set equal to zero, that is $g_{skin} = s_{skin} = 0$ then the late-time approximate radial solution is equal to the quadrilateral fracture solution. The approximate late-time radial fracture solution is therefore validated.

6.1.2 Solution with Constant Rate Inner Boundary Condition

Hurst and van Everdingen (1949) presented a function in Laplace space that gives the relationship between the solution to the constant rate inner boundary condition and the constant pressure inner boundary condition. This relationship is presented in equation 6.48;

$$\overline{\overline{p}}_{wD}(s)=\frac{1}{s^2\overline{\overline{q}}_D(s)}. \tag{6.48}$$

In equation 6.48 $\overline{\overline{p}}_{wD}$ is the solution for the constant rate inner boundary condition and $\overline{\overline{q}}_D$ is the solution for the constant pressure inner boundary condition. We will derive the constant rate inner boundary condition solution from equation 6.25 by using this relationship. Substituting equation 6.25 in to equation 6.48 we obtain:

$$\overline{\overline{p}}_{wD}(s)=\frac{\left[k_1(r_{De}\sqrt{sf(s)})I_o(\sqrt{sf(s)})+k_o(\sqrt{sf(s)})I_1(r_{De}\sqrt{sf(s)})\right]}{s^{\frac{3}{2}}\sqrt{f(s)}\left[k_1(r_{De}\sqrt{sf(s)})I_1(\sqrt{sf(s)})-k_1(\sqrt{sf(s)})I_1(r_{De}\sqrt{sf(s)})\right]}. \tag{6.49}$$

6.1.2.1 Approximate Early-Time Solution

Applying the same approximations that were used earlier we obtain the early-time approximate solution for the constant rate as shown below:

$$\overline{\overline{p}}_{wf_D}(s)=\frac{\coth\left[\sqrt{sf(s)}(r_{De}-1)\right]}{s\sqrt{sf(s)}}. \tag{6.50}$$

6.1.2.2 Approximate Late-Time Solution

The late-time approximation is obtained as shown below:

$$\overline{\overline{p}}_{wf_D}(s)=\frac{2}{\left[r_{De}^2-1\right]sf(s)}-\frac{r_{De}^2}{2\left[r_{De}^2-1\right]}\frac{\ln\left[sf(s)\right]}{s}. \tag{6.51}$$

These solutions were developed from the solution of the constant pressure solution which was validated; therefore, we can infer that these solutions derived for the constant rate boundary condition are also valid.

6.2 Sensitivity Analysis of Model Parameters for the Constant Pressure Solution

In this section we present the result of sensitivity analysis of the model given by equations 6.30 and 6.36. The sensitivity analysis is a one-at-a-time sensitivity study where we change a single parameter at a time and leaving the other parameters at their respective values.

6.2.1 Approximate Early-Time Solution

This section presents the result of the sensitivity analysis of equation 6.30.

6.2.1.1 Effect of Storativity Ratio, ω

The effect of the storativity ratio on the producing characteristics is investigated by keeping the value of $\lambda = 10^{-12}$, $z_{Dw} = 10^{-5}$ and $r_{De} = 10^{3}$. The storativity ratio ω is then varied from 0, 10^{-1} , 10^{-3} and 1. The result of this sensitivity analysis is shown on a log-log plot of q_D vs t_D in Figure 6-2. $\omega = 1$ is a limiting condition that corresponds to the homogenous case (solid red curve in Figure 6-2). It plots as at first as a half slope which is followed by an exponential decline. $\omega = 0$ is another limiting case that can be interpreted as the fracture having an infinite conductivity, that is, no storage capacity (green curve in Figure 6-2). This curve starts with a quarter (1/4) slope and followed by a one half (1/2) slope and finally an exponential decline. The curves corresponding to $\omega = 10^{-1}$ and $\omega = 10^{-3}$ lie between these two limiting cases and exhibit two time scales where the first scale starts with a slope of one half and this is followed by an exponential decline. The second time scale starts after the end of the first time scale, and it also has starts with a slope of one half which changes into an exponential decline. ω decreases as the duration of the first time scale decreases and, at late time, all the cures converge to one curve (except the homogeneous case, $\omega = 1$). It is also noted that for small values of the storativity ratio, the exponential transition period from the fracture flow to matrix flow is absent. We can therefore conclude that the storativity ratio only affects early time flow and determines the time at which flow from the fracture (first time scale) will end.

6.2.1.2 Effect of Fracture Radius, r_{De}

The effect of the fracture radius was investigated by setting the other model parameters as follows: $\omega = 10^{-1}$, $\lambda = 10^{-12}$ and $z_{Dw} = 10^{-5}$. The fracture radius is then assigned the following values $r_{De} = 10$, 10^2 , 10^3 and 10^4. The result for this analysis is summarized in Figure 6-3. All the curves on this figure exhibit two time scales, the first time scale is because production from the fracture while second time scale is because flow from the reservoir matrix. At early time all the curves converge to a single curve with a slope of one-half. At intermediate time they begin to separate when the effect of the fracture boundary is felt. The only difference between all the cases is the length of the fracture; as a result, flow at early time is identical for all the cases but once the effect of the boundary is felt in the smallest fracture flow starts to decline exponential before it transitions to transient flow from the reservoir matrix. The larger the fracture radius the longer the transient flow period observed from the fracture. Therefore the dimensionless fracture radius affects the end of transient flow from the fracture and also determines the relative magnitude of production from the reservoir matrix; larger fracture half lengths should yield higher matrix flow as observed from Figure 6-3. It has a strong influence on the early and late time flow from the matrix.

6.2.1.3 Effect of Fracture Width, z_{Dw}

The other parameters for this analysis are assigned as follows $\omega = 10^{-1}$, $\lambda = 10^{-12}$ and $r_{De} = 10^3$. We then vary the dimensionless fracture thickness as $z_{Dw} = 0$, 10^{-3} , 2.5×10^{-1} and 1. The result for this analysis is presented in Figure 6-4. Again, all the cases exhibit two time scales which is because of flow from the fracture and reservoir matrix respectively. The case with $z_{Dw} = 1$ does not show the two time scales because it is a limiting case that physically corresponds to a homogeneous case. $z_{Dw} = 0$ is another limiting case that means that the fracture is a plane source. From Figure 6-4 we can conclude that the fracture width has little or no effect on the general producing characteristics.

6.2.1.4 Effect of Transmissibility Ratio, λ

The effect of the transmissibility ratio was investigated by setting the other model parameters as follows: $\omega = 10^{-3}$, $r_{De} = 10^{3}$ and $z_{Dw} = 10^{-5}$. The transmissibility ratio is then assigned the following values $\lambda = 10^{-12}$, 10^{-8} , 10^{-4} and 1. The result for this analysis is summarized in Figure 6-5. Again, all the curves on this figure exhibit two time scales, the first time scale is due to production from the fracture while second time scale is due to flow from the reservoir matrix. At early time all the curves converge to a single curve with a slope of one-half and at intermediate time they begin to separate depending on the value of the transmissibility ratio, λ. The smallest value of λ shows two time scales that is a sequence of one half slope followed by an exponential decline, for each time scale. As the value of λ increases the exponential decline in the first time scale is replaced by a quarter slope.

6.2.2 Approximate Late Time Solution

This section presents the result of the sensitivity analysis of equation 6.36. We used the same parameters as those used for the early time approximation for the analysis presented below. The plots are also log-log plots of dimensionless rate versus dimensionless time.

6.2.2.1 Effect of Storativity Ratio, ω

The effect of the storativity ratio on the late time solution is summarized in Figure 6-6. The homogeneous limiting case (ω = 1, green curve) started out almost flat after which it transitions into a line with a slope of -2. The second limiting case (ω = 0, red curve) also started almost flat before becoming a line with a slope of -1/2. This is then followed by an exponential decline and it finally changes to a slope of -2. The other two cases in the figure show a similar behavior except that they have a somewhat exponential decline before the one-half slope. The initially flat part of the curves is the result of the skin effect which is caused by the presence of the fracture (refer to section 6.1.1.3.2). As the value of the storativity ratio decreases the skin effect decreases. It is also observed that all the curves converge to a single curve at late time. We can therefore conclude that the storativity ratio only affects early time flow, hence, it only influences the duration of the skin effect.

6.2.2.2 Effect of Fracture Radius, r_{De}

Figure 6-7 presents the results of the sensitivity analysis of the fracture radius on the producing characteristics of the approximate late time solution. All the curves in this analysis show the same general characteristic. The important points from Figure 6-7 are the fracture radius affects the end of the skin effect, the larger the fracture radius the longer the duration of the skin effect created by the presence of the fracture. Radius also has a strong effect on the early time performance of the matrix (magnitude and duration of transient flow). And the last flow period is characterized by a slope -2.

6.2.2.3 Effect of Fracture Width, z_{Dw}

Results from the sensitivity analysis of the fracture width are in Figure 6-8. All the curves in this figure have the same general characteristics except the homogeneous case ($z_{Dw} = 1$, red curve). The conclusion from this analysis is that the fracture width has little or no effect on the producing characteristics. Same as in 6.2.1.3.

6.2.2.4 Effect of Transmissibility Ratio, λ

Figure 6-9 presents the summary of the effect of the transmissibility factor. All the curves on this figure exhibit two time scales. The first time scale is because production of from the fracture while second time scale is because of flow from the reservoir matrix. At early time all the curves converge to a single flat curve that represents the effect of skin (caused by the presence of the fracture) and at intermediate time they begin to separate depending on the value of the transmissibility ratio, λ. After which they all converge to a single curve with a slope of two.

6.3 Sensitivity Analysis of Model Parameters for the Constant Rate Solution

In this section we present the result of sensitivity analysis of the constant rate solution. The sensitivity analysis performed is a one at a time sensitivity study where we change a single parameter at a time and leaving the other parameters at their respective values.

6.3.1 Approximate Early-Time Solution

This section presents the result of the sensitivity analysis of equation 6.50.

6.3.1.1 Effect of Storativity Ratio, ω

The storativity ratio ω is varied from 0, 10^{-3} , 10^{-1} and 1. The other parameters were assigned as follows $\lambda = 10^{-12}$, $z_{De} = 10^{-5}$ and $r_{De} = 10^{3}$. The result of this sensitivity analysis is shown in Figure 6-10, a log-log plot of q_D vs t_D. $\omega = 1$ is a limiting condition that corresponds to the homogenous case (solid red curve in Figure 6-10). It plots as at first as a half slope which is followed by unit slope, typical of a single porosity solution. In this case the one-half slope line indicatives transient flow in the reservoir matrix and the unit slope means the effect of the boundary has become dominant in the flow. The other limiting condition is when $\omega = 0$, this physically means that the fracture is an infinite conductivity system (with zero storage capacity). This condition is represented by the green curve in Figure 6-10. This figure starts with a one quarter slope, then a half slope and finally a unit slope. The one quarter slope indicates simultaneous transient linear flow in the fracture and reservoir matrix, the one half slope indicates transient linear flow in the reservoir matrix and the unit slope indicates boundary dominated flow. The other two cases shown in Figure 6-10 (dashed red, $\omega = 10^{-3}$ and the blue lines, $\omega = 10^{-1}$) lie within the two limiting cases. The $\omega = 10^{-3}$ case starts with transient linear flow in the fracture and then transitions to another one half slope that indicates transient linear flow in the reservoir matrix before it shows the boundary dominated unit slope. The case with $\omega = 10^{-1}$ also starts with a one half slope, fracture transient flow, then it changes to a unit slope, boundary dominated flow from the fracture then it transitions to another unit slope that represents boundary dominated flow from the reservoir matrix.

Based on the results in Figure 6-10 we can conclude that as the value of the storativity ratio increases, the behavior of the system gradually approaches that of the homogenous case.

6.3.1.2 Effect of Fracture Radius, r_{De}

The effect of the fracture radius was investigated by setting the other model parameters as follows: $\omega = 10^{-1}$, $\lambda = 10^{-12}$ and $z_{Dw} = 10^{-5}$. The fracture radius is then assigned the following values $r_{De} = 10$, 10^2 , 10^3 and 10^4. The result for this analysis is summarized in Figure 6-11. All the curves in this figure have an identical shape, they start with a slope of one half (transient linear flow in the fracture) and then it changes to a unit slope (boundary dominated flow in the fracture) before it transitions in to another unit slope (boundary dominated flow from the reservoir matrix. From this figure we can conclude that as the as the fracture radius increases the duration of the transient flow from the fracture increases.

6.3.1.3 Effect of Fracture Width, z_{Dw}

The dimensionless fracture width was varied as $z_{Dw} = 0$, 10^{-3} , 2.5×10^{-1} and 1. The other parameters for this analysis were assigned as follows $\omega = 10^{-1}$, $\lambda = 10^{-12}$ and $r_{De} = 10^3$. This result for this analysis is shown in Figure 6-12 where it can be observed that the fracture width has no significant impact on the solution.

6.3.1.4 Effect of Transmissibility Ratio, λ

The transmissibility ratio is varied as $\lambda = 10^{-12}$, 10^{-8}, 10^{-4} and 1. The other model parameters were fixed as follows: $\omega = 10^{-3}$,$r_{De} = 10^3$ and $z_{Dw} = 10^{-5}$. Figure 6-13 summarizes the result of this analysis from which we observe that the transmissibility ratio only affects the time that flow transitions from being fracture flow dominated to matrix flow dominated. For really small values of the transmissibility ratio, fracture flow is the dominant flow while for larger values; the flow is matrix flow dominant.

6.3.2 Approximate Late-Time Solution

This section presents the result of the sensitivity analysis of equation 6.51. We used the same parameters as those used for the early time approximation for the analysis presented below. The plots are also log-log plots of dimensionless rate versus dimensionless time.

6.3.2.1 Effect of Storativity Ratio, ω

The effect of the storativity ratio on the late time solution is summarized in Figure 6-14. The homogeneous limiting case (ω = 1, green curve) started out almost flat after which it transitions into a line with a slope of one. The second limiting case (ω = 0, red curve) also started almost flat then it became a line with a slope of one-half this is then followed by a slope with a unit slope. The other two cases lie between the two limiting cases. The almost flat portion of the curves is interpreted as the effect of skin created by the presence of the fracture. It is observed that as the storativity ratio increases the effect of the fracture skin on the model predictions increases.

6.3.2.2 Effect of Fracture Radius, r_{De}

Figure 6-15 presents the results of the sensitivity analysis of the fracture radius on the producing characteristics of the approximate late time solution. All the curves in this analysis show the same general characteristic. They start out with a flat portion and then transition in to a unit slope line. The larger the fracture radius the longer the duration of the skin effect created by the presence of the fracture.

6.3.2.3 Effect of Fracture Width, z_{Dw}

Results from the sensitivity analysis of the fracture width are summarized in Figure 6-16. All the curves in this figure have the same general characteristics except the homogeneous case ($z_{Dw} = 1$, red curve). The conclusion from this analysis is that the fracture width has little or no effect on the producing characteristics.

6.3.2.4 Effect of Transmissibility Ratio, λ

Figure 6-17 presents the summary of the effect of the transmissibility factor on the model forecast. The fracture skin effect is also observed in this figure and the transmissibility ratio does not appear to have a significant effect on the producing characteristics of the model.

6.4 New Skin and Storage Equations

The approximate late time solution to the diffusivity equation when the fracture is assumed to be circular and the wellbore is at a constant pressure is given as shown below:

$$q_D(s) = \frac{f(s)}{\left[1 - \frac{r_{De}^2 sf(s)}{4} \ln\left(sf(s)\right)\right]}, \tag{6.52}$$

where $f(s) = \omega + \sqrt{\frac{\lambda(1-\omega)}{12s}} \tanh\sqrt{\frac{12s(1-\omega)}{\lambda}}(1-z_{Dw})$. Equation 6.52 gives the dimensionless flow rate. Substituting for f(s) in equation 6.52 we obtain:

$$q_D(s) = \frac{\omega + \sqrt{\frac{\lambda(1-\omega)}{12s}} \tanh\sqrt{\frac{12s(1-\omega)}{\lambda}}(1-z_{Dw})}{1 - \frac{r_{De}^2}{4} \ln\left(\omega s + \sqrt{\frac{\lambda(1-\omega)s}{12}} \tanh\sqrt{\frac{12s(1-\omega)}{\lambda}}(1-z_{Dw})\right)\left[\omega s + \sqrt{\frac{\lambda(1-\omega)s}{12}} \tanh\sqrt{\frac{12s(1-\omega)}{\lambda}}(1-z_{Dw})\right]}. \tag{6.53}$$

Upon simplifying equation 6.53 we obtain:

$$q_D(s) = \frac{\omega\sqrt{\frac{12s}{\lambda(1-\omega)}} + \tanh\sqrt{\frac{12s(1-\omega)}{\lambda}}(1-z_{Dw})}{\sqrt{\frac{12s}{\lambda(1-\omega)}} - \frac{r_{De}^2}{4} \ln\left(\omega s + \sqrt{\frac{\lambda(1-\omega)s}{12}} \tanh\sqrt{\frac{12s(1-\omega)}{\lambda}}(1-z_{Dw})\right)\left[\omega\sqrt[3]{s}\sqrt{\frac{12}{\lambda(1-\omega)}} + s\tanh\sqrt{\frac{12s(1-\omega)}{\lambda}}(1-z_{Dw})\right]}. \tag{6.54}$$

The solution to the 1D diffusivity equation in linear coordinates with storage and skin is given below as:

$$q_D(s) = \frac{-C_D\sqrt{s} + \tanh\left[\sqrt{s}\right]}{\sqrt{s} + \bar{S}\left[-C_D\sqrt[3]{s} + s\tanh\left[\sqrt{s}\right]\right]}. \tag{6.55}$$

In equation 6.55 C_D and $\overline{S}$ are the dimensionless wellbore storage and skin factor, respectively. Comparing equations 5.54 and 6.55, the following expressions can be defined for the dimensionless wellbore storage and skin:

$$C_D = \omega\sqrt{\frac{12s}{\lambda(1-\omega)}}\,, \tag{6.56}$$

$$\overline{S} = -\frac{r_{De}^2}{4}\ln\left(\omega s + \sqrt{\frac{\lambda(1-\omega)s}{12}}\tanh\sqrt{\frac{12s(1-\omega)}{\lambda}}(1-z_{Dw})\right). \tag{6.57}$$

6.5 Summary and Conclusions

The conceptual model presented in this chapter is new because all existing analytical models for fractured reservoirs assume that the fracture geometry is quadrilateral in shape while in this study we have assumed a circular geometry. The resulting mathematical model is identical to those presented by Da Prat (1981) and El-bambi (1998) but the physical interpretations of the model are quite different. A thorough review of the literature also revealed that the analysis of the resulting mathematical model in the manner presented in this study has never been done before now.

The resulting mathematical model was solved using the Laplace transform method (Kreyszig, 2006) and the solutions were obtained for a constant inner boundary and a constant pressure inner boundary condition. The constant inner rate boundary condition solution was obtained from the constant pressure inner boundary condition by using the relation provided by Hurst and van Everdigen (1944). The two solutions contained a combination of Bessel functions, and the combination was such that the final solutions cannot be inverted back into real time space to obtain a closed form analytical expression. Real time solutions can be obtained by numerically inverting the solutions using a numerical inversion algorithm such as the Stehfest algorithm (Stehfest, 1970).

We derived limiting forms of the solutions for early time and late time by using the Taubarien result for Laplace space, Lake (1973) and Bourgeois (1992); and approximate representations of the Bessel functions. All the limiting solutions derived have a striking similarity to the corresponding solutions for the linear/quadrilateral fractures. However the approximate solutions presented had extra terms that provide new functional expression for skin and storage effects. The importance and utility of these expressions are presented in the next chapter. Further analysis of the solution also revealed that the late time solutions should be equal when the area per unit volume in the radial case is equal to that of the linear/quadrilateral case. When this condition is satisfied, the results are identical across the early and late time periods. This observation contradicts the results presented by Bello (2009) where it was stated that the area per unit volume should be equal for the solutions to be identical. The solution they presented only matched during the transient flow period.

In addition we performed a detailed sensitivity analysis on the approximate expressions/models to understand how the model parameters affect the producing characteristics obtained from these models.

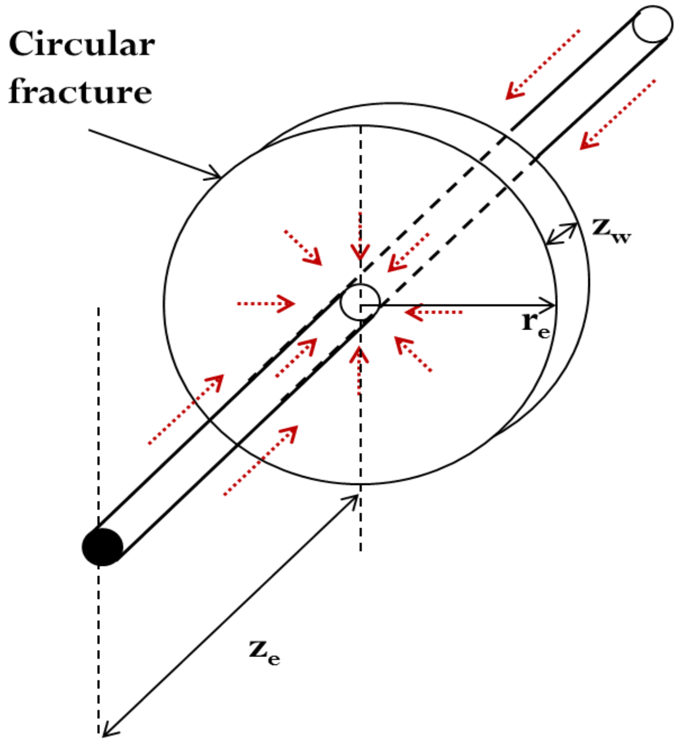

Figure 6-1: Hydraulically fractured horizontal well with a perpendicular fracture that has a circular shape

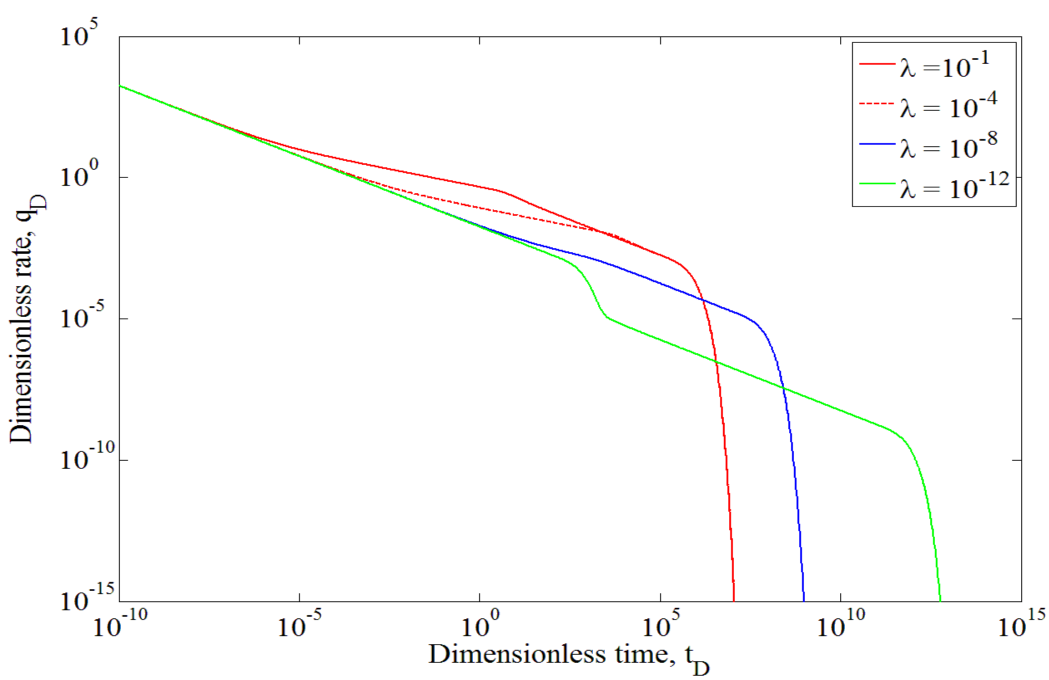

Figure 6-2: Effect of storativity ratio on the producing characteristic of a fractured horizontal well with a radial fracture geometry for the constant pressure inner boundary condition

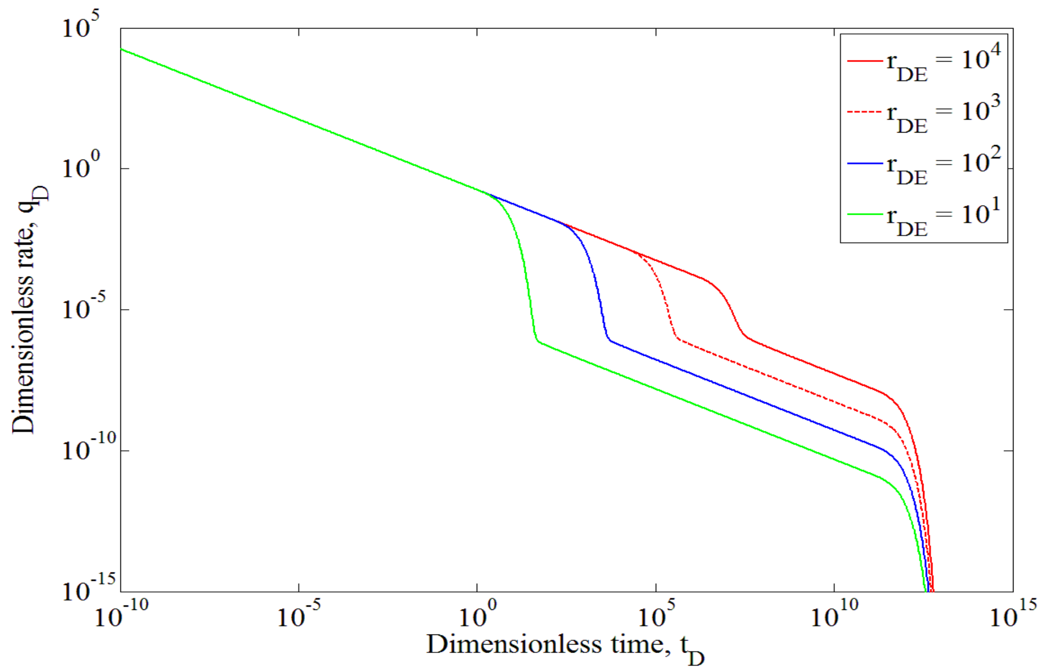

Figure 6-3: Effect of fracture radius on the producing characteristic of a fractured horizontal well with a radial fracture geometry for the constant pressure inner boundary condition

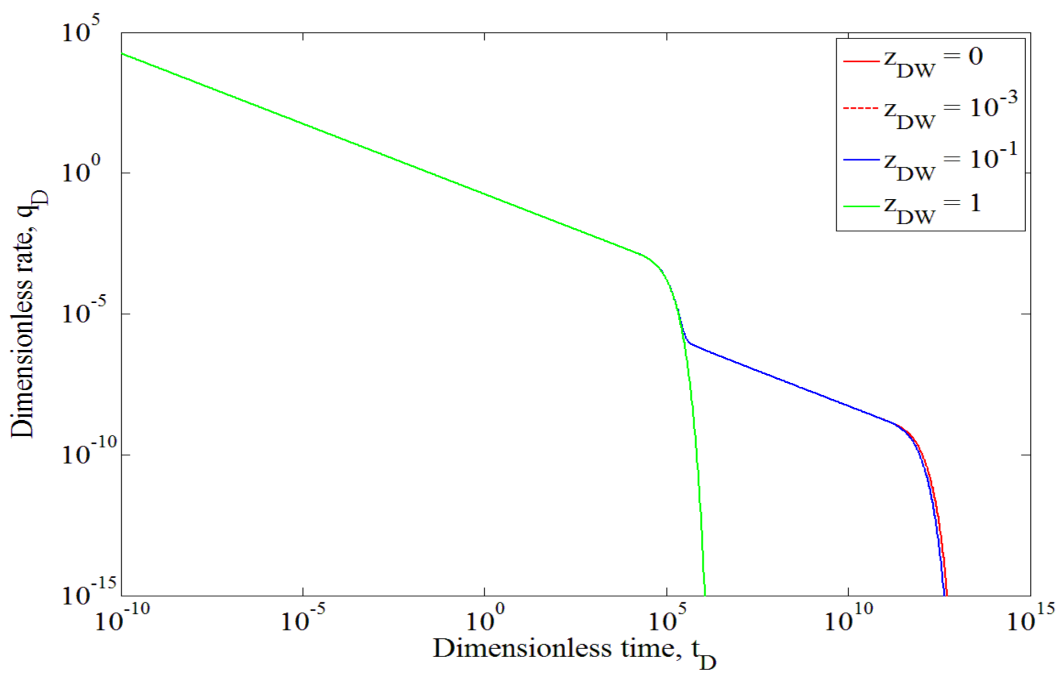

Figure 6-4: Effect of fracture width on the producing characteristics from a fractured horizontal well with a radial fracture geometry for the constant pressure inner boundary condition

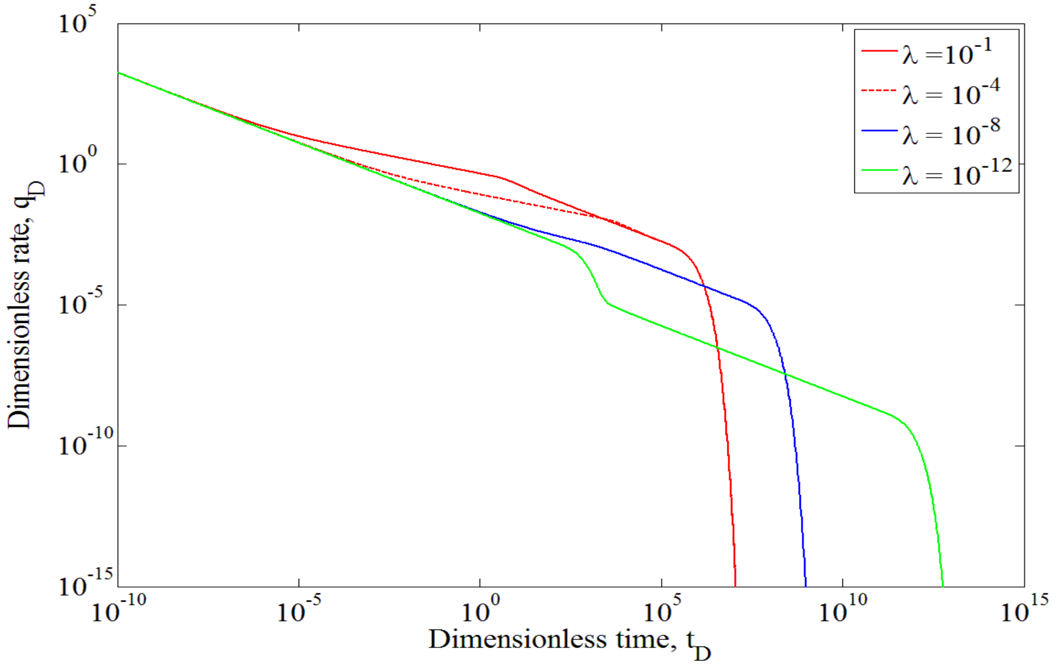

Figure 6-5: Effect of transmissibility ratio on the producing characteristics from a fractured horizontal well with a radial fracture geometry for the constant pressure inner boundary condition

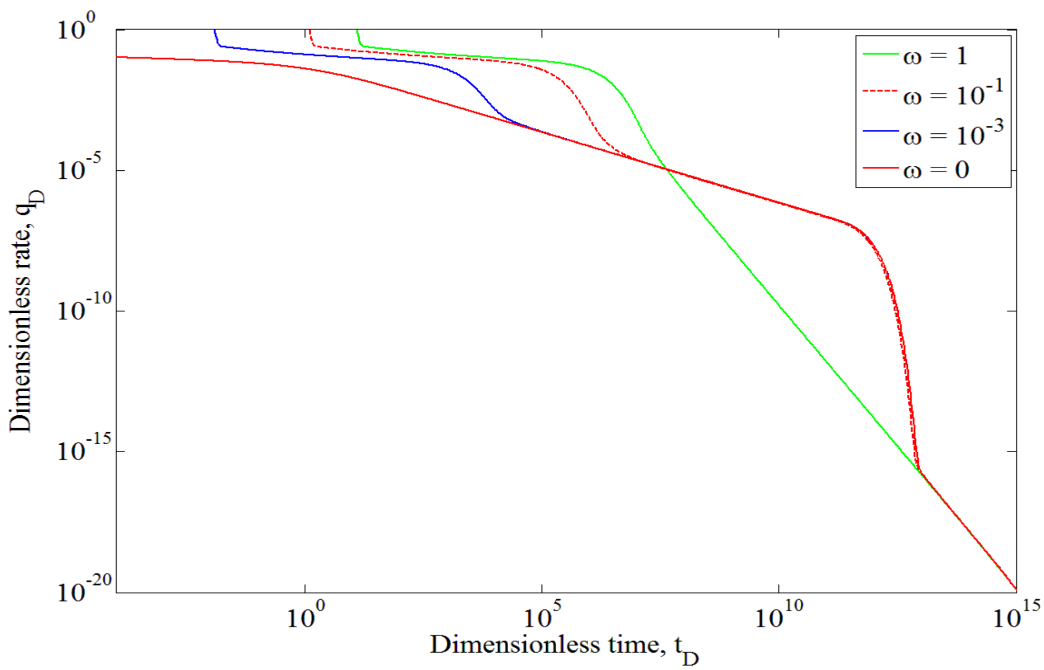

Figure 6-6: Effect of storativity ratio on the producing characteristic of the approximate late time solution for a fractured horizontal well in which the fracture geometry is radial for the constant pressure inner boundary condition

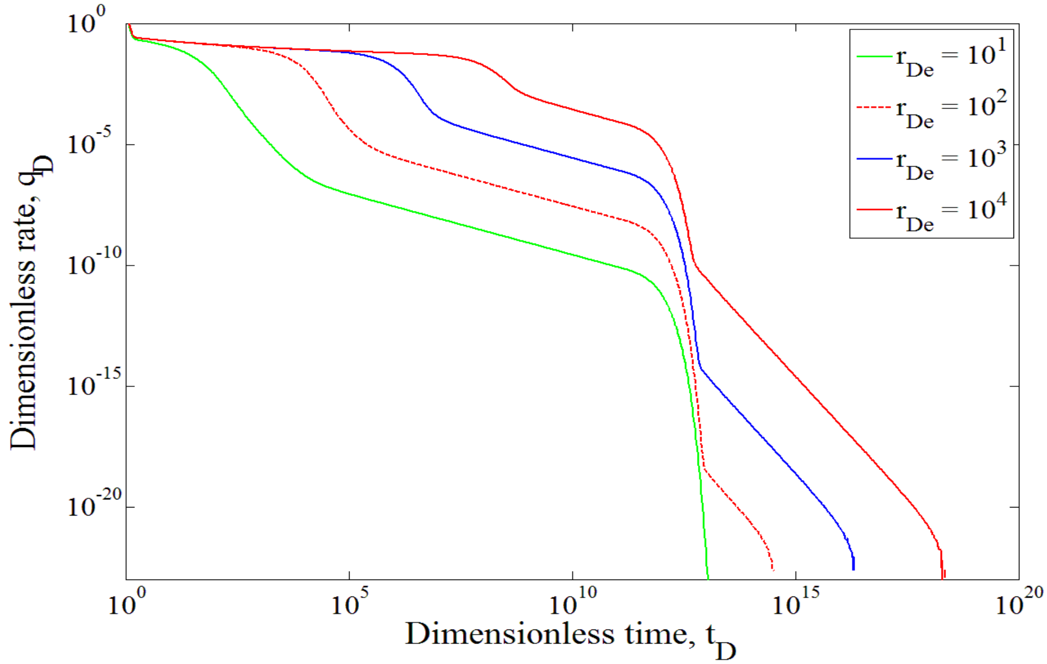

Figure 6-7: Effect of fracture radius on the producing characteristic of the approximate late time solution for a fractured horizontal well in which the fracture geometry is radial

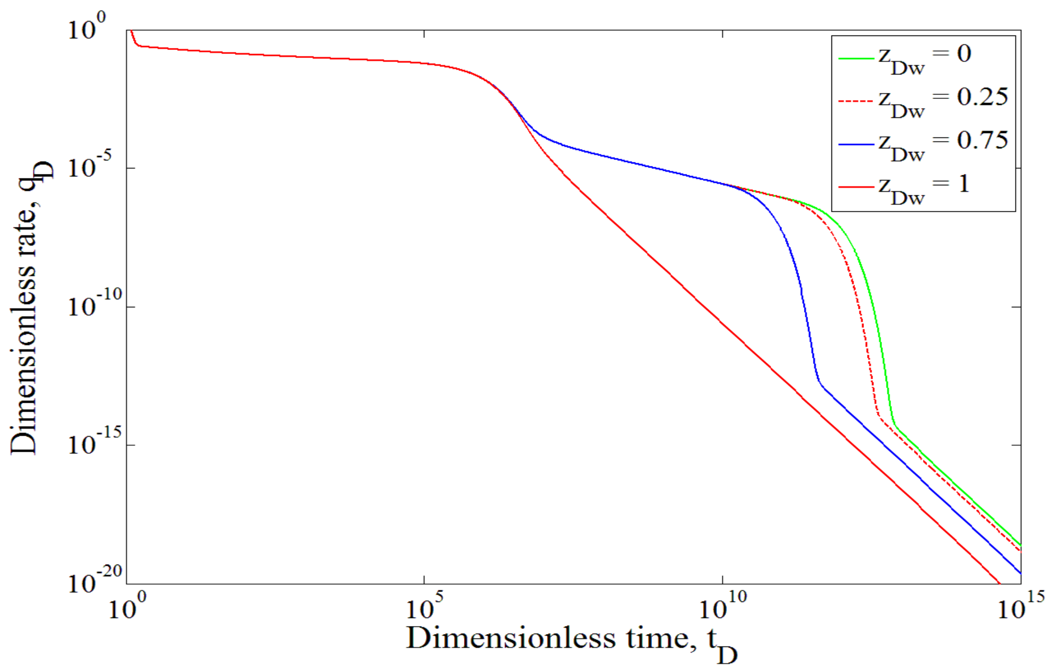

Figure 6-8: Effect of fracture width on the producing characteristic of the approximate late time solution for a fractured horizontal well in which the fracture geometry is radial for the constant pressure inner boundary condition

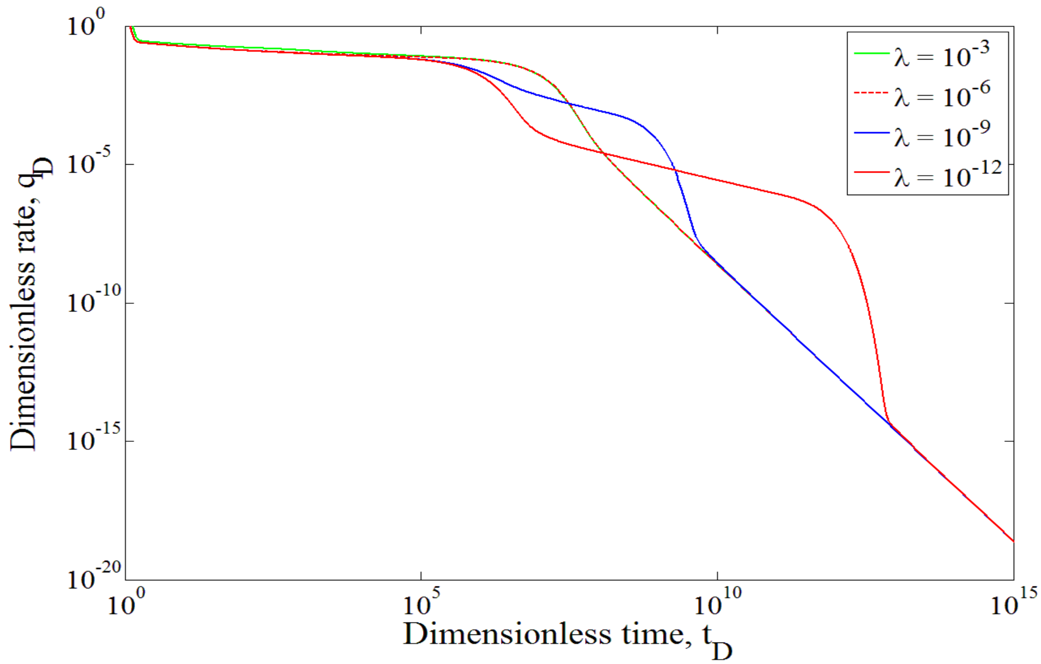

Figure 6-9: Effect of transmissibility ratio on the producing characteristic of the approximate late time solution for a fractured horizontal well in which the fracture geometry is radial for the constant pressure inner boundary condition

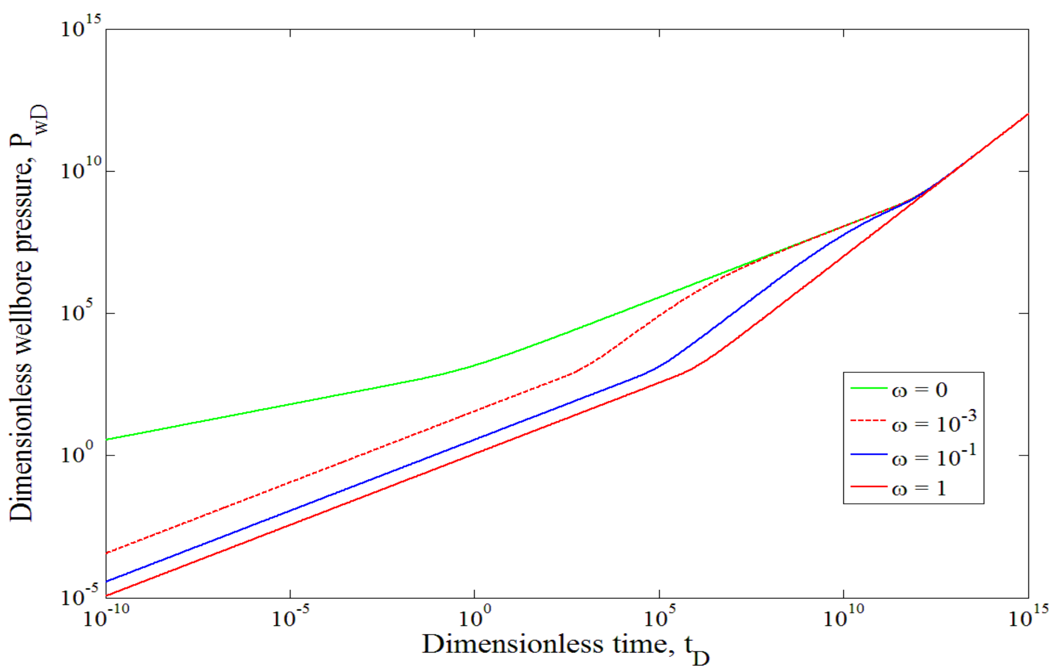

Figure 6-10: Effect of storativity ratio on the producing characteristic of the approximate early time solution for a fractured horizontal well in which the fracture geometry is radial for the constant rate inner boundary condition

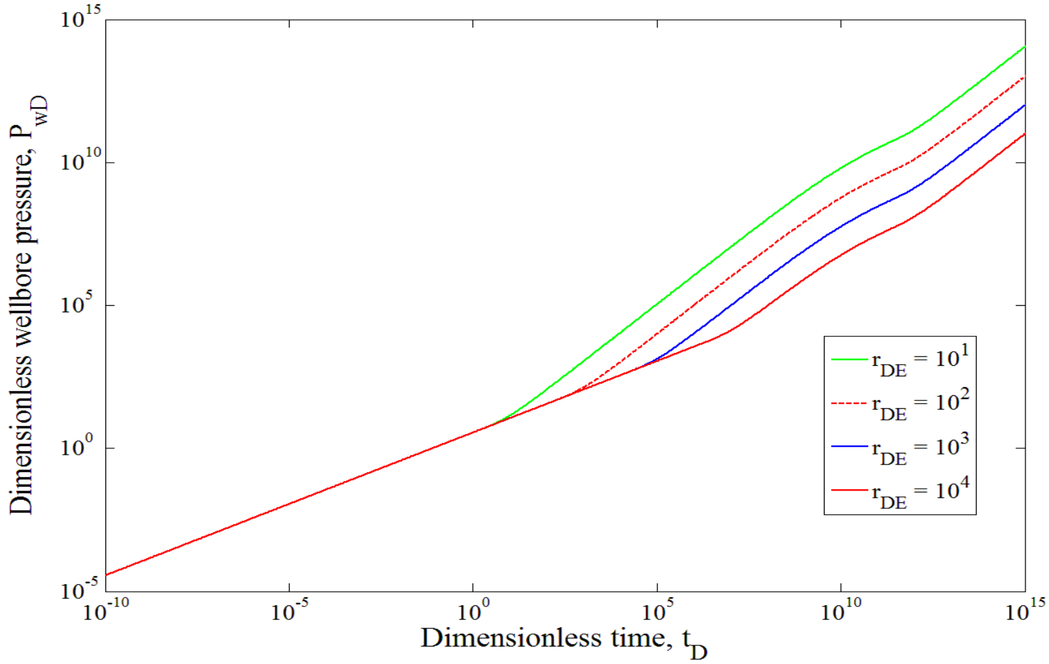

Figure 6-11: Effect of fracture radius on the producing characteristic of the approximate early time solution for a fractured horizontal well in which the fracture geometry is radial with a constant rate inner boundary condition

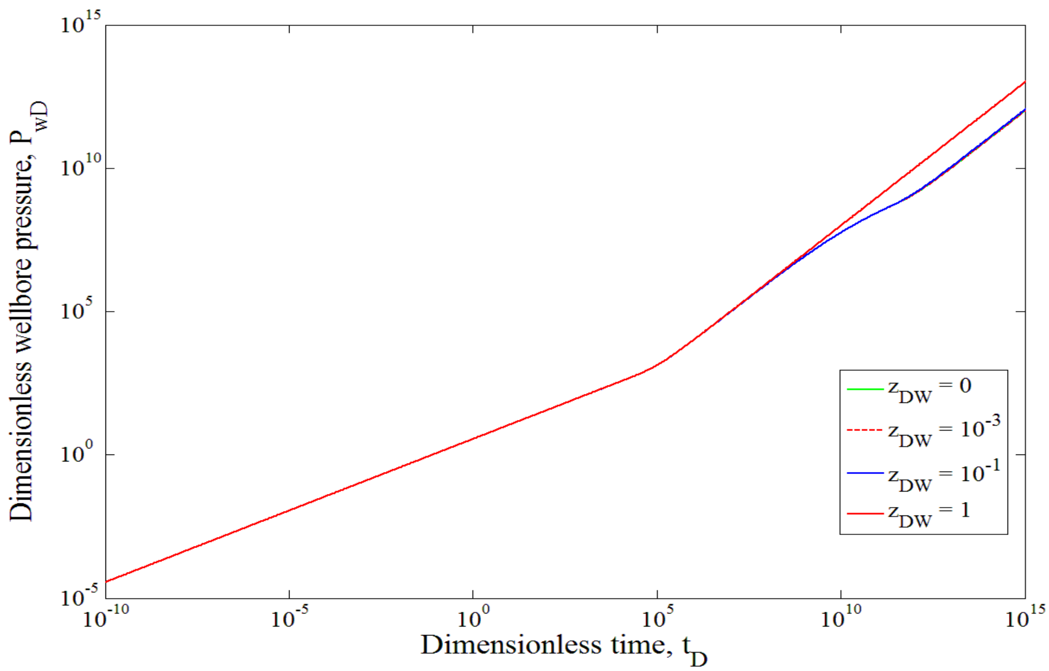

Figure 6-12: Effect of fracture thickness on the producing characteristic of the approximate early time solution for a fractured horizontal well in which the fracture geometry is radial with a constant rate inner boundary condition

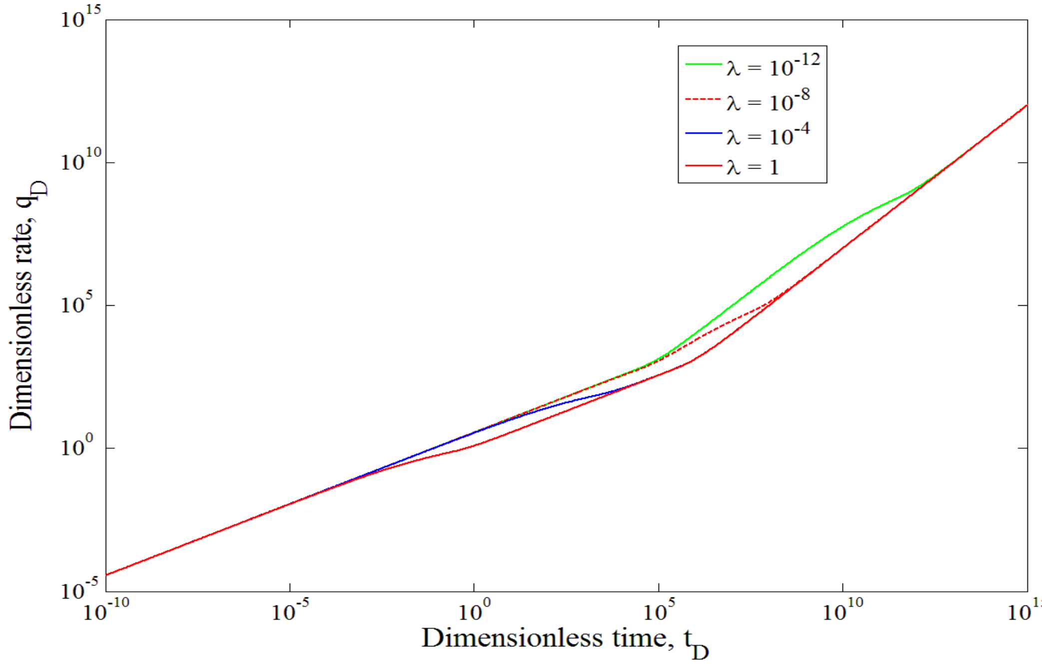

Figure 6-13: Effect of transmissibility ratio on the producing characteristic of the approximate early time solution for a fractured horizontal well in which the fracture geometry is radial with a constant rate inner boundary condition

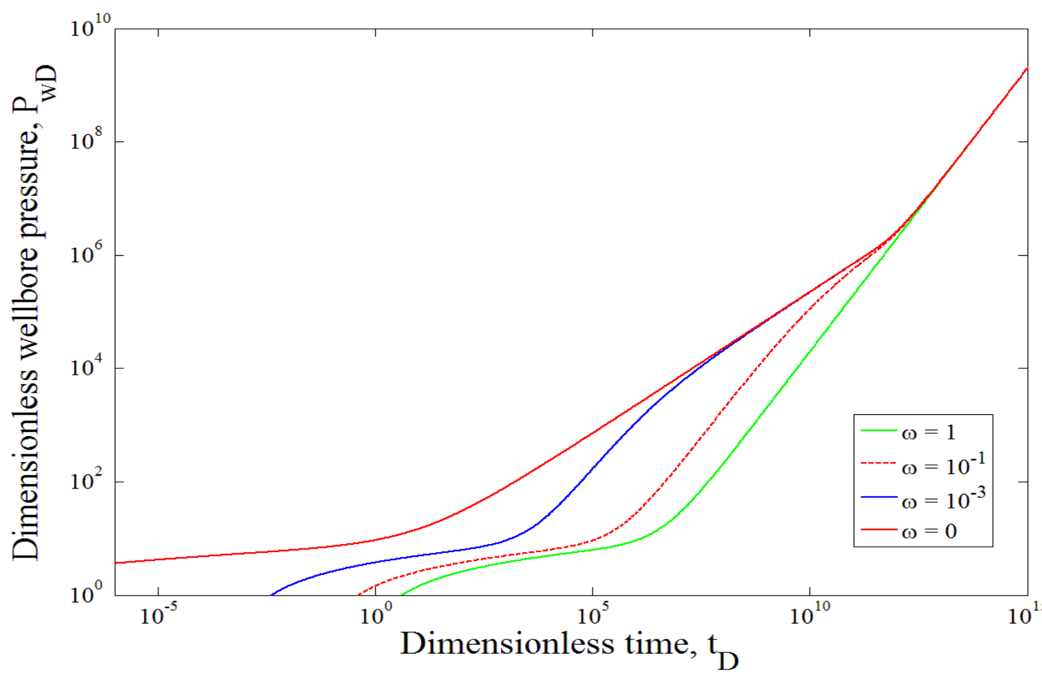

Figure 6-14: Effect of storativity ratio on the producing characteristic of the approximate late time solution for a fractured horizontal well in which the fracture geometry is radial with a constant rate inner boundary condition

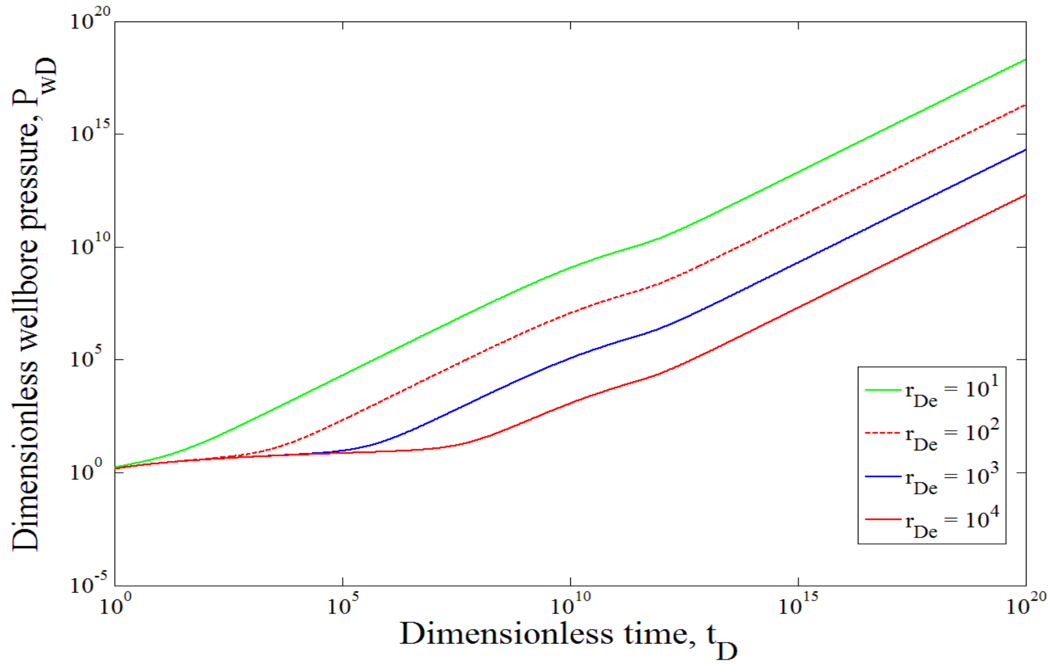

Figure 6-15: Effect of fracture radius on the producing characteristic of the approximate late time solution for a fractured horizontal well in which the fracture geometry is radial with a constant rate inner boundary condition

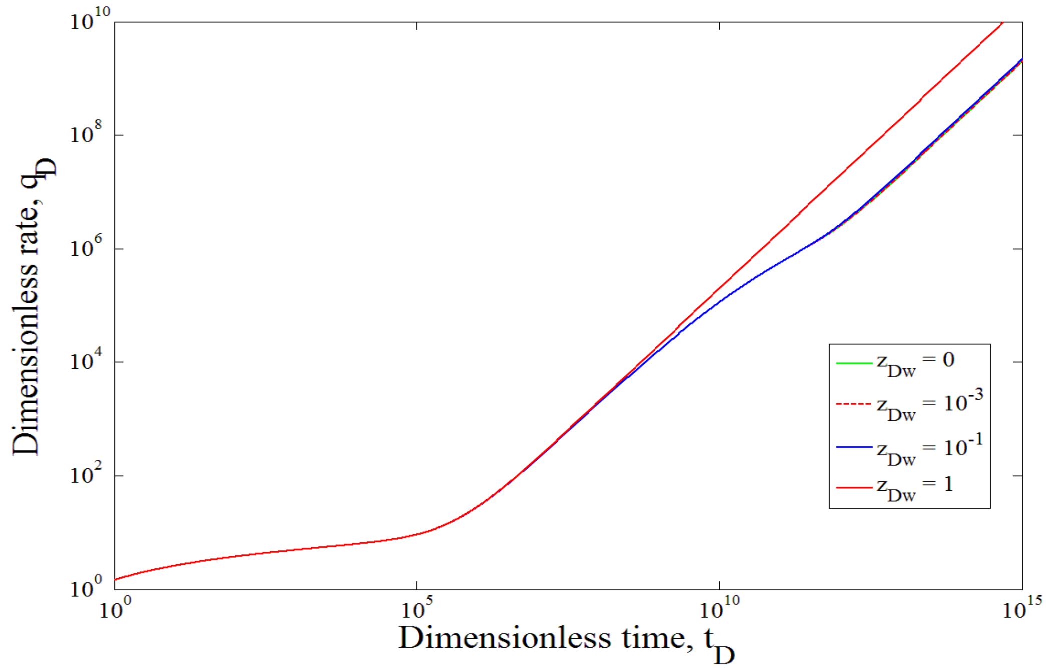

Figure 6-16: Effect of fracture thickness on the producing characteristic of the approximate late time solution for a fractured horizontal well in which the fracture geometry is radial with a constant rate inner boundary condition

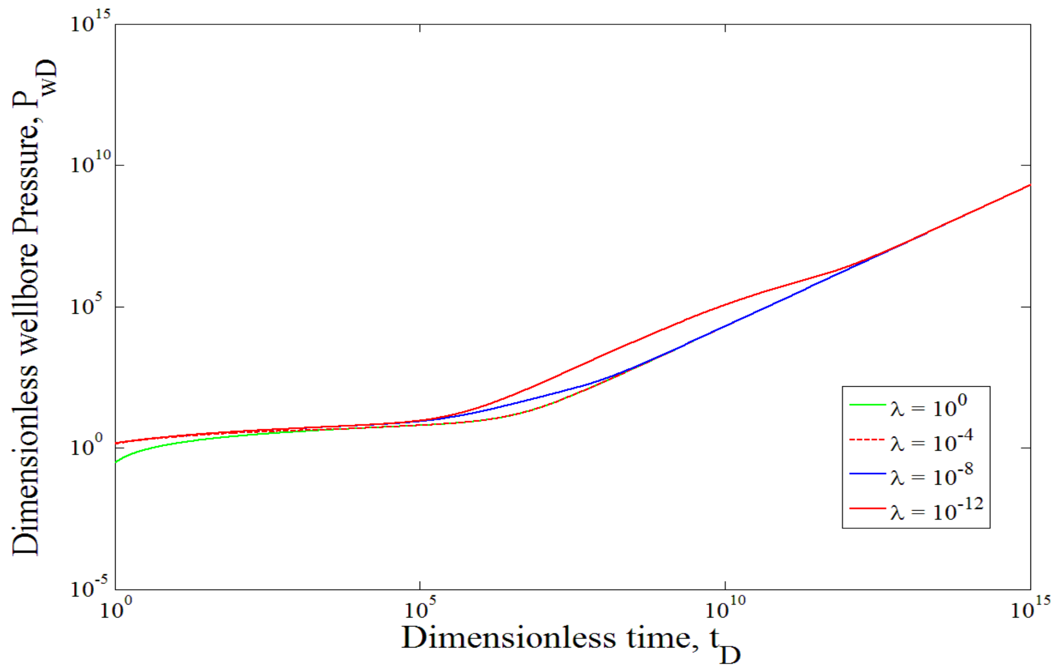

Figure 6-17: Effect of fracture thickness on the producing characteristic of the approximate late time solution for a fractured horizontal well in which the fracture geometry is radial with a constant rate inner boundary condition

Chapter 7: Modeling the Performance of Complex Hydraulic Fractures

Production data from fractured horizontal wells have been observed to plot as straight lines with a slope of negative one and half (-1/2) when plotted on a log-log graph of rate vs time. This production signature is identical to that obtained from the analytical solution to the linear diffusivity equation in which flow occurs perpendicular to a fracture face at constant pressure. Because of this observation, production data from fractured horizontal wells are typically modeled with solution to the linear diffusivity equation where it is assumed that the fracture is perpendicular to the wellbore. Hurst and van Everdingen (1945) showed that at very early time the solution of the radial diffusivity equation also plots as a straight line with a slope of -1/2 on a log-log plot of rate vs time. This observation raises the question: are there other geometries that can be used to model production from fracture horizontal wells?

In this chapter we present a fundamental solution to the three dimensional diffusivity equation and show how to use this solution in conjunction with line, surface and volume integral concept to derive an analytical solution to any fracture geometry.

7.1 Analytical Model Development

The conceptual model used in the model development is presented in Figure 7-1. The diffusivity equation for this system, the initial condition and the associated boundary conditions are given as shown below:

$$\frac{\phi\mu c_t}{k_x}\frac{\partial p}{\partial t}=\frac{\partial^2 p}{\partial x^2}+\frac{k_y}{k_x}\frac{\partial^2 p}{\partial y^2}+\frac{k_z}{k_x}\frac{\partial^2 p}{\partial z^2}+\sum_{i=1}^{N}\frac{\mu}{k_x}q_i^*\delta\left(x-x_i^{'}\right)\delta\left(y-y_i^{'}\right)\delta\left(z-z_i^{'}\right), \qquad (7.1)$$

$$p(x,y,z,0)=p_i, \qquad (7.2)$$

$$\nabla p(x,y,z,t)=0, \text{ on the boundary}. \qquad (7.3)$$

We make the following assumptions in the model development:

1. Flow is single-phase and slightly compressible,
2. Flow occurs in the reservoir isothermally.

In equation 7.1 k_x, k_y and k_z respectively are the principal values of permeability in the x, y and z directions. And q^* is the flow rate per unit volume of the source. N is the total number of point sources in the reservoir, when the reservoir only has one source then N = 1. δ is the dirac delta function (Kreyszig, 2006). x_i, y_i and z_i are the coordinate locations of the point source i. Equation 7.2 is the initial condition that states that at time t = 0, the pressure everywhere in the reservoir is equal to the initial reservoir pressure p_i and equation 7.3 is the boundary condition that states that there is no flow across the reservoir boundary. We proceed to solve this equation by the Green's function method for a point source (N = 1) to obtain (the detailed derivation of this solution is available in appendix B); the Green's function is the integrand in equation 7.4.

The definition of the dimensionless variables in equation 7.4 are given as:

$t_D = \dfrac{k_x t}{\phi \mu c_t L_x^2}$: Dimensionless time

$p_D = \dfrac{(p_i - p)k_x}{q^* \mu L_x^2}$: Dimensionless pressure

$x_D = \dfrac{x}{L_x}$: Dimensionless distance in the x direction

$y_D = \dfrac{y}{L_y}$: Dimensionless distance in the y direction

$z_D = \dfrac{z}{L_z}$: Dimensionless distance in the z direction

$\lambda_{xy} = \dfrac{k_y}{k_x}\left[\dfrac{L_x}{L_y}\right]^2$: Transmissibility ratio in the x – y direction

$\lambda_{xz} = \dfrac{k_z}{k_x}\left[\dfrac{L_x}{L_z}\right]^2$: Transmissibility ratio in the x – z direction

$$
p_D\left(x_{D,}y_{D,}z_{D,}t_D \mid x_D^{'}, y_D^{'}, z_D^{'}\right) =
$$

$$
\int_{v_D^{'}} \left[\begin{array}{l}
t_D \\
+\dfrac{2}{\pi^2}\sum_{n=1}^{\infty}\dfrac{\left[1-e^{-(n\pi)^2 t_D}\right]}{n^2} Cos(n\pi x_D)Cos(n\pi x_D^{'}) \\
+\dfrac{2}{\pi^2}\sum_{m=1}^{\infty}\dfrac{\left[1-e^{-(m\pi)^2 \lambda_{xy} t_D}\right]}{m^2\lambda_{xy}} Cos(m\pi y_D)Cos(m\pi y_D^{'}) \\
+\dfrac{2}{\pi^2}\sum_{k=1}^{\infty}\dfrac{\left[1-e^{-(k\pi)^2 \lambda_{xz} t_D}\right]}{k^2\lambda_{xz}} Cos(k\pi z_D)Cos(k\pi z_D^{'}) \\
+\dfrac{4}{\pi^2}\sum_{n=1}^{\infty}\sum_{m=1}^{\infty}\dfrac{\left[1-e^{-\left[n^2+m^2\lambda_{xy}\right]\pi^2 t_D}\right]}{n^2+m^2\lambda_{xy}} Cos(m\pi y_D)Cos(m\pi y_D^{'})Cos(n\pi x_D)Cos(n\pi x_D^{'}) \\
+\dfrac{4}{\pi^2}\sum_{k=1}^{\infty}\sum_{m=1}^{\infty}\dfrac{\left[1-e^{-\left[m^2\lambda_{xy}+k^2\lambda_{xz}\right]\pi^2 t_D}\right]}{m^2\lambda_{xy}+k^2\lambda_{xz}} Cos(m\pi y_D)Cos(m\pi y_D^{'})Cos(k\pi z_D)Cos(k\pi z_D^{'}) \\
+\dfrac{4}{\pi^2}\sum_{k=1}^{\infty}\sum_{n=1}^{\infty}\dfrac{\left[1-e^{-\left[n^2+k^2\lambda_{xz}\right]\pi^2 t_D}\right]}{n^2+k^2\lambda_{xz}} Cos(n\pi y_D)Cos(n\pi y_D^{'})Cos(k\pi z_D)Cos(k\pi z_D^{'}) \\
+\dfrac{8}{\pi^2}\sum_{k=1}^{\infty}\sum_{n=1}^{\infty}\sum_{m=1}^{\infty}\dfrac{\left[1-e^{-\left[n^2+m^2\lambda_{xy}+k^2\lambda_{xz}\right]\pi^2 t_D}\right]}{n^2+m^2\lambda_{xy}+k^2\lambda_{xz}} Cos(m\pi y_D)Cos(m\pi y_D^{'})Cos(n\pi x_D) \\
\qquad Cos(n\pi x_D^{'})Cos(k\pi z_D)Cos(k\pi z_D^{'})
\end{array}\right] dv_D^{'} \quad . \qquad (7.4)
$$

Equation 7.4 is the fundamental solution to the 3D diffusivity equation with a point source. By combing this solution with the method of line integrals, the solution to any fracture geometry can be constructed. Figure 7-2 presents the solution given by equation 7.4 for a point source located at $x_D^{'} = 0.5, y_D^{'} = 0.5$ at a t_D value of 0.2. The result in

Figure 7-2 is for a 2D case where equation 7.4 was integrated over the z-direction to obtain equation 7.5.

$$p_D(x_D, y_D, z_D, t_D : x_D^{'}, y_D^{'}) = t_D + \frac{2}{\pi^2}\sum_{n=1}^{\infty}\frac{\left[1-e^{-(n\pi)^2 t_D}\right]}{n^2}\cos(n\pi x_D^{'})\cos(n\pi x_D)$$
$$+\frac{2}{\pi^2}\sum_{m=1}^{\infty}\frac{\left[1-e^{-\lambda_{xy}(m\pi)^2 t_D}\right]}{m^2\lambda_{xy}}\cos(m\pi y_D^{'})\cos(m\pi y_D) \qquad . \qquad (7.5)$$
$$+\frac{4}{\pi^2}\sum_{m=1}^{\infty}\sum_{n=1}^{\infty}\frac{\left[1-e^{-\left[n^2+\lambda_{xy}m^2\right]\pi^2 t_D}\right]}{n^2+m^2\lambda_{xy}}\cos(m\pi y_D^{'})\cos(m\pi y_D)\cos(n\pi x_D^{'})\cos(n\pi x_D)$$

7.2 Validation of the Solution

The solution and method presented are validated by comparing the solution derived from with this method with existing standard analytical solutions. For this exercise, the solution to the 1D diffusivity equation in Cartesian coordinate (with constant rate inner boundary condition) is used for the validation. Wattenbarger et al. (1998) presented the analytical solution for this case as:

$$p_{wD}\left(x_D, t_D\right) = \frac{t_D}{2} + \frac{1}{\pi^2}\sum_{n=1}^{\infty}\frac{(-1)^n}{n^2}\left[1-e^{-n^2\pi^2 t_D}\right]\cos\left(n\pi x_D\right). \qquad (7.6)$$

The equivalent solution is derived from equation 7.4 by integrating it over the y_D and z_D direction, that is, $p_{wD} = \int_0^1\int_0^1 p_D\left(x_{D,}y_{D,}z_{D,}t_D \mid x_D^{'}, y_D^{'}, z_D^{'}\right)dy_D^{'}dz_D^{'}$. After evaluating this integral, the solution is obtained as:

$$p_D(x_D, t_D : x_D^{'}) = t_D + \frac{2}{\pi^2}\sum_{n=1}^{\infty}\frac{\left[1-e^{-n^2\pi^2 t_D}\right]}{n^2}\cos(n\pi x_D^{'})\cos(n\pi x_D). \qquad (7.7)$$

The plane source is located at $x_D^{'} = 0.5$, therefore $\cos(n\pi x_D^{'}) = \cos(\frac{n\pi}{2}) = (-1)^n$ and equation 7.7 can be re-written as:

$$p_D(x_D, t_D : 0.5) = t_D + \frac{2}{\pi^2}\sum_{n=1}^{\infty}\frac{(-1)^n}{n^2}\left[1 - e^{-n^2\pi^2 t_D}\right]\cos(n\pi x_D). \tag{7.8}$$

Equation 7.8 is the solution for the case where the fracture plane is located at the mid-section of a square/rectangular geometry while equation 7.6 is for half of the same geometry. Equation 7.8 is therefore divided by two to get the equivalent solution and it is shown below:

$$p_{wD}(x_D, t_D : x_D^{'} = 0.5) = \frac{t_D}{2} + \frac{1}{\pi^2}\sum_{n=1}^{\infty}\frac{(-1)^n}{n^2}\left[1 - e^{-n^2\pi^2 t_D}\right]\cos(n\pi x_D). \tag{7.9}$$

By comparing equation 7.6 and 7.9 it is found that they are identical hence, the fundamental solution and method is validated.

7.3 Example Solutions for Complex Fracture Geometry

This section presents example application of the solution presented above to the derivation of the solution for complex fracture geometries. The geometries considered in this section are: Planar fracture with a partial fracture length, planar fracture that intersects the wellbore at an angle of 45 degrees and a curved/circular fracture.

7.3.1 Fully Penetrating Transverse Fracture with a Partial Fracture Length

The solution for this case is obtained by integrating equation 7.4 with respect to $z_D^{'}$ from 0 to 1 (this creates a fully penetrating fracture). To obtain a partial fracture length, we integrate from $y_{D1}^{'}$ .to $y_{D2}^{'}$, that is,

$p_D(x_D, y_D, z_D, t_D : x_D^{'}, y_D^{'}, z_D^{'}) = \int_{y_{D1}^{'}}^{y_{D2}^{'}} \int_0^1 p_D(x_D, y_D, z_D, t_D : x_D^{'}, y_D^{'}) dz_D^{'} dy_D^{'}$. The solution obtained is given below:

$$
\begin{aligned}
&p_D(x_D, y_D, z_D, t_D : x_D^{'}, y_D^{'}) = t_D \left[y_{D2}^{'} - y_{D1}^{'} \right] \\
&+2\sum_{n=1}^{\infty} \frac{\cos(n\pi x_D^{'})\cos(n\pi x_D)}{(n\pi)^2} \left[y_{D2}^{'} - y_{D1}^{'} \right] \left[1 - e^{-(n\pi)^2 t_D} \right] \\
&+2\sum_{m=1}^{\infty} \frac{\cos(m\pi y_D)}{\lambda_{xy}(m\pi)^3} \left[\sin(m\pi y_{D2}^{'}) - \sin(m\pi y_{D1}^{'}) \right] \left[1 - e^{-\lambda_{xy}(m\pi)^2 t_D} \right]. \\
&+4\sum_{m=1}^{\infty}\sum_{n=1}^{\infty} \frac{\cos(m\pi y_D)\cos(n\pi x_D^{'})\cos(n\pi x_D)}{m\left[n^2 + \lambda_{xy} m^2 \right]\pi^3} \left[\sin(m\pi y_{D2}^{'}) - \sin(m\pi y_{D1}^{'}) \right] \left[1 - e^{-\left[n^2 + \lambda_{xy} m^2 \right]\pi^2 t_D} \right]
\end{aligned}
\qquad (7.10)
$$

The pressure distribution given by equation 7.10 at $t_D = 0.05$ with integration limits from $y_{D1}^{'} = 0.215$ to $y_{D2}^{'} = 0.785$ is shown in Figure 7-3.

7.3.2 Planar Fracture Inclined to the Wellbore at an angle of 45 Degrees

The solution for this case is obtained by using equation 7.4 the line integral concept. Mathematically the solution is derived by evaluating the following integral

$$p_D(x_D, y_D, z_D, t_D : x_D^{'}, y_D^{'}, z_D^{'}) = \int_{x_{D1}^{'}}^{x_{D2}^{'}} \int_0^1 p_D(x_D, y_D, z_D, t_D : x_D^{'}, y_D^{'}, z_D^{'}) dz_D^{'} dS \qquad (7.11)$$

where $dS = \sqrt{1 + \left[\frac{dy_D^{'}}{dx_D^{'}} \right]^2} dx_D^{'}$. To obtain a planar fracture that is inclined at an angle of Θ to the horizontal we must have $y_D^{'} = ax_D^{'} + c$. Substituting for dS and $y_D^{'}$ in equation 7.11 and evaluating the integral we obtain:

$$
\begin{aligned}
&p_D(x_D, y_D, z_D, t_D : x_D^{'}) = t_D(x_{D2}^{'} - x_{D1}^{'})\sqrt{1+a^2} \\
&+2\sqrt{1+a^2}\sum_{n=1}^{\infty}\frac{\cos(n\pi x_D)}{(n\pi)^3}\left[\sin(n\pi x_{D2}^{'}) - \sin(n\pi x_{D1}^{'})\right]\left[1-e^{-(n\pi)^2 t_D}\right] \\
&+2\sqrt{1+a^2}\sum_{m=1}^{\infty}\frac{\cos(m\pi y_D)}{a\lambda_{xy}(m\pi)^3}\left[\sin(m\pi\left(ax_{D2}^{'}+c\right)) - \sin(m\pi\left(ax_{D1}^{'}+c\right))\right]\left[1-e^{-\lambda_{xy}(m\pi)^2 t_D}\right] \\
&+4\sum_{m=1}^{\infty}\sum_{n=1}^{\infty}\left[\begin{array}{l}\left[\dfrac{\sin(\pi\left(am-n\right)x_{D2}^{'}+mc)}{am-n}+\dfrac{\sin(\pi\left(am+n\right)x_{D2}^{'}+mc)}{am+n}\right] \\ -\left[\dfrac{\sin(\pi\left(am-n\right)x_{D1}^{'}+mc)}{am-n}+\dfrac{\sin(\pi\left(am+n\right)x_{D1}^{'}+mc)}{am+n}\right]\end{array}\right] \\
&\qquad\frac{\cos(m\pi y_D)\cos(n\pi x_D)}{\left[n^2+\lambda_{xy}m^2\right]\pi^3}\left[\sin(m\pi y_{D2}^{'}) - \sin(m\pi y_{D1}^{'})\right]\left[1-e^{-\left[n^2+\lambda_{xy}m^2\right]\pi^2 t_D}\right]
\end{aligned}
\qquad (7.12)
$$

To obtain the solution for a planar fracture inclined at an angle of 45^{o} to the horizontal wellbore, we set a = 1 and c = 0 in equation 7.12 and the integration limits are $x_D^{'} = 0.3$ and $x_D^{'} = 0.7$. The pressure distribution at t_D = 0.05 for this case is given in Figure 7-4.

7.3.3 Circular/Curved Fracture

For a circular/curved fracture, a parametric representation of a circle is applied. The parametric relationship used is given by:

$$x_D^{'} = a + r\cos(t^{'}), \qquad (7.13)$$

$$y_D^{'} = b + r\sin(t^{'}). \qquad (7.14)$$

$0 \le t^{'} \le 2\pi$. In equation 7.13 and 7.14, *a* and *b*, respectively, are the x and y coordinates for the center of the circle, *r* is the radius of the circle and *t'* is the parameter. For this parametric representation the differential arc length is given as $dS = \sqrt{\left(\frac{dx_D^{'}}{dt}\right)^2 + \left(\frac{dy_D^{'}}{dt}\right)^2}dt = rdt$. Upon substituting for $x_D^{'}$, $y_D^{'}$ and dS in equation 7.11 and evaluating we obtain:

$$
\begin{aligned}
&p_D\left(x_{D,}y_{D,}z_{D,}t_D \mid x_D^{'}, y_D^{'}, z_D^{'}\right) = t_D \int_{t_1^{'}}^{t_2^{'}} r dt^{'} \\
&+\frac{2}{\pi^2}\int_{t_1^{'}}^{t_2^{'}} \sum_{n=1}^{\infty} \frac{\left[1-e^{-(n\pi)^2 t_D}\right]}{n^2} Cos(n\pi x_D) Cos(n\pi\left(a + r\cos(\mathrm{t})\right)) r dt^{'} \\
&+\frac{2}{\pi^2}\int_{t_1^{'}}^{t_2^{'}} \sum_{m=1}^{\infty} \frac{\left[1-e^{-(m\pi)^2 \lambda_{xy} t_D}\right]}{m^2 \lambda_{xy}} Cos(m\pi y_D) Cos(m\pi\left(b + r\sin(\mathrm{t})\right)) r dt^{'} . \\
&+\frac{4}{\pi^2}\int_{t_1^{'}}^{t_2^{'}} \sum_{n=1}^{\infty}\sum_{m=1}^{\infty} \frac{\left[1-e^{-\left[n^2+m^2\lambda_{xy}\right]\pi^2 t_D}\right]}{n^2+m^2\lambda_{xy}} Cos(m\pi y_D) Cos(n\pi x_D) \\
&\qquad Cos(n\pi\left(a + r\cos(\mathrm{t})\right)) Cos(m\pi\left(b + r\sin(\mathrm{t})\right)) r dt^{'}
\end{aligned}
\tag{7.15}
$$

The result of evaluating equation 7.15 is shown in Figure 7-5, where the integration limits are $t_1^{'} = \pi$ and $t_2^{'} = 2\pi$, the center of the circle is located at $(a,b) = (0.5, 0.8)$ and the radius of the circle is 0.36.

7.3.4 Sinusoidal Fracture

In order to construct the solution for a sinusoidal fracture the relationship between the coordinates of the point source solution is given by;

$$y_D^{'} = a + b\sin(cx_D^{'}) . \tag{7.16}$$

The differential arc length is therefore $dS = \sqrt{1+\left(bc\cos(cx_D^{'})\right)^2} dx_D^{'}$ after substituting in to equation 7.11 the solution is found to be given by:

$$
\begin{aligned}
&p_D\left(x_{D,}y_{D,}z_{D,}t_D \mid x_D^{'},y_D^{'},z_D^{'}\right)=t_D\int_{x_{D1}^{'}}^{x_{D2}^{'}}\sqrt{1+\left(bc\cos(cx_D^{'})\right)^2}dx_D^{'} \\
&+\frac{2}{\pi^2}\int_{x_{D1}^{'}}^{x_{D2}^{'}}\sum_{n=1}^{\infty}\frac{\left[1-e^{-(n\pi)^2 t_D}\right]}{n^2}Cos(n\pi x_D)Cos(n\pi x_D^{'})\sqrt{1+\left(bc\cos(cx_D^{'})\right)^2}dx_D^{'} \\
&+\frac{2}{\pi^2}\int_{x_{D1}^{'}}^{x_2^{'}}\sum_{m=1}^{\infty}\frac{\left[1-e^{-(m\pi)^2\lambda_{xy}t_D}\right]}{m^2\lambda_{xy}}Cos(m\pi y_D)Cos(m\pi\left(a+b\sin(\mathrm{cx}_D^{'})\right))\sqrt{1+\left(bc\cos(cx_D^{'})\right)^2}dx_D^{'} \\
&+\frac{4}{\pi^2}\int_{x_{D1}^{'}}^{x_{D2}^{'}}\sum_{n=1}^{\infty}\sum_{m=1}^{\infty}\frac{\left[1-e^{-\left[n^2+m^2\lambda_{xy}\right]\pi^2 t_D}\right]}{n^2+m^2\lambda_{xy}}Cos(m\pi y_D)Cos(n\pi x_D) \\
&\qquad Cos(m\pi\left(a+b\sin(\mathrm{cx}_D^{'})\right))Cos(n\pi x_D^{'})\sqrt{1+\left(bc\cos(cx_D^{'})\right)^2}dx_D^{'}
\end{aligned} \quad (7.17)
$$

The pressure distribution obtained with this solution is shown in Figure 7-6. The parameters used for this solution are given as follows a = 0.5, b = 0.25 and c = 30.

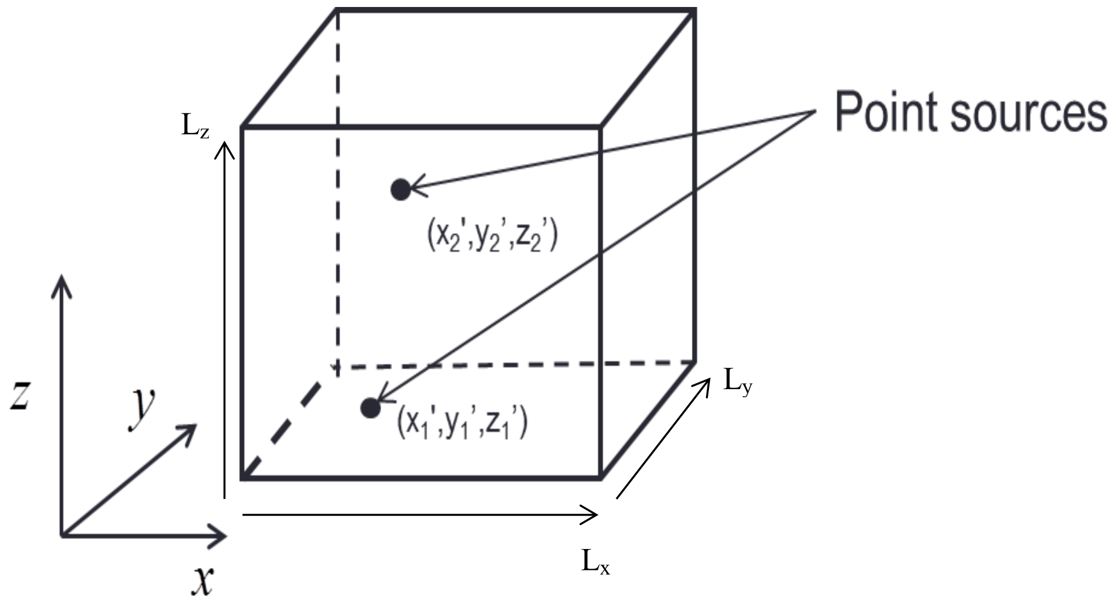

Figure 7-1: Schematic representation of a reservoir as a cube with two point sources

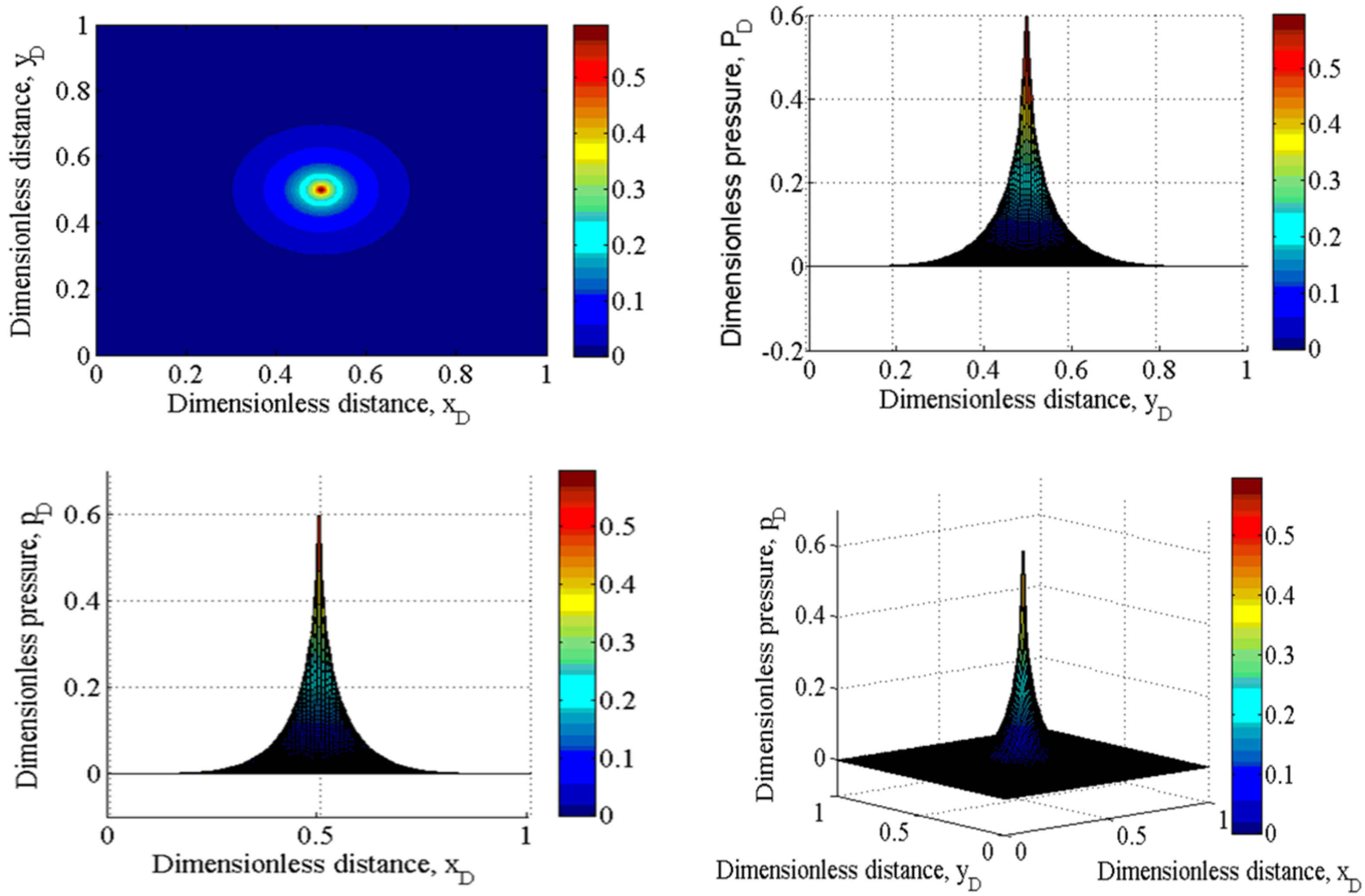

Figure 7-2: Pressure distribution created by a point source in a reservoir (t_D = 0.2) with the source located at x_D = 0.5 and y_D = 0.5

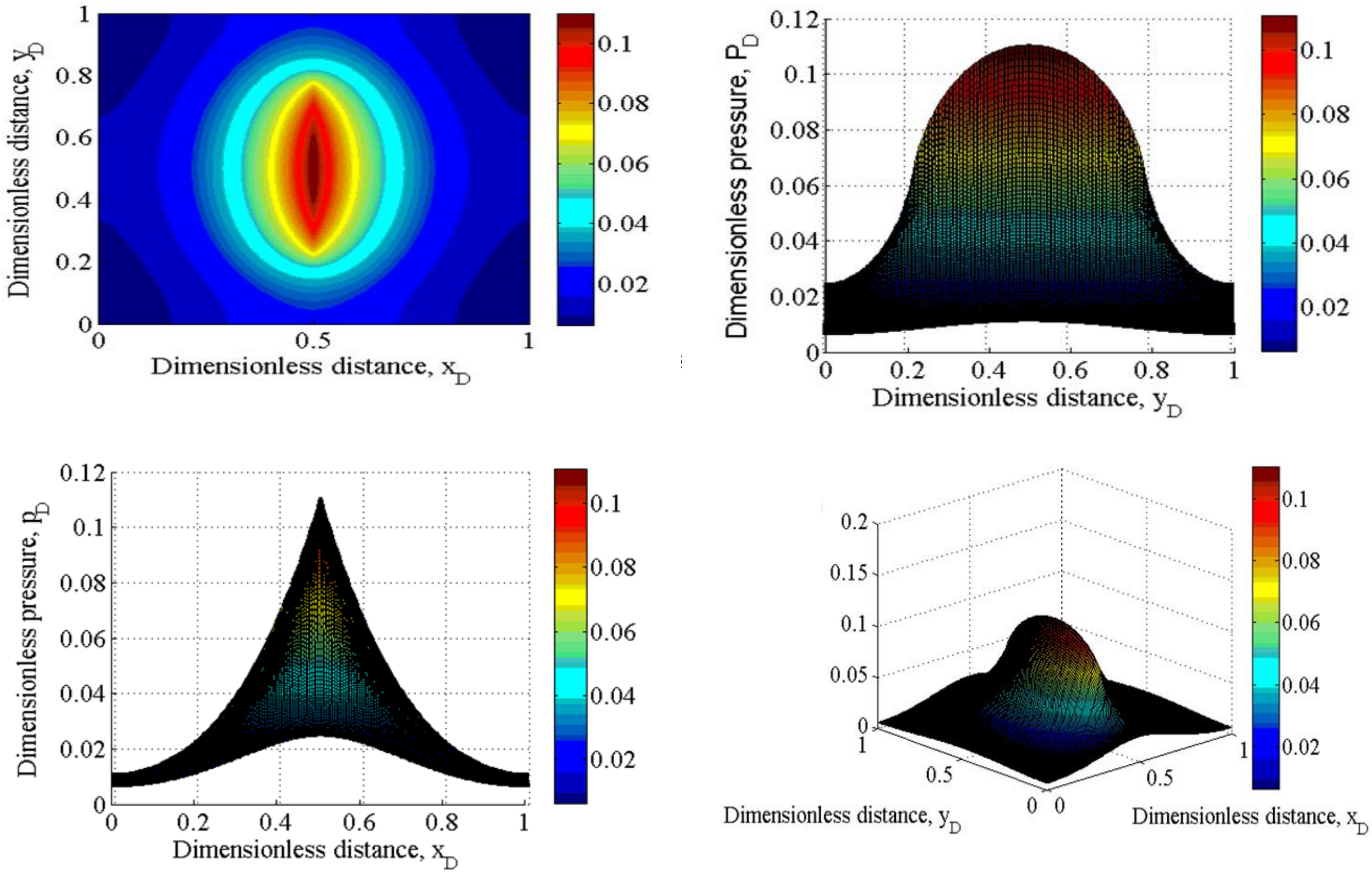

Figure 7-3: Pressure distribution at t_D = 0.05 for a fully penetrating fracture with a partial fracture length

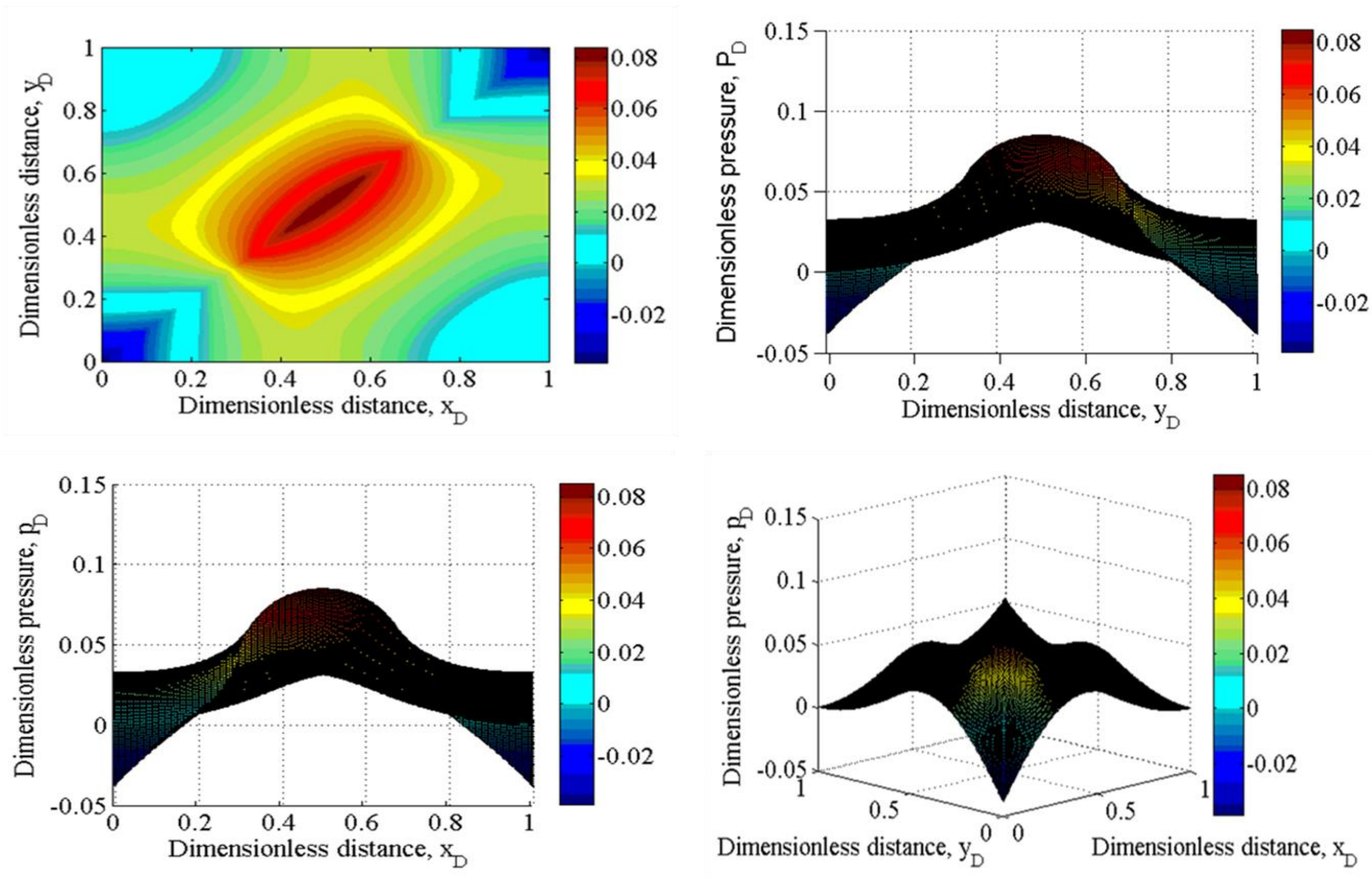

Figure 7-4: Pressure distribution at t_D = 0.05 for a fully penetrating fracture inclined at an angle of 45^o to the horizontal wellbore

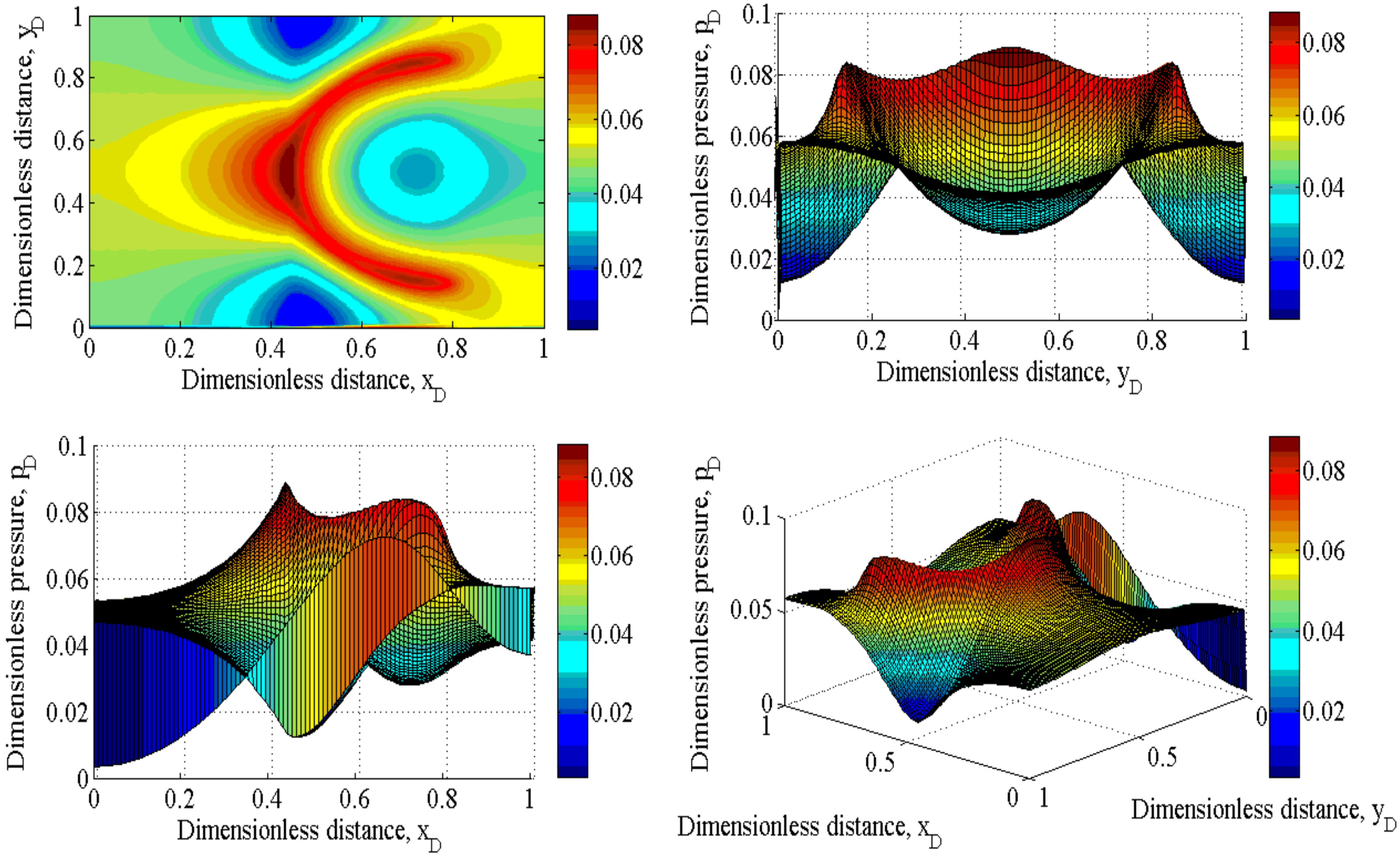

Figure 7-5: Pressure distribution at t_D = 0.05 for a circular/curved fracture

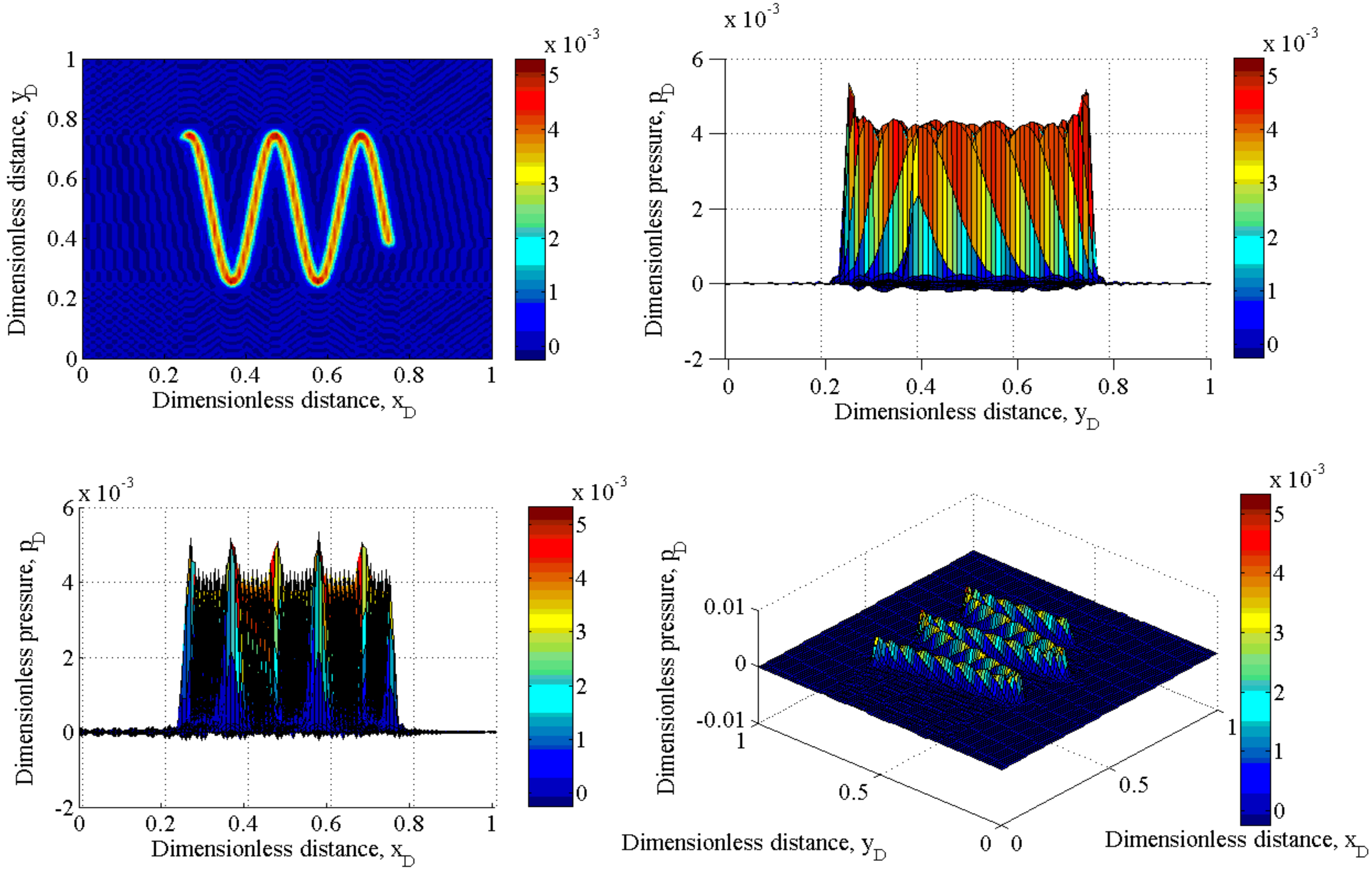

Figure 7-6: Pressure distribution at t_D = 1x10^{-4} for a sinusoidal fracture

Chapter 8: Summary, Conclusions and Recommendations for Future Work

This chapter provides a summary of the worked presented in this dissertation and the conclusions derived from the results obtained. This chapter also highlights some ideas for future work.

8.1 Summary

As stated earlier, recent advances in horizontal well drilling and hydraulic fracturing has made unconventional reservoirs economic so much so that it is projected much of the future energy demand is going to be met by production from unconventional reservoirs. Application of existing models for predicting production rate and reserves to unconventional reservoirs show that they are not accurate and result in unrealistic values of reserves (infinite values) and a lot of uncertainty in forecasts. These limitations of existing models make it difficult to make optimal field development planning decisions and can result in significant loss in project value. This dissertation developed new and simple analytical models that overcome the limitations of existing models in forecasting rate and reserves from unconventional reservoirs.

In order to achieve the main objective stated above, the following primary objectives were defined:

1. Understand the decline behavior and producing characteristics of oil wells by carefully and thoroughly analyzing production data from unconventional reservoirs to identify the predominant flow regimes and producing characteristics from these reservoirs.
2. Investigate the existence of any relationship between empirical model parameters and reservoir and/or well completion properties. The two empirical models considered in this study are the parallel flow and the logistic growth models. These two models were chosen because they have a finite upper limit when time approaches infinity, $\lim_{t\to\infty}$.
3. Develop "simple" analytical and physics based models that describe and predict the production rate performance of unconventional oil wells/reservoir. To this end, an

approximate analytical solution, in real time space, to the double porosity model was developed.

4. Verify the ability of the models developed to accurately predict the performance of unconventional wells/reservoirs with synthetic data and show their utility by applying it to field data.
5. Present new analytical models that can be used to model the performance of fractured horizontal wells with complex geometries.

8.2 Conclusions

The result obtained from this study has led to the following conclusions:

1. A detailed analysis of production data from an unconventional oil reservoir revealed that the production performance of these reservoirs are highly variable and that there are multiple time scales in the production data. Furthermore, model based analysis, revealed that the logistic growth model and parallel flow model fit the production data very well and that the parallel flow model accounts for the time scales observed in the data while the logistic growth model does not. The result of an analysis of the relationship between empirical model parameters and the reservoir/well completion properties was used to develop correlations between model parameters and reservoir/well properties. These correlations were developed with design of experiment and multivariate non-linear regression. These functions are only valid within the range that was used to develop them and any application should put this fact in consideration before use.
2. A new conceptual model for parallel flow in unconventional reservoirs and the associated mathematical model was presented and solved. The new model was shown to accurately model the decline behavior of fractured horizontal wells in unconventional reservoirs. A detailed sensitivity analysis was performed on the model from which it was determined that the storativity ratio has the greatest influence on the performance of the first time scale while the permeability ratio has the greatest effect on the performance of the second time scale.

3. An approximate analytical solution to the double porosity model, in real time space, was developed and applied to modeling production from unconventional oil reservoirs. The new solution was shown to have model parameters that are functions of the reservoir and well completion properties and it also accounts for the multiple time scales observed in field production data. It also results in finite values of reserves when time is extrapolated to infinity. Therefore, the new model overcomes the limitations of existing empirical models. It was also shown that the model parameters can be used to estimate the drainage volume of a well; with a potential application for in-fill drilling and well spacing optimization studies. The closed analytical form of the solution also makes it suitable for field development optimization studies that account for uncertainties in the reservoir/well completion properties.
4. Most solutions used to model production from fractured horizontal wells in unconventional formations assume the fractures to have a linear/quadrilateral geometry. New solutions were presented for the case where the fracture is assumed to have a circular geometry and bounded (no flow) at the external boundary with constant pressure and constant rate inner boundary conditions. These solutions were obtained with Laplace transforms method. Using special properties of these solutions and the Laplace transform space; approximate late and early-time solutions were obtained. The early-time solution obtained was identical to that obtained for the case when a linear/quadrilateral fracture geometry is assumed while the approximate late-time solution lead to the development of new analytical functions for skin and storage. A sensitivity analysis also revealed that the late-time solution produces a profile identical to that observed in field production data, especially at early time; this part of the data is usually ignored by existing models. The new skin and storage models provide a new insight into how to decouple the product of fracture half-length and the square-root of permeability.
5. Lastly, while it has been shown experimentally that hydraulic fractures have very complex shapes/geometries, all the solutions that have been presented to model production from these wells assume the fractures to have simple planar shapes/geometries. A new method was

presented to model production from fractures with complex shapes/geometries. The new method was derived by combing a fundamental solution of the diffusivity equation (obtained with Green's functions) with the method of line/surface/volume integrals. The method was shown to reproduce existing analytical solutions with simple fracture shapes/geometries and then extended to produce solutions for very complex fracture shapes/geometries.

8.3 Recommendations for future work

Below is a summary of ideas recommended for future work;

1. A simple rate-time model was developed for forecasting rate and reserves in unconventional oil reservoirs. Because this model is analytical and the parameters are functions of the reservoir/well properties and it accounts for the multiple time scales that these wells exhibit, it is ideal for use in integrated asset models (IAM) for unconventional reservoirs. IAM can be used in field development optimization studies to answer questions about the optimum well spacing, optimum number of wells and infill well location problems that account for uncertainties in input parameters/properties.
2. The capacitance resistance model (CRM) can only be applied to fields or wells that have attained stabilized flow. Some of the results presented in this work can be extend to the development of a CRM for unconventional reservoirs because it is valid for early and late time flow and across time scales.
3. A major problem in reserves forecasting from unconventional reservoirs is that it is impossible to decouple the product of fracture half-length and the square root of matrix permeability from early time production data only. One of the reasons for this is that early time production data is often assumed to be strongly affected by wellbore/fracture storage and skin effect. As a result they are not included in the analysis of production data. The result presented in chapter six gave explicit functions for storage and skin that are functions of the fracture/reservoir/well properties. These functions can be further

analyzed for the possibility of decoupling the product of fracture half-length and the square root of permeability.

4. A systematic method should be developed for analyzing flow back fluids (multiphase flow of gas, oil and water) to estimate fracture half-length and matrix permeability.
5. Processed micro-seismic data show that when horizontal wells in unconventional reservoirs are fractured, the recorded rock shear/slip events occur as discrete points in the reservoir. With this observation it might be possible to treat each point as a source. The Green function solution for multiple point sources can then be used to model the production behavior from these well/reservoirs. This might eliminate the need to explicitly define a fracture half-length when making performance predictions. A study to investigate this further might be a worthy endeavor.
6. There has been much discussion in the reservoir engineering community that the simple models (DCA models) that are being developed are unreliable because they don't account for all the mechanisms that are believed to govern flow from unconventional reservoirs. Ozkan (2010) and Bumb and McKee (1998) respectively have published results that show that these secondary physics (desorption and stress dependence of permeability/porosity) do not change the production rate profile. And existing methods in well testing cannot decouple the contribution from each secondary flow mechanism. Many studies are currently being conducted to understand how the different processes affect production but none has attempted to systematically decouple the effects of the different secondary phenomenon. A study to develop a systematic method of decoupling these effects from production data would be very useful in rate and reserves forecasting in unconventional reservoirs.
7. It has been reported that the recovery factor from unconventional reservoirs is about fifteen percent. This number is very small. Several studies have been conducted to improve the recovery factor in unconventional oil reservoirs by using the CO_2 huff and puff process. In unconventional reservoirs hydrocarbons are stored as free and adsorbed

hydrocarbons. Existing enhanced oil recovery techniques mainly target the free hydrocarbons; new methods should be developed that specifically target the adsorbed hydrocarbons.

Appendix A: Analytical Solution to the 1-D Linear Flow Problem

This appendix presents the analytical solution to the 1-D diffusivity equation in linear coordinates. The solutions presented are for a constant pressure inner boundary and the constant rate inner boundary condition where both solutions have a sealed outer boundary (inner as used here refers to the fracture face).

A.1 Constant Pressure Inner Boundary Condition

The 1-D partial differential equation (PDE) that controls flow for the conceptual model shown in Figure A-1 is given below in dimensionless form:

$$\frac{\partial^2 P_D}{\partial {x_D}^2} = \frac{\partial P_D}{\partial t_D}, \tag{A.1}$$

$$P_D(x_D, t_D = 0) = 0, \tag{A.2}$$

$$\left.\frac{\partial P_D}{\partial x_D}\right|_{x_D=0} = 0, \tag{A.3}$$

$$P_D(1, t_D) = 1, \tag{A.4}$$

where the dimensionless variables are defined as:

$$p_D = \frac{p - p_i}{p_f - p_i}, \tag{A.5}$$

$$t_D = \frac{kt}{\phi \mu c_t (x_{wf} - x_e)}, \tag{A.6}$$

$$x_D = \frac{x - x_e}{x_{wf} - x_e}. \tag{A.7}$$

Applying Laplace transforms to equation A.1, its initial condition and associated boundary conditions and it becomes an ordinary differential equation (ODE). In these set of equations the over-bar is used to represent Laplace space variable and s is the Laplace space parameter.

$$\frac{d^2 \overline{P}_D}{d{x_D}^2} = s\overline{P}_D, \tag{A.8}$$

$$\bar{P}_D\left(x_D, s=0\right)=0, \tag{A.9}$$

$$\left.\frac{d\bar{P}_D}{dx_D}\right|_{x_D=0}=0, \tag{A.10}$$

$$\bar{P}_D\left(1, s\right)=\frac{1}{s}. \tag{A.11}$$

The solution to this ODE is given by:

$$\bar{P}_D\left(x_D, s\right)=Asinh\left[x_D\sqrt{s}\right]+Bcosh\left[x_D\sqrt{s}\right]. \tag{A.12}$$

Next the boundary conditions are used to determine the constants (A and B) in this solution. Using the no-flow boundary condition; we determine A to be equal to zero.

$$\left.\frac{d\bar{P}_D(s)}{dx_D}\right|_{x_D=0}=A\sqrt{s}\,cosh\left[x_D\sqrt{s}\right]+B\sqrt{s}\,sinh\left[x_D\sqrt{s}\right]=0, \tag{A.13}$$

$\Rightarrow A=0$. From the constant pressure boundary condition, B is determine to be given by:

$$\bar{P}_D\left(1, s\right)=Bcosh\left[x_D\sqrt{s}\right]=\frac{1}{s}, \tag{A.14}$$

$\Rightarrow B=\dfrac{1}{s\,cosh\left[\sqrt{s}\right]}$. Therefore the Laplace space solution to the PDE is obtained to be:

$$\bar{P}_D=\frac{cosh\left[x_D\sqrt{s}\right]}{s\,cosh\left[\sqrt{s}\right]}. \tag{A.15}$$

From a table of inverse Laplace transforms, the real space solution to the PDE is obtained as:

$$P_D\left(x_D, t_D\right)=1+\frac{4}{\pi}\sum_{n=1}^{\infty}\frac{(-1)^n}{2n-1}e^{-\left[\left[\frac{(2n-1)\pi}{2}\right]^2 t_D\right]}cos\left[\frac{(2n-1)\pi}{2}x_D\right]. \tag{A.16}$$

This is the complete solution to the problem. It is valid during both the early time (transient) and late time (pseudo steady state) flow periods. At large values of the argument in the exponential term (late time) this solution can be approximated by keeping the first term of the solution. For early time flow, more terms of the solution would be required.

A.1.1 Derivation of an Approximate Analytical Solution for Production Rate

Using equation 6.16, the dimensionless production rate at the fracture face (x_D) is obtained as:

$$q_D\left(t_D\right)=\left.\frac{dP_D}{dx_D}\right|_{x_D=1}=-2\sum_{n=1}^{\infty}\left(-1\right)^n e^{-\left[\left[\frac{(2n-1)\pi}{2}\right]^2 t_D\right]} sin\frac{\left(2n-1\right)\pi}{2}. \tag{A.17}$$

By inspecting equation A.17, it is observed that all the terms of the series are positive. The exponential term has two coefficients $sin\frac{(2n-1)\pi}{2}$ and $(-1)^n$. For odd values of n $sin\frac{(2n-1)\pi}{2}$ is +1 (positive 1) and $(-1)^n$ is -1 (negative 1). As a result the product of these two coefficients is always negative. When the product of these two coefficients is multiplied by the negative sign outside the summation, it is realized that all the terms of this solution are always positive. This observation is made clearer in the Table A-1.

Therefore, the dimensionless production rate can be simplified as shown below in equation A.18:

$$q_D\left(t_D\right)=2\sum_{n=1}^{\infty} e^{-\left[\left[\frac{(2n-1)\pi}{2}\right]^2 t_D\right]}. \tag{A.18}$$

The infinite sum in equation A.18 is eliminated by using the Riemann integral (Abbott, 2001), which is simply approximating the discrete sum with a continuous integral. If we write the first term of equation A.18 and then let $z=\frac{(2n-1)\pi\sqrt{t_D}}{2}$ the dimensionless production rate (equation A.18) can be re-written as:

$$q_D\left(t_D\right)=2e^{-\frac{\pi^2 t_D}{4}}+\lim_{z\to\infty}2\int_{\zeta=\frac{3}{2}\pi\sqrt{t_D}}^{\zeta=z}\frac{e^{-\zeta^2}}{\pi\sqrt{t_D}}d\zeta\ . \tag{A.19}$$

After evaluating the integral in equation A.19, the dimensionless production rate can be written as:

$$q_D\left(t_D\right)=2e^{-\frac{\pi^2 t_D}{4}}+\frac{erfc\left[\frac{3}{2}\pi\sqrt{t_D}\right]}{\sqrt{\pi t_D}}. \tag{A.20}$$

The first term of this solution corresponds to the boundary dominated flow regime while the second term accounts for the early time flow regime.

This approximate solution is validated through numerical simulation. The input to the simulation model is presented in Table A-2 below

Figure A-2 shows a plot of the approximate analytical solution (equation A.20), the transient solution, pseudo steady state solution and the solution from numerical simulation. From this figure it is observed that the approximate analytical solution provides a good match to the numerical solution. It is further observed that this solution covers the early time and late time flow periods. The exact solution for the early time and late time boundary conditions are also shown on this figure. The approximate analytical solution is therefore validated.

A.1.2 Derivation of an Approximate Analytical Solution for Average Reservoir Pressure

The average reservoir pressure (volume weighted average) is defined as:

$$\overline{p}\left(t\right)=\frac{\int_v p dv}{\int_v dv}. \tag{A.21}$$

For the geometry shown in Figure A-1, $v=2x_f hx_D$ and $dv=2x_f hdx_D$. From equation A.16, the dimensionless reservoir pressure is, $P_D\left(x_D,t_D\right)=1+\frac{4}{\pi}\sum_{n=1}^{\infty}\frac{\left(-1\right)^n}{2n-1}e^{-\left[\left[\frac{(2n-1)\pi}{2}\right]^2 t_D\right]}cos\left[\frac{(2n-1)\pi}{2}x_D\right]$

Therefore,

$$\overline{p}_D\left(t_D\right)=\frac{\int_1^{x_D}1+\frac{4}{\pi}\sum_{n=1}^{\infty}\frac{\left(-1\right)^n}{2n-1}e^{-\left[\left[\frac{(2n-1)\pi}{2}\right]^2 t_D\right]}cos\left[\frac{(2n-1)\pi}{2}x_D\right]dx_D}{\int_1^{x_D}2x_f hdx_D} \tag{A.22}$$

where $\overline{p}_D$ is the dimensionless average reservoir pressure. Performing this integration results in

$$\overline{p}_D(t_D) = -\frac{\varsigma\Big|_1^{x_D}}{1-x_D} + \frac{-\frac{4}{\pi}\left[\sum_{n=1}^{\infty}\frac{(-1)^n}{(2n-1)}e^{-\frac{(2n-1)^2\pi^2 t_D}{4}}\frac{2\sin(\frac{(2n-1)\pi}{2}\varsigma)}{(2n-1)\pi}\right]\Bigg|_1^{x_D}}{1-x_D} \tag{A.23}$$

$$\overline{p}_D(t_D) = \frac{1-x_D}{1-x_D} + \frac{\frac{8}{\pi^2}\left[\sum_{n=1}^{\infty}\frac{(-1)^n}{(2n-1)^2}e^{-\frac{(2n-1)^2\pi^2 t_D}{4}}\left[\sin(\frac{(2n-1)\pi}{2}) - \sin(\frac{(2n-1)\pi x_D}{2})\right]\right]}{1-x_D}$$

(A.24)

At the outer boundary, $x_D = 0$ therefore the equation A.24 simplifies to

$$\overline{p}_D(t_D) = 1 + \frac{8}{\pi^2}\sum_{n=1}^{\infty}\frac{(-1)^n}{(2n-1)^2}e^{-\frac{(2n-1)^2\pi^2 t_D}{4}}\sin\left[\frac{(2n-1)\pi}{2}\right] \tag{A.25}$$

As with the rate equation, the terms of the infinite series are always negative therefore equation A.25 can be rewritten as

$$\overline{p}_D(t_D) = 1 - \frac{8}{\pi^2}\sum_{n=1}^{\infty}\frac{e^{-\frac{(2n-1)^2\pi^2 t_D}{4}}}{(2n-1)^2} \tag{A.26}$$

If the first term of the summation is written and we let $z = \frac{(2n-1)\pi\sqrt{t_D}}{2}$, $dz = \pi\sqrt{t_D}dn$ and $(2n-1) = \frac{2z}{\pi\sqrt{t_D}}$ equation A.26 then becomes

$$\overline{p}_D(t_D) = 1 - \frac{8}{\pi^2}\left[e^{-\frac{\pi^2 t_D}{4}} + \lim_{z\to\infty}\int_{\frac{3}{2}\pi\sqrt{t_D}}^{z}\frac{e^{-z^2}}{4z^2}\pi^2 t_D^{\frac{1}{2}}\frac{dz}{\pi\sqrt{t_D}}\right] \tag{A.27}$$

Evaluating the integral,

$$\overline{p}_D(t_D) = 1 - \frac{8}{\pi^2}\left[e^{-\frac{\pi^2 t_D}{4}} + \lim_{z\to\infty}\frac{\pi\sqrt{t_D}}{4}\left[-\sqrt{\pi}erf(\tau) - \frac{e^{-\tau^2}}{\tau}\right]\Bigg|_{\frac{3}{2}\pi\sqrt{t_D}}^{z}\right] \tag{A.28}$$

After evaluating the limits equation A.28 simplifies to

$$\overline{p}_D\left(t_D\right)=1-\frac{8}{\pi^2}\left[e^{-\frac{\pi^2 t_D}{4}}+\frac{e^{-\frac{9}{4}\pi^2 t_D}}{6}-\frac{\sqrt{\pi^3 t_D}}{4}erfc\left[\frac{3}{2}\pi\sqrt{t_D}\right]\right] \tag{A.29}$$

Equation A.29 is the average dimensionless pressure in the reservoir for a constant pressure inner boundary condition for linear flow in 1D.

A.2 Constant Rate Inner Boundary Condition

The solution for the constant rate inner boundary condition can be obtained from the constant pressure inner boundary condition by using the identity provided by Hurst and van Everdigen (1949). This relation is shown below. It is only valid in Laplace space.

$$\overline{q}_D\left(s\right)=\frac{1}{s^2\overline{p}_{wD}\left(s\right)} \tag{A.30}$$

$\overline{q}_D$ is the constant pressure solution and $\overline{p}_{wD}$ is the constant rate solution. From equation A.15 the dimensionless production rate in Laplace space is obtained as shown below:

$$\overline{q}_D\left(s\right)=\left.\frac{d\overline{p}_D}{dx}\right|_{x_D=1}=\frac{\tanh\left[\sqrt{s}\right]}{\sqrt{s}}$$

Therefore, the constant rate solution at the wellbore is obtained as shown below:

$$\overline{p}_{wD}\left(s\right)=\frac{\coth\left[\sqrt{s}\right]}{s\sqrt{s}} \tag{A.31}$$

Equation A.31 can be inverted back to real space by using the convolution property of Laplace transforms to obtain

$$p_{wD}\left(t_D\right)=\frac{t_D}{2}+\frac{1}{\pi^2}\sum_{n=1}^{\infty}\frac{\left(-1\right)^n}{n^2}(1-e^{-n^2\pi^2 t_D})\cos\left[n\pi\right] \tag{A.32}$$

Next the infinite sum in equation A.32 is eliminated. Using the same argument as explained in Table A-1 equation A.32 can be re-written as

$$p_{wD}\left(t_D\right)=\frac{t_D}{2}+\frac{1}{\pi^2}\sum_{n=1}^{\infty}\frac{(1-e^{-n^2\pi^2 t_D})}{n^2} \tag{A.33}$$

The infinite sum is eliminated by approximating it by using a Riemann integral. Let $z=n\pi\sqrt{t_D}$, $dz=\pi\sqrt{t_D}dn$, $n=\dfrac{z}{\pi\sqrt{t_D}}$ and $n=\dfrac{z^2}{\pi^2 t_D}$

Then the solution becomes

$$p_{wD}\left(t_D\right)\approx\frac{t_D}{2}+\frac{1}{\pi^2}\lim_{z\to\infty}\int_{n=1}^{z}\frac{\left[1-e^{-n^2\pi^2 t_D}\right]}{n^2}dn$$

$$\approx\frac{t_D}{2}+\frac{1}{\pi^2}\lim_{z\to\infty}\left[\int_{n=1}^{z}\frac{d\xi}{\xi^2}-\int_{n=1}^{z}\frac{e^{-\xi^2\pi^2 t_D}}{\xi^2}\right]d\xi$$

$$\approx\frac{t_D}{2}+\lim_{z\to\infty}\left[\frac{\sqrt{t_D}}{\pi}\left[-\frac{1}{\xi}\right]\Bigg|_{\pi\sqrt{t_D}}^{z}+\frac{\sqrt{t_D}}{\pi}\left[\sqrt{\pi}erf\left[\xi\right]+\frac{e^{-\xi^2}}{\xi}\right]\Bigg|_{\pi\sqrt{t_D}}^{z}\right]$$

$$\approx\frac{t_D}{2}+\lim_{z\to\infty}\left[\frac{\sqrt{t_D}}{\pi}\left[\frac{1}{\pi\sqrt{t_D}}-\frac{1}{z}\right]+\frac{\sqrt{t_D}}{\pi}\left[\sqrt{\pi}erf\left[z\right]+\frac{e^{-z^2}}{z}-\sqrt{\pi}erf\left[\pi\sqrt{t_D}\right]-\frac{e^{-\pi^2 t_D}}{\pi\sqrt{t_D}}\right]\right]$$

Taking the limit as z tends to infinity, the expression simplifies to

$$\approx\frac{t_D}{2}+\frac{1}{\pi^2}+\sqrt{\frac{t_D}{\pi}}erfc\left[\pi\sqrt{t_D}\right]-\frac{e^{-\pi^2 t_D}}{\pi^2}$$

This can be further simplified to give the complete approximate solution as

$$\approx\frac{t_D}{2}+\frac{\left[1-e^{-\pi^2 t_D}\right]}{\pi^2}+\sqrt{\frac{t_D}{\pi}}erfc\left[\pi\sqrt{t_D}\right] \tag{A.34}$$

Table A-1: Summary of coefficients in the series solution of the dimensionless flow rate for n = 1 to 5

n	$(-1)^n$	$\mathrm{Sin}((2n-1)\pi/2)$	$(-1)^n \times \mathrm{Sin}((2n-1)\pi/2)$	$-1 \times (-1)^n \times \mathrm{Sin}((2n-1)\pi/2)$
1	-1	1	-1	1
2	1	-1	-1	1
3	-1	1	-1	1
4	1	-1	-1	1
5	-1	1	-1	1

Table A-2: Numerical reservoir simulation input for the validation of approximate analytical solution to 1D flow problem

Simulator Input	Value
k (md)	25
x_f (ft)	275
φ	0.3
μ (cp)	2
c_t (psi^{-1})	2.9E-5
L (ft)	2500
P_{wf} (psi)	1000
P_i (psi)	5300
h (ft)	50

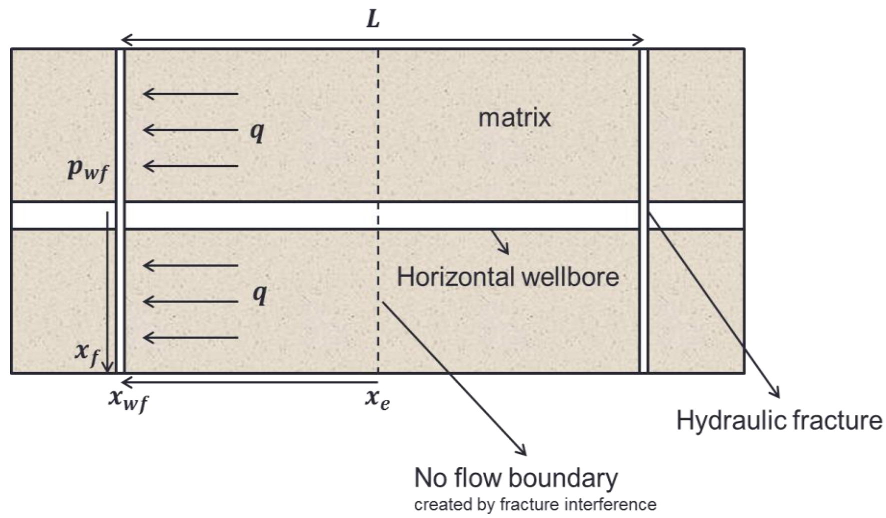

Figure A-1: Schematic diagram of a horizontal wellbore with planar hydraulic fracture

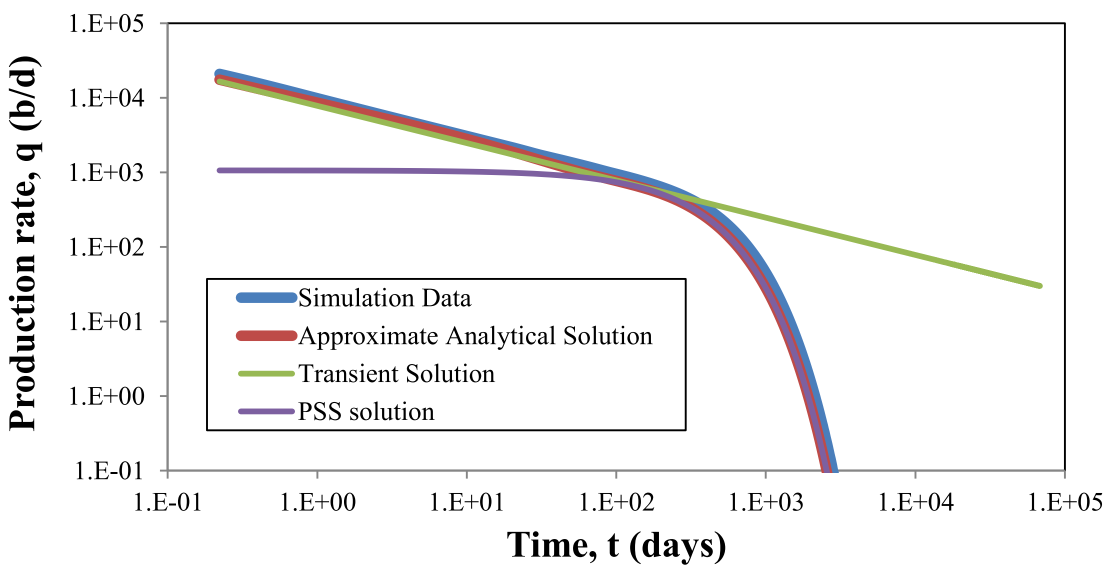

Figure A-2: Validation of approximate analytical solution to the 1D flow problem with numerical simulation

Appendix B: Solution to the Three Dimensional (3D) Diffusivity Equation

The solution to the 3D diffusivity equation with a point source is presented in this appendix. The solution presented is a fundamental solution. This solution can be used to obtain the solution to any arbitrary fracture shape using a line, surface or volume integral.

The diffusivity equation in 3D is given below:

$$\frac{\phi\mu c_t}{k_x}\frac{\partial p}{\partial t} = \frac{\partial^2 p}{\partial x^2} + \frac{k_y}{k_x}\frac{\partial^2 p}{\partial y^2} + \frac{k_z}{k_x}\frac{\partial^2 p}{\partial z^2}\,. \tag{B.1}$$

The associated initial and boundary conditions are:

$$p(x,y,z,0) = p_i\,, \tag{B.2}$$

$$\left.\frac{dp}{dx}\right|_{x=0} = \left.\frac{dp}{dx}\right|_{x=L_x} = 0\,, \tag{B.3}$$

$$\left.\frac{dp}{dy}\right|_{y=0} = \left.\frac{dp}{dy}\right|_{y=L_y} = 0\,, \tag{B.4}$$

$$\left.\frac{dp}{dz}\right|_{z=0} = \left.\frac{dp}{dz}\right|_{z=L_z} = 0\,. \tag{B.5}$$

Equation B.1 is the diffusivity equation in 3D Cartesian coordinate. Equation B.2 is the initial condition that states that at time t = 0, the pressure everywhere in the reservoir is equal to the initial reservoir pressure, p_i and Equations B.3 – B.5 are the boundary conditions that states that there is no flow across the reservoir boundary. We proceed to solve this equation by the Green’s function method (Baker and Sutlief, 2003) for a point source; as a result the problem is re-formulated as shown below

$$\frac{\phi\mu c_t}{k_x}\frac{\partial p}{\partial t} = \frac{\partial^2 p}{\partial x^2} + \frac{k_y}{k_x}\frac{\partial^2 p}{\partial y^2} + \frac{k_z}{k_x}\frac{\partial^2 p}{\partial z^2} + \frac{\mu}{k_x}q_i^*\delta\left(x-x'\right)\delta\left(y-y'\right)\delta\left(z-z'\right)\delta\left(t-t'\right), \tag{B.6}$$

In equation B.6, q_i^* is the source strength per unit volume (or area in 2D) of the source and δ is the Dirac delta function. The x', y' and z' are the coordinate locations of the source. The initial and boundary conditions remain the same as in equations B.2 – B.5.

In dimensionless form these set of equations become:

$$\frac{\partial p_D}{\partial t_D}=\frac{\partial^2 p_D}{\partial x_D^2}+\lambda_{xy}\frac{\partial^2 p_D}{\partial y_D^2}+\lambda_{xz}\frac{\partial^2 p_D}{\partial z_D^2}+\frac{\mu}{k_x}q_i^*\delta\left(x_D-x_D'\right)\delta\left(y_D-y_D'\right)\delta\left(z_D-z_D'\right)\delta\left(t_D-t_D'\right), \tag{B.7}$$

$$p_D(x_D,y_D,z_D,0)=0, \tag{B.8}$$

$$\left.\frac{dp_D}{dx_D}\right|_{x_D=0}=\left.\frac{dp_D}{dx_D}\right|_{x_D=1}=0, \tag{B.9}$$

$$\left.\frac{dp_D}{dy_D}\right|_{y_D=0}=\left.\frac{dp_D}{dy_D}\right|_{y_D=1}=0, \tag{B.10}$$

$$\left.\frac{dp_D}{dz_D}\right|_{z_D=0}=\left.\frac{dp_D}{dz_D}\right|_{z_D=1}=0. \tag{B.11}$$

The dimensionless variables and parameters are defined as follows:

$t_D=\dfrac{k_x t}{\phi\mu c_t L_x^2}$: Dimensionless time

$p_D=\dfrac{(p_i-p)k_x}{q^*\mu L_x^2}$: Dimensionless pressure

$x_D=\dfrac{x}{L_x}$: Dimensionless distance in the x direction

$y_D=\dfrac{y}{L_y}$: Dimensionless distance in the y direction

$z_D=\dfrac{z}{L_z}$: Dimensionless distance in the z direction

$\lambda_{xy}=\dfrac{k_y}{k_x}\left[\dfrac{L_x}{L_y}\right]^2$: Transmissibility ratio in the x – y direction

$\lambda_{xz} = \frac{k_z}{k_x}\left[\frac{L_x}{L_z}\right]^2$: Transmissibility ratio in the x – z direction

To solve the problem the Greens function, G, is introduced and the coefficients of the second and third terms on the right hand side of equation B.7 are eliminated by introducing the following variables $y_D = \bar{y}_D\sqrt{\lambda_{xy}}$ and $z_D = \bar{z}_D\sqrt{\lambda_{xz}}$. These variables transform the problem into:

$$\frac{\partial G_D}{\partial t_D} = \frac{\partial^2 G_D}{\partial x_D^2} + \frac{\partial^2 G_D}{\partial \bar{y}_D^2} + \frac{\partial^2 G_D}{\partial \bar{z}_D^2} + \delta\left(x_D - x_D'\right)\delta\left(y_D - y_D'\right)\delta\left(z_D - z_D'\right)\delta\left(t_D - t_D'\right), \tag{B.12}$$

$$G_D(x_D, \bar{y}_D\sqrt{\lambda_{xy}}, \bar{z}_D\sqrt{\lambda_{xz}}, 0) = 0, \tag{B.13}$$

$$\left.\frac{dG_D}{dx_D}\right|_{x_D=0} = \left.\frac{dG_D}{dx_D}\right|_{x_D=1} = 0, \tag{B.14}$$

$$\left.\frac{dG_D}{d\bar{y}_D}\right|_{y_D=0} = \left.\frac{dG_D}{d\bar{y}_D}\right|_{y_D=\frac{1}{\sqrt{\lambda_{xy}}}} = 0, \tag{B.15}$$

$$\left.\frac{dG_D}{d\bar{z}_D}\right|_{z_D=0} = \left.\frac{dG_D}{d\bar{z}_D}\right|_{z_D=\frac{1}{\sqrt{\lambda_{xz}}}} = 0. \tag{B.16}$$

We can write equation B.12 as:

$$\frac{\partial G_D}{\partial t_D} + \nabla^2 G_D = 0. \tag{B.17}$$

Using separation of variable technique, we define $G_D = TU$, substituting into equation B.12 we have:

$$U\frac{\partial T}{\partial t_D} + T\nabla^2 U = 0. \tag{B.18}$$

Dividing equation B.18 by $T\left(t_D\right)U\left(x_D, \bar{y}_D, \bar{z}_D\right)$ it is separated as shown below:

$$\frac{1}{T}\frac{\partial T}{\partial t_D} = -\frac{\nabla^2 U}{U} = -\alpha^2. \tag{B.19}$$

From equation B.19, we have:

$$\frac{\nabla^2 U}{U} = \alpha^2 \tag{B.20}$$

$$\left.\frac{dU}{dx_D}\right|_{x_D=0} = \left.\frac{dU}{dx_D}\right|_{x_D=1} = 0 \tag{B.21}$$

$$\left.\frac{dU}{d\bar{y}_D}\right|_{y_D=0} = \left.\frac{dU}{d\bar{y}_D}\right|_{y_D=\frac{1}{\sqrt{\lambda_{xy}}}} = 0 \tag{B.22}$$

$$\left.\frac{dU}{d\bar{z}_D}\right|_{z_D=0} = \left.\frac{dU}{d\bar{z}_D}\right|_{z_D=\frac{1}{\sqrt{\lambda_{xz}}}} = 0 \tag{B.23}$$

Letting $U = X\left(x_D\right)V\left(\bar{y}_D, \bar{z}_D\right)$

$$\frac{X''}{X} + \frac{V''}{V} - \alpha^2 = 0,$$

$$\frac{X''}{X} = \frac{V''}{V} - \alpha^2 = -\beta^2. \tag{B.24}$$

For the x_D variable:

$$\frac{X''}{X} = -\beta^2, \tag{B.25}$$

$$X'(0) = X'(1) = 0. \tag{B.26}$$

The solution to equation B.25 – B.26 is:

$$X(x_D) = A_{x1}\cos(\beta x_D) + A_{x2}\sin(\beta x_D).$$

By using the boundary condition at $x_D = 0$, we find that $A_{x2} = 0$ and also using the boundary condition at $x_D = 1$ we have $\sin(\beta) = 0$. Therefore,

$$\beta = \sin^{-1}(0) = n\pi, \text{ where n = 0,1,2,...} \tag{B.27}$$

The solution to equations B.25 – B.26 is $X_n(x_D) = A_n cos(n\pi x_D)$. The total solution is therefore given by:

$$X(x_D) = \sum_{n=0}^{\infty} X\left(x_D\right) = \sum_{n=0}^{\infty} A_n cos(n\pi x_D). \tag{B.28}$$

From equation B.24

$$\frac{V^{"}}{V} = -(\alpha^2 - \beta^2) = -\lambda^2, \tag{B.29}$$

$$V^{'}(0) = V^{'}(1) = 0. \tag{B.30}$$

Letting $V\left(\overline{y}_D, \overline{z}_D\right) = Y(\overline{y}_D)Z(\overline{z}_D)$ we obtain:

$$\frac{Y^{"}}{Y} + \frac{Z^{"}}{Z} + \lambda^2 = 0,$$

$$\frac{Y^{"}}{Y} = -\left[\frac{Z^{"}}{Z} + \lambda^2\right] = -\phi^2. \tag{B.31}$$

For the Y variable the equation becomes:

$$\frac{Y^{"}}{Y} = -\phi^2, \tag{B.32}$$

$$Y^{'}(0) = Y^{'}(\frac{1}{\sqrt{\lambda_{xy}}}) = 0. \tag{B.33}$$

The solution of equation B.32 – B.33 is;

$$Y(\overline{y}_D) = B_{y1}\cos(\phi \overline{y}_D) + B_{y2}\sin(\phi \overline{y}_D).$$

From the boundary condition at $\overline{y}_D = 0$, we find that $B_{y2} = 0$ and also using the boundary condition at $\overline{y}_D = \frac{1}{\sqrt{\lambda_{xy}}}$ we have $\sin(\phi) = 0$. Therefore,

$$\frac{\phi}{\sqrt{\lambda_{xy}}} = \sin^{-1}(0) = m\pi, \text{ where m = 0,1,2,...}, \tag{B.34}$$

$$Y(y_D) = \sum_{m=0}^{\infty} B_m cos(m\pi \sqrt{\lambda_{xy}}\, \overline{y}_D) = \sum_{m=0}^{\infty} B_m cos(m\pi y_D). \tag{B.35}$$

From equation B.31, we have:

$$\frac{Z^{''}}{Z} = -\left(\lambda^2 - \phi^2\right) = -\xi^2 , \tag{B.36}$$

$$Z^{'}(0) = Z^{'}(\frac{1}{\sqrt{\lambda_{xz}}}) = 0 . \tag{B.37}$$

The solution to equation B.36 – B.37 is obtained by analogy to the solution of equation B.32 – B.33.

$$\frac{\xi}{\sqrt{\lambda_{xz}}} = \sin^{-1}(0) = k\pi, \text{ where k = 0,1,2,...,} \tag{B.38}$$

$$Z(z_D) = \sum_{k=0}^{\infty} C_k cos(k\pi\sqrt{\lambda_{xz}}\,\bar{z}_D) = \sum_{k=0}^{\infty} C_k cos(k\pi z_D) . \tag{B.39}$$

From equation B.27, B.34 and B.38 it can be shown that

$$\alpha^2 = \xi^2 + \phi^2 + \beta^2 = \left[n^2 + m^2\lambda_{xy} + k^2\lambda_{xz}\right]\pi^2 .$$

From equation B.19,

$$\frac{1}{T}\frac{\partial T}{\partial t_D} = -\alpha^2 , \tag{B.40}$$

$$T(t_D = 0) = 0 . \tag{B.41}$$

which is solved to obtain:

$$T(t_D) = e^{-\alpha^2 t_D} = e^{-\left[n^2 + m^2\lambda_{xy} + k^2\lambda_{xz}\right]\pi^2 t_D} . \tag{B.42}$$

Therefore the solution to equation B.17 is:

$$G_D = \left[A_0 + \sum_{n=1}^{\infty} A_n e^{-n^2\pi^2 t_D} cos(n\pi x_D)\right]\left[B_0 + \sum_{m=1}^{\infty} B_m e^{-m^2\lambda_{xy}\pi^2 t_D} cos(m\pi y_D)\right]\left[C_0 + \sum_{k=1}^{\infty} C_k e^{-k^2\lambda_{xy}\pi^2 t_D} cos(k\pi z_D)\right], \tag{B.43}$$

$$G_D = \sum_{n=0}^{\infty} A_n e^{-(n\pi)^2 t_D} cos(n\pi x_D) \sum_{m=0}^{\infty} B_m e^{-(m\pi)^2 \lambda_{xy} t_D} cos(m\pi y_D) \sum_{k=0}^{\infty} C_k e^{-(k\pi)^2 \lambda_{xz} t_D} cos(k\pi z_D) . \tag{B.44}$$

Integrating equation B.12 over the entire volume and time domains

$$\int_0^{t_D}\int_0^1\int_0^1\int_0^1 \left[\frac{\partial G_D}{\partial t_D} - \nabla^2 G_D\right] dt_D dv_D = \int_0^{t_D}\int_0^1\int_0^1\int_0^1 \delta\left(x_D - x_D^{'}\right)\delta\left(y_D - y_D^{'}\right)\delta\left(z_D - z_D^{'}\right)\delta\left(t_D - t_D^{'}\right) dt_D dv_D , \tag{B.45}$$

where $dv_D = dx_D dy_D dz_D$.

Evaluating the integral in equation B.45 we obtain the condition shown in equation B.46;

$$\int_0^1\int_0^1\int_0^1 G_D dv_D = \int_0^{t_D}\int_0^1\int_0^1\int_0^1 \delta\left(x_D - x_D^{'}\right)\delta\left(y_D - y_D^{'}\right)\delta\left(z_D - z_D^{'}\right)\delta\left(t_D - t_D^{'}\right)dt_D dv_D. \tag{B.46}$$

Substituting for each independent solution of G_D into equation B.46;

$$\begin{aligned}&\int_0^1\int_0^1\int_0^1\left[A_n e^{-(n\pi)^2 t_D} cos(n\pi x_D) B_m e^{-(m\pi)^2 \lambda_{xy} t_D} cos(m\pi y_D) C_k e^{-(k\pi)^2 \lambda_{xz} t_D} cos(k\pi z_D)\right]dv_D \\ &= \int_0^{t_D}\int_0^1\int_0^1\int_0^1 \delta\left(x_D - x_D^{'}\right)\delta\left(y_D - y_D^{'}\right)\delta\left(z_D - z_D^{'}\right)\delta\left(t_D - t_D^{'}\right)dt_D dv_D\end{aligned}. \tag{B.47}$$

Multiplying both sides of equation B.47 by $\cos(\bar{n}\pi x_D)e^{-n^2\pi^2 t_D}$,

$$\begin{aligned}&\int_0^1\int_0^1\left[\left[A_n\int_0^1 cos(n\pi x_D)\,cos(\bar{n}\pi x_D)\right]dx_D B_m cos(m\pi y_D) C_k cos(k\pi z_D)\right]dy_D dz_D \\ &= \int_0^{t_D}\int_0^1\int_0^1\int_0^1 \delta\left(x_D - x_D^{'}\right)\delta\left(y_D - y_D^{'}\right)\delta\left(z_D - z_D^{'}\right)\delta\left(t_D - t_D^{'}\right)cos(\bar{n}\pi x_D)e^{-n^2\pi^2 t_D} dt_D dv_D\end{aligned}. \tag{B.48}$$

Noting that,

$$\int_0^1 cos(n\pi x_D)\,cos(\bar{n}\pi x_D)dx_D = \begin{cases}\dfrac{1}{2} & n = \bar{n} \\ 0 & n \neq \bar{n}\end{cases}$$

Therefore,

$$\begin{aligned}&\frac{A_n}{2}\int_0^1\int_0^1 B_m cos(m\pi y_D) C_k cos(k\pi z_D) dy_D dz_D \\ &= cos(n\pi x_D^{'})\int_0^{t_D}\int_0^1\int_0^1 \delta\left(y_D - y_D^{'}\right)\delta\left(z_D - z_D^{'}\right)\delta\left(t_D - t_D^{'}\right)e^{-n^2\pi^2 t_D^{'}} dt_D dy_D dz_D\end{aligned}. \tag{B.49}$$

Repeating the previous steps for y_D and z_D,

$$A_n B_m C_k = 8e^{-\left[n^2 + m^2\lambda_{xy} + k^2\lambda_{xz}\right]\pi^2 t_D^{'}} cos(n\pi x_D^{'})\,cos(m\pi y_D^{'})\,cos(k\pi z_D^{'}) \tag{B.50}$$

From equation B.50 it can be deduce that:

$$A_n = 2cos(n\pi x_D^{'})e^{-(n\pi)^2 t_D^{'}}, \tag{B.51}$$

$$B_m = 2cos(m\pi y_D^{'})e^{-(m\pi)^2 \lambda_{xy} t_D^{'}}, \tag{B.52}$$

$$C_k = 2cos(k\pi z_D^{'})e^{-(k\pi)^2 \lambda_{xz} t_D^{'}}. \tag{B.53}$$

For the special case where $n = 0$, equation B.46 becomes:

$$\begin{aligned} &\left[A_0 \int_0^1 dx_D\right] \int_0^1 \int_0^1 \left[\sum_{m=0}^{\infty} B_m cos(m\pi y_D) \sum_{k=0}^{\infty} C_k cos(k\pi z_D)\right] dy_D dz_D \\ &= \int_0^{t_D} \int_0^1 \int_0^1 e^{-\left[m^2 \lambda_{xy} + k^2 \lambda_{xz}\right]\pi^2 t_D} \delta\left(y_D - y_D^{'}\right)\delta\left(z_D - z_D^{'}\right)\delta\left(t_D - t_D^{'}\right) dt_D dy_D dz_D \end{aligned}, \tag{B.54}$$

$\Rightarrow A_0 = 1$. By analogy it is found that $B_0 = 1$ and $C_0 = 1$. Upon substituting for the coefficients given by equations B.51-B.53, $A_0 = 1$, $B_0 = 1$ and $C_0 = 1$ into equation B.43 the complete solution to equation B.12 – B.16 is found to be given by:

$$\begin{aligned} &G_D\left(x_{D,} y_{D,} z_{D,} t_D \mid x_D^{'}, y_D^{'}, z_D^{'}, t_D^{'}\right) = \left[1 + \sum_{n=1}^{\infty} 2e^{-n^2\pi^2\left(t_D - t_D^{'}\right)} cos(n\pi x_D^{'}) cos(n\pi x_D)\right] \\ &\left[1 + \sum_{m=1}^{\infty} 2e^{-m^2\pi^2\lambda_{xy}\left(t_D - t_D^{'}\right)} cos(m\pi y_D^{'}) cos(m\pi y_D)\right] \\ &\left[1 + \sum_{k=1}^{\infty} 2e^{-k^2\pi^2\lambda_{xy}\left(t_D - t_D^{'}\right)} cos(k\pi z_D^{'}) cos(k\pi z_D)\right] \end{aligned}. \tag{B.55}$$

Equation B.55 is the instantaneous point source solution to the diffusivity equation with the source located at $L(x_D^{'}, y_D^{'}, z_D^{'})$. Using Green's identity (Baker and Sutlief, 2003);

$$p_D\left(x_{D,} y_{D,} z_{D,} t_D \mid x_D^{'}, y_D^{'}, z_D^{'}\right) = \int_0^{t_D} \left[\int_{v_D^{'}} G_D\left(\frac{\partial p_D}{\partial t_D} - \nabla^2 p_D\right) dv_D^{'} + \int_s \left[p_D \nabla G_D - G_D \nabla p_D\right].nds\right] dt_D^{'} . \tag{B.56}$$

The integral with respect to time in equation B.56 is used to convert the instantaneous point source solution to a continuous point source solution and the integral in $v_D^{'}$ (where $v_D^{'} = x_D^{'} y_D^{'} z_D^{'}$) is the integral over the volume of the source. The integral in s is the surface integral on the reservoir boundary. From equation B.7

$$\nabla^2 p_D + \frac{\partial p_D}{\partial t_D} = \frac{\mu}{k_x} q_i^* \delta\left(x_D - x_D^{'}\right)\delta\left(y_D - y_D^{'}\right)\delta\left(z_D - z_D^{'}\right)\delta\left(t_D - t_D^{'}\right) = q_D(\mathbf{x}_\mathrm{D}, t_D)$$ and

$\nabla G_D = \nabla p_D = 0$ on the boundary, hence equation B.56 simplifies to:

$$p_D\left(x_{D,} y_{D,} z_{D,} t_D \mid x_D^{'}, y_D^{'}, z_D^{'}\right) = \int_0^{t_D}\left[\int_{v_D} G_D\left(x_{D,} y_{D,} z_{D,} t_D \mid x_D^{'}, y_D^{'}, z_D^{'}, t_D^{'}\right) q_D(\mathbf{x}_D, t_D) dv_D\right] dt_D^{'}. \tag{B.57}$$

For a constant rate solution $q_D(x_D, t_D) = 1$ and equation B.57 simplifies to:

$$p_D\left(x_{D,} y_{D,} z_{D,} t_D \mid x_D^{'}, y_D^{'}, z_D^{'}\right) = \int_0^{t_D}\left[\int_{v_D} G_D\left(x_{D,} y_{D,} z_{D,} t_D \mid x_D^{'}, y_D^{'}, z_D^{'}, t_D^{'}\right) dv_D\right] dt_D^{'}, \tag{B.58}$$

Evaluating the integral with respect to $t_D^{'}$ from 0 to t_D:

$$p_D\left(x_{D,} y_{D,} z_{D,} t_D \mid x_D^{'}, y_D^{'}, z_D^{'}\right) =$$

$$\int_{v_D^{'}} \left[\begin{array}{l} t_D \\ + \dfrac{2}{\pi^2}\displaystyle\sum_{n=1}^{\infty}\dfrac{\left[1 - e^{-(n\pi)^2 t_D}\right]}{n^2} cos(n\pi x_D) cos(n\pi x_D^{'}) \\ + \dfrac{2}{\pi^2}\displaystyle\sum_{m=1}^{\infty}\dfrac{\left[1 - e^{-(m\pi)^2 \lambda_{xy} t_D}\right]}{m^2 \lambda_{xy}} cos(m\pi y_D) cos(m\pi y_D^{'}) \\ + \dfrac{2}{\pi^2}\displaystyle\sum_{k=1}^{\infty}\dfrac{\left[1 - e^{-(k\pi)^2 \lambda_{xz} t_D}\right]}{k^2 \lambda_{xz}} cos(k\pi z_D) cos(k\pi z_D^{'}) \\ + \dfrac{4}{\pi^2}\displaystyle\sum_{n=1}^{\infty}\sum_{m=1}^{\infty}\dfrac{\left[1 - e^{-\left[n^2 + m^2 \lambda_{xy}\right]\pi^2 t_D}\right]}{n^2 + m^2 \lambda_{xy}} cos(m\pi y_D) cos(m\pi y_D^{'}) cos(n\pi x_D) cos(n\pi x_D^{'}) \\ + \dfrac{4}{\pi^2}\displaystyle\sum_{k=1}^{\infty}\sum_{m=1}^{\infty}\dfrac{\left[1 - e^{-\left[m^2 \lambda_{xy} + k^2 \lambda_{xz}\right]\pi^2 t_D}\right]}{m^2 \lambda_{xy} + k^2 \lambda_{xz}} cos(m\pi y_D) cos(m\pi y_D^{'}) cos(k\pi z_D) cos(k\pi z_D^{'}) \\ + \dfrac{4}{\pi^2}\displaystyle\sum_{k=1}^{\infty}\sum_{n=1}^{\infty}\dfrac{\left[1 - e^{-\left[n^2 + k^2 \lambda_{xz}\right]\pi^2 t_D}\right]}{n^2 + k^2 \lambda_{xz}} cos(n\pi y_D) cos(n\pi y_D^{'}) cos(k\pi z_D) cos(k\pi z_D^{'}) \\ + \dfrac{8}{\pi^2}\displaystyle\sum_{k=1}^{\infty}\sum_{n=1}^{\infty}\sum_{m=1}^{\infty}\dfrac{\left[1 - e^{-\left[n^2 + m^2 \lambda_{xy} + k^2 \lambda_{xz}\right]\pi^2 t_D}\right]}{n^2 + m^2 \lambda_{xy} + k^2 \lambda_{xz}} cos(m\pi y_D) cos(m\pi y_D^{'}) cos(n\pi x_D) \\ \qquad cos(n\pi x_D^{'}) cos(k\pi z_D) cos(k\pi z_D^{'}) \end{array}\right] dv_D^{'} . \tag{B.59}$$

The solution in equation B.59 is a fundamental solution to the diffusivity equation. This means that it can be used to construct the solution for any fracture geometry or shape when it is combined with line (or surface) integral. It should also be noted that this solution is for a constant source, Gringarten and Ramey (1974) and Cinco Ley et al. (1978) have presented methods that can be used to derive the solution for constant pressure case from the constant rate solution.

Appendix C: Example Application to Field Data

This Appendix presents the result of example application of the approximate analytical solution to the double porosity model.

ID-3

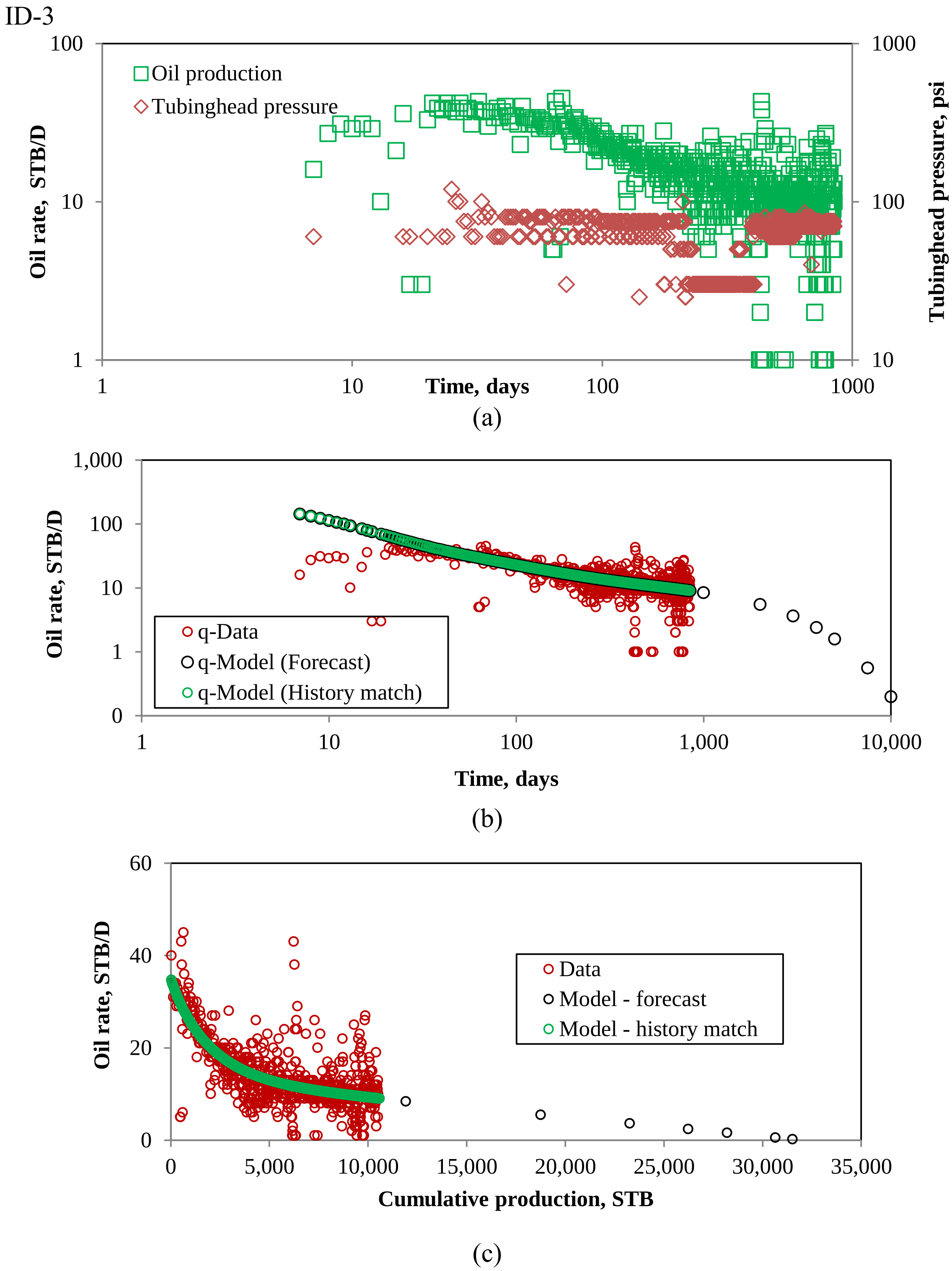

Figure C-1: Summary of production profile for well ID-3, (a). is the production rate plotted on a log-log scale. (b). represents the history match result and the forecast of production rate. (c). represents the history match of the cumulative production and reserves forecast

ID-4

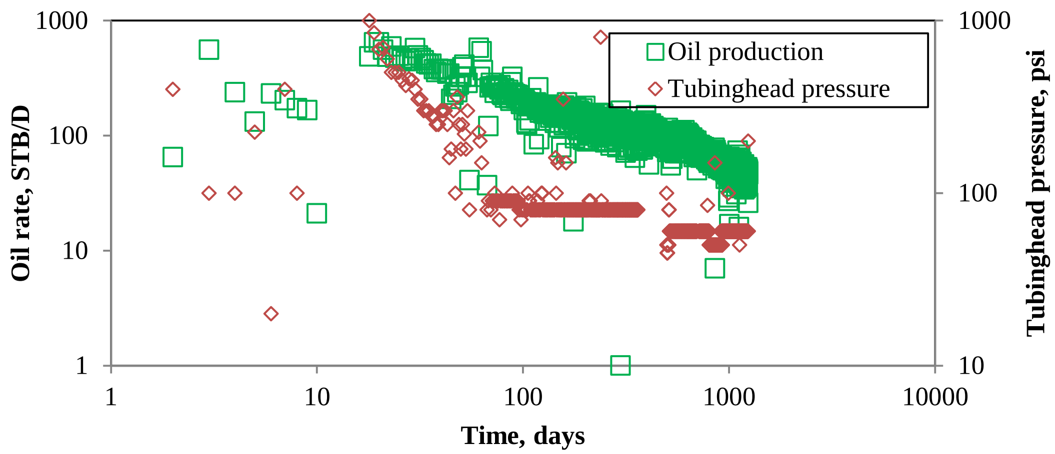

(a)

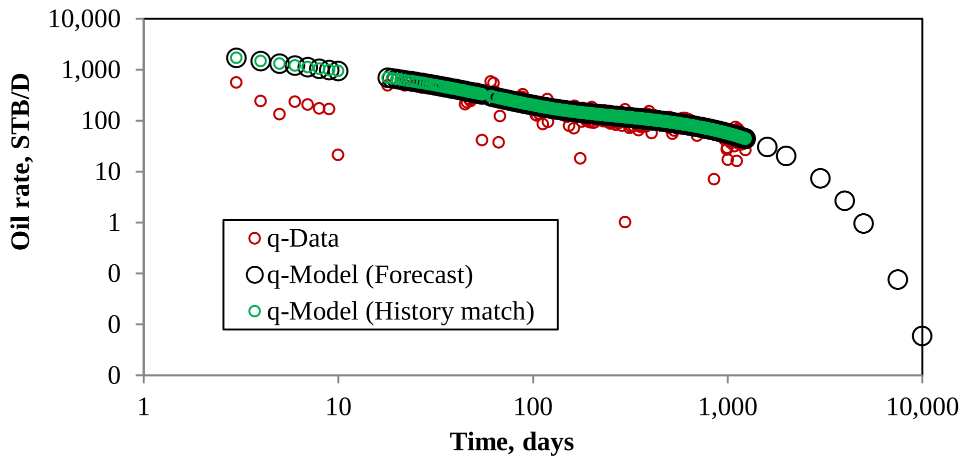

(b)

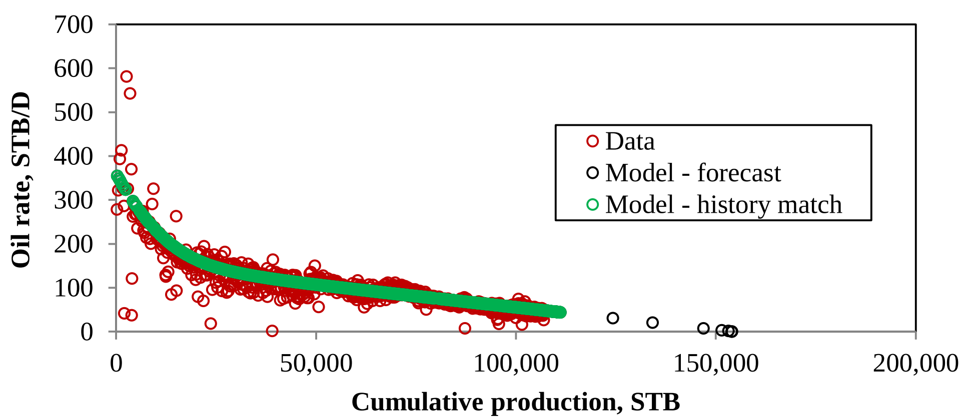

(c)

Figure C-2: Summary of production profile for well ID-4, (a). is the production rate plotted on a log-log scale. (b). represents the history match result and the forecast of production rate. (c). represents the history match of the cumulative production and reserves forecast

ID-82

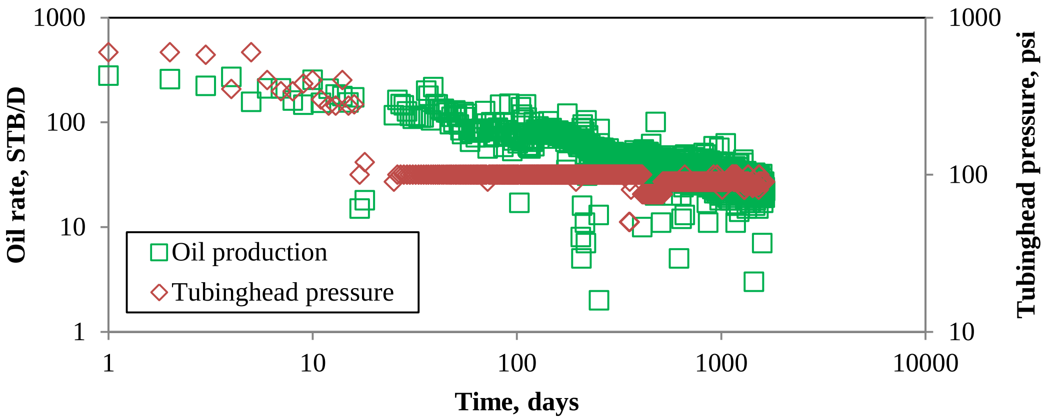

(a)

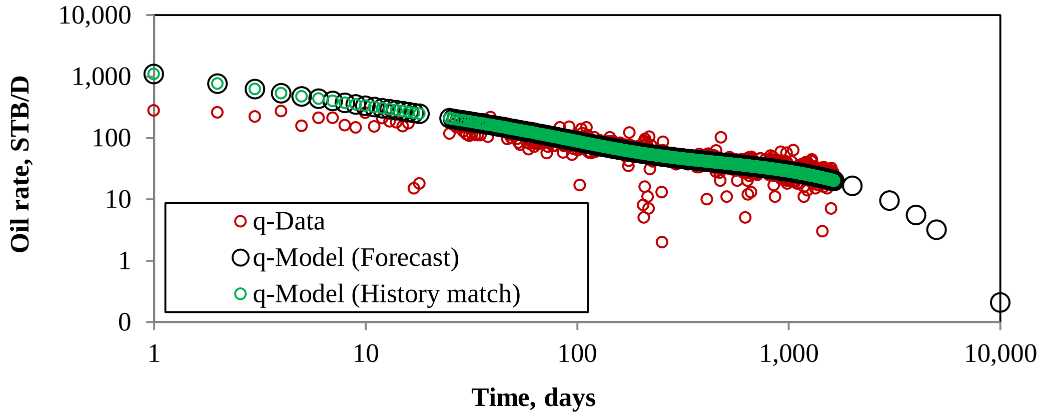

(b)

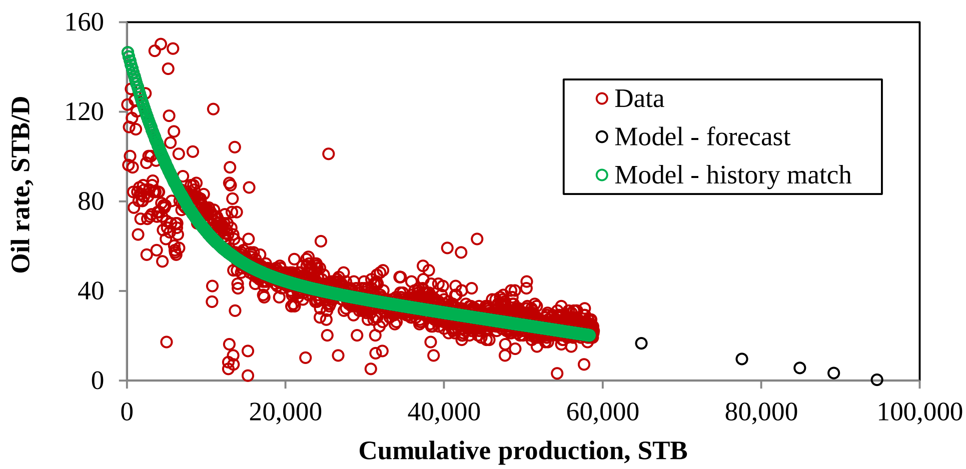

(c)

Figure C-3: Summary of production profile for well ID-82, (a). is the production rate plotted on a log-log scale. (b). represents the history match result and the forecast of production rate. (c). represents the history match of the cumulative production and reserves forecast

ID-68

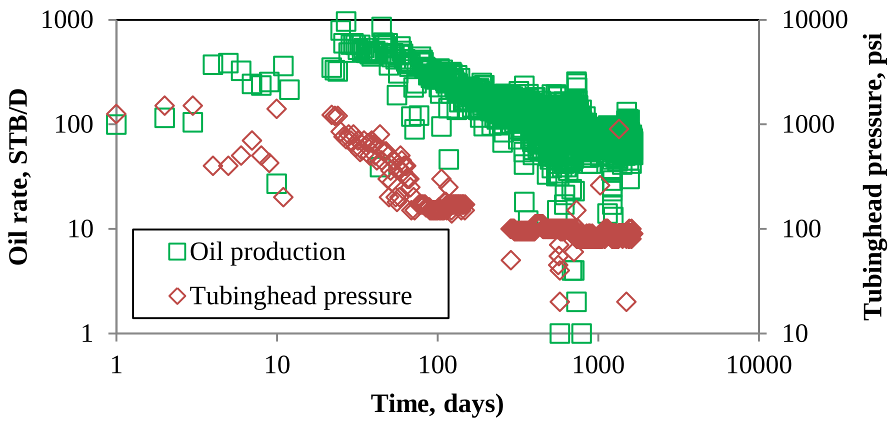

(a)

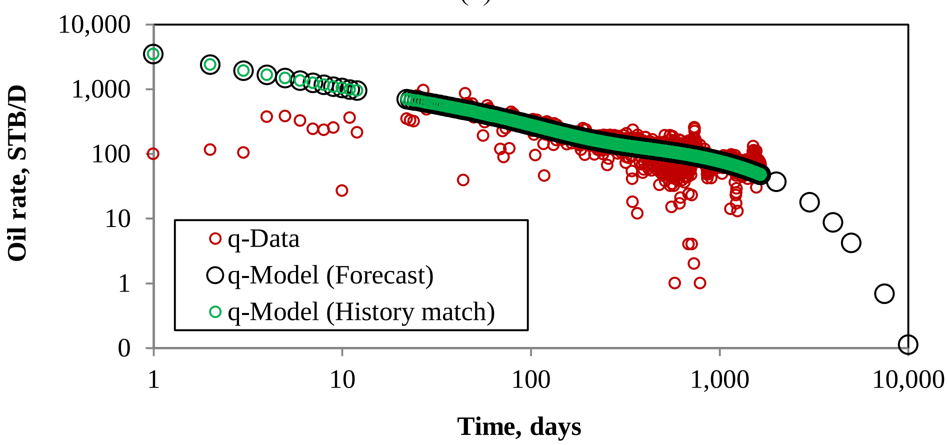

(b)

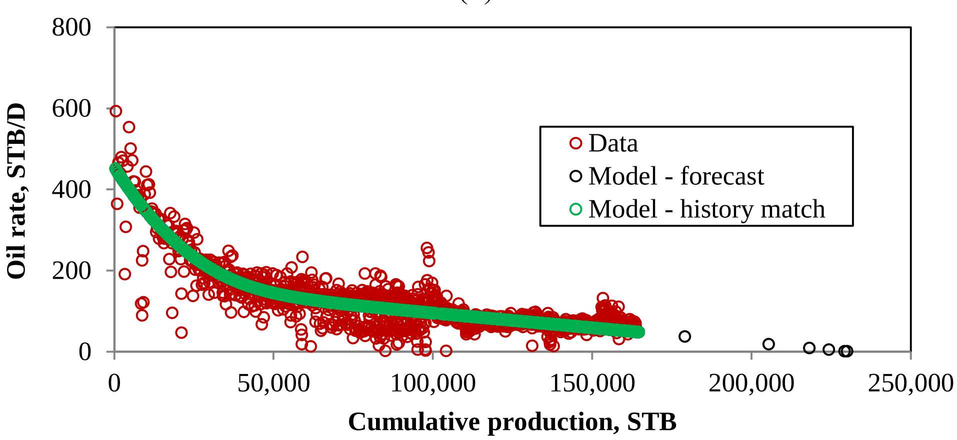

(c)

Figure C-4: Summary of production profile for well ID-68, (a). is the production rate plotted on a log-log scale. (b). represents the history match result and the forecast of production rate. (c). represents the history match of the cumulative production and reserves forecast

ID-81

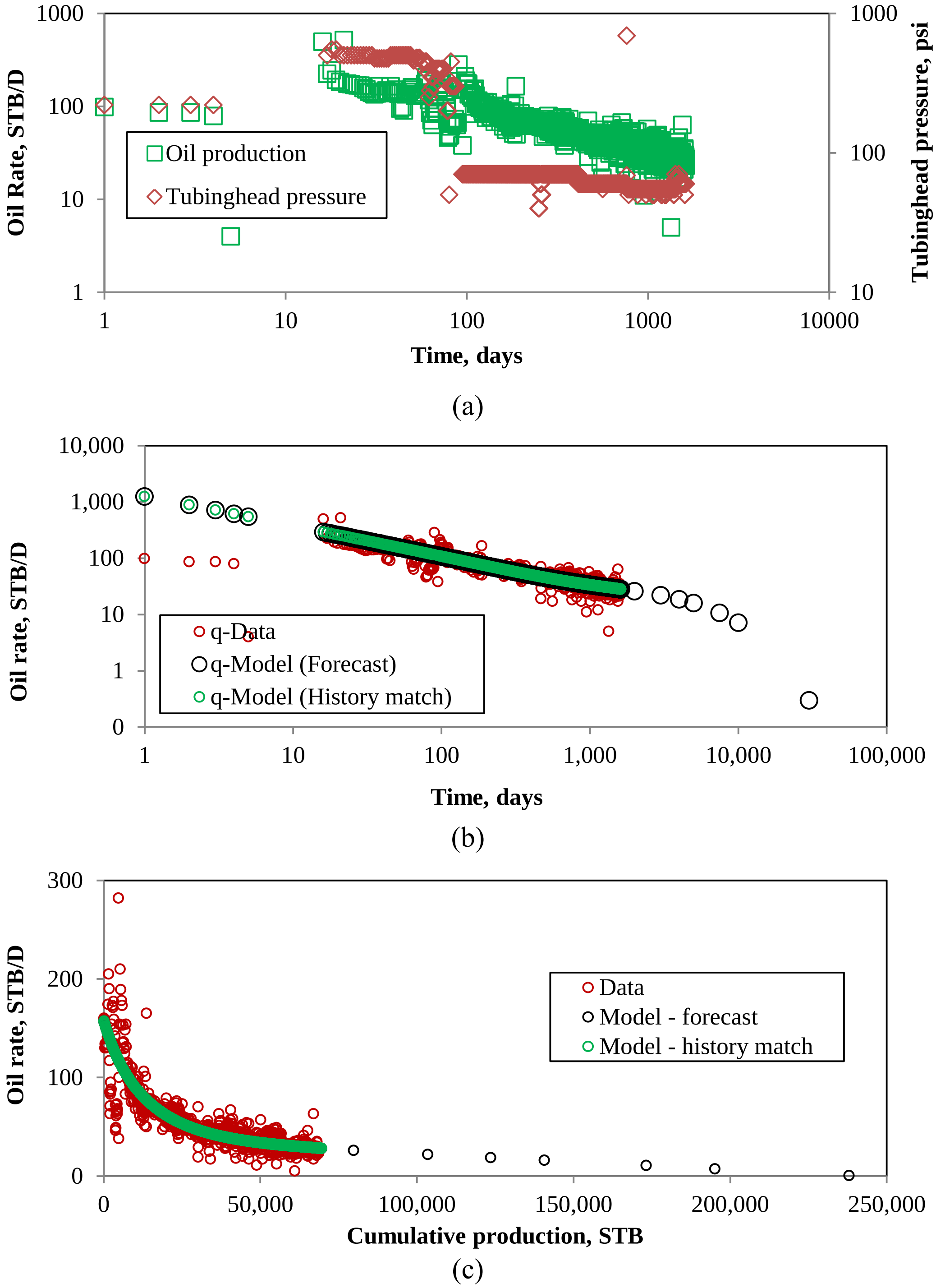

Figure C-5: Summary of production profile for well ID-81, (a). is the production rate plotted on a log-log scale. (b). represents the history match result and the forecast of production rate. (c). represents the history match of the cumulative production and reserves forecast

ID-70

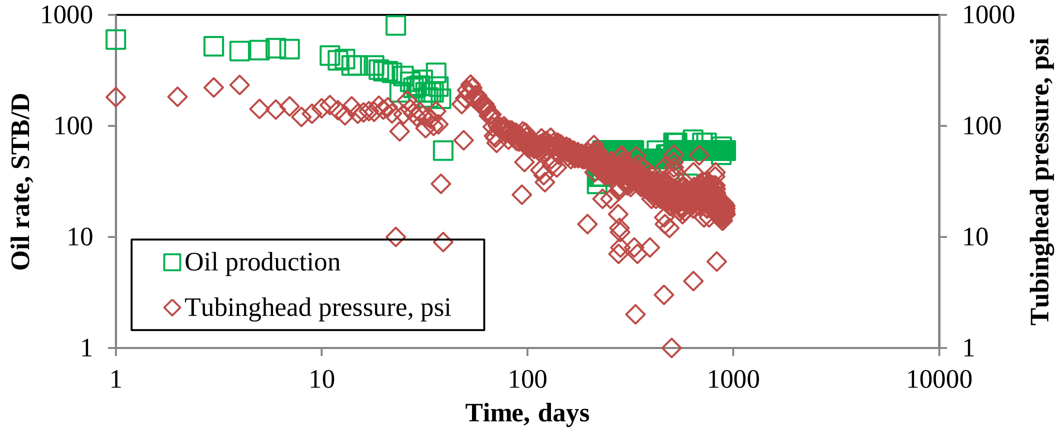

(a)

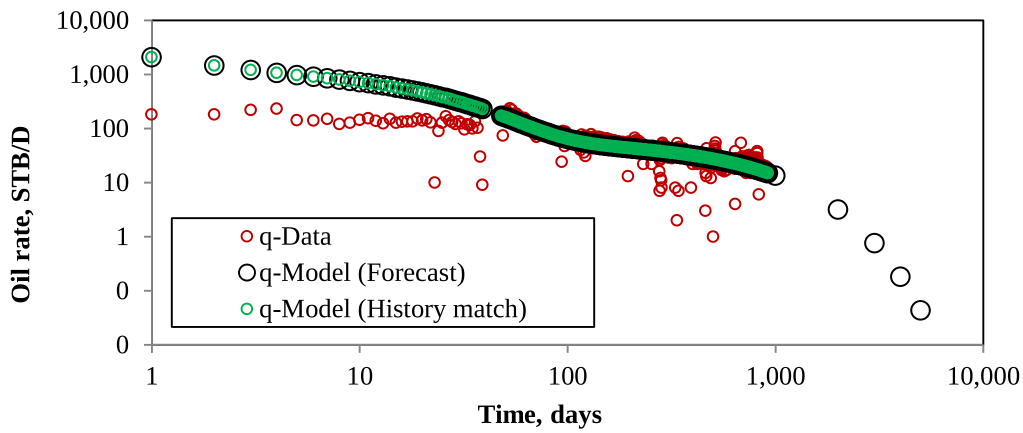

(b)

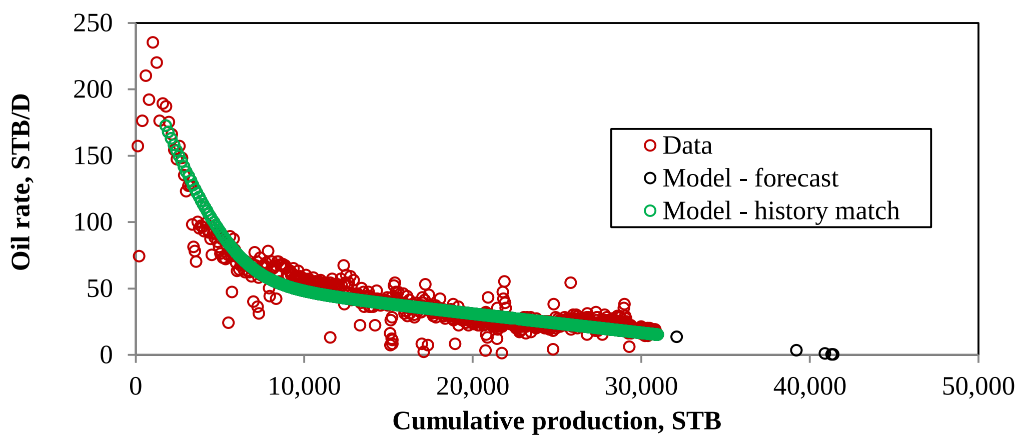

(c)

Figure C-6: Summary of production profile for well ID-70, (a). is the production rate plotted on a log-log scale. (b). represents the history match result and the forecast of production rate. (c). represents the history match of the cumulative production and reserves forecast

ID-74

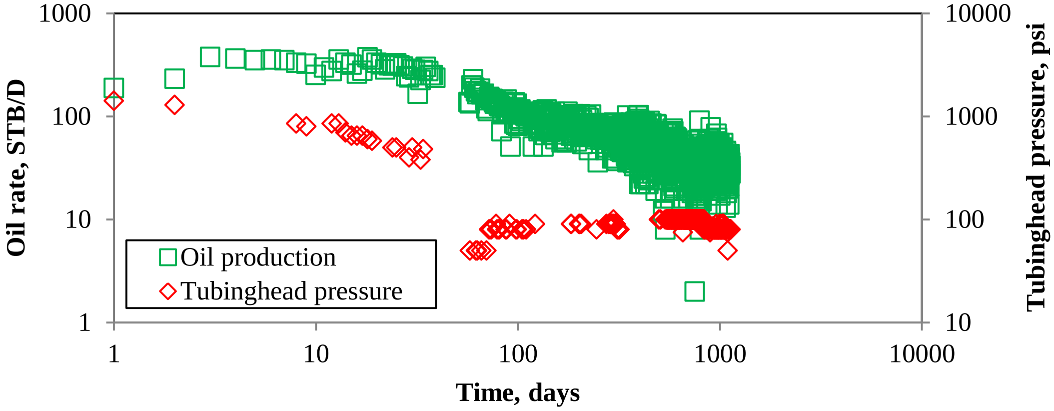

(a)

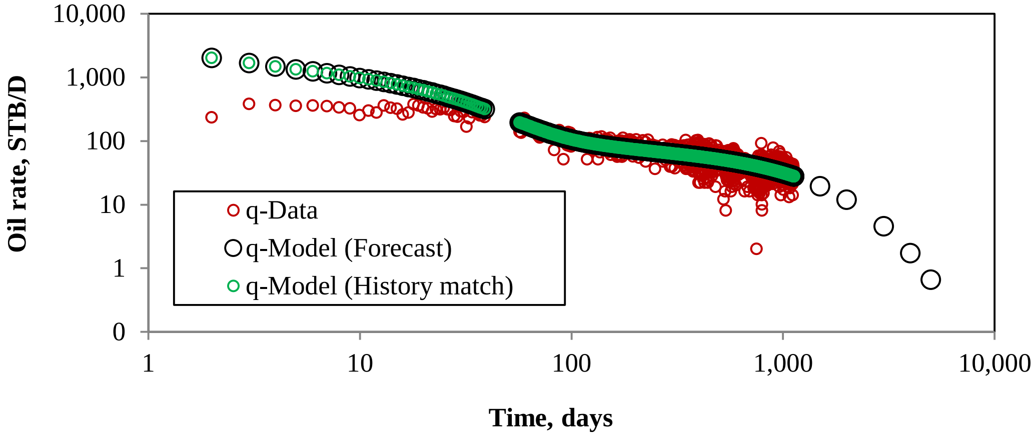

(b)

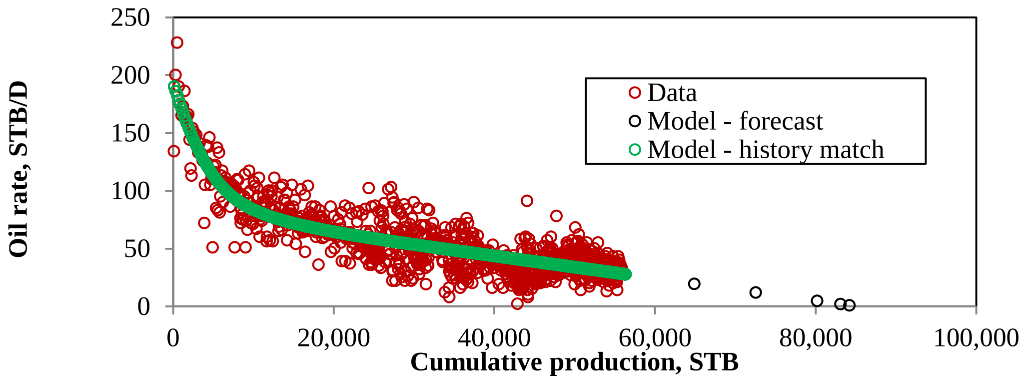

(c)

Figure C-7: Summary of production profile for well ID-74, (a). is the production rate plotted on a log-log scale. (b). represents the history match result and the forecast of production rate. (c). represents the history match of the cumulative production and reserves forecast

ID-75

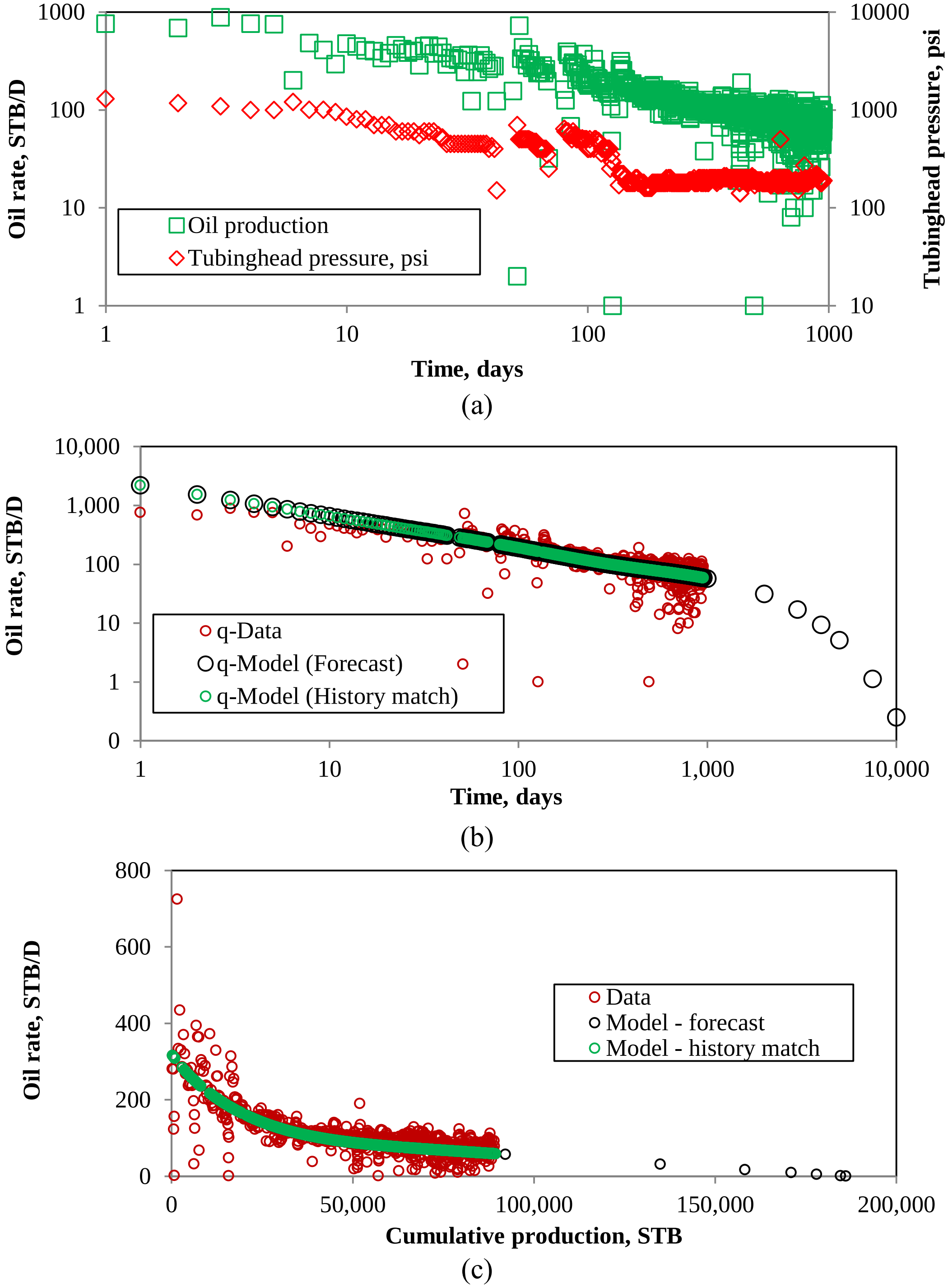

Figure C-8: Summary of production profile for well ID-75, (a). is the production rate plotted on a log-log scale. (b). represents the history match result and the forecast of production rate. (c). represents the history match of the cumulative production and reserves forecast

ID-78

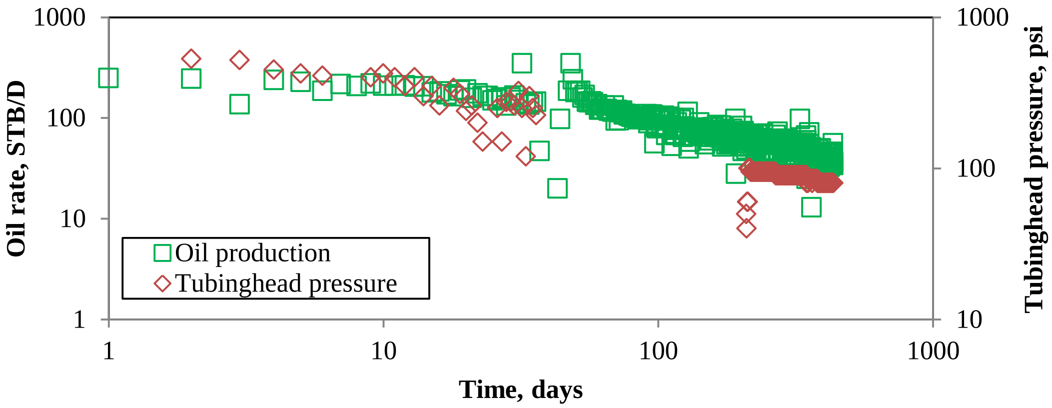

(a)

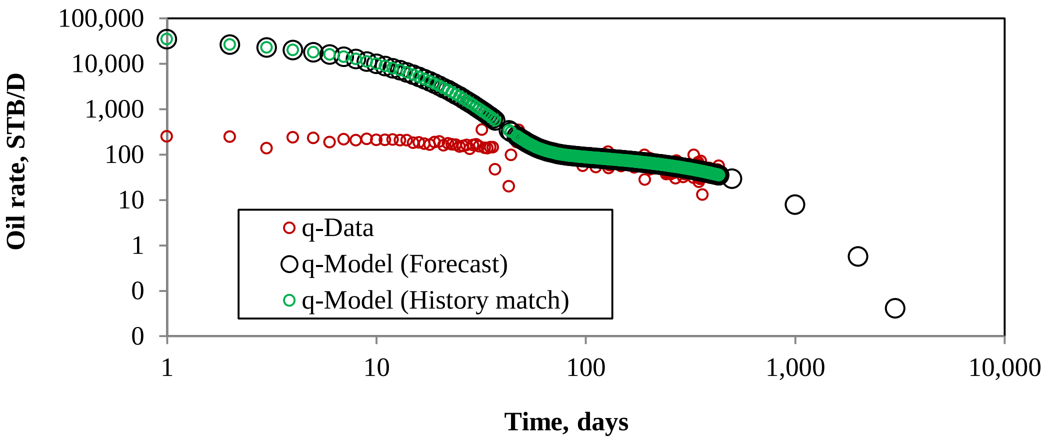

(b)

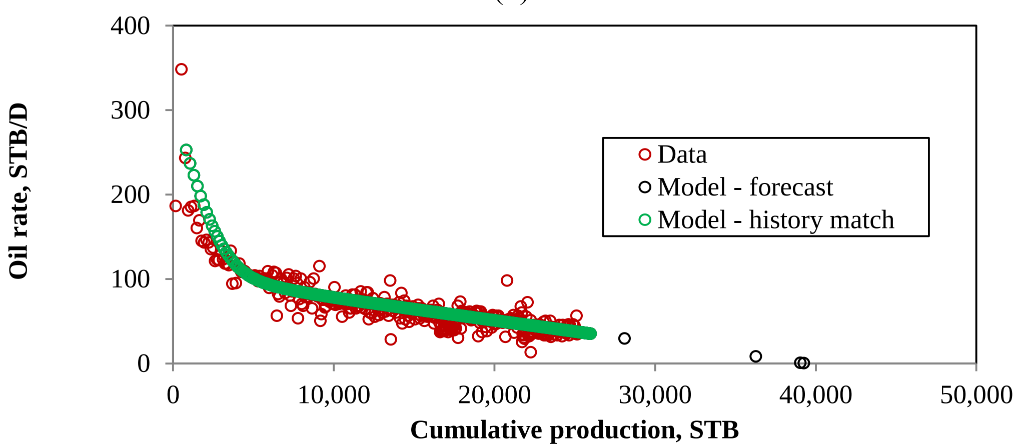

(c)

Figure C-9: Summary of production profile for well ID-78, (a). is the production rate plotted on a log-log scale. (b). represents the history match result and the forecast of production rate. (c). represents the history match of the cumulative production and reserves forecast

ID-79

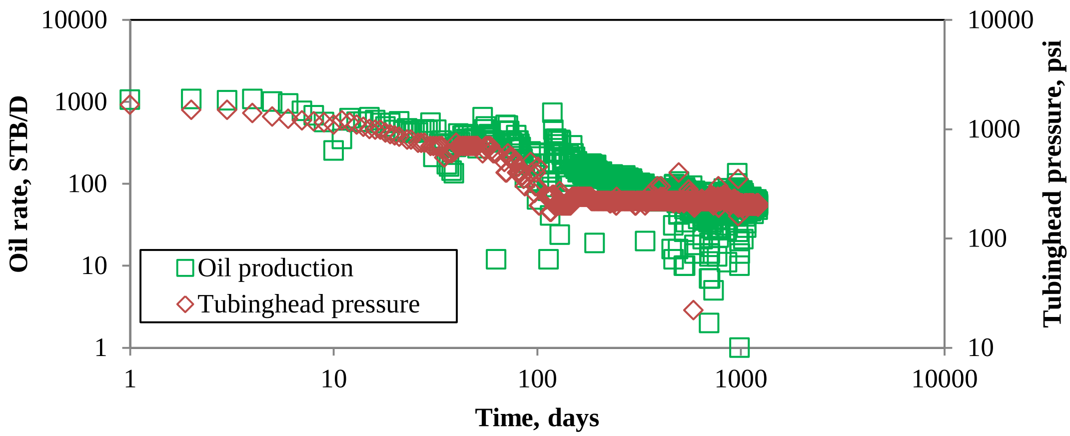

(a)

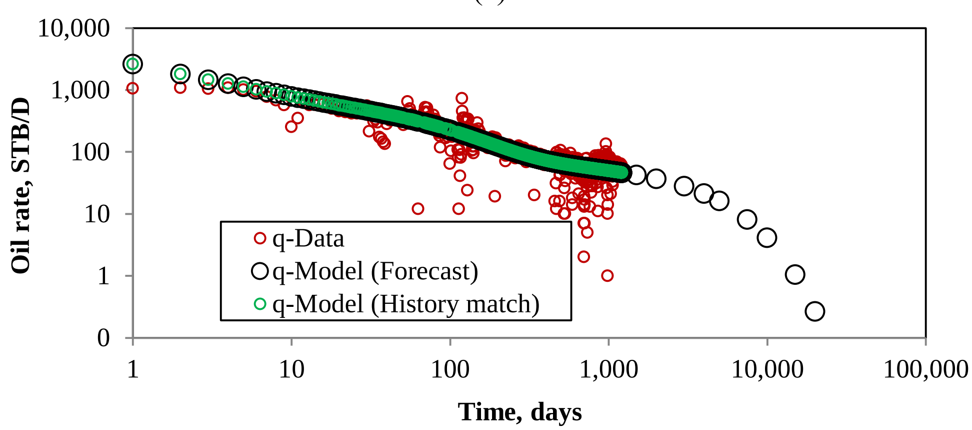

(b)

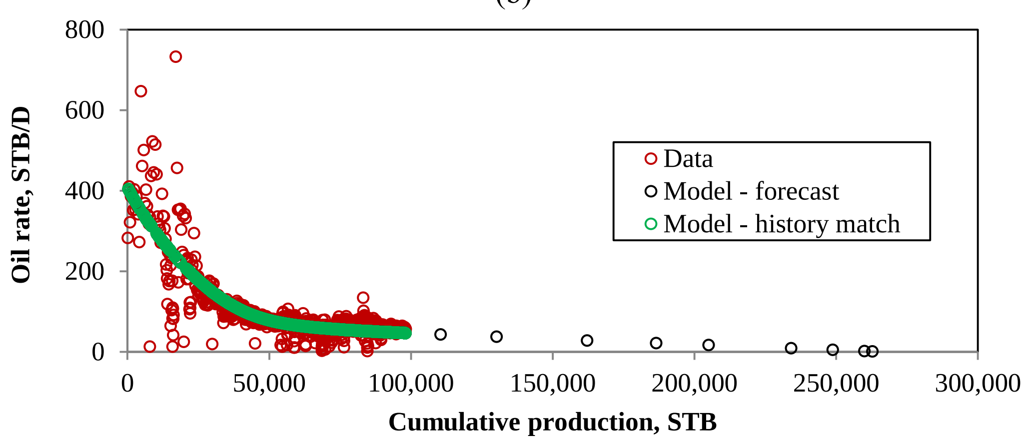

(c)

Figure C-10: Summary of production profile for well ID-79, (a). is the production rate plotted on a log-log scale. (b). represents the history match result and the forecast of production rate. (c). represents the history match of the cumulative production and reserves forecast

Nomenclature

τ_1 = Time constant one, day

τ_2 = Time constant two, day

D_i = Initial decline rate, day^{-1}

b = Derivative of inverse of initial decline rate, unitless

q_i = Initial production rate, STB/D

N_p = Cumulative production, STB

q_D = Dimensionless flow rate, dimensionless

t_D = Dimensionless time, dimensionless

p_{wD} = Dimensionless wellbore pressure, dimensionless

q_T = Production rate from fractured horizontal well, STB/D

N_e = Number of discrete reservoir elements, unitless

q_{i_k} = Initial production rate from reservoir element k, unitless

τ_k = Time constant for reservoir element k, day

N = Carrying capacity, STB

a = Constant a

n = Hyperbolic constant, unitless

M = Number of data points, unitless

t = Time, day

f_m = Normalized data initial production rate, fraction

f_k = Normalized model initial production rate, fraction

k_f = Fracture permeability, md

k_m = Matrix permeability, md

L_w = Well length, ft

p_i = Initial reservoir pressure, psi

p_{wf} = Wellbore flowing pressure, psi

h = Reservoir thickness, ft

φ = Porosity, fraction

τ_f = Fracture time constant, day

τ_m = Matrix time constant, day

T_x = Transmissibility factor between fracture and matrix compartment, barrel per day per psi

$f(s)$ = Laplace space inter-porosity transfer function, dimensionless

p_D = Dimensionless pressure

t_D = Dimensionless time

x_D = Dimensionless distance in the x-direction

y_D = Dimensionless distance in the y-direction

λ = Inter-porosity transfer parameter, dimensionless

ω = Storativity ratio

p_m = Matrix pressure, psi

p_f = Fracture pressure, psi

p_i = Initial reservoir pressure, psi

p_{wf} = Bottomhole flowing well pressure, psi

n = Index for normal mode

q_{f_n} = Production rate for the nth normal mode for the fracture compartment, dimensionless

q_{m_n} = Production rate for the nth normal mode for the matrix compartment, dimensionless

q_{f_i} = Initial production rate from the fracture's nth normal mode, dimensionless

q_{m_i} = Initial production rate from the matrix's nth normal mode, dimensionless

J_f = Fracture productivity index, barrel per day per psi

$\bar{p}_f$ = Average pressure in fracture compartment, psi

$\bar{p}_m$ = Average pressure in matrix compartment, psi

k_f = Effective fracture permeability, md

k_m = Effective matrix permeability, md

λ_1, λ_2 = Eigenvalues of the A matrix for the system of ODEs, day^{-1}

ρ = First element of the eigen-vector corresponding to λ_1 the other element is 1, dimensionless

γ = First element of the eigen-vector corresponding to λ_2 the other element is 1, dimensionless

References

Abbott S. 2001. Understanding Analysis. Springer. ISBN: 978-0-387-21506-8

Abramowitz M. and Stegun I. A. 1964. Handbook of Mathematical Functions With Formulas, Graphs and Mathematical Tables. National Bureau of Standards, Applied Mathematics Series 55

Ambrose R.J., Clarkson C.R., Youngblood J.E., Adams R., Nguyen P., Nobakht M. and Biseda B. 2011. Life-Cycle Decline Curve Estimation for Tight/Shale Gas Reservoirs. Paper SPE 140519 presented at the SPE Hydraulic Fracturing Technology Conference and Exhibition, the Woodlands, Texas, USA 24 – 26, January. doi: http://dx.doi.org/10.2118/140519-MS

Amini S. and Valko P. P. 2010. Using Distributed Volumetric Sources to Predict Production from Multiple-Fractured Horizontal Wells Under Non-Darcy Flow Conditions. *SPE J* **15** (01): 105 – 115. doi:10.2118/120110-PA

Anderson D. M., Nobakht M., Moghadam S. and Mattar L., 2010. Analysis of Production Data from Fractured Shale Gas Wells. Paper SPE 131787 presented at the SPE Unconventional Gas Conference, Pittsburgh, Pennyslvania, USA. 23 – 25 February.

Arps, J.J. 1945. Analysis of Decline Curves. *SPE J* **01** (160): 228 - 247. http://dx.doi.org/10.2118/945228-G.

Barenblatt, G. I. and Zheltov, Y. P. 1960. Fundamentals Equations of Filtration of Homogeneous Liquids in Fissured Rocks. *Soviet Physics*, Doklady Vol. 5 page 522.

Becker G. F. and van Orstrand C. E. 1909. Hyperbolic Functions. Smithsonian Institution. (http://hdl.handle.net/2027/nyp.33433069105231)

Bello R. O. and Wattenbarger R. A., 2008. Rate Transient Analysis in Naturally Fractured Shale Gas Reservoirs. Paper SPE 114591 presented at the CIPC/SPE Gas Technology Symposium 2008 Joint Conference, Calgary, Alberta, Canada, 16 – 19 June.

Bello, R. O. 2009. Rate Transient Analysis in Shale Gas Reservoirs with Transient Linear Behavior. PhD Dissertation, Texas A&M University, College Station, Texas, USA.

Bourgeois M. 1992. Well Test Interpretation Using Laplace Space Type Curves. Master's Thesis, Stanford University, Stanford, California, USA

Box G.E., Hunter J.S. and Hunter W. G. 2005. Statistics for Experimenters, John Wiley & Sons. ISBN: 0-471-71813-0.

Bumb A. C. and McKee C. R., 1988. Gas – Well Testing in the Presence of Desorption for Coalbed Methane and Devonian Shale. SPE Formation Evaluation, March 1988, Pg 179 – 185.

Can B. and Kabir C.S. 2014. Containing Data Noise in Unconventional Reservoir Performance Forecasting. Journal of Natural Gas Science and Engineering 18 (2014) 13 – 22. doi: 10.1016/j.jngse.2014.01.010.

Cao F. 2014. Development of a Coupled Two Phase Flow Capacitance Resistance Model, PhD Dissertation. The University of Texas at Austin, Austin, Texas.

Cao F., Luo H. and Lake L. W. 2014. Development of a Fully Coupled Two-Phase Flow Based Capacitance-Resistance Model (CRM). Paper SPE 169485-MS presented at the SPE Improved Oil Recovery Symposium, Tulsa, Oklahoma, USA 12–16 April. http://dx.doi.org/10.2118/169485-MS.

Carlson E. S. and Mercer J. C. 1991. Devonian Shale Gas Production: Mechanisms and Simple Models. *J Pet Tech* **43** (4): 476–482. http://dx.doi.org/10.2118/19311-PA.

Carslaw H. S. and Jaeger J. C. 1959. Conduction of Heat in Solids. Oxford University Press. ISBN: 0-19-853368-3

Cheng Y., Lee W.J. and McVay D.A. 2008. Improving Reserves Estimates from Decline-Curve Analysis of Tight and Multilayer Gas Wells. SPE Reservoir Evaluation. & Engineering. 11 (05): 912 – 920 SPE 108176 – PA. doi: 10.2118/108176-PA.

Churchill R. V. 1958. Operational Mathematics, 3rd Edition. McGraw-Hill Inc. ISBN: 07-010870-6

Cinco H.L., Samaniego F.V. and Dominguez N.A. 1978. Transient Pressure Behavior for a Well with a Finite-Conductivity Vertical Fracture. SPE *J* 18 (04): 253 – 264. SPE 6014-PA. doi: 10.2118/6014-PA

Cipolla C. L., Erdle J. C. and Rubin B.: Reservoir Modeling in Shale Gas Reservoirs, Paper SPE 125530 presented at the 2009 SPE Eastern Regional Meeting held in Charleston, West Virginia, USA 23 – 25 September 2009.

Clark A. J., Lake L.W. and Patzek T.W. 2011. Production Forecasting with Logistic Growth Models. Paper SPE 144790 presented at the SPE Annual Technical Conference and Exhibition, Denver, Colorado USA 30 October – 2 November. doi: 10.2118/144790-MS

Cox S. A., Gilbert J. V., Sutton R. P., and Stoltz R. P., 2002. Reserve Analysis for Tight Gas. Paper SPE 78695 presented SPE Eastern Regional Meeting, Lexington, Kentucky, USA, 23 – 25 October.

Da Prat G., Cinco-Ley H. and Ramey H. J. 1981. Decline Curve Analysis Using Type Curves for Two-Porosity Systems. *SPEJ: 354–362*; doi: 10.2118/9292-PA

de Swaan-O., A. 1976. Analytic Solutions for Determining Naturally Fractured Reservoir Properties by Well Testing. *SPEJ* **16** (3): 117–122; *Trans.,* AIME, **261.**

Doublet L. E., Pande P. K., McCollum T. J. and Blasingame T. A., 1994. Decline Curve Analysis Using Type Curves – Analysis of Oil Well Production Data Using Material Balance Time: Application to Field Cases. Paper SPE 28688 presented at the Petroleum Conference and Exhibition of Mexico, Veracruz, Mexico, 10 – 13 October.

Duong A.N. 2011. Rate – Decline Analysis for Fracture Dominated Shale Reservoirs. SPE Reservoir Evaluation & Engineering 14 (03): 277 – 387 SPE 137748-PA. doi: 10.2118/137748-PA

El-Banbi A. H. 1998. Analysis of Tight Gas Wells. PhD Dissertation, Texas A&M University, College Station, Texas, USA

Ettehad, A., Jablonowski, C., and Lake, L. W. 2010. Gas Storage Facility Design Under Uncertainty. SPE J 05 (03): 155 - 165. http://dx.doi.org/10.2118/123987-PA

Fetkovich M .J., 1980. Decline Curve Analysis Using Type Curves. Journal of Petroleum Technology, June 1980, Pg 1065 – 1077.

Fetkovich M.J. 1980 Decline Curve Analysis Using Type Curves. J Pet Technol 32 (6): 1065 – 1077 SPE 4629-PA. doi: 10.2118/4629-PA

Gringarten A.C. and Ramey, Jr. H.J. 1973. The Use of Source and Green's Functions in Solving Unsteady Flow Problems in Reservoirs. *SPE J* **13** (05): 285 – 296. SPE 3818-PA. doi: 10.2118/3818-PA

Gringarten A.C. and Ramey, Jr. H.J. 1974. Unsteady-State Pressure Distributions Created by a Well with a Single Horizontal Fracture, Partial Penetration or Restricted Entry. SPE Journal 14 (04): 413 – 426. SPE 3819-PA. doi: 10.2118/3819-PA

Gringarten A.C., Ramey, Jr. H.J. and Raghavan R. 1974. Unsteady-State Pressure Distributions Created by a Well with a Single Infinite-Conductivity Vertical Fracture. SPE Journal 14 (04): 347 – 360. SPE 4051-PA. doi: 10.2118/4051-PA

Hagoort J. 2009. The Productivity of a Well with a Vertical Infinite Conductivity Fracture in a Rectangular Closed Reservoir. *SPE J* **14** (04): 715 – 720. SPE 112975. doi: 10.2118/112975-PA

Harrell D.R., Hodgin J.E. and Wagenhofer T. 2004. Oil and Gas Reserves Estimates: Recurring Mistakes and Errors. Paper 91069 presented at the SPE Annual Technical Conference and Exhibition, Houston, 26 – 29 September. doi: 10.2118/91069-MS.

Ilk D. 2010. Well Performance Analysis For Low to Ultra Low Permeability Reservoir Systems. PhD Dissertation, Texas A&M University, College Station, Texas, USA.

Ilk D., Rushing J.A., Perego A.D. and Blasingame T.A. 2008. Exponential vs. Hyperbolic Decline in Tight Gas Sands – Undestanding the Origin and Implications for Reserve Estimates Using Arp's Decline Curves. Paper SPE 116731 presented at the SPE Annual Technical Conference and Exhibition, Denver, Colorado, USA 21 – 24 September. doi: 10.2118/116731-MS

Jensen J.L., Corbett P.W.M., Lake L. W. and Goggin D.J. 2000. Statistics for Petroleum Engineers and Geoscientists. Elsevier Amsterdam-Boston-London-New York-Oxford-San Francisco-Singapore-Sydney-Tokyo. ISBN: 0-444-50552-0.

Johnston D.C. 2006. Stretched Exponential Relaxation Arising from a Continuous Sum of Exponential Decays. *Physical Review* B 74, 184430. doi: 10.1103/PhysRevB.74.184430

Kabir C.S. and Lake L. W. 2011. A Semianalytical Approach to Estimating EUR in Unconventional Reservoirs. Paper SPE 144311 presented at the SPE North American Unconventional Gas Conference and Exhibition, Woodlands, Texas, USA, 14 – 16 June

Kan Wu. 2014. Numerical Modeling of Complex Hydraulic Fracture Development in Unconventional Reservoirs, PhD Dissertation. The University of Texas at Austin, Texas.

Kreyszig E. 2006. Advanced Engineering Mathematics, 9th Edition. John Wiley & Sons, Inc. ISBN: 0-471-48885-2

Kuchuk F. and Biryukov D. 2013. Pressure Transient Tests and Flow Regimes in Fractured Reservoirs. Paper SPE 166296 presented at the SPE Annual Technical Conference and Exhibition, New Orleans, Louisiana, USA, 30 September – 2 October

Kuchuk F. and Biryukov D. 2014. Pressure Transient Behavior of Continuously and Discretely Fractured Reservoirs. SPE Reservoir Evaluation and Engineering 17 (01) 82 – 87 SPE 158096 – PA. doi: 10.2118/158096-PA

Lee W.J. and Sidle R.E. 2010. Gas Reserves Estimation in Resource Plays, SPE Economics & Management (Oct. 2010) 86 - 91

Lewis A. M. and Hughes R. G., 2008. Production Data Analysis of shale Gas Reservoirs. Paper SPE 116688 presented at the SPE Annual Technical Conference and Exhibition, Denver, Colorado, USA, 21 – 24 September.

Mavor M. J. and Cinco H. L. 1979. Pressure Transient Behavior of Naturally Fractured Reservoirs. Paper SPE 7977 presented at the 1979 California Regional Meeting of the SPE, Ventura, California April 18 – 20. doi:10.2118/7977-MS

Mayerhofer M.J., Lolon E. P., Youngblood J. E., and Heinze J. R. 2006. Integration of Microseismic Fracture Mapping Results with Numerical Fracture Network Production Modeling in the Barnett Shale. Paper SPE 102103 presented at the SPE Annual Technical Conference and Exhibition, San Antonio, Texas, 24–27 September. http://dx.doi.org/10.2118/102103-MS.

McKinney P. D., Rushing J. A. and Sanders L. A. 2002 Applied Characterization for Maximizing Reserve Growth and Profitability in Tight Gas Sands: A Paradigm Shift in Development Strategies for Low Permeability Gas Reservoirs, Paper SPE 75708 presented at the SPE Gas Technology Symposium, Calgary, Alberta, Canada 30 April – 2 May.

Medeiros F. Jr., Ozkan E. and Kazemi H. 2010. A Semianalytical Approach to Model Pressure Transients in Heterogeneous Reservoirs. SPE *Res Eval & Eng* **13** (02): 341 – 358

Micheal Eugene Taylor. 1946. Measure Theory and Integration. American Mathematical Society, Providence, Rhode Island. ISBN-13: 978-0-8218-4180-8

Miller M. A., Jenkins C. and Rai R., 2010. Applying Innovative Production Modeling Techniques to Quantify Fracture Characteristics, Reservoir Properties and Well Performance in Shale Gas Reservoirs. SPE Paper 139097 presented the Eastern Regional Meeting, Morgantown, West Virginia, USA, 12 – 14 October. http://dx.doi.org/10.2118/139097-MS

Moridis G. J., Blasingame T. A. and Freeman C.M.: Analysis of Mechanisms of Flow in Fractured Tight-Gas and Shale Gas Reservoirs, Paper SPE 139250 presented at the SPE Latin American and Caribbean Petroleum Engineering Conference held in Lima, Peru, 1 – 3 December 2010.

Myers R.H and Montgomery D.C. 2002. Response Surface Methodology: Process and Product Optimization Using Design of Experiments, John Wiley & Sons. ISBN: 0-470-17446-3.

National Petroleum Council (NPC): Topic Paper number 29, Unconventional Gas, 2007

Navidi W. 2008. Statistics for Engineers and Scientists. McGraw – Hill. ISBN: 978-0-07-337633-2

Nguyen, A. P. 2012. Capacitance Resistance Modeling for Primary Recovery, Waterflood, and Water/CO_2 Flood. PhD Dissertation. The University of Texas at Austin, Austin, Texas, USA.

Nobakht M., Ambrose R., Clarkson C.R., Youngblood J. and Adams R. 2013. Effect of Completion Heterogeneity in a Horizontal Well With Multiple Fractures on the Long-Term Forecast in Shale-Gas Reservoirs. *J. Cdn. Pet. Tech*. **52** (06): 417 – 425. doi: http://dx.doi.org/10.2118/149400-PA

Odeh, A. S. 1965. Unsteady-State Behavior of Naturally Fractured Reservoirs. *SPE J* : 60 - 66. doi:10.2118/966-PA

Ogunyomi B. A. 2010. Petroleum Development Optimization under Uncertainty: Integrating Multi-Compartment Tank Models in Mixed Integer Non-Linear Programs. Master's Thesis. The University of Texas at Austin, Austin, TX, USA

Ogunyomi B.A., Kabir. C.S., Patzek T., and Lake L.W. 2014. History Matching and Rate Forecasting in Unconventional Oil Producing Reservoirs Using an Approximate Analytical Solution to the Double Porosity Model. Paper SPE 171031-MS presented at the SPE Eastern Regional Meeting, Charlston, West Virginia, USA. 21 – 23 October 2014.

Ogunyomi, B. A., Jablonowski, C. J., and Lake, L. W. 2011. Field Development Optimization Under Uncertainty: Screening-Models for Decision Making. Paper SPE 146788 presented at the Annual Technical Conference and Exhibition, 30 October – 2 November, Denver, Colorado. http://dx.doi.org/10.2118/146788-MS

Ogunyomi, B. A., Song, S., La, N., Lake, L. W., and Kabir, C. S. 2014. A New Approach to Modeling Production Decline in Unconventional Formations. Paper SPE 170899 presented at the Annual Technical Conference and Exhibition, Amsterdam, The Netherlands 27 – 29 October. doi:10.2118/170899-MS

Olanrewaju J. S. and Lee W. J., 1989. New Pressure – Testing Analysis Model for Dual – Porosity Reservoirs. Paper SPE 15634 presented at the SPE Annual Technical Conference and Exhibition, New Orleans, USA, 5 – 8 October.

Ozkan E. 1988. Performance of Horizontal Wells. PhD Dissertation The Univeristy of Tulsa, Tulsa, USA

Ozkan E., Ohaeri U. and Raghavan R. 1987. Unsteady Flow to a Well-Produced at a Constant Pressure in a Fractured Reservoir. *SPE Form Eval* **2** (2): 186–200. http://dx.doi.org/10.2118/9902-PA.

Ozkan E., Raghavan R. and Apaydin O. G. 2010. Modeling of Fluid Transfer from Shale Matrix to Fracture Network. Paper SPE 134830 presented at the SPE Annual Technical Conference and Exhibition, Florence, Italy, 19 – 22 September

Palacio, J. C. and Blasingame, T. A. 1993. Decline-Curve Analysis with Type Curves - Analysis of Gas Well Production Data. Paper SPE 25909 presented at SPE Joint Rocky Mountain

Regional and Low Permeability Reservoir Symposium, Denver, Colorado USA April 26 - 28. doi:10.2118/25909-MS

Patzek T.W., Male F., and Marder M. 2014. Gas Production from Barnett Shale Obeys a Simple Scaling Theory. Proceedings of the National Academy of Sciences of the United States of America. *PNAS* December 3, 2013 vol. 110 no. 49 19731-19736 doi:10.1073/pnas.1313380110.

Ramey H.J. and Gringarten A.C. 1975. Effect of High Volume Vertical Fractures on Geothermal Steam Well Behavior. Proc., Second United Nations Symposium on the Use and Development of Geothermal Energy, San Francisco, May 20-29

Rotondi M., Cominelli A., Di Giorgio C., Rossi R., Vignati E. and Carati B.: The Benefits of Integrated Asset Modeling: Lesson Learned from Field Case, paper SPE 113831 presented at the 2008 SPE Europe/EAGE Annual Conference and Exhibition held in Rome, Italy 9 – 12 June 2008.

Rushing J.A., Perego A. D., Sullivan R.B. and Blasingame T.A. 2007. Estimating Reserves in Tight Gas Sands at HP/HT Reservoir Conditions: Use and Misuse of an Arps Decline Curve Methodology. Paper SPE 109625 presented at the SPE Annumal Technical Conference and Exhibition, Anaheim, California, USA 11 – 14 November. doi: 10.2118/109625-MS

Samandarli, O., Al-Ahmadi H., and Wattenbarger R. A. 2011. A New Method for History Matching and Forecasting Shale Gas Reservoir Production Performance with a Dual Porosity Model. Paper SPE 144335 presented at the SPE North American Gas Conference and Exhibition, the Woodlands, Texas, USA, 12 – 16 June. http://dx.doi.org/10.2118/144335-MS.

Saputelli L., Lujan L., Garibaldi L., Smyth J., Ungredda A., Rodriguez J., and Cullick S.: How Integrated Field Studies Help Asset Teams Make Optimal Field Development Decisioins, paper SPE 110250 presented at the 2008 SPE Western Regional and Pacific Section AAPG Joint Meeting held in Bakersfield, California, USA, 31 March – 2 April 2008.

Sayarpour M., Zuluaga E., Kabir C.S. and Lake L.W. 2007. The Use of Capacitance –Resistive Models for Rapid Estimation of Waterflood Performance and Optimization. Paper SPE 110081 presented at the SPE Annual Technical Conference and Exhibition, Anaheim, California, USA 11 – 14 November 2007. doi: 10.2118/110081-MS

Seborg, D. E., Edgar, T. F., and Mellichamp, D. A. 2003. Process Dynamic and Control, 2nd edition. Wiley, John & Sons, Inc., New York. ISBN-13: 9780471000778.

Song D. H. 2014. Using Simple Models to Describe Oil Production from Unconventional Reservoirs. Master’s Thesis, The University of Texas at Austin, Austin, Texas, USA

Stehfest H. 1970. Numerical Inversion of Laplace Transforms. Communications of the ACM. **13** (1) 47 – 49. doi: http://dx.doi.org/10.1145/361953.361969

Tsoularis A. and Wallace J. 2002. Analysis of Logistic Growth Models. Mathematical Biosciences 179 (1) 21 – 55.

Valko P. P. 2010. A Better Way to Forecast Production From Unconventional Gas Wells. Paper SPE 134231-MS presented at the SPE Annual Technical Conference and Exhibition, Florence, Italy 19 – 22 September. doi: 10.2118/134231-MS

Van Everdingen A. F. and Hurst W. 1949. The Application of the Laplace Transformation to Flow Problems in Reservoirs. SPE JPT. **1** (12) 305-324. http://dx.doi.org/10.2118/949305-G

Walsh M. P. and Lake L. W. 2003. A Generalized Approach to Primary Hydrocarbon Recovery. Elsevier. ISBN: 978-0-444-50683-2.

Warren J.E. and Root P.J. 1963. The Behavior of Naturally Fractured Reservoirs. *SPE J.* **3** (3): 245–255. http://dx.doi.org/10.2118/426-PA.

Wattenbarger R. A., El-Banbi A. H, Villegas M.E., and Maggard J. B. 1998. Production Analysis of Linear Flow into Fractured Tight Gas Wells. Paper SPE 39931 presented at the 1998 SPE Rocky Mountain Regional/Low permeability Reservoirs Symposium and Exhibition, Denver, Colorado, 5–8 April. http://dx.doi.org/10.2118/39931-MS.